

FRACTURE EFFECT LIMITATION ON RESIDUAL OIL SATURATION &  
VISUALIZATION BY COMPUTER TOMOGRAPHY

A THESIS SUBMITTED TO  
THE GRADUATE SCHOOL OF NATURAL AND APPLIED SCIENCES  
OF  
MIDDLE EAST TECHNICAL UNIVERSITY

SERHAT CANBOLAT

IN PARTIAL FULFILLMENT OF THE REQUIREMENTS  
FOR  
THE DEGREE OF DOCTOR OF PHILOSOPHY  
IN  
PETROLEUM AND NATURAL GAS ENGINEERING

JUNE 2018



Approval of the thesis:

**FRACTURE EFFECT LIMITATION ON RESIDUAL OIL SATURATION  
& VISUALIZATION BY COMPUTER TOMOGRAPHY**

submitted by **SERHAT CANBOLAT** in partial fulfillment of the requirements for the degree of **Doctor of Philosophy in Petroleum and Natural Gas Engineering Department, Middle East Technical University** by,

Prof. Dr. Halil KALIPÇILAR \_\_\_\_\_  
Dean, Graduate School of **Natural and Applied Sciences**

Prof. Dr. Serhat AKIN \_\_\_\_\_  
Head of Department, **Petroleum and Natural Gas Engineering**

Prof. Dr. Mahmut PARLAKTUNA \_\_\_\_\_  
Supervisor, **Petroleum and Natural Gas Engineering**

**Examining Committee Members**

Assoc.Prof. Dr. Çağlar SINAYUÇ \_\_\_\_\_  
Petroleum and Natural Gas Eng. Dept., METU

Prof. Dr. Mahmut PARLAKTUNA \_\_\_\_\_  
Petroleum and Natural Gas Eng. Dept., METU

Assist.Prof. Dr. İsmail DURGUT \_\_\_\_\_  
Petroleum and Natural Gas Eng. Dept., METU

Assoc.Prof. Dr. Emre ARTUN \_\_\_\_\_  
Petroleum and Natural Gas Eng. Dept.,  
(METU Northern Cyprus Campus)

Assist.Prof. Dr. Tuna EREN \_\_\_\_\_  
Petroleum and Natural Gas Eng. Dept.,  
İzmir Katip Çelebi University

**Date:** 25 June 2018

**I hereby declare that all information in this document has been obtained and presented in accordance with academic rules and ethical conduct. I also declare that, as required by these rules and conduct, I have fully cited and referenced all material and results that are not original to this work.**

Name, Last Name: SERHAT CANBOLAT

Signature :

## **ABSTRACT**

### **FRACTURE EFFECT LIMITATION ON RESIDUAL OIL SATURATION & VISUALIZATION BY COMPUTER TOMOGRAPHY**

CANBOLAT, Serhat

Ph.D. Department of Petroleum and Natural Gas Engineering

Supervisor: Prof.Dr.Mahmut PARLAKTUNA

June 2018, 205 pages

Recovery estimations of fractured reservoirs are considered to be extremely challenging due to complexity and heterogeneity of the geological patterns. Most reservoirs consist of natural and artificial fractures, including isolated microscopic fissures. These fractures form complicated paths for reservoir characterization and fluid movement that ultimately impacts production performance and ultimate recovery.

In naturally fractured reservoirs, the matrix is the dominant storage area, while the main flowing channels are fractures. Oil production from fractured reservoirs results in varying saturation values throughout the reservoir. This is due to the microscopic fissures and heterogeneity of the fracture environment, which could not be swept thoroughly. Higher production / injection ratios also enhance the fingering effect by passing oil through the reservoir. To get rid off fingering or minimize, a polymer gel application is applied to the fractured cores to reduce residual oil saturation and to increase oil production.

In this study, naturally and artificially fractured cores were used. Analytical and experimental calculations were performed in order to understand the physical

structure of the cores. After the characterization of the fractured cores a polymer gel application is done to limit the fracture effect and increase oil recovery.

Equivalent fracture aperture measurements were done by microscope and compared with the analytical calculations with cubic law. Using CT scanner images, matrix porosity and saturation calculations were done. Matrix permeability and fracture permeability values were found before and after the polymer gel injection application.

Measurements of the fractures were completed by using microscope to verify the analytical calculations. Laboratory results were defined by the equation developed for predicting equivalent fracture apertures with and without polymer gel as Improved Cubic Law (ICL). Shrinkage in equivalent fracture aperture was also defined by ICL observed by microscope.

Using ICL, analytical calculations were done in different environments. Equivalent fracture apertures were calculated for all the experimental flow rates under laminar flow. ICL has worked with the fractured cores flow definition whereas not for homogeneous cores.

There is a direct relation between fracture permeability with equivalent fracture aperture. The experiments with different environments (initially oil saturated and water saturated) in the cores, with calculations of equivalent fracture aperture and fracture permeability, showed similar results.

The effect of polymer gel conformance to increase recovery by decreasing equivalent fracture aperture plugging was proven. Moreover, the decrease in equivalent fracture aperture in the cores were resulted in decreasing fracture permeability respectively.

**Keywords:** Natural Fracture, Fracture Aperture, Polymer Gel Injection, Reservoir Characterization, Computer Tomography (CT), Improved Cubic Law (ICL)

## ÖZ

### **ÇATLAK ETKİSİNİN SINIRLANDIRILARAK, REZERVDE KALAN PETROL DOYMUŞLUĞUNUN, BILGISAYARLI TOMOGRAFI İLE GÖZLENMESİ**

CANBOLAT, Serhat  
Doktora, Petrol ve Doğal Gaz Mühendisliği Bölümü  
TezYöneticisi: Prof.Dr.Mahmut PARLAKTUNA

Haziran 2018, 205 sayfa

Çatlaklı rezervuarlardaki kesin üretim ve kurtarım tahmini yapmanın oldukça zor olmasının sebebi, kompleks ve heterojen yapıların bulunmasıdır. Karbonatlı rezervler çoğunlukla çatlaklı ve izole edilmiş çatlaklı yapılardan oluşmaktadır. Bu çatlaklar sıvı akışı için kompleks yollar doğurması neticesi ile, rezervuar karakterizasyonu, maksimum kurtarım ve üretim performansı için önem arz etmektedir.

Çatlaklı rezervuarlarda, çatlak ana akış kanalı, matris ise daha çok depolama alanıdır. Çatlaklı rezervuarlarda petrol üretimi rezerv içinde yoğun veya seyrek petrol doymuşluğu gösterir. Bunun sebebi de mikro ölçekteki yarıkların ve heterojen yapıdaki çatlakların iyi süpürülebilmesidir. Yüksek enjeksiyon/üretim hızları da parmaklaşma etkisiyle petrolün süpürülmeden rezervde kalmasına neden olur. Bu etkileri azaltmak/bertaraf etmek için polimer jel uygulaması çatlağa tatbik edilir, bu sayede kalan petrol doymuşluğu oranı azaltılır ve petrol üretimi arttırılır.

Bu çalışmada doğal ve yapay çatlaklı karotlarla yapılan analitik ve deneysel hesaplamalar, karotların yapısı hakkında bilgi sahibi olmamızı sağladı. Karakterizasyonu yapılan karotlara polimer jel uygulaması yapıldı ve çatlak sınırlaması etkisiyle üretim artışı sağlandı. Eşdeğer çatlak aralığı ölçümleri mikroskopla ölçüldü ve analitik yoldan kübik yasası ile hesaplanarak doğrulandı. Bilgisayarlı Tomografi (BT) görüntüleri kullanılarak, matris gözeneklilik ve doymuşluk hesaplamaları yapıldı. Polimer jel uygulaması öncesinde ve sonrasında matris ve çatlak geçirgenlikleri hesaplandı.

Çatlak ölçümleri, analitik hesaplamaları doğrulamak için mikroskop kullanılarak tamamlandı. Laboratuvar sonuçları, Geliştirilmiş Kübik Yasası (GKY) olarak polimer jel uygulanan ve uygulanmayan eşdeğer çatlak aralıklarını tahmin etmek üzere geliştirilen denklem ile yapıldı. Eşdeğer çatlak aralıklarındaki küçülme, mikroskop yardımıyla gözlemlenerek, GKY ile de teyit edilmiştir.

GKY kullanılarak analitik hesaplamalar, farklı akışkanlarla doyurulmuş ortamlarda yapıldı. Eşdeğer çatlak aralığı laminar akış altında tüm deneyler için hesaplandı. GKY, homojen karotlardan çok, çatlaklı karotlarda akışı tanımlamada daha başarılı olmuştur.

Çatlak geçirgenliği ve eşdeğer çatlak aralığı arasında doğrusal bir bağlantı vardır. Kıyaslanan farklı doymuşluk değerlerine sahip, karot deneylerinde (önceden suyla doyurulmuş ve önceden petrolle doyurulmuş) eşdeğer çatlak aralığı ve çatlak geçirgenliği hesaplamaları benzer sonuçlar vermiştir

Polimer jel uygunluğunda kurtarımın artması, yapılan yapay çatlaklı karot deneylerinde, eşdeğer çatlak aralığının azalması/tıkanması ile ispatlandı. Karotlardaki çatlak aralığının azalması, çatlak geçirgenliğininin de azalmasıyla sonuçlanmıştır..

**Anahtar Kelimeler:** Doğal Çatlak, Çatlak Aralığı, Polimer Jel Enjeksiyonu, Bilgisayarlı Tomografi (BT), Rezervuar Karakterizasyonu, Geliştirilmiş Kübik Yasası (GKY)

## ACKNOWLEDGMENTS

First of all, I would like to express my sincere gratitude to my supervisor Dr.Mahmut PARLAKTUNA for his guidance, insightful suggestions and comments throughout the study.

Besides, many thanks go to Dr.Çağlar SINAYUÇ, for his valuable suggestions, insightful comments and guidance throughout the study for this Ph.D. study.

Moreover, many thanks to Dr.Emre ARTUN, for his valuable suggestions and comments on this Ph.D. study.

I wish to express my sincere thanks to my committee members, Dr.İsmail DURGUT and Dr.Tuna EREN for their comments and suggestions over this study.

In addition special thanks go to Dr.Hasan ÖZTÜRK for his support during the study.

Also, the technicians, Mr.Naci DOĞRU, Mr.Hasan TURMUŞ and Mr.Murat AKIN's support during the experimental study is unforgettable.

Furthermore, special thanks go to Northern Cyprus starting from, Dr.Cavit ATALAR, Dr.Salih SANER, Mr.Hilmi DİNDAR and Mr.Arif ÖZYANKI for their encouraging motivation and the energy provided during the final stage of the study.

I am grateful to my family for their material and moral support giving me the confidence during the study.

Finally, many thanks and apologies to others whom I may have inadvertently forgotten to mention.

**To Canbolats...**

## TABLE OF CONTENTS

ABSTRACT .....	V
ÖZ.....	VII
ACKNOWLEDGMENTS .....	IX
TABLE OF CONTENTS .....	XI
LIST OF FIGURES .....	XIII
LIST OF TABLES.....	XVII
LIST OF SYMBOLS.....	XX
LIST OF ABBREVIATIONS.....	XXII
CHAPTERS	
1.INTRODUCTION.....	1
2. COMPUTER TOMOGRAPHY IN CORE ANALYSIS .....	5
2.1 Computer Tomography .....	5
2.3 CT scan application.....	8
2.4 Porosity determination and core characterization.....	8
2.5 Determination of the two-phase saturation .....	9
3.BEHAVIOUR OF NATURALLY FRACTURED RESERVOIRS .....	11
3.1 Naturally Fractured Reservoirs .....	11
3.2 Analytical Definition of Fluid Flow in Natural Fractures .....	13
4.POLYMER GEL TREATMENT .....	21
4.1 Water Treatment .....	21
4.2 Field Applications.....	23
5.MICROSCOPE USAGE FOR EQUIVALENT APERTURES.....	31
6.STATEMENT OF THE PROBLEM.....	35
7.EXPERIMENTAL DESIGN.....	37
7.1Materials .....	37
7.2Experimental set-up .....	39
7.3Experimental Procedure.....	41
8.EXPERIMENTAL DATA ANALYSIS.....	47
8.1 Discussion on Naturally Fractured vs. Non- Fractured Core Plugs....	48
8.2 Porosity Calculation of Artificially Fractured Cores .....	68
8.3 Analysis of Polymer Gel Addition.....	77
8.4 Summary of the Results .....	95
8.5 Improved Cubic Law for Fractured Medium.....	100

9.CONCLUSIONS AND RECOMENDATIONS.....	105
REFERENCES .....	107
APPENDICES .....	115
A.CORE SAMPLE XRF ANALYSIS .....	115
B.INITIALY WATER SATURATED DECANE FLOODED NATURALLY FRACTURED CT SCAN IMAGES OF CORE#2.....	117
C.SAMPLE FRACTURE APERTURE & PERMEABILITY CALCULATION .....	137
D.INITIALY WATER SATURATED DECANE FLOODED ARTIFICIALLY FRACTURED CT NUMBERS OF CORE#3 .....	141
E.CORE SAMPLE NUMERICAL POROSITY CALCULATION CODE BY MATLAB .....	183
CURRICULUM VITAE.....	205

## LIST OF FIGURES

### FIGURES

Figure 2.1 Computer Tomography. ....	6
Figure 2.2 CT radiograph scan (left) and axial scans (right) showing damaged core within core tube after Withjack et.al. (2003). ....	6
Figure 2.3 CT scans of a heterogeneous (left) and damaged plug (right) after Withjack et.al. (2003). ....	6
Figure 2.4 Core plug scans in orthogonal planes (0 and 90 degrees) after.....	7
Figure 3.1 Conventional and Fractured Reservoirs after Akbar, et al., (1993). ....	11
Figure 3.2 Water-Cut in the Fractured and Conventional Reservoirs after Buckley and Liu, (1988). ....	12
Figure 3.3 Parallel Plate Flow Model for Fractures. ....	13
Figure 3.4 Experimentally Measured Effective Aperture as a Function of the Reynolds Number after Renshaw et al., (2000).....	16
Figure 3.5 Matrix Block Containing a Single Fracture, Fracture1 ( $\alpha = 0$ ), Fracture 2 ( $\alpha \neq 0$ ) after van Golf-Racht, (1982).....	19
Figure 5.1 The Autofocus Function is Defined over a range of Focal Distance Encompassing the in-focus Imaging Position after Chen, (1989). ....	32
Figure 5.2 Equivalent Fracture Aperture Measurement by Autofocus Imaging Position. ....	33
Figure 5.3 Autofocused Image of the Core Sample.....	34
Figure 7.1 Original CT Slice Views of Core#2; a) 2 mm from the inlet, b) 5 mm from the inlet, c) 5 mm away from the outlet, d) 2 mm from the inlet.....	38
Figure 7.2 Original CT Slice Views of Core#8 a) 2 mm from the inlet, b) 5 mm from the inlet, c) 5 mm away from the outlet, d) 2 mm from the inlet.....	38
Figure 7.3 Original CT Slice Views of Core#8. ....	39
Figure 7.4 Experimental Set-Up Schematic. ....	40
Figure 7.5 Photographs of the Core-flood Experimental Set-Up. ....	40
Figure 7.6 CT scanner HITACHI Radix Turbo. ....	41
Figure 7.7 a) Polymer Gel Amount b) Preparation Equipment (Magnetic Stirrer) c)Prepared Gel. ....	46
Figure 7.8 After the Polymer Gel Injection Experiment, Artificially Fractured ...	46
Figure 8.1 CT Scan Images of the Same Cross-Section from Different Stages of a Given Experiment: From left to right: dry scan (top left), 100% water saturated (top right), irreducible water saturation (bottom left), after waterflooding (bottom right). ....	49
Figure 8.2 CT Scan Images of Core#8, Dry ( $CT_{dry}$ ). ....	56

Figure 8.3 CT Scan Images of Core#8, 100% Water Saturated ( $CT_{wsat}$ ).....	57
Figure 8.4 CT Scan Images of Core#8, 100% n-Decane Saturated ( $CT_o$ ).....	58
Figure 8.5 CT Scan Images of Core#8, Irreducible Water Saturated ( $CT_x$ ). ....	59
Figure 8.6 CT Scan Images of Core#8, Waterflooded ( $CT_x$ ).....	60
Figure 8.7 Change in Porosity and Water Saturation along Core#8.....	61
Figure 8.8 Change in Porosity and Water Saturation along Core #2.....	61
Figure 8.9 n-Decane and Water Production values of Run #1. ....	62
Figure 8.10 n-Decane and Water Production values of Run #3. ....	62
Figure 8.11 n-Decane and Water Production values of Run #2. ....	63
Figure 8.12 n-Decane and Water Production values of Run #4. ....	63
Figure 8.13 Equivalent Fracture Aperture and Permeability for Run #1.....	66
Figure 8.14 Equivalent Fracture Aperture and Permeability for Run #2.....	66
Figure 8.15 Equivalent Fracture Aperture and Permeability for Run #3.....	67
Figure 8.16 Equivalent Fracture Aperture and Permeability for Run #4.....	67
Figure 8.17 Naturally Fractured Core#2 Fracture Aperture Measurement by Microscope.....	68
Figure 8.18 CT Scan Images Arificially Fractured Core#3 Left Half Dry ( $CT_{dry}$ ). 71	
Figure 8.19 CT Scan Images of Arificially Fractured Core#3 Right Half Dry ( $CT_{dry}$ ). ....	72
Figure 8.20 CT Scan Images of Arificially Fractured Core#3 Left Half Water Saturated( $CT_{wsat}$ ).....	73
Figure 8.21 CT Scan Images of Arificially Fractured Core#3 Right Half Water Saturated ( $CT_{wsat}$ ).....	74
Figure 8.22 Permeability Measurement of Core#3.....	78
Figure 8.23 Permeability Measurement of Artificially Fractured Core#3.....	78
Figure 8.24 Permeability Reduction after 4,500 ppm Polymer Gel Injection to Artificially Fractured Core#3.....	79
Figure 8.25 Change in Porosity and Water Saturation along Core#3.....	79
Figure 8.26 0.2 ml/min Injection Rate, Production in Artificially Fractured Core#3 after Gel Injection Run#5.....	80
Figure 8.27 Artificially Fractured Core#3 0.2 ml/min Injection Rate after Gel Injection, Recovery and Equivalent Fracture Aperture Run#5.....	81
Figure 8.28 Artificially Fractured Core#3 0.2 ml/min Injection Rate after Gel Injection, Fracture Permeability Run#5. ....	82
Figure 8.29 Artificially Fractured Core#3 Fracture Aperture Measurement by Microscope.....	82
Figure 8.30 Permeability Measurement of Core#7.....	84
Figure 8.31 Permeability Measurement of Artificially Fractured Core#7.....	84
Figure 8.32 Permeability Reduction after 4,500 ppm Polymer Gel Injection to ..	84
Figure 8.33 Change in Porosity and Water Saturation along Core#7.....	85
Figure 8.34 0.2 ml/min Injection Rate, Production in Artificially Fractured Core#7after Gel Injection. ....	85

Figure 8.35 Artificially Fractured Core#7 0.2 ml/min Injection Rate, Recovery and Equivalent Fracture Aperture.....	88
Figure 8.36 Artificially Fractured Core#7 0.2 ml/min Injection Rate, Fracture Permeability.....	88
Figure 8.37 Artificially Fractured Core#7 Fracture Aperture Measurement by Microscope. ....	89
Figure 8.38 Permeability Measurement of Artificially Fractured Core#5.....	90
Figure 8.39 Permeability Reduction after 4,500 ppm Polymer Gel Injection to Artificially Fractured Core#5. ....	91
Figure 8.40 Change in Porosity and Water Saturation along Core#5.....	91
Figure 8.41 0.2 ml/min Injection Rate, Production in Core#5 after Gel Injection. ....	92
Figure 8.42 Core#5 Fracture Aperture Measurement by Microscope. ....	93
Figure 8.43 Core#5 0.2 ml/min Injection Rate after Gel Injection, Recovery and Equivalent Fracture Aperture.....	94
Figure 8.44 Core#5 Fracture Aperture Measurement by Microscope after Gel Injection. ....	94
Figure 8.45 Core#5 0.2 ml/min Injection Rate after Gel Injection, Fracture Permeability.....	95
Figure 8.46 Tortuosity of Rock. ....	102
Figure B.1 CT Slice Views of Core#2 Dry.....	117
Figure B.2 CT Slice Views of Core#2 Water Saturated.....	118
Figure B.3 CT Slice Views of Core#2 Decane Flooded.....	119
Figure B.4 CT Slice Views of Core#2 Dry Scanned. ....	120
Figure B.5 CT Slice Views of Core#2 Decane Saturated.....	121
Figure B.6 CT Slice Views of Core#2 Water Flooded. ....	122
Figure E.1 Porosity Calculation of CT Slice Views of 0 and 3 for Core#2. ....	185
Figure E.2 Porosity Calculation of CT Slice Views of 4 and 5 for Core#2. ....	185
Figure E.3 Porosity Calculation Code of CT Slice Views of Core#2. ....	185
Figure E.4 Porosity Calculation Code of CT Slice Views of Dry, Wet, Difference, for Core#5. ....	186
Figure E.5 Porosity Calculation Code of CT Slice Views of Dry, Wet, Difference, for Core#5. ....	187
Figure E.6 Porosity Calculation Code of CT Slice Views of Dry, Wet, Difference, for Core#5. ....	188
Figure E.7 Saturation Calculation Code of CT Slice Views of Saturation (left), 100% Decane (center), 100% Water (right) for Core#5.....	191
Figure E.8 Saturation Calculation Code of CT Slice Views of Saturation (left), 100% Decane (center), 100% Water (right) for Core#5.....	192
Figure E.9 Saturation Calculation Code of CT Slice Views of Saturation (left), 100% Decane (center), 100% Water (right) for Core#5.....	193
Figure E.10 Saturation Calculation Code of CT Slice Views of Saturation (left), 100% Decane (center), 100% Water (right) for Core#5.....	196

Figure E.11 Saturation Calculation Code of CT Slice Views of Saturation (left),  
100% Decane (center), 100% Water (right) for Core#5. ....197  
Figure E.12 Saturation Calculation Code of CT Slice Views of Saturation (left),  
100% Decane (center), 100% Water (right) for Core#5. ....198  
Figure E.13 Saturation Calculation Code of CT Slice Views of Saturation (left),  
100% Decane (center), 100% Water (right) for Core#5. ....201  
Figure E.14 Saturation Calculation Code of CT Slice Views of Saturation (left),  
100% Decane (center), 100% Water (right) for Core#5. ....202  
Figure E.15 Saturation Calculation Code of CT Slice Views of Saturation (left),  
100% Decane (center), 100% Water (right) for Core#5. ....203

## LIST OF TABLES

### TABLES

Table 4.1 The Summary of WSO Polymer Gel Application. ....	29
Table 7.1 Porosity and permeability values of core plugs. ....	38
Table 7.2 Porosity and permeability values of artificially fractured core plugs. ....	38
Table 7.3 Experimental Sequence of Naturally/Artificially Fractured Core Plugs. ....	44
Table 7.4 The Description of all Sydansk’s Gel Codes,1998. ....	45
Table 7.5 Tests Done With Marcit Gel Mixtures and Effect Code after Demir, 2008. ....	45
Table 7.6 X-Linker-Polymer Concentration Ratios after Demir, 2008. ....	45
Table 8.1a CT Numbers of Core#8. ....	50
Table 8.2 CT Numbers of Core#8 for Saturation Calculations. ....	54
Table 8.3 CT Numbers of Core#2 for Saturation Calculations. ....	55
Table 8.4 CT Numbers of Core#2 & #8 for Saturation Calculations. ....	56
Table 8.5 CL Rates at 0.1 ml/min Pump injection in Core#2 (Run #1). ....	65
Table 8.6 CT Numbers of Artificially Fractured Core#3 ....	69
Table 8.7 CT Numbers of Artificially Fractured Core#3 ....	69
Table 8.8a CT Numbers of Artificially. ....	70
Table 8.9 CT Numbers of Artificially Fractured Core#7 ....	75
Table 8.10 CT Numbers of Artificially Fractured Core#7 ....	76
Table 8.11a CT Numbers of Artificially. ....	76
Table 8.12 Cubic Law Rates at 0.2 ml/min Pump injection in Artificially Fractured Core#3 Run#5. ....	81
Table 8.13 Cubic Law Rates at 0.2 ml/min Pump injection in Artificially Fractured Core#7. ....	87
Table 8.14 Cubic Law Rates at 0.2 ml/min Pump injection in Core#5. ....	92
Table 8.15 The Comparison of Average Porosity Numbers by CT and Experimental Measurements. ....	96
Table 8.16 Experimental and CT Scan Calculated Results of the Final Saturations of the Cores. ....	97
Table 8.17 Summary of Equivalent Fracture Aperture and Permeability Calculation by Cubic Law for All Cores. ....	99
Table 8.18 Summary of Experimentally Measured Permeability and Fracture Permeability Calculation by Cubic Law for All Cores. ....	100
Table 8.19 Summary of Measured Permeability and Fracture Permeability Calculation by Cubic Law for All Cores. ....	101
Table 8.20 C Coefficient Calculation for Improved Cubic Law for All Cores. ..	103

Table A. 1 Core Sample Element Analysis. ....	115
Table B.1 CT Numbers of Slices for Core#2 Porosity Calculation. ....	123
Table B.2 CT Numbers of Slices for Core#2 Saturation Calculation. ....	124
Table B.3 CT Numbers of Slices for Core#2 Saturation Calculation. ....	125
Table B.4 CT Numbers of Slices for Core#2 Saturation Calculation. ....	126
Table B.5 CT Numbers of Slices for Core#2 Porosity Calculation. ....	127
Table B.6 CT Numbers of Slices for Core#2 Saturation Calculation. ....	128
Table B.7 CT Numbers of Slices for Core#2 Saturation Calculation (ios). ....	129
Table B.8 CT Numbers of Slices for Core#8 Porosity Calculation. ....	130
Table B.9 CT Numbers of Slices for Core#8 Saturation Calculation. ....	131
Table B.10 CT Numbers of Slices for Core#8 Saturation Calculation. ....	132
Table B.11 CT Numbers of Slices for Core#8 Saturation Calculation. ....	133
Table B.12 CT Numbers of Slices for Core#8 Porosity Calculation. ....	134
Table B.13 CT Numbers of Slices for Core#8 Saturation Calculation. ....	135
Table B.14 CT Numbers of Slices for Core#8 Saturation Calculation. ....	136
Table C.1 Cubic Law Rates at 0.1 ml/min Pump injection in Core#2 (Run#1). .	138
Table C.2 Initially Oil Saturated Cubic Law Rates at 0.1 ml/min Pump injection in Core#2 (Run#2). ....	138
Table AC.3 Initially Water Saturated Cubic Law Rates at 0.1 ml/min Pump injection in Core#8 (Run#3). ....	139
Table C.4 Initially Oil Saturated Cubic Law Rates at 0.1 ml/min Pump injection in Core#8 (Run#4). ....	139
Table D.1 CT Numbers of Slices for Core#3 Porosity Calculation. ....	141
Table D.2 CT Numbers of Slices for Core#3 Saturation Calculation. ....	142
Table D.3 CT Numbers of Slices for Core#3 Saturation Calculation. ....	143
Table D.4 CT Numbers of Slices for Core#3 Saturation Calculation. ....	144
Table D.5 CT Numbers of Slices for Core#3 Porosity Calculation. ....	145
Table D.6 CT Numbers of Slices for Core#3 Saturation Calculation. ....	146
Table D.7 CT Numbers of Slices for Core#3 Saturation Calculation. ....	147
Table D.8 CT Numbers of Slices for Core#3 Saturation Calculation. ....	148
Table D.9 CT Numbers of Slices for Core#3 Porosity Calculation. ....	149
Table D.10 CT Numbers of Slices for Core#3 Saturation Calculation. ....	150
Table D.11 CT Numbers of Slices for Core#3 Saturation Calculation. ....	151
Table D.12 CT Numbers of Slices for Core#3 Saturation Calculation. ....	152
Table D.13 CT Numbers of Slices for Core#7 Porosity Calculation. ....	158
Table D.14 CT Numbers of Slices for Core#7 Saturation Calculation. ....	159
Table D.15 CT Numbers of Slices for Core#7 Saturation Calculation. ....	160
Table D.16 CT Numbers of Slices for Core#7 Saturation Calculation. ....	161
Table D.17 CT Numbers of Slices for Core#7 Saturation Calculation after Gel Injection and Production. ....	162
Table D.18 CT Numbers of Slices for Core#7 Porosity Calculation. ....	163
Table D.19 CT Numbers of Slices for Core#7 Saturation Calculation. ....	164
Table D.20 CT Numbers of Slices for Core#7 Saturation Calculation. ....	165

Table D.21 CT Numbers of Slices for Core#7 Saturation Calculation. ....	166
Table D.22 CT Numbers of Slices for Core#7 Saturation Calculation after Gel Injection and Production. ....	167
Table D.23 CT Numbers of Slices for Core#7 Porosity Calculation. ....	168
Table D.24 CT Numbers of Slices for Core#7 Saturation Calculation. ....	169
Table D.25 CT Numbers of Slices for Core#7 Saturation Calculation. ....	170
Table D.26 CT Numbers of Slices for Core#7 Saturation Calculation. ....	171
Table D.27 CT Numbers of Slices for Core#7 Saturation Calculation after Gel Injection and Production. ....	172
Table D.28 CT Numbers of Slices for Core#5 Porosity Calculation. ....	178
Table D.29 CT Numbers of Slices for Core#5 Saturation Calculation. ....	179
Table D.30 Saturation Calculation of CT Numbers of Slices for Core#5 Before Production. ....	180
Table D.31 Saturation Calculation of CT Numbers of Slices for Core#5 After Production. ....	181
Table D.32 Saturation Calculation of CT Numbers of Slices for Core#5 After Polymer Gel Injection. ....	182

## LIST OF SYMBOLS

A	: cross sectional area, ft <sup>2</sup>
a	: width of the fracture, mm
b	: aperture of the fracture, mm
CT <sub>wsat</sub>	: CT number of 100% water saturated core inside core-holder
CT <sub>dry</sub>	: CT-number for dry core inside core-holder
CT <sub>w</sub>	: CT-number for water
CT <sub>A</sub>	: CT-number for air
CT <sub>ow</sub>	: CT-number of porous media saturated with oil and brine
CT <sub>o</sub>	: CT-number for oil
C <sub>Tx</sub>	: CT-number for image
h	: thickness of fracture, mm
I <sub>o</sub>	: incident X-ray intensity
I	: intensity remaining
k	: effective permeability of reservoir rock to a given fluid, darcy
k <sub>m</sub>	: matrix permeability, darcy
k <sub>f</sub>	: fracture permeability, darcy
k <sub>ff</sub>	: intrinsic fracture permeability, darcy
k <sub>t</sub>	: total permeability, darcy
l	: length, mm
Q	: total flow rate, ml/min
Q <sub>x</sub>	: volumetric flux, m <sup>3</sup> /day
$\bar{u}$	: average velocity, m/sec
P	: pressure, psi
$\Delta P$	: drawdown, psi
P <sub>o</sub>	: outlet pressure, bar
P <sub>i</sub>	: inlet pressure, bar
Re	: Reynolds number
S <sub>D</sub>	: n-decane saturation, fraction
S <sub>o</sub>	: oil saturation, fraction
S <sub>w</sub>	: water saturation, fraction
S <sub>wir</sub>	: irreducible water saturation, fraction
T	: transmissivity, cm <sup>4</sup>
v	: velocity, m/sec
w	: width of the fracture, mm
WC	: water cut, %

### **Greek Symbols**

$\alpha$	: attenuation coefficient, 1/cm
$\mu$	: fluid viscosity, cP
$\rho_o$	: density of oil, g/cc
$\rho_w$	: density of water, g/cc
$\sigma$	: interfacial tension, N/m
$\phi$	: porosity, fraction
$\alpha_r$	: attenuation coefficients for rock, 1/cm
$\alpha_w$	: attenuation coefficients core fully saturated with water, 1/cm
$\alpha_o$	: attenuation coefficients core fully saturated with oil, 1/cm
$\tau$	: tortuosity,

## LIST OF ABBREVIATIONS

<b>BP</b>	: British Petroleum
<b>CT</b>	: Computer Tomography
<b>CL</b>	: Cubic Law
<b>EFA</b>	: Equivalent Fracture Aperture
<b>EOR</b>	: Enhanced Oil Recovery
<b>ICL</b>	: Improved Cubic Law
<b>IOR</b>	: Improved Oil Recovery
<b>MCL</b>	: Modified Cubic Law
<b>LCL</b>	: Local Cubic Law
<b>OOIP</b>	: Original Oil In Place
<b>OCP</b>	: Organically Cross-linked Polymer
<b>PI</b>	: Productivity Index
<b>PNL</b>	: Pulse Neutron Log
<b>PLT</b>	: Production Logging
<b>PV</b>	: Pore Volume
<b>SCAL</b>	: Special Core Analysis
<b>WOR</b>	: Water Oil Ratio
<b>WSO</b>	: Water Shut-Off
<b>XRF</b>	: x-ray fluorescence

### Lower case letters

<b>afm</b>	: artificially fractured matrix
<b>afmw</b>	: artificially fractured matrix water
<b>afmwd</b>	: artificially fractured matrix water decane
<b>d</b>	: decane
<b>ios</b>	: initially oil saturated

**iws** : initially water saturated  
**lm** : left matrix  
**lmw** : left matrix water  
**lmwd** : left matrix water decane  
**lmwdw** : left matrix water decane water  
**n** : normal  
**rm** : right matrix  
**rmw** : right matrix water  
**rmwd** : right matrix water decane  
**rmwdw** : right matrix water decane water  
**w** : water  
**wd** : water decane  
**wdw** : water decane water



## CHAPTER 1

### INTRODUCTION

Fractures are the primary oil-water-bearing openings in the majority of oil reservoirs and can strongly affect fluid flow and transport in all subsurface flow systems. Thus accurate analysis of the influence of fractures on fluid storage and transport is important for resource recovery.

Several theoretical models have been proposed for flow from single fractures. For many years, it is believed that large-scale flow along a rough walled fracture was similar to that through two smooth parallel plates. In this description, the effect of the aperture on the flow is generally described by the steady state solution for laminar viscous flow between two smooth parallel plates known as cubic law (CL) (Lomize, 1951; Bear, 1972).

However, surface roughness of fractures has an effect on the fluid flow which causes a deviation from the real flow rate predicted by CL (Brown, 1987; Zimmerman et al., 1991). The correctness of CL can be improved by including a correction factor based on fracture roughness (Renshaw, 1995).

Attempts have been made to model single-phase flow behavior in rough-walled fractures and to more accurately account for flow tortuosity caused by fracture roughness. By this way pore-scale approaches such as channel models or local cubic law (LCL) method were developed, considering for the aperture variation and more recently surface ripple to better model local flow behavior (Brown, 1987; Tsang and Tsang, 1990; Hakami and Larson, 1996).

The classical LCL, sometimes referred to as the Reynolds equation, has been extensively applied in single fracture studies involving fluid related conservative and reactive solute transport through a single fracture (Nicholl et al., 1999; Brush and Thomson, 2003).

Existence of high fluid conductivity fractures within the reservoir may result with the early breakthrough of the injected water or invasion by aquifer (Portwood, 2005; Demir et al., 2008). Such analysis requires knowledge of the variation in the opening or aperture along the fracture.

The basic understanding of fluid formation and transfer processes through interconnected fractures is critical for many environmental and engineering problems and geophysical phenomena. However, the detailed characterization of flow and transport processes in complex fracture networks is still challenging, so a large number of studies have focused on separate single rough-walled fractures (Zimmerman et al., 2004; Cardenas et al., 2007). The CL is further improved and modified by research studies generally, for simplification purpose, which used glass plates or concrete slabs instead of real rock fractures. Nevertheless, they identify some key issues about fluid flow in fractures, such as effect of small-scale roughness, larger-scale aperture variation and nonlinearity at high Reynolds number (Renshaw, 2000).

Witherspoon et al. (1980) proposed the modified cubic law (MCL) by introducing a friction factor to account for the fracture roughness and tortuosity. Accurate estimation of flow process through rough and tortuous fractures aids in understanding transport problems in fractured media, and can provide a method to estimate effective transport parameters based on the geometric properties of fractures (Wang and Cardenas, 2014).

Besides, fractured reservoirs are considered to be extremely challenging in terms of accurate recovery prediction because of their complexity and heterogeneity. Most reservoirs consist of natural fractures and fractures that contain isolated microscopic fissures inside. These fractures create complex paths for fluid movement which impact reservoir characterization and ultimately production performance with total recovery (van Golf-Racht T.D., 1982 39; Sydansk, 1988, 40, Seright et al., 2003).

Moreover, using computer tomography (CT) the benefits of CT scanned images of oil and water saturations before and after corefloods aided to explain the reservoir

conditions from macro to micro scales in an economical way (Honarpour et al., 1985; Wang et al., 1984). In qualitative CT analysis information about heterogeneities vugs, fractures can also be collected (Vinegar, 1987). Information from the CT scan can be useful to predict the flow behavior in the porous medium (Withjack and Akervoll, 1988). Quantitatively, CT data can be used to measure the bulk density and porosity; as well as to quantify heterogeneity (Akin and Kovseck, 1999).

In this study, experiments were done with naturally/artificially fractured cores, in order to understand the effect of fractures and fracture like features on the oil production mechanism causing the limitations of ultimate recovery.

Oil saturated and water saturated environments were studied with the cores. CT scanner is used to quantify porosity and saturations in the cores which were identified by thin sections with a color scale approach manually and a computer program prepared for direct calculations for the verifications. Analytical explanations of the fracture flow behavior during experiments were tried to define using CL by calculation of equivalent fracture apertures.

This work also describes an experimental study to quantify the effect of polymer gel injection into natural and artificially fractured core samples. Permeability measurements before and after gel injection showed the efficiency of gel injection. The effect of polymer gel in the fractured reservoir is to increase recovery by increasing sweep efficiency by plugging the permeable path way in the core causing sweeping in the unswept zone (Canbolat and Parlaktuna, 2012).

All artificially fractured cores showed a decrease in permeability after gel injection and experiments showed that polymer gel plugging the fracture and diverting the water for matrix production.

Laboratory results were defined with an improved cubic law (ICL) equation with and without polymer gel injection application. Measurements of the fractures were completed by using microscope to verify the analytical calculations. The equation was developed for predicting equivalent fracture apertures that combines ideas from Ge (1997), considering tortuosity, from Renshaw (1995), considering

roughness. Shrinkage in equivalent fracture aperture was determined using a microscope confirmed by ICL.

## CHAPTER 2

### COMPUTER TOMOGRAPHY IN CORE ANALYSIS

#### 2.1 Computer Tomography

X-ray computer tomography (CT) (**Figure 2.1**) has gained acceptance as a routine core analysis tool in the petroleum and natural gas engineering research. The main principles of CT for core studies are expressed in several early papers.

Whole core scanning of unconsolidated rock from the Alaskan North Slope was performed by Mac Gregor et al. (1981) to estimate core retrieval rates for minimal core damage. Honarpour et al. (1985), showed the benefits of CT scanning to oil industry. Vinegar and Wellington (1987) provided the industry with a comprehensive study on the methodology and application of CT scanning for coreflood monitoring. These authors further demonstrated CT scanning for use with tertiary miscible flooding and the coupling of CT coreflooding with numerical simulation (Vinegar, 1986; Vinegar and Wellington, 1987).

Withjack and Akervoll, (1988) proved CT scanning for special core analysis (SCAL) including CT porosity determination and relative permeability measurement. Hunt et al. (1988) showed the imaging capabilities of CT to reveal mud invasion, inspect core within core barrels and determine core heterogeneities. and Wang et al. (1989), described the early use of CT for obtaining images of oil and water saturations during corefloods.

CT usage in petroleum industry covers most of the core scale analysis from macro scale (0.25-0.30 millimeters) to micro scale (5-10 microns). Applications include improving reservoir evaluation and recovery processes by core description and fluid flow characterization (Akin and Kovscek, 1999). **Figure 2.2, 2.3 & 2.4** illustrate the details observable in CT scans of a heterogeneous core plug and one from the damaged sample.



**Figure 2.1** Computer Tomography.

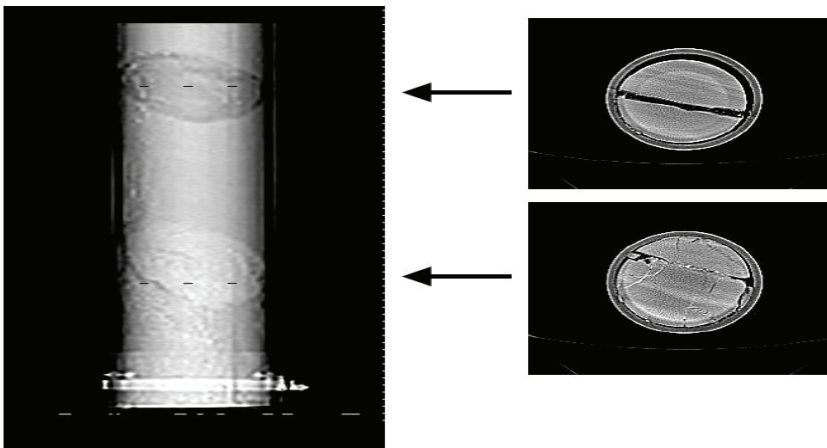


**Figure 2.2** CT radiograph scan (left) and axial scans (right) showing damaged core within core tube after Withjack et.al. (2003).

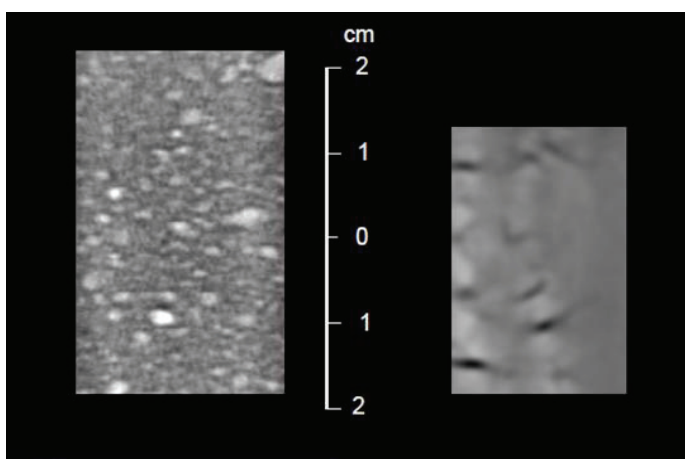


**Figure 2.3** CT scans of a heterogeneous (left) and damaged plug (right) after Withjack et.al. (2003).

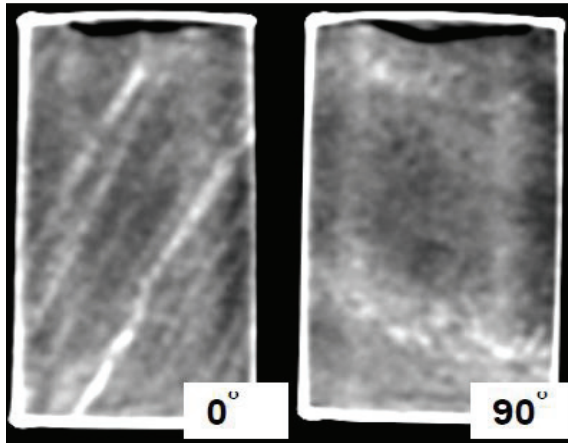


**Figure 2.4** Core plug scans in orthogonal planes (0 and 90 degrees) after Withjack et al.(2003).

## 2.2 CT scan principles

The principles of CT for core studies are expressed in several early papers which include both core description and coreflooding aforementioned previously. Honarpour et al.'s (1985) work was one of the earliest efforts demonstrating the benefits of CT scanning to the oil industry by describing the use of CT for obtaining images of oil and water saturations during corefloods by Wang et al. (1989).

CT scan technique is based on the attenuation of the X-ray beams penetrating the scanned object at different angles as the X-ray source rotate around the object. Series of detectors records the transmitted X-ray intensity data. Far from these projections, a cross sectional slice is generated through the core by reconstruction by the computer. A three dimensional image can be reconstructed from the cross-sectional slices taken across the sample. The basic quantity measured in CT is the linear attenuation coefficient  $\alpha$ . This is defined from Beer's law:

$$\frac{I}{I_0} = \exp(-\alpha h) \quad (\text{Equation 2.1})$$

where  $I_0$  is the incident X-ray intensity.  $I$  is the intensity remaining after passing through a thickness  $h$  of homogeneous sample (Wellington and Vinegar, 1987; Akin and Kovscek, 1999 ; Al-Muntasheri, et al., 2010).

### 2.3 CT scan application

Withjack et al. presented a comprehensive list for applications of CT in oil industry in 2003. They grouped these applications and give examples for each application. The following are the suggested categories: core description, desaturation studies, improvement of recovery, hydrate studies, recovery of viscous oil, formation damage, and perforation analysis.

Fluid flow visualization during core flooding is one of established techniques to study displacement efficiency and saturation changes using different EOR processes. Researchers used CT to understand the effects of viscous gravity, trapping, bypassing and heterogeneity on flow inside the rock (Akbar et al., 1993; Siddiqui and Khamees, 2004). More description to the saturation determination will be given in following section.

In qualitative CT analysis information about heterogeneities, vugs, fractures, bedding planes and lithology can also be collected. Information from the CT scan can be useful to predict the flow behavior in the porous medium. Quantitatively, CT data can be used to measure the bulk density and porosity; to quantify heterogeneity, to make core to log comparison for depth matching and log calibration (Siddiqui and Khamees, 2004).

### 2.4 Porosity determination and core characterization

Porosity and porosity distribution through the core can be determined using CT scan with high agreement ( $\pm 1$  porosity %) as stated by Akin and Kovscek in 2003. The following equation is used to determine the porosity for each volume element;

$$\phi = \frac{CT_{wsat} - CT_{dry}}{CT_w - CT_A} \quad (\text{Equation 2.2})$$

where  $\phi$  is porosity (fraction).  $CT_{wsat}$  is the CT number of 100% water saturated core inside core-holder.  $CT_{dry}$  is the CT-number for dry core inside core-holder.  $CT_w$  is the CT-number for water and  $CT_A$  is the CT-number for air. CT

scan applications in core characterization involve whole cores and plugs (Akin and Kavscek, 2003).

## 2.5 Determination of the two-phase saturation

A single energy scan is sufficient to determine two phase saturation. Linear interpolation between the pure states is used for determining the saturation. For porous media containing oil and brine, a scan gives the following (Akin and Kavscek, 2003).

$$CT_{ow} = (1 - \phi)\alpha_r + \phi S_o \alpha_o + \phi S_w \alpha_w \quad (\text{Equation 2.3})$$

where  $CT_{ow}$  is the CT-number of porous media saturated with oil and brine,  $\alpha_r$ ,  $\alpha_w$  and  $\alpha_o$  are the attenuation coefficients for rock core, fully saturated with water and oil.  $S_o$  is the oil saturation.

$$S_w + S_o = 1 \quad (\text{Equation 2.4})$$

The water saturation ( $S_w$ ) can be calculated using the following equation (Siddiqui and Khamees, 2004; Al-Muntasheri et al., 2010):

$$S_w = \frac{CT_x - CT_o}{CT_w - CT_o} \quad (\text{Equation 2.5})$$

where  $CT_x$  is the CT-number for image in question.  $CT_w$  and  $CT_o$  are 100% water and 100% oil saturated core samples. One way to obtain  $CT_w$  and  $CT_o$  is by scanning the 100% water saturated core, then cleaning the core and totally saturating it by oil and take the second scan to determine  $CT_o$ .



## CHAPTER 3

### BEHAVIOUR OF NATURALLY FRACTURED RESERVOIRS

#### 3.1 Naturally Fractured Reservoirs

The fractures exist at all scales, from microscopic fissures to kilometer sized structures called fracture swarms or corridors, creating complex flow networks in the reservoir. That's why, the movement of hydrocarbons and other fluid is often not as expected or predicted. Just a few very large fracture corridors can be highways for fluids in the middle of a carbonate reservoir; therefore, knowing their exact position is critical for planning new wells and for simulating and forecasting reservoir production (Akbar et al., 1993).

A fractured reservoir is a dual-porosity system consisting of primary intergranular matrix interlaced by a network of channels comprising the fracture network. Usually the fracture system is extensive and has considerable surface area contact with matrix; oil is easily transferred into the fracture system where it is delivered to the producing wells with very little loss of pressure. Thus, a fractured reservoir is capable of surprising performance compared with a conventional reservoir of similar matrix porosity and permeability (**Figure 3.1**) (Akbar, et al., 1993).

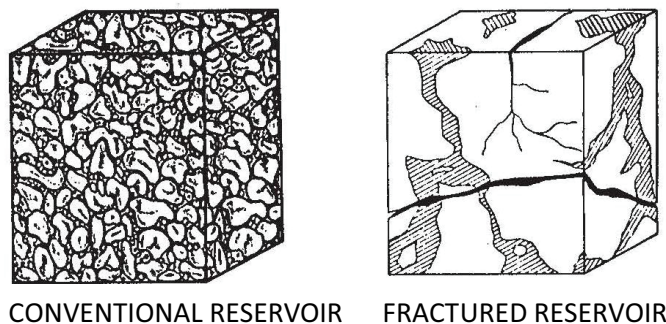


**Figure 3.1** Conventional and Fractured Reservoirs after Akbar, et al., (1993).

van Golf-Racht and Fernand in 1994, have implemented the properties and mechanical behavior of a fractured reservoir based on the matrix and fracture characteristics. Particularly important properties are the capability of the matrix and fractures to store (porosity) and transport (permeability) fluids. A commonly used classification subdivides fractured reservoirs into types based on the matrix and fracture contribution to porosity and permeability.

Water cut in the fractured reservoir is essentially a function of production rate while in the conventional reservoir it depends on the conditions of the reservoir causing the breakthrough, both cases coning and displacement processes. In a fractured reservoir the water-cut increases rapidly from 0 to 100 % if a well rate is higher than critical rate (**Figure 3.2**) (van Golf-Racht and Fernand, 1994).

Due to the heterogeneity of fractured carbonate rock and its wettability characteristics which are believed to be mixed or oil-wet, water cut in the reservoir increases unexpectedly as in **Figure 3.2A**. In conventional reservoir the water-cut increases slowly 0 to 100 % due to condition of displacement-uniformity of permeability distribution, viscosity ratio etc. (**Figure 3.2B**) (Buckley and Liu, 1988).

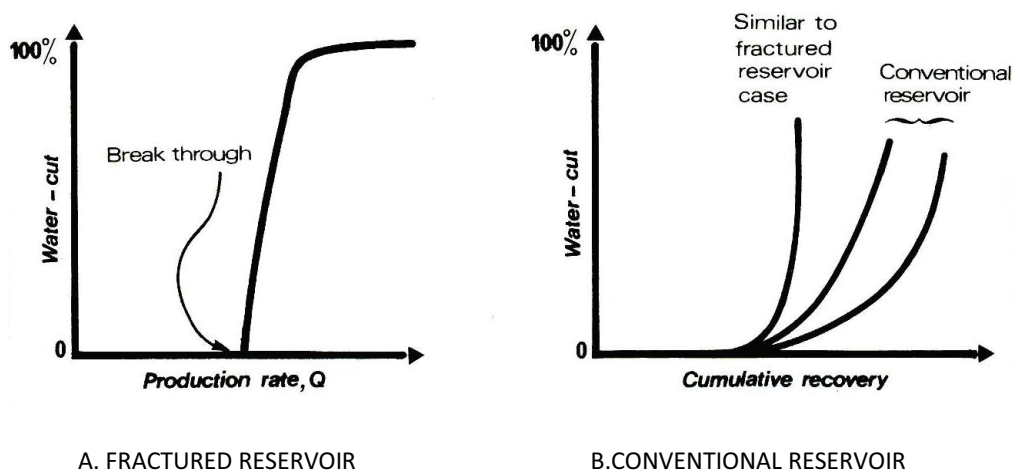


**Figure 3.2** Water-Cut in the Fractured and Conventional Reservoirs after Buckley and Liu, (1988).

## 3.2 Analytical Definition of Fluid Flow in Natural Fractures

### 3.2.1 Fluid Flow Through Fractures

For many years it was believed that the large-scale flow through a rough-walled fracture was similar to that through two smooth, parallel plates. In this definition the influence of aperture on flow is commonly described by the steady-state solution for laminar viscous flow between two smooth parallel plates which is known as the Cubic Law (CL) (Lomize, 1951; Zimmerman, 1966; Bear, 1972). The common approach in studying fluid flow in a single rough walled fracture is to use CL formula which is a simplified version of the Navier-Stokes equation (Zimmerman and Bodvarsson, 1996; Witherspoon et al., 1980).

One of the first comprehensive works on flow analysis through fractures was presented by Lomize in 1951. He developed several empirical equations for friction factors as a function of both Reynolds number and roughness.

The fracture walls can be represented by two smooth parallel plates separated by an aperture  $h$  (Figure 3.3). Flow takes place in the space between these parallel plates—from inlet to outlet as marked by the arrows with a commonly used boundary condition: constant static pressures at inlet and outlet.

The flow space remains bounded by impermeable and rigid fracture walls (no-slip boundary conditions) elsewhere. The fracture width is expressed as  $W$  and the distance between the inlet and outlet (fracture length) is  $l$ . The system creates a uniform pressure gradient which lies entirely in the plane of the fracture resulting in a unidirectional flow through the system. The flow in this case is in the  $x$ -direction, so that the  $x$ -component velocity exists (Sarkar et al., 2004).

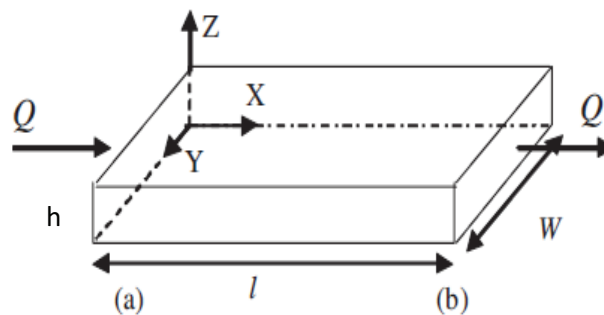


**Figure 3.3** Parallel Plate Flow Model for Fractures.

The total volumetric flux  $Q_x$  through the fracture for a width  $W$  is found by integrating the velocity across the fracture from  $z=0$  to  $z=h$  resulting in;

$$Q_x = \frac{Wh^3}{12\mu} \left( \frac{P_o - P_i}{l} \right) \quad (\text{Equation 3.1})$$

The average velocity  $\bar{u}$  is found by dividing the flux by the cross-sectional area,  $Wh$ :

$$\bar{u} = \frac{Q_x}{Wh} = \frac{h^2}{12\mu} \left( \frac{P_o - P_i}{l} \right) \quad (\text{Equation 3.2})$$

Darcy's law for flow through porous media in one dimension can be written as;

$$Q = \frac{kA}{\mu} \left( \frac{P_o - P_i}{l} \right) \quad (\text{Equation 3.3})$$

The cross-sectional area  $A$  is equal to  $Wh$ . Therefore, the permeability of the fracture can be identified as;

$$k = \frac{h^2}{12} \quad (\text{Equation 3.4})$$

The product of the permeability and area also known as transmissivity is equal to;

$$T = kA = \frac{Wh^3}{12} \quad (\text{Equation 3.5})$$

The dependence of the  $T$  on  $h^3$  is the essence of the well-known CL. Then the derivation of the CL for a rough walled fracture begins by assuming that the fracture walls can be represented by two smooth parallel plates separated by an aperture  $h$ . Discarding the effect of gravity, the CL for a fracture with planar surfaces, assuming they remain in parallel and not in contact at any point is

expressed as below equation (Witherspoon et al., 1980).

$$Q = \frac{h^3}{12\mu} \left( \frac{\Delta p}{L} \right) \quad (\text{Equation 3.6})$$

The influence of aperture on flow is commonly described by the steady-state solution to the Navier-Stokes equations for laminar viscous flow between two smooth parallel plates. This solution known as the CL stated previously. Most of the authors agree on the calculations of the apertures with CL (Renshaw et al, 2000; Xiao et al. 2013).

The CL accurately describes flow between smooth-walled plates. However, natural fractures are more likely to be rough walled with walls contacting each other at discrete points (Gangi, 1978; Brown and Schultz, 1985; Brown, 1987; Bandis et al., 1985) and lowering total flow. In this case, the equivalent aperture through which fluids can flow called the hydraulic aperture is smaller than the actual opening displacement of the fracture or mechanical aperture. The pursuit of correlating mechanical to hydraulic apertures has been met with limited success. Different approaches have attempted to find a representative hydraulic aperture by introducing an empirical relation between mechanical and hydraulic aperture based on hydromechanical coupling experiments, corrections with a friction factor due to the tortuosity of the flow path in the fracture (Barton et al., 1985; Wang et al., 1988; Cook et al., 1990; Hakami and Barton, 1990; Renshaw, 1995) or the geometric mean of the aperture distribution (Hakami, E. and E. Larson. 1996; Renshaw and Park, 1997; Lanaro, 1999; Tatone and Graselli, 2012).

This is the classic cubic law (CL) from which it can be drawn a conclusion that the aperture plays an important role in fluid flow through a fracture and controls the flowrate to a large extent. Therefore, accurate measurement of aperture distribution is crucial for evaluating the hydraulic behavior of a fracture (Renshaw and Park, 1997).

The ratio of the experimentally to numerically determined effective aperture for each trial as a function of the Reynolds number (Renshaw, 1995; Renshaw and Park, 1997) is shown in **Figure 3.4**.

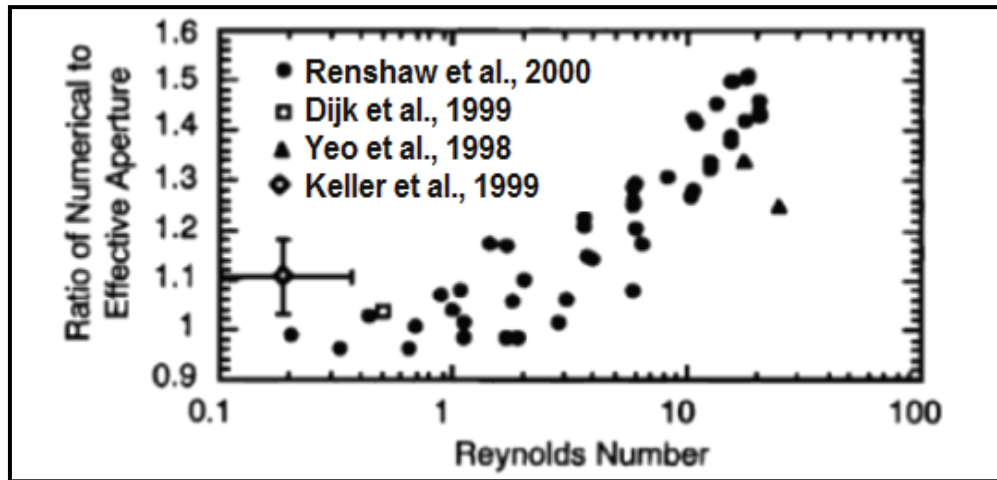


**Figure 3.4** Experimentally Measured Effective Aperture as a Function of the Reynolds Number after Renshaw et al., (2000).

The dimensionless Reynolds number ( $Re$ ) represents the ratio of inertial to viscous forces where,  $v$  is the fluid velocity,  $h$  is the hydraulic aperture,  $\rho$  fluid density and  $\mu$  is the viscosity of the fluid (Liu et al., 2014).

$$Re = \frac{\rho \cdot v \cdot h}{\mu} \quad (\text{Equation 3.7})$$

High Reynolds numbers indicate that the inertial terms in the Navier-Stokes equations which are neglected in deriving the CL are of the same order or greater than the viscous terms invalidating the CL. For flow in fractures with small aspect ratios, the inertial terms are expected to become significant and the CL invalid for  $Re$  greater than 26.67. The tests and numerical simulations show that the fracture apertures can be accurately calculated by applying the CL to each fracture at low  $Re$  (Liu et al., 2014).

### 3.2.2 Development of Cubic Law

Attempts to model the single phase flow behaviour in rough-walled fractures have improved. Besides, to more accurately account for flow tortuosity caused by fracture roughness led to the development of pore-scale approaches such as channel models or the local cubic law method, which better model the local

flow behavior by accounting for the aperture variation and more recently, the fracture surface ripple (Brown, 1987; Tsang and Tsang, 1990; Hakami and Larson, 1996). The classical local cubic law (LCL), sometimes called the Reynolds equation, has been extensively applied in investigations of fluid flow, and related conservative and reactive solute transport through a single fracture (Nicholl et al., 1999; Brush and Thomson, 2003).

Presence of high fluid transmissivity fractures within the reservoir may result with the early breakthrough of the injected water or invasion by aquifer (Portwood, 2005). Such analysis requires knowledge of the variation in the opening or aperture along the fracture.

It is critical for many environmental and engineering problems and geophysical phenomena to understand the fundamentals of fluid flow and transport processes through connected fractures. Nevertheless, detailed characterization of flow and transport processes within complex fracture networks remains a challenge, thus numerous studies have been focused on discrete single rough-walled fractures (Zimmerman et al., 2004; Cardenas et al., 2007).

Generally, researches have further improved and modified the CL by using glass plates or concrete slabs rather than real rock fractures. Nevertheless, they identify some key issues about fluid flow in fractures, such as effect of small-scale roughness, larger-scale aperture variation and nonlinearity at high Reynolds number (Renshaw, 2000).

Modified cubic law (MCL) was first proposed by Witherspoon et al. (1980) by introducing a friction factor to account for the fracture roughness and tortuosity. Precise estimation of flow process through rough and tortuous fractures supports in understanding transport problems in fractured media, and can provide a method to estimate effective transport parameters based on the geometric properties of fractures (Wang and Cardenas, 2014).

### **3.2.3 Consideration for Tortuosity**

Tortuosity is a macroscopic feature defined as the ratio of actual flow path length over a straight-line distance. A measure of the geometric complexity of a porous medium. Tortuosity is a ratio that characterizes the complicated pathways of

fluid diffusion and electrical conduction through porous media. In the fluid mechanics of porous media, tortuosity is the ratio of the length of a streamline, a flow line or path, between two points to the straight-line distance between those points. Tortuosity is thus related to the ratio of a fluid's diffusion coefficient when it is not confined by a porous medium to its effective diffusion coefficient when confined in a porous medium.

Normally, the actual flow field can be obtained through either direct simulation or experimental observation, and it varies depending on aperture field and  $Re$ . Thus, it is difficult to correct the LCL with macroscopic tortuosity since this rests on precise knowledge of flow paths. (Nicholl et al., 1999; Nicholl and Detwiler, 2001).

### 3.2.4 Intrinsic Fracture Permeability, $k_{ff}$

The intrinsic fracture permeability is associated to the conductivity measured during the fluid flow through a single fracture or through a fracture network independent of the surrounding rock (matrix) (van Golf-Racht, 1982).

It is in fact, the conductivity of a single channel (fracture) or of a group of channels (fracture network). In this case the flow of cross section is represented only by the fracture void areas (excluding the surrounding matrix area) (van Golf-Racht, 1982).

In a simplified case of a block where the fracture is parallel to the flow direction (**Figure 3.5**) (fracture 1 is parallel to the horizontal flow direction), the flow rate through the fracture is given by;

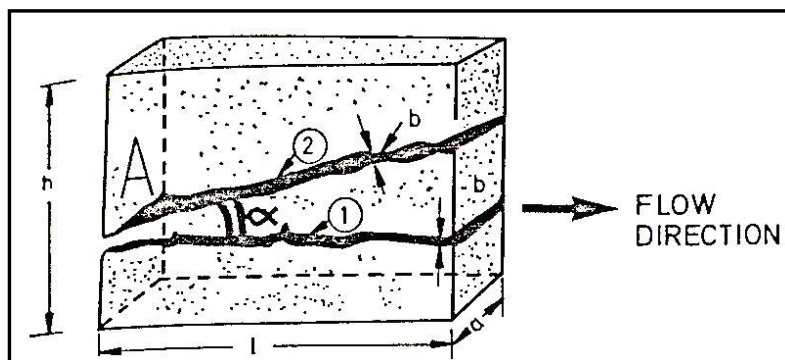


**Figure 3.5** Matrix Block Containing a Single Fracture, Fracture1 ( $\alpha = 0$ ), Fracture 2 ( $\alpha \neq 0$ ) after van Golf-Racht, (1982).

$$Q_f = a \cdot b \frac{b^2}{12\mu} \left( \frac{\Delta p}{L} \right) \quad (\text{Equation 3.8})$$

On the other hand, based on the Darcy concept, if limited to the entire cross flow section,  $A=a \times b$  where  $a$  is the width,  $b$  is the aperture of the fracture. And the rate is expressed by van Golf-Racht, 1982 as;

$$Q = A \frac{k_{ff}}{\mu} \left( \frac{\Delta p}{L} \right) = a \cdot b \frac{k_{ff}}{\mu} \left( \frac{\Delta p}{L} \right) \quad (\text{Equation 3.9})$$

The further comparison of Equation 3.8 and 3.9 will lead to intrinsic fracture permeability,  $k_{ff}$  as;

$$k_{ff} = \frac{b^2}{12} \cos^2 \alpha \quad (\text{Equation 3.10})$$

### 3.2.5 Conventional Fracture Permeability, $k_f$

The intrinsic fracture permeability, disregards the rock bulk volume associated to the single fracture; on the contrary, in the conventional fracture permeability the fracture and associated rock bulk form a hydrodynamic unit (van Golf-Racht, 1982). This means that the flow cross section, if referring to **Figure 3.5** is not expressed by section  $A=a \times b$ , but instead by  $A_B = a \times h$  and therefore;

$$Q = A_B \frac{k_f}{\mu} \left( \frac{\Delta p}{L} \right) = a \cdot h \frac{k_f}{\mu} \left( \frac{\Delta p}{L} \right) \quad (\text{Equation 3.11})$$

If Equations 3.8 and 3.9 are compared, and the result then applied to Equation 3.11, the following expression will be obtained for fracture permeability,  $k_f$ ;

$$k_f = k_{ff} \frac{a.b}{a.h} = k_{ff} \frac{b}{h} = \frac{b^3}{12h} \quad (\text{Equation 3.12})$$

### 3.2.6 Permeability of fracture-matrix system

The permeability of a fracture-matrix system may be represented by the simple addition of the permeabilities of matrix  $k_m$  and fractures  $k_f$ .

$$k_t = k_m + k_f \quad (\text{Equation 3.13})$$

If Equation 3.6 refers to the block described in **Figure 3.5** where the specific permeabilities of matrix and fracture were discussed, it is evident that the total permeability will depend on flow direction. Any change in direction of flow will change the value of  $k_f$ , since  $k_f$  depends on the relationship between fracture and flow directions (van Golf-Racht, 1982). Then by using the conventional cylindrical cores and a conventional permeameter the permeability, based on Darcy's equation is expressed by;

$$k_t = \frac{Q\mu l}{A.\Delta p} \quad (\text{Equation 3.14})$$

Through which is obtained the total permeability of the system and not the single permeabilities of matrix and fractures.

## CHAPTER 4

### POLYMER GEL TREATMENT

#### 4.1 Water Treatment

Almost all oil and gas reservoirs produce water, because water usually replaces oil as hydrocarbon reserves decline in the field. Usually, water production increases as oil or gas decline. In mature or old reservoirs, most of the time fluid production increases as oil or gas representing a few percent of total production. Also water is injected for providing pressure and improving sweep efficiency. By this way, large quantities of injected water are produced in the field. Thus, a continuous increase in water production is a normal behavior of a mature oil field.

Excessive water production can not only reduce the project economics by excessive water treatment and disposal cost but also can completely prevent the production from gas and oil wells, from which the production has become uneconomic. Sydansk, (1988) and Seright et al. (2003), have mentioned that, numerous mechanical and chemical methods are available for water shut-off treatments in the hydrocarbon wells. Mechanical methods, which include drilling horizontal, multi-lateral wells, placing a liner to block water production and down-hole separation equipment such as hydro-cyclones, usually require a work-over rig. These methods are often costly. Different kinds of chemicals have been used as blocking and diverting agents to treat injection and production wells for more than six decades (Sydansk, 1988; Seright et al., 2003).

To deal with excessive water, injected chemicals create either permanent such as cement, resins or selective barriers such as; hydro-soluble polymers, weak gels. The characteristics of the permanent barriers are, good results when clearly separated oil and water zones, risky otherwise with possible plugging of formation and workover always required. Characteristics of the selective barriers

applied to multilayered reservoirs, reversible process, i.e. chemicals can be removed, workover sometimes required (Cholet, 2000).

Well cementing consists of two principal operations primary cementing and remedial cementing. Primary cementing is the process of placing a cement slurry in the annulus between the casing and the formation. Remedial cementing occurs after primary cementing, when engineers inject cements into strategic well locations for various purposes, including well repair, squeeze for water out perforation and well abandonment. Primary cementing is a critical procedure in the well construction process. The cement sheath provides a hydraulic seal that establishes zonal isolation, preventing fluid communication between producing zones in the borehole and blocking the escape of fluids to the surface (Nelson, 2012).

Sydansk and Portwood have impressed that several factors determine the success of a chemical treatment in the field, including: candidate selection, identification of the source and control technology of the water production problem, proper choice of the chemical system, and placement of the chemicals into the target zone. Water production problems often are not properly diagnosed. In fact, inaccurate, insufficient, or lack of diagnostic have been cited as one of the major reasons that water control treatments have been unsuccessful (Seright et al.,2003; Portwood, 2005).

Sydansk has proposed that, gel polymer systems are typically composed of a water soluble polymer and a crosslinking agent which are dissolved in water. This solution is considered as gellant solution. After allowing sufficient time, the gellant sets into a semisolid mass, and behaves as flow diverting or blocking agent. Selection of a gel polymer system for a given well treatment strongly depends on reservoir conditions such as temperature, salinity, hardness and the pH of the water used for preparation of the gellant. Other parameters to be considered for the proper selection of a given gel polymer system include salinity of the formation water, permeability of the target zone, and the lithology of the formation (Sydansk, 1988).

Willhite and Pancake (2004) have stated that, gel polymer treatment is one of the most useful chemical methods to reduce water production. Gel polymer systems have a penetration property greater than the mechanical methods and cement to provide a deeper barrier against the excess water. Also, plugging due to gel polymers can be removed unlike physical cement plugging which leads to a permanent plug in the porous media so that the residual oil cannot be produced from the treated region by cementing method after decreasing of excess water production (Willhite and Pancake, 2004).

Gel polymer treatment can be used as an improved oil recovery (IOR) method in injection and production wells. In the injection well treatment, the gellant is placed into high permeability fractures. This application, called profile modification or conformance control, diverts injected water or gas to un-swept zones and improves the distribution of injected fluids into a heterogeneous reservoir. The production well treatment involves injection of the gellant into the fractures or high permeability zones that produces a lot of water, thereby reducing oil production. This application not only improves drawdown from the productive zones; but, it also reduces or eliminates the costs associated with the produced water (Perez et al., 2001; Moradi-Araghi et al., 2005; Green and Willhite, 1998).

Burrafato has suggested, several gelled polymer systems are available for water shut-off treatment. Most polymers are polyacrylamide with different degrees of hydrolysis (partially hydrolyzed polyacrylamide) and polysaccharide such as xanthan biopolymer. These polymers can be cross-linked with metallic and organic crosslinkers to produce a three dimensional polymer structure of the gel (Sydansk, 1990; Burrafato et al., 1999).

#### **4.2 Field Applications**

Water Shut Off (WSO) treatments in production wells are routine part of standard well service work. It is used like cement squeezes or mechanical isolation methods with high success rates for “straight forward” WSO targets. Polymer gel treatments are effective at shutting off unwanted water and improving oil recovery from producing wells. Many successful gel applications have been reported in the literature.

In 1988 Sydansk and Smith first reported results relating to the new technology for the nine field tests that were performed in Wyoming's Big Horn Basin in 1985 and 1986 that involved fracture conformance problems. The field tests were conducted soon after initial laboratory development of the new gel technology. Gels were injected to the seven injection-wells which were active and to test the field application of conformance technology. Also the gel technology applied to shut-in production wells in the first treatments. These wells were reported as shut-in due to the high water cut. After gel injection the wells were kept five days shut-in. When they started production 16 bbls/day oil production was 60 bbls/day and in the second one 25 bbls/day was increased to 145 bbls/day. In other words the first applied selection criteria was the high water cut shut-in wells. The reported gel technology is particularly well suited for fractured carbonate reservoir having a reservoir temperature of 110°F (43°C) field application. The gels were effective at reducing fluid-flow capacity of reservoir fractures (Sydansk and Smith, 1988).

The first application of water shut-off polymer gel injection was learned from BP's twelve "modern" production well WSO treatments in Alaska and the North Sea, carried out between years 1993-1996. In this application, three types of treatment were discussed: The first one near well bore, total shut-off of an isolated zone, which one entire section of well bore is being abandoned in order to allow production from other zones. In the second case a relative permeability modifier injected to full well bore, into all perforated zones. Thirdly, dual injection treatments applied, for either total shut-off or relative permeability modification targeting as a single reservoir zone, but mechanical well bore control of fluid placement was not available. While applying these treatments wells were selected by measuring the injectivity (PI) of wells, open fractures present from logs and clay content were also considered for selection criteria (Fulleylove et al., 1996).

In 1999 the chemistry and treatment design of the first field application was published. The candidate well, for which this treatment designed, was a production well. The developed, organically cross-linked polymer (OCP) system for water shutoff was in North Sea that completed in naturally fractured chalk.

Each of the completed intervals was acid fractured to further open the existing natural fractures and increase production. The recommended treatment volume calculations took into account the leak-off considerations and the acid fracture volume. The method by which the leak-off requirements calculated was described. The placement and shut-in temperatures of the recommended treatment volume were then calculated as a function of time. These simulations used a production - operation wellbore simulator in combination with an advanced processes reservoir simulator. The fractures in the target zone were defined in the grid-block system that was used in these temperature simulations. The results of these temperature calculations were used to formulate the chemical compositions of the stages of the OCP treatment and to calculate gel times and shut-in times. The calculations of these gel times and how they correspond to the gel times during the actual treatment were also described. The candidate well selection were based on the analysis of the produced water, water cut value and the fracture distribution parameters. The analysis of the produced water showed that invasion to the well both from formation and also from injection wells mean that a well-developed fracture system is present (Hardy et al., 1999).

The article published in 1999 about a field in Kansas which has been producing from Arbuckle fractured carbonate formation and having a mechanism of strong natural edge/bottom water drive. The fluid flow is controlled by large void space features like fracture connected vuggs and/or high permeability dolomite matrix rock. WSO gel treatments original process first developed in the late 1960's by Phillips Petroleum Company in that field. Later, the field application and evaluation of polymer gel treatments was started in 1989. The first application started with a decision to re-open the prolific Arbuckle zone and attempt to shut-off unwanted water with gel treatment. Previously the zone was isolated with packer. Chromium III Carboxylate Polyacrylamide gels have been placed into more than 300 producing wells in such a way as to reduce water flow and lower fluid levels resulting many times with increased oil production due to improved drawdown. The best candidates for water shut-off gel treatments in these fields were selected with water-cuts of 95% or greater, producing with high fluid levels, and naturally water driven. The recoverable oil in place to produce after the water

has been shut-off were also considered. While identifying candidates, the reason of excess water production was also detected. The water coning through matrix rock, or presence of conductive fractures extending from the wellbore to an underlying aquifer were also questioned. If water channeling through high permeable matrix or through fractures from a water injection well in a waterflood causing unwanted water production were checked (Portwood, 2005; Willhite and Pancake, 2004; Portwood, 1999).

Also in 1999 a successful WSO application tried in Ashley Valley field, located in the Uintah basin of northeastern Utah, producing oil from the Pennsylvanian Weber Sandstone. The active water drive in the oil bearing reservoir intervals, a substantial vertical fracturing network connects to reservoir underlying Mississippian limestone. In this field, the wells flowed water free oil two years, water breakthrough was widespread on the leasehold regardless of structural position. All attempts at zonal isolation to reduce water production failed until the installation of high rate electrical submersible pumps (ESP). WSO polymer gel technology applied to reduce concurrent water production without effecting the oil production. Although, matrix permeability heterogeneity is extreme, ( $k_m$  varies 1-700 md, with a porosity of %13) conformance control from the reduction of excessive water production, the field exhibited potential for improved oil recovery from polymer treatment. The best candidates were selected with respect to high water cut wells producing at tremendous WOR values (Larson, 1999).

In 2003 rigless water shut-off efforts were reported, to retrieve dead wells in Saudi Aramco's Northern Area offshore fields to extend the producing life of the well and enhance oil recovery. Prior to any WSO job to restore productivity of dead wells due to high water cut, a Pulsed Neutron Log (PNL) is run to identify the type of water movement and remaining pay zones for recompletion potential. After the type of water movement is clearly identified, the most appropriate WSO technique is applied. During the study period, 46 rigless water shut-off jobs were executed with a 91% success rate. Of the 46 WSO jobs, three jobs were successfully implemented on dead horizontal cased hole wells using coiled tubing. The selected candidates were selected from the dead wells with respect to

location, pressure support mechanism and reservoir characteristics. (Makki, 2003).

In 2004 north-east Syria, production logging (PLT) surveys combined with a reservoir study showed that good-quality sands were not properly swept by water due to channeling and poor connectivity in the reservoir. It was anticipated that these sands could contribute to production if watered out sands were shut-off.

A field application of WSO reported that 84 meters perforations were squeezed off with gel-cement in a single attempt. After re-perforation of the top and the middle zone the well produced at strongly reduced water cut i.e. 25-33% compared to 60-62% before the treatment and increased oil production i.e. 3,000 bbls/day compared to 1,000 bbls/day before the treatment. The oil production declined to 2,000 bbls/day over a year. The water cut gradually increased over the period to 56%. The field case gel-cement system showed excellent shut-off behavior at high bottom hole temperatures (118-144 °C) and has proven to be a very cost effective method for solving water problems (van-Ejden, 2004).

In 2005, four successful selective WSO applications in producing wells from mature light oil reservoirs at Maracaibo Lake Basin were performed. The main recovery mechanism of these important oil accumulations is water drive, in some cases supported by flanks with water injection. The consolidated sandstone reservoirs of fluvial-deltaic origin are characterized by highly complex stratigraphy, which determines its lenticularity. In this application WSO polymers corrected problems resulting from channeling and behind casing communication. Using the elastic gel system the water production has been reduced to a minimum, obtaining an increase in wells productive life-time, which in global terms reaches a volume higher than 2 million barrels of additional oil recovered in seven years. For best candidates an excess water production wells were selected which were water out by channeling through a high permeability strake and partially communication problem inside a casing (Der Sarkisyan et al., 2005).

In Turkey, as a pilot application, WSO gels were used in 7 wells in September 2007 in Raman Field producing from a fractured carbonate reservoir with a strong aquifer/water drive. Wells with different behavior were selected as candidates on

purpose, in order to see the effect of gel treatments on reduction of WOR. These are high water cut producers, shut-in due to high water cut and high PI value wells. The main purpose of the treatments was to increase oil recovery, decreasing the waste water amount was considered as a secondary benefit. The polymer gels first were prepared in lower concentrations in order to spread through the wellbore penetrating deeper into the high permeability fractures till to aquifer. In the second step higher concentrations were injected to create a more stable and steady state structure around the water producing zones. Because of the favorable results of pilot application polymer gels were injected to 20 more wells in October and November 2008 (Demir et al., 2008).

In 2008, it was reported that the WSO application practiced in a heavy oil field producing 10.5 °API gravity asphaltic oil from the upper Eocene, Boscan (Misoa) Formation with a live oil viscosity ( $\mu_{lo}$ ) ranging 200-400 cP at reservoir conditions west of Venezuela. A modified temporary rigid gel system with an in-situ dispersing mechanism for the polymer solids was engineered. The modified gel has similar properties as the original blocking gel system with an additional feature of being able to pass through the stainless steel mesh of the sand control screen without plugging. The results of ten water control treatments were presented and candidates were selected from high water cut wells. After the application the average water cut was reduced to 30% from 88% and oil production was increased by an average 300 bbls/day per well through the application of WSO solution (Anderson et al., 2008).

The summary of the aforementioned polymer gel applications in the literature is tabulated as, field names, application year, reservoir type, lithology, porosity, permeability, temperature; drive mechanisms are listed in the **Table 4.1**.

**Table 4.1** The Summary of WSO Polymer Gel Application.

Field Name	Year	Reservoir Type	Reservoir Porosity %	Reservoir Permeability md	Reservoir Temperature °F (°C)	Fractured	Water Injection	# of Wells	Remarks
Ashley Valley, Utah	1984	Weber Sandstone	13	1-700		Yes	Yes	1	Open Hole Production wells. 29.5°API Crude Oil
Big Horn Basin, Wyoming	1985-1986	Fractured Carbonate			110°F	Yes	Yes	9	
North-Sea – Alaska	1993	Sandstone	30	100-2.000	112-116°C	No	Yes	12	
Ellenburger Texas, USA	1994	Fractured Dolomite				Yes	Yes		Vertical Fractures
Kansas Arbuckle, USA	1997	Fractured Dolomite	20	1.000-1.500	103-112 °F	Yes	Yes	300	
Maracaibo Lake Basin Venezuela	1997-1999	Heterogeneous Sandstone		200-1.000			Yes	4	High Permeability strikes
Ekofiks, North Sea	1999	Fractured Carbonate (chalk)	30-45	100-10.000	95°C	Yes	Yes		
Northeast Syria	1999	Sandstone			118°C	Yes	Yes		Gel-Cement
Offshore Saudi Arabia	1998-2001	Sandstone					Yes	46	Directional/Horizontal Wells
Boscan Field Venezuela	2005-2006	Sandstone			180°F		Yes		Water Channeling; 10.5°API heavy oil
Raman Turkey	2007	Fractured Limestone	14-20		140°F	Yes	Yes	7	18°API heavy oil



## CHAPTER 5

### MICROSCOPE USAGE FOR EQUIVALENT APERTURES

#### 5.1 Autofocus Methods

Academically, both for geological and earth sciences, the analysis of rock and minerals is important in oil and mineral-related industries. The techniques are applied to enhance the understanding of what is happening to the earth, to date rock, mineral and microfossil samples and for mineral typing. Fracture apertures can also be determined using microscopy. The major techniques used are bright-field, fluorescence stereo microscopy and polarization microscopy for the analysis of fractures respectively.

Two types of autofocus technique are used in automatic microscope instruments. The first type, known as dynamic focusing, uses dynamic surface detection of the sample, directing the energy towards the object as a laser beam. These methods measure the distance to the object independently from the optic and automatically adjust the optical system for accurate focusing. It is fast and can be used for real-time imaging because multiple image capture is not necessary (Liron et al., 2006). However, dynamic methods generally require calibration of the in-focus imaging position with a single surface from which the light beam is reflected. (Price and Gough, 1994).

The latter type is known as inactive focusing because it is based only on the analysis of the content of captured images. The focus position is determined by searching the maximum of an autofocus function using measurements taken from a series of images taken at different focus planes. Although inactive autofocus methods are slower depending on the time required to capture multiple images, they are not affected by the reflective surfaces of a sample (Liron et al., 2006).

## 5.2 Principles of Microscope Autofocusing

In general, a microscope auto-focus system determines the focal position of a view at a given location by searching for the maximum of an autofocus function according to the orientation of the z-axis positions. An autofocus function, calculated on images captured at various z-axis positions, provides focus accuracy measurement at each location for a given image area (**Figure 5.1**). By searching along the Z-axis and comparing the values of the obtained autofocus function, the focus position can be located as the point at which the auto focus function is maximized (Chen, 1989).

In the following section, automatic focusing techniques based on single-channel grayscale images are discussed. For microscope systems that use RGB color images, images are usually converted to grayscale by calculating the brightness. The resulting monochromatic images are then used to calculate the auto-focus function, because most of the information about the focus is encoded in a much brighter color than the chromatic components of a color image.

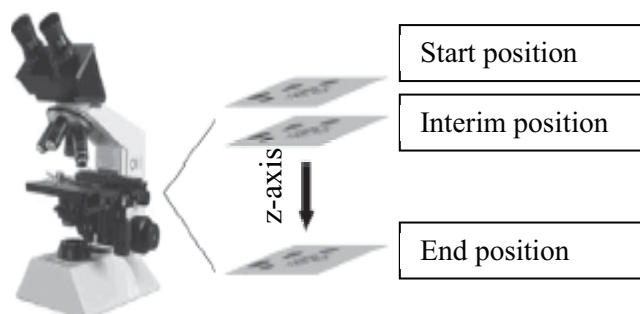


**Figure 5.1** The Autofocus Function is Defined over a range of Focal Distance Encompassing the in-focus Imaging Position after Chen, (1989).

## 5.3 Fluorescence and Brightfield Autofocusing

The two main methods for the samples analysis are fluorescence and brightfield microscopy, using different illumination sources and imaging conditions. Fluorescent microscopy used to analyze the samples prepared with the light-absorbing stains are labeled with fluorescent dyes while using bright field microscopy.

In fluorescence microscopy, the samples are processed with specific reagents that allow the individual molecules to absorb and emit light at different wavelengths. The fluorescent image can be used directly for automatic focusing. However, due to the formation of photo bleaching and destructive byproducts, exposure of light sensitive samples to light should be kept to a minimum (Chen, 1989). This introduces a strict requirement for the speed of automatic focusing algorithms. On a bright field microscopy, the autofocus function is the only model with tails extending generally over a wide depth range. In contrast, fluorescence images typically have a low signal-to-noise ratio (SNR) and the above-mentioned assumptions are not always true (**Figure 5.2**).

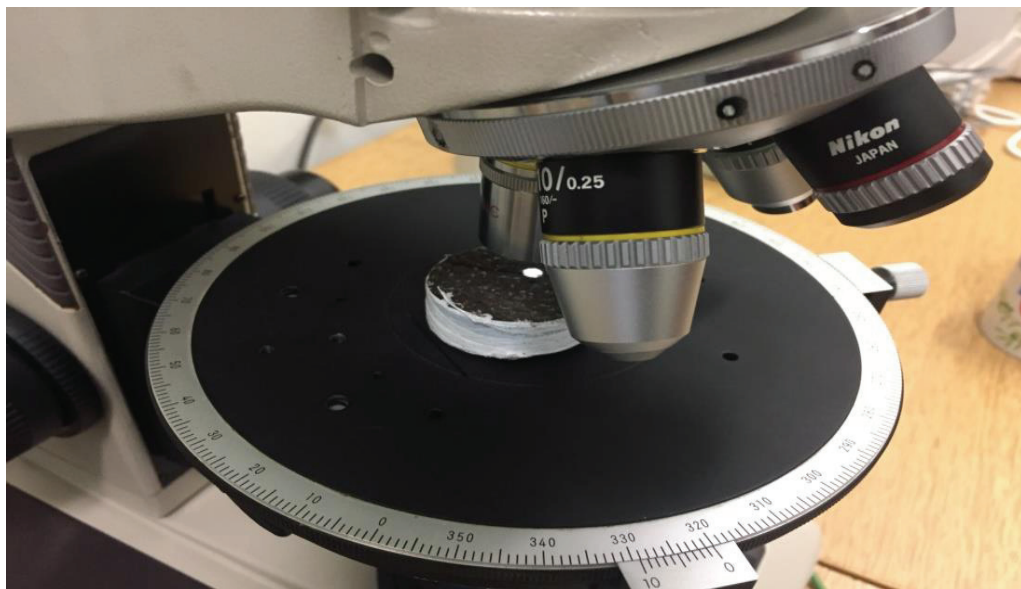


**Figure 5.2** Equivalent Fracture Aperture Measurement by Autofocus Imaging Position.

On a brightfield microscopy, the specimens are illuminated by the transmitted light condensed by a lower condenser. The samples typically appear dark against a bright background with a high SNR. In addition, the samples are generally not destroyed as quickly as fluorescence-labeled samples. For this reason, most of the existing autofocusing methods work better than fluorescence counterparts for brightfield microscopy (**Figure 5.3**) (Chen, 1989).



**Figure 5.3** Autofocused Image of the Core Sample.

In the following chapter the definition of the problem and the objectives of the thesis would be given.

## **CHAPTER 6**

### **STATEMENT OF THE PROBLEM**

In naturally fractured reservoirs, the matrix is the dominant storage area while the main flowing channels are fractures. Oil production in fractured reservoirs shows high and low oil saturation values throughout the reservoir. This is due to the microscopic fissures and heterogeneity of the poorly swept fracture environment. Also, in the literature the analytical solutions of the fractures were defined by cubic law (CL), local cubic law (LCL) and modified cubic law (MCL). However, due to the lack of consideration of fracture properties with limited experimental work, there needs still a work on this field.

This study is aimed to show the effect of fractures and fracture like features on the fluid flow mechanism both in oil saturated and water saturated environments using the core plugs naturally and artificially fractured. CT scanner will be used to visualize the saturation distributions and fracture effect on the cores.

Finally, equivalent fracture aperture calculations will be compared analytically by CL equation and measured by microscope. In order to find an empirical equation that can be used to define the flow behavior of the fractured system experiments will be carried out with/without polymer gel application.



## CHAPTER 7

### EXPERIMENTAL DESIGN

This study is aiming to investigate the use of polymer gel for the limitation of water production through fractures experimentally. This chapter discusses the material, experimental set-up and procedure used throughout the study.

#### 7.1 Materials

The experimental study is mainly carried out by core-flooding tests in which six different core plugs drilled from a tuff outcrop were used. All core samples have the dimensions of 3.7 cm (1.5") in diameter and 7.4 cm in length (3"). The XRF analysis of core plugs is given in APPENDIX-A, **Table A.1**. It is seen that the most abundant element is SiO<sub>2</sub> with a weight percent of 58.65 followed by Al<sub>2</sub>O<sub>3</sub> with 16.86%. Therefore, the core plugs are assumed to be sandstones.

All core plugs were analyzed initially with respect to their porosity and permeability values in **Table 7.1**. The porosity was measured by saturating the dry core samples with de-ionized water and helium permeameter was used to measure the permeability. As seen, all core plugs have porosity values closer to each other on the order of 30 % but different permeabilities. Core #2 exhibits higher permeability compared to other core plugs. In order to find the reason for the difference in the permeability of Core #2, dry sample CT scans of all samples were analyzed. It is found that Core 2# is a naturally fractured sample. **Figure 7.1** and **Figure 7.2** show the CT scan cross-sections of Core #2 and Core #8 for comparison. It is clear that all four sections of Core #2 exhibit a line representing the natural fracture while there is no indication of fracture in the CT scans of Core #8. The other four core samples had the same characteristic of Core #8 with no natural fracture. Finally, **Figure 7.3** presents all 16 CT cross-sections of Core #2 where the location of the fracture moves

which indicates that the orientation of fracture is not parallel to the sides of the cylindrical core but skewed.

During the course of study three of the six core samples (Core #3, Core #6, and Core #7) were artificially fractured (AF) by cutting them in two halves in longitudinal direction. Porosity and permeability of those core plugs were measured again after cutting operation and the results are presented in **Table 7.2**. As observed, both porosity and permeability values of core samples were increased compared to original values as expected, except the porosity of Core #3.

**Table 7.1** Porosity and permeability values of core plugs.

Core	#2	#3	#5	#6	#7	#8
Permeability (md)	207	81	41	87	116	74
Porosity (%)	34	34	31	32	31	32

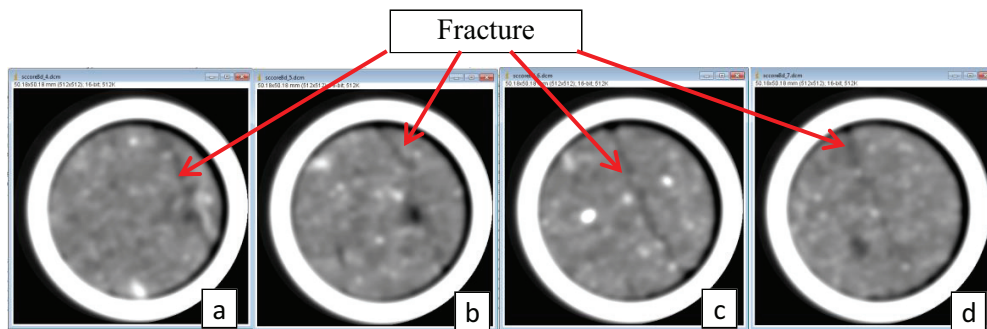


**Figure 7.1** Original CT Slice Views of Core#2; a) 2 mm from the inlet, b) 5 mm from the inlet, c) 5 mm away from the outlet, d) 2 mm from the inlet.

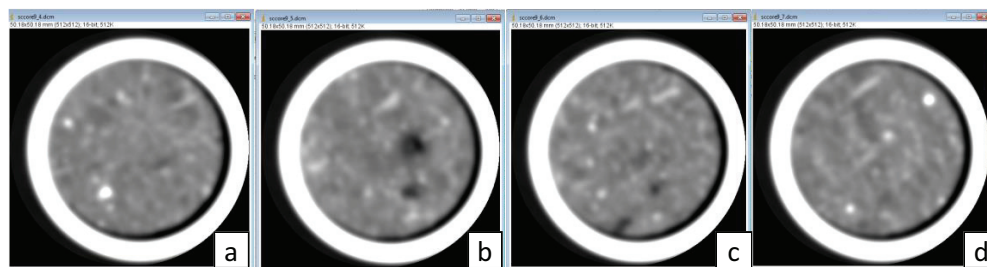


**Figure 7.2** Original CT Slice Views of Core#8 a) 2 mm from the inlet, b) 5 mm from the inlet, c) 5 mm away from the outlet, d) 2 mm from the inlet.

**Table 7.2** Porosity and permeability values of artificially fractured core plugs.

Core	#3	#3 AF	#6	#6 AF	#7	#7 AF
Permeability (md)	81	285	87	301	116	293
Porosity (%)	34	34	32	34	31	34

De-ionized water and n-decane were used in this study as displacing and saturating fluids of the core plugs.

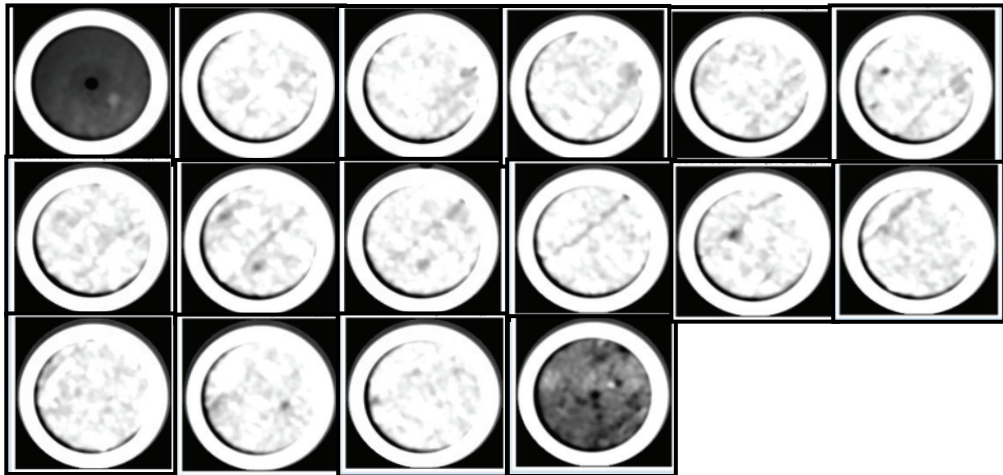


**Figure 7.3** Original CT Slice Views of Core#2.

## 7.2 Experimental set-up

The experimental set-up consists of two main parts, a core-flood system and a CT scanner. A simplified schematic diagram of the core-flood experimental set-up is shown in **Figure 7.4**. The main components of the core flood system are data logger, PC, positive displacement pump, core-holder, two absolute pressure transducers, collector and high-pressure nitrogen cylinder.

The core holder that is designed to accommodate core plug samples with diameter of 1.5” and length up to 4”. The core holder is made of polytetrafluoroethylene (teflon) for scanning purpose because it has lower X-ray attenuation compared to commonly used metal materials. A rubber sleeve surrounds the core plug and is closed by two end pieces at the both ends of the core holder. Confining pressure at the core is applied by injecting nitrogen from high-pressure cylinder (**Figure 7.4** and **7.5**).

The injection system consists of a positive displacement pump (ISCO 500 D syringe pump) equipped with a programmable controller which can be set to deliver constant pressure or flow rate. The pump is connected directly either to core-holder to inject water or n-decane into the core sample. Pressure transducers are connected to the inlet and outlet of the core holder. They are used to measure the flowing pressure during the experiment (**Figure 7.4** and **7.5**).

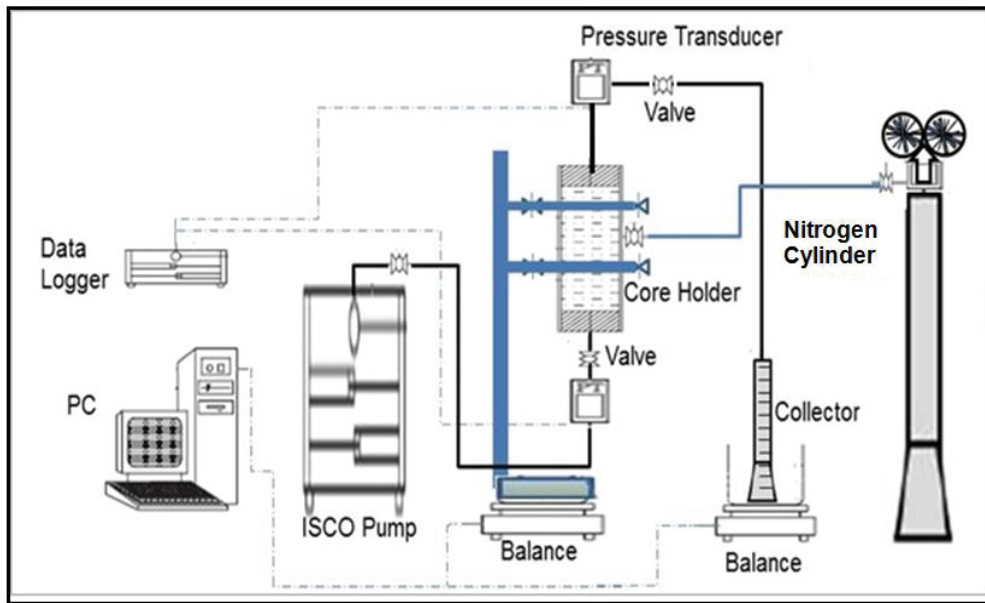


**Figure 7.4** Experimental Set-Up Schematic.

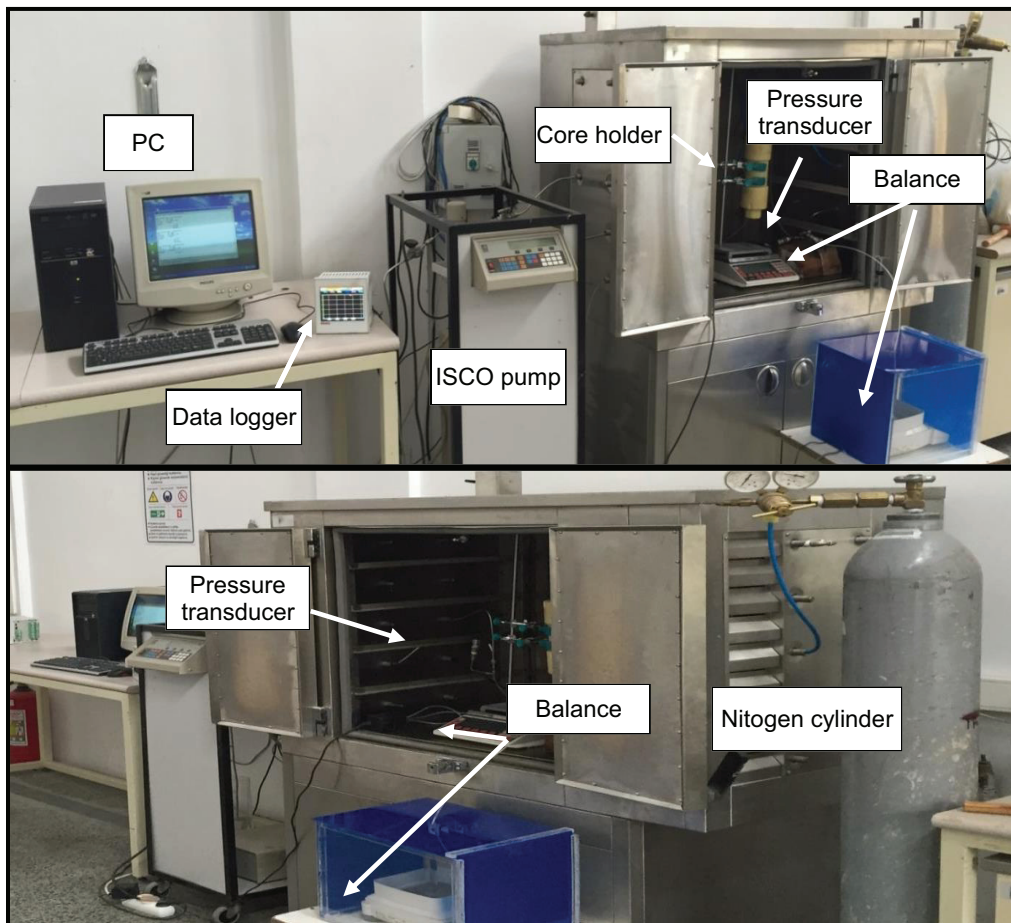


**Figure 7.5** Photographs of the Core-flood Experimental Set-Up.

The X-Ray CT scanner is a fourth generation HITACHI Radix Turbo system with a resolution of  $0.35 \times 0.35 \times 1.00$  mm. The CT system includes a central processor and an auxiliary array processor. The operator's console contains a video monitor for image display (512 pixels  $\times$  512 pixels, 256 shades of gray) (**Figure 7.6**). This scanner is used to collect cross-sectional images along the core. Cross sectional scans of the core sample are made at regular intervals during the experiments. Each cross-sectional slice is 2 mm thick and 3 mm apart. The data obtained from the CT scanner is transferred to a PC for image processing. The cross-sectional images can then be used for porosity and saturation determination for visualization of each experimental core.

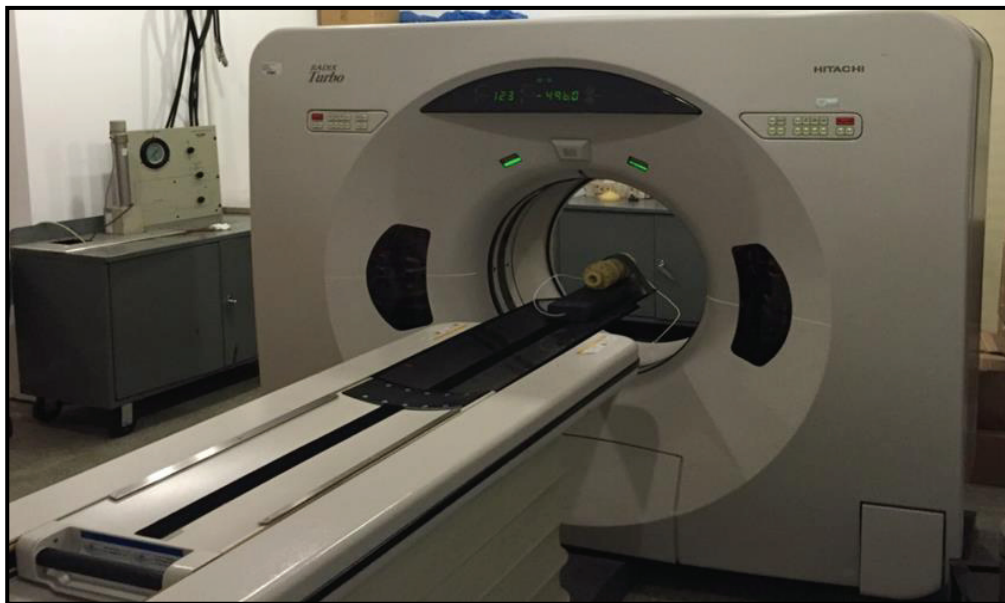


**Figure 7.6** CT scanner HITACHI Radix Turbo.

### 7.3 Experimental Procedure

Eight core-flood experiments have been carried out to investigate different aspects of polymer gel treatment. **Table 7.3** gives the conditions of all eight experiments. As indicated several CT scans were realized at different stages of each experiment. First four experiments were done with two core plugs, one of them is naturally fractured while the other has no fracture. Another application in these experiments is the change in initially saturating fluid, water and n-decane saturated cases. Other four tests were designed to see the effect of artificial fracturing as well as the polymer gel treatment on oil recovery.

The core samples #3, #6 and #7 were artificially fractured then treated with polymer gel while #5 treated with polymer gel without fracturing.

Each experiment starts with taring the core and placing it in the core holder, then, the core in the holder is scanned with CT scanner in order to have the dry slice views at every three mm (16 cross-sections).

After completing dry scan, the core holder is placed into the experimental set-up and connected to the injection, data logging, taring and collecting system. Then saturation run at a lower injection rate (0.1 ml/min) is carried out either with de-ionized water or n-decane. 100 % saturated core holder is taken out from experimental set-up after injecting two pore volumes of saturating fluid, tarred and scanned again (day 1).

In day 2, the core holder is mounted into the experimental set-up once more. Then, 100% water saturated core was flooded with n-decane (if the experiment is started with 100% water) at 0.1 ml/min rate to prepare the core with irreducible water saturation. At the end of this flooding procedure one more CT scan is achieved.

Next, the core is ready for the final step to sweep the n-decane by injecting two pore volumes of water. End of the run, the core is tarred within core holder and CT scanned (day 3).

In addition to the above procedure, as mentioned earlier, polymer gel treatment was applied in four experiments. Polymer Gel Injection is used for natural fracture isolation. Polymer Gel fills the fractures, stops water from the aquifer/reservoir and by this way lets the oil flow from matrix to well. The polymer gel solution must have certain characteristics to have a successful treatment. Polymer concentration is the main parameter dictating the gel strength as well as the viscosity of solution. Gels having viscosity slightly greater than fresh water to rubber can be created in virtually any water. Polymer powder should be mixed carefully with water. The solution should be prepared slowly in order to not create fish eye. Another item of polymer gel treatment is the cross-linker. The gelation reaction starts right after the addition of cross-linker to polymer solution. The polymer solution should be

homogeneous before cross linker addition (Sydansk,1988; Sydansk,1990; Sydansk,1998).

The codes prepared by Sydansk's are given in **Table 7.4**. Polymer gel solution must be flowing in to place properly to the target. In that respect Codes B, C and D must be achieved by polymer and cross-linker concentrations (Sydansk,1988; Sydansk,1990; Sydansk,1998).

Marcit brand polymers and Cr acetate cross-linkers were used in this study. **Table 7.5** lists the Sydansk's gel codes for the Marcit brand polymers. **Table 7.6** shows the amount of cross-linker necessary for polymer gel concentration preparation. Two different concentrations (8,500 ppm and 4,500 ppm) of polymer gel prepared for the experiments. **Figure 7.7** depicts the preparation of polymer gel and **Figure 7.8** shows the cores after experiment.

**Table 7.3** Experimental Sequence of Naturally/Artificially Fractured Core Plugs.

Exp. No	Core #	Initial saturating fluid	Fracture type	Gel Injection / Concentration (ppm)	Experimental sequence
1	2	Water	Natural	No / -	<u>Dry scan</u> , 100 % water saturation, <u>Scan</u> , n-decane injection, <u>Scan</u> , Water injection, <u>Scan</u>
2	2	Oil	Natural	No / -	<u>Dry scan</u> , 100 % n-decane saturation, <u>Scan</u> , Water injection, <u>Scan</u>
3	8	Water	No	No / -	<u>Dry scan</u> , 100 % water saturation, <u>Scan</u> , n-decane injection, <u>Scan</u> , Water injection, <u>Scan</u>
4	8	Oil	No	No / -	<u>Dry scan</u> , 100 % n-decane saturation, <u>Scan</u> , Water injection, <u>Scan</u>
5	3	Water	Artificial	Yes / 4,500	<u>Dry scan</u> , 100 % water saturation, <u>Scan</u> , n-decane injection, <u>Scan</u> , Water injection, <u>Scan</u> , Gel treatment, Water injection, <u>Scan</u>
6	7	Water	Artificial	Yes / 4,500	<u>Dry scan</u> , 100 % water saturation, <u>Scan</u> , n-decane injection, <u>Scan</u> , Water injection, <u>Scan</u> , Gel treatment, <u>Scan</u> , Water injection, <u>Scan</u>
7	5	Water	No	Yes / 4,500	<u>Dry scan</u> , 100 % water saturation, <u>Scan</u> , n-decane injection, <u>Scan</u> , Water injection, Gel treatment, Water injection, Change inlet – outlet ports and water injection, <u>Scan</u>
8	6	Water	Artificial	Yes / 8,500	<u>Dry scan</u> , 100 % water saturation, <u>Scan</u> , n-decane injection, <u>Scan</u> , Water injection, <u>Scan</u> , Gel treatment, Water injection, <u>Scan</u>

**Table 7.4** The Description of all Sydansk's Gel Codes, 1998.

GEL CODE	VIEW	DESCRIPTION
A	No Detectable Gel Formed	The gel appears to have the same viscosity as the original polymer solution and no gel is visually detectable
B	Highly Flowing Gel	The gel appears to be only slightly more viscous than the original polymer solution.
C	Flowing Gel	Most of the obviously detectable gel flows to the bottle cap when inverted.
D	Moderately Flowing Gel	A small portion (about 5-15%) of the gel does not readily flow to the bottle cap upon inversion. Usually characterized as a "tonguing" gel (i.e. after hanging out of the bottle, gel can be made to flow back into the bottle by slowly turning the bottle up right).
E	Barely Flowing Gel	The gel slowly flows to the bottle cap and/or a significant portion (~15%) of the gel does not flow upon inversion.
F	Highly Deformable Non-flowing Gel	The gel does not flow to the bottle cap upon inversion (gel flows to just short of reaching the bottle cap).
G	Moderately Deformable Non-flowing Gel	The gel flows about halfway down the bottle upon inversion.
H	Slightly Deformable Non-flowing Gel	Only the gel surface deforms slightly upon inversion.
I	Rigid Gel	There is no gel surface deformation upon inversion.
J	Ringing Rigid Gel	A tuning fork-like mechanical vibration can be felt after the bottle is tapped.

**Table 7.5** Tests Done With Marcit Gel Mixtures and Effect Code after Demir, 2008.

Time (hours)	4,500 ppm	5,500 ppm	7,000 ppm	8,500 ppm	10,000 ppm
1	A	A	A	A	B
2	B	B	B	C	D
3	C	C	C	D	E
4	C	C	D	E	F
5	D	D	E	F	G
6	D	D	E	F	H
7	D	D	E	F	H
24+	D	E	F	G	H

**Table 7.6** X-Linker-Polymer Concentration Ratios after Demir, 2008.

Concentration, ppm	X-Linker, It
2,400 < x < 4,500	0.2025 × Polymer (lbs)
4,501 < x < 8,499	0.1620 × Polymer (lbs)
8,500 < x < 17,000	0.1341 × Polymer (lbs)
17,001 < x < 30,000	0.1010 × Polymer (lbs)

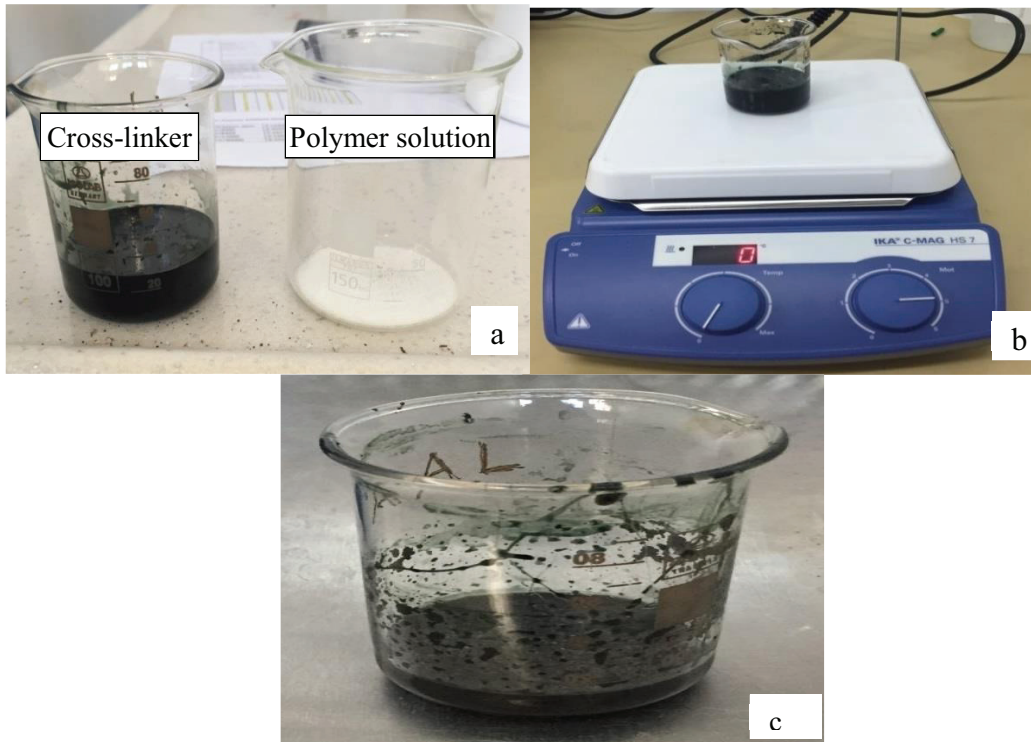


**Figure 7.7** a) Polymer Gel Amount b) Preparation Equipment (Magnetic Stirrer)  
c) Prepared Gel.



**Figure 7.8** After the Polymer Gel Injection Experiment, Artificially Fractured  
a) Core#3 and b) Core#6.

## CHAPTER 8

### EXPERIMENTAL DATA ANALYSIS

The following data is recorded during the course of each experiment:

- Weight of core holder holding the core plug at different stages of experiment;
  - Clean, dry, air-saturated core plug,
  - 100 % water or 100 % n-decane saturated core plug,
  - Core plug having irreducible water saturation,
  - Waterflooded core plug with 2 PV water injection.
- Volume of produced water and n-decane as function of time.
- Inlet and outlet pressures of the core holder.

In addition, CT scans of the core holder holding the core plug is taken at the following time steps:

- Clean, dry, air-saturated core plug,
- 100 % water or 100 % n-decane saturated core plug,
- Core plug having irreducible water saturation,
- Waterflooded core plug with 2 PV water injection before gel treatment,
- Waterflooded core plug with 2 PV water injection after gel treatment.

All these recorded data are utilized to estimate/calculate the following properties:

- Permeability of the core plug by using flow rate and inlet – outlet pressure data,
- Porosity of the core plug by using the weight measurements of 100 % water saturated and dry core plug,
- Porosity of the core plug with the help of CT scans of 100 % water saturated and dry core plug,
- Water and n-decane saturations of core plug with the help of CT scans of core plug having multiple fluid saturations.

The following sections will first introduce the method of porosity and saturation calculations from CT scan data then a general discussion of experiments will be made by grouping the experiments.

### 8.1 Discussion on Naturally Fractured vs. Non- Fractured Core Plugs

Porosity and saturation determination from CT scan data have been discussed in Chapter 2 and the following two equations were given for the calculations:

$$\phi = \frac{CT_{wsat} - CT_{dry}}{CT_w - CT_A} \quad (\text{Equation 2.2})$$

where  $\phi$  is porosity (fraction).  $CT_{wsat}$  is the CT number of 100% water saturated core inside core-holder.  $CT_{dry}$  is the CT-number for dry core inside core-holder.  $CT_w$  is the CT-number for water, and  $CT_A$  is the CT-number for air. Among these four values  $CT_{wsat}$  and  $CT_{dry}$  are obtained from CT scan runs of each experiment. On the other hand,  $CT_w$  and  $CT_A$  are taken from literature with the numerical values of 0 and -1000, respectively.

A single scan of a multiple fluid saturated core plug is sufficient to determine two phase (water and n-decane) saturation. Linear interpolation between the pure states is used for determining the saturation. The water saturation ( $S_w$ ) can be calculated by using the following equation:

$$S_w = \frac{CT_x - CT_o}{CT_w - CT_o} \quad (\text{Equation 2.5})$$

where  $CT_x$  is the CT-number of multiple fluid saturated core plug,  $CT_w$  and  $CT_o$  are 100% water and 100% n-decane saturated core samples. One way to obtain  $CT_w$  and  $CT_o$  is by scanning the 100% water saturated core, then cleaning the core and totally saturating it by oil and take the second scan to determine  $CT_o$ .  $CT_w$  is actually the same of  $CT_{wsat}$ .

In total, the following four different CT scans are required to be able to determine porosity and saturation values of a given core sample at the desired condition:

- $CT_{wsat}$ : CT number of 100% water saturated core inside core-holder,
- $CT_{dry}$ : CT number for dry core inside core-holder,
- $C_{Tx}$ : CT number of multiple fluid saturated core plug inside core-holder,
- $CT_o$ : 100% n-decane saturated core inside core-holder.

CT scan of any cross-section show different CT-numbers depending on the type of fluid saturating the core sample. In this study, each cross-sections of CT scans were converted with a *MATLAB* code to a distribution of color scale (Matlab, 2014). **Figure 8.1** depicts the results of the MatLab code as color scales of 4 different runs at the same cross-section. In order to customize the results from those color scaled images a fixed area of a circle denoted by dots in each image is considered. Then, these images were analyzed and processed with *ImageJ* software to find the arithmetic average of CT numbers which is considered as the overall CT number of the image.

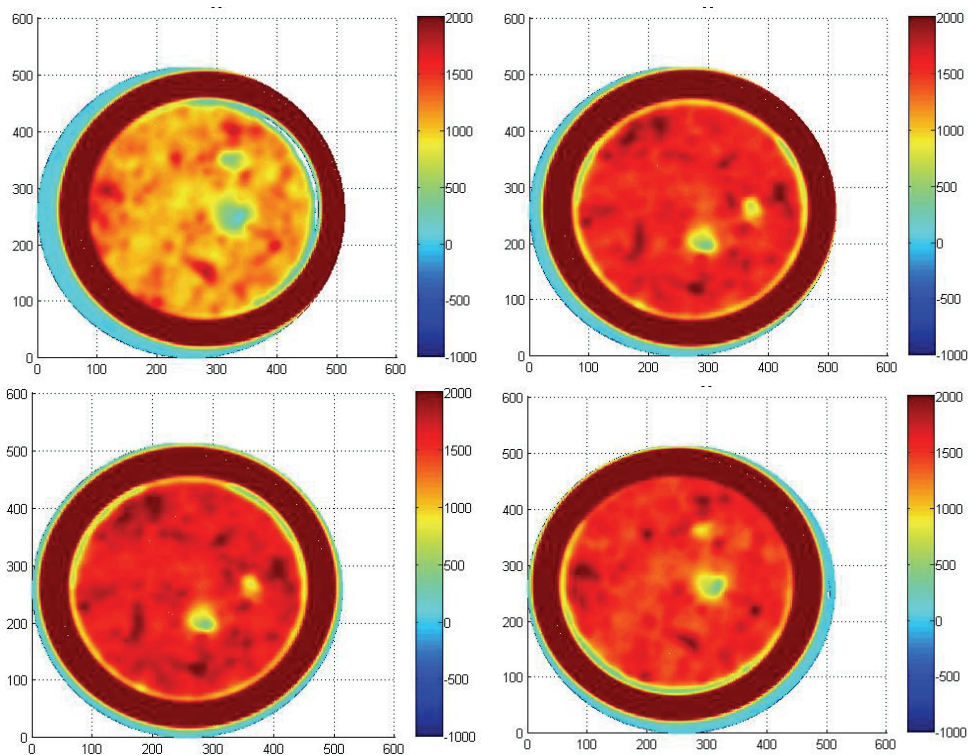


**Figure 8.1** CT Scan Images of the Same Cross-Section from Different Stages of a Given Experiment: From left to right: dry scan (top left), 100% water saturated (top right), irreducible water saturation (bottom left), after waterflooding (bottom right).

Porosity and saturation calculations of Core #8 are taken as an example. **Figures 8.2, 8.3, 8.4, 8.5** and **8.6** present the CT scan images at five different stages of a single experiment. Average CT numbers of the slices were obtained from the representative color code scale generated by ImageJ software for each 16 views. However, the first and last cross-sections are not suitable since an unknown section of those two images are outside the core sample and representing cross-sections without rock.

**Table 8.1a** lists the average CT numbers of all 16 cross-sections of dry and 100 % water saturated cases (**Figures 8.3** and **8.4**). Using **Equation 2.2**, calculated porosity for 14 cross-sections is in the range of 30.5 % to 34.8 % and the arithmetic average results with a porosity value of 32.52% for Core #8. This result is comparable with porosity calculated from gravimetric measurement of 32% (**Table 8.1b**).

**Table 8.1a** CT Numbers of Core#8  
Dry and 100 %Water Saturated).

slice	Dry Scanned	Water Saturated	Porosity
#	CT#	CT#	fraction
1	580	600	
2	1,050	1,386	0.336
3	1,052	1,400	0.348
4	1,051	1,386	0.336
5	1,061	1,388	0.327
6	1,067	1,384	0.317
7	1,075	1,381	0.316
8	1,065	1,387	0.321
9	1,068	1,396	0.328
10	1,065	1,399	0.334
11	1,060	1,388	0.328
12	1,066	1,385	0.320
13	1,075	1,380	0.305
14	1,076	1,384	0.308
15	1,047	1,386	0.339
16	0	610	
	<b>average porosity</b>		<b>32.52%</b>

**Table 8.1b** Experimental Porosity  
Calculation of Core#8.

<b>Core Number</b>	<b>tuff #8</b>
<b>Length, cm</b>	7.400
<b>Diameter, cm</b>	3.700
<b>Area, cm<sup>2</sup></b>	10.752
<b>Permeability</b>	
<b>Viscosity of Liquid, cP</b>	1
<b>Saturated, gr</b>	140
<b>Dry, gr</b>	114.2
<b>Exp1</b>	
<b>Bulk volume, cc</b>	79.525
<b>Pore volume, cc</b>	25.8
<b>Porosity, %</b>	<b>32.00%</b>

**Table 8.2.** lists the CT numbers and calculated water saturations by using the CT scan images from **Figures 8.3, 8.4 and 8.5.** As explained before n-decane is injected into 100 % water saturated core sample to reach irreducible water saturation. It should be mentioned that core holder is kept in vertical position through out the experiment. CT scan is carried out at the end of n-decane injection. The next step is to inject water into core plug (waterflooding) to produce n-decane and after injection of 2 PV of water another CT scan is taken.

Using **Equation 2.5** the water saturation values of the core#8 were calculated (**Table 8.2**). The final average water saturations of two injection runs were found to be 47.82% after n-decane injection and 66.83% after waterflooding.. Saturation calculations by CT scan application is verified by making a material balance on injected fluids. It is assumed that the core plug is saturated only by water and n-decane and all air inside the core sample was removed by injected liquids. The slow injection rate (0.1 ml/min) and vertical arrangement of core holder with injection from the bottom, support this assumption. In that respect, n-decane saturation after n-decane injection and waterflooding would be 52.18% and 33.17%, respectively. Pore volume of core #8 is 25.8 cm<sup>3</sup>. During n-decane injection 52 cm<sup>3</sup> n-decane was injected and 38.5 cm<sup>3</sup> of it was produced. Therefore 13.5 cm<sup>3</sup> of n-decane remained in the core sample which corresponds to n-decane saturation value of 52.32%. The same calculation is done for waterflooding process where 5.0 cm<sup>3</sup> of 13.5 cm<sup>3</sup> was produced by water injection. The remaining volume of 8.5 cm<sup>3</sup> of n-decane makes the final n-decane saturation as 32.94%.

Change in water saturation along the core #8 at the end of n-decane injection and waterflooding applications are given in **Figure 8.7.** As seen two profiles show parallel behavior from inlet to outlet with relatively higher saturations at the inlet (bottom) of the core holder. This gradient in water saturation is attributed to the vertical position of core holder where water has tendency to stay closer to inlet because of its higher density. Change in porosity calculated by CT scan is also given in the same figure. The change in the water saturation has similar behavior with the change in porosity along the core plug. Saturation distribution of core#2 were also calculated with the CT numbers (APPENDIX-B) obtained

(**Table 8.3**) and the calculated water saturation values along the core plug are presented in **Figure 8.8**.

Water saturation at the end of n-decane injection is found to be 52.63 % which makes the n-decane saturation 47.37 %. On the other hand, n-decane saturation from material balance is calculated as 47.43 % (PV of Core#2 is 25.3 cm<sup>3</sup> and 12 cm<sup>3</sup> remained in the core at the end of n-decane injection).

Water saturation at the end of waterflooding is obtained as 65.88 % by CT scan calculations. Material balance calculations result with a n-decane saturation of 29.64 % (4.5 cm<sup>3</sup> n-decane was produced during water flooding, therefore 7.5 cm<sup>3</sup> remained in the core at the end of water flooding). This brings the highest difference between the CT scan derived average saturations and material balance calculated saturations. In all previous cases, the difference was less than 1 % but this time it is about 5 %.

The parallel behavior of water saturation change along the core sample is again seen in core #2 (**Figure 8.8**). The change in porosity has no similarity with the change in saturation.

As mentioned in Chapter 7 (**Figure 7.3**) core #2 has at least one natural fracture determined from CT scan analysis, on the other hand core #8 does not show any fracture. Experiments 1 and 3 listed in **Table 7.3** have the same operational conditions except the core plugs. It is postulated that comparison of the final water saturations of n-decane injection and waterflooding applications of these two experiments may give the effect of natural fracture on sweep efficiency during injection. Change in water saturations during n-decane injection and waterflooding applications for both experiments are listed **Table 8.4**. It is clear that the change in water saturations with core #8 is higher than the changes observed by core #2. This observation shows that the sweep efficiency in core #8 is better than the sweep efficiency in core #2 and the only difference to give this result is the fractured characteristic of core #2. The injected fluid finds easier path to flow through fracture and by-passes the fluid to be displaced. This difference in sweep efficiency shows itself at the recovery graphs of these experiments (**Figure 8.9** and **8.10**). The ultimate n-decane recovery from natural fractured core (core #2) is 36.66 % (**Figure 8.9**). On the other hand, the ultimate

recovery from non-fractured core (core #8) is 42.50 % (**Figure 8.10**). This again shows the adverse effect of fracture on sweep efficiency.

The other two runs with core #2 and core #8 are Run #2 and Run #4. In these tests the core plugs were initially 100 % saturated with n-decane rather than de-ionized water. The production curves of these runs are given in **Figure 8.11** and **Figure 8.12**. There are two main outcomes from the interpretation of these Figures:

- Ultimate recoveries of n-decane are higher in case of 100 % n-decane saturated core plug compared to 100 % water saturated core plug, as expected. The main cause for this higher recovery could be the sole production of n-decane until water breakthrough.

- The ultimate recovery of n-decane is higher with core #8 (non-fractured core) compared to core #2 (naturally fractured core). This is the same result that was obtained by 100% water saturated cores. In either case, the fractured characteristics of core #2 decreased the sweep efficiency and resulted with lower recoveries.

**Table 8.2** CT Numbers of Core#8 for Saturation Calculations.

Slice	CT number of 100 % Water Saturated Core	CT number of 100 % n-decane Saturated Core	CT number of core with irreducible water saturation	Water saturation initially (percent)	CT number of waterflooded Core	Water saturation after waterflood (percent)
1	600	610	600		615	
2	1,386	1,100	1,285	65	1,360	91
3	1,400	1,130	1,283	57	1,372	90
4	1,386	1,119	1,238	45	1,317	74
5	1,388	1,115	1,242	47	1,306	70
6	1,384	1,112	1,233	44	1,292	66
7	1,381	1,115	1,218	39	1,277	61
8	1,387	1,116	1,237	45	1,285	63
9	1,396	1,129	1,264	50	1,309	68
10	1,399	1,128	1,265	51	1,306	66
11	1,388	1,124	1,239	43	1,278	58
12	1,385	1,120	1,244	47	1,274	58
13	1,380	1,107	1,228	44	1,257	55
14	1,384	1,120	1,240	45	1,273	58
15	1,386	1,117	1,247	48	1,275	59
16	610	611	605		605	
<b>average water saturation (percent)</b>				<b>47.82</b>		<b>66.83</b>

**Table 8.3** CT Numbers of Core#2 for Saturation Calculations.

Slice	CT number of 100 % Water Saturated Core	CT number of 100 % n-decane Saturated Core	CT number of core with irreducible water saturation	Water saturation initially (percent)	CT number of waterflooded Core	Water saturation after waterflood (percent)
1	620	-285	590		615	
2	1,400	1,100	1,253	61	1,300	80
3	1,387	1,071	1,234	48	1,276	68
4	1,370	1,067	1,221	46	1,253	60
5	1,374	1,066	1,234	51	1,267	65
6	1,366	1,073	1,240	53	1,272	66
7	1,366	1,075	1,253	56	1,282	68
8	1,361	1,068	1,241	54	1,269	66
9	1,370	1,054	1,228	45	1,262	61
10	1,376	1,065	1,241	51	1,263	61
11	1,366	1,071	1,226	47	1,250	58
12	1,371	1,071	1,250	55	1,275	66
13	1,368	1,071	1,265	62	1,282	68
14	1,367	1,073	1,268	61	1,298	73
15	1,375	1,058	1,215	46	1,250	63
16	615	-285	605		605	
<b>average water saturation (percent)</b>				<b>52.63</b>		<b>65.88</b>

**Table 8.4** CT Numbers of Core#2 & #8 for Saturation Calculations.

Application	Water saturation (%)					
	n-decane injection			Waterflooding		
	Initial %	Final %	Difference %	Initial %	Final %	Difference %
Core #2	100	52.63	47.37	52.63	65.88	13.25
Core #8	100	47.82	52.18	47.82	66.83	19.01

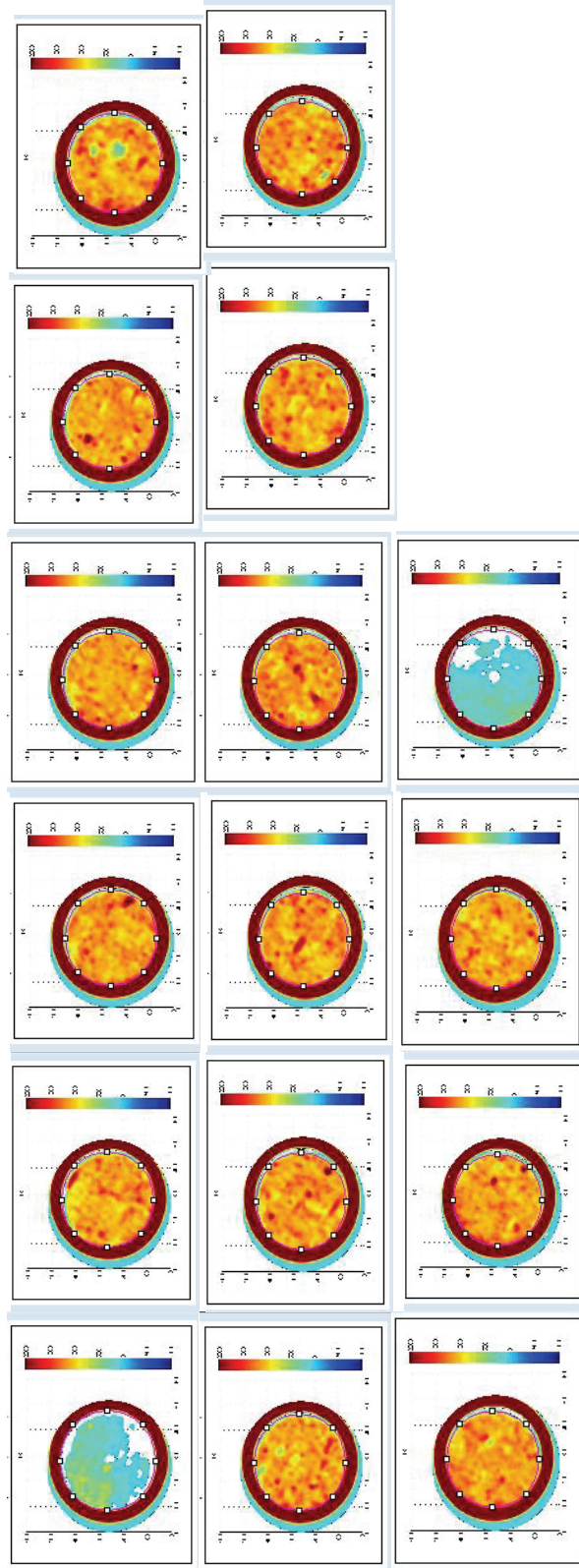


**Figure 8.2** CT Scan Images of Core#8, Dry ( $CT_{dry}$ ).

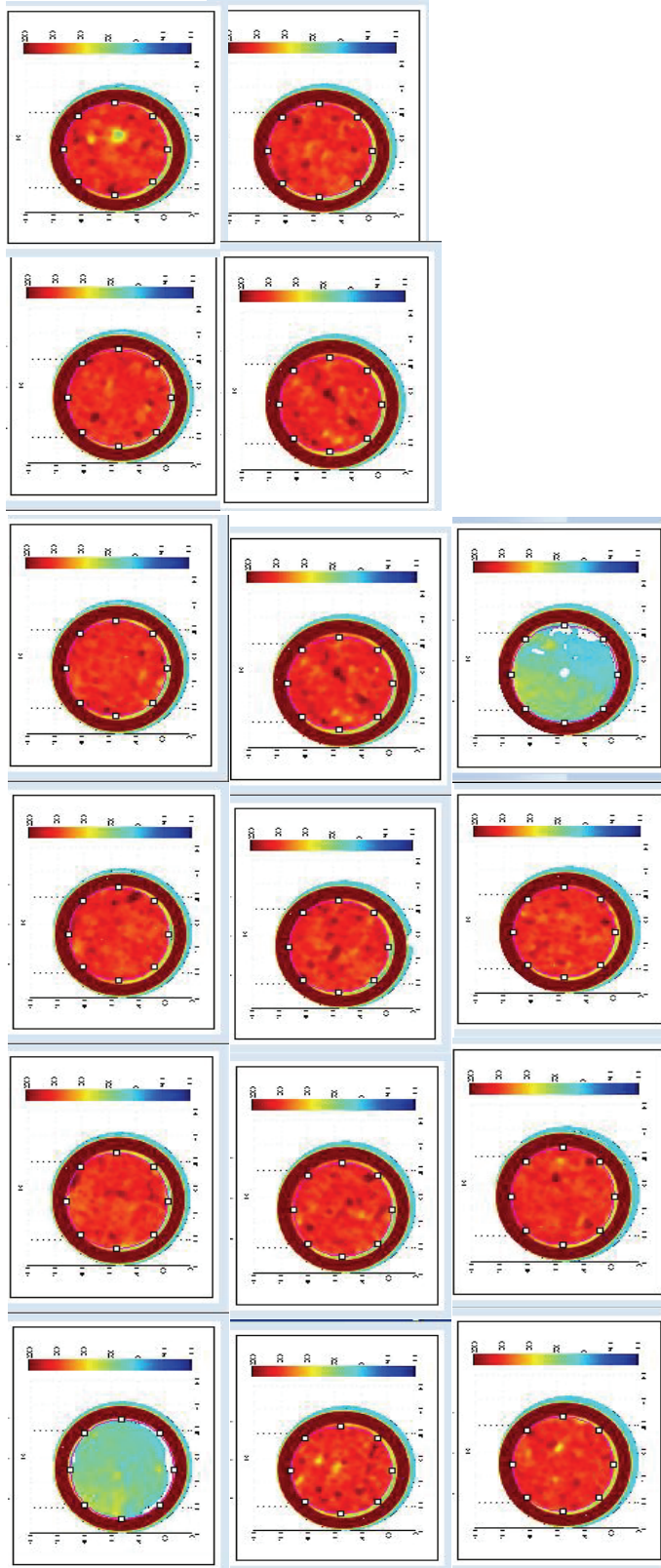


**Figure 8.3** CT Scan Images of Core#8, 100% Water Saturated ( $CT_{wsat}$ ).

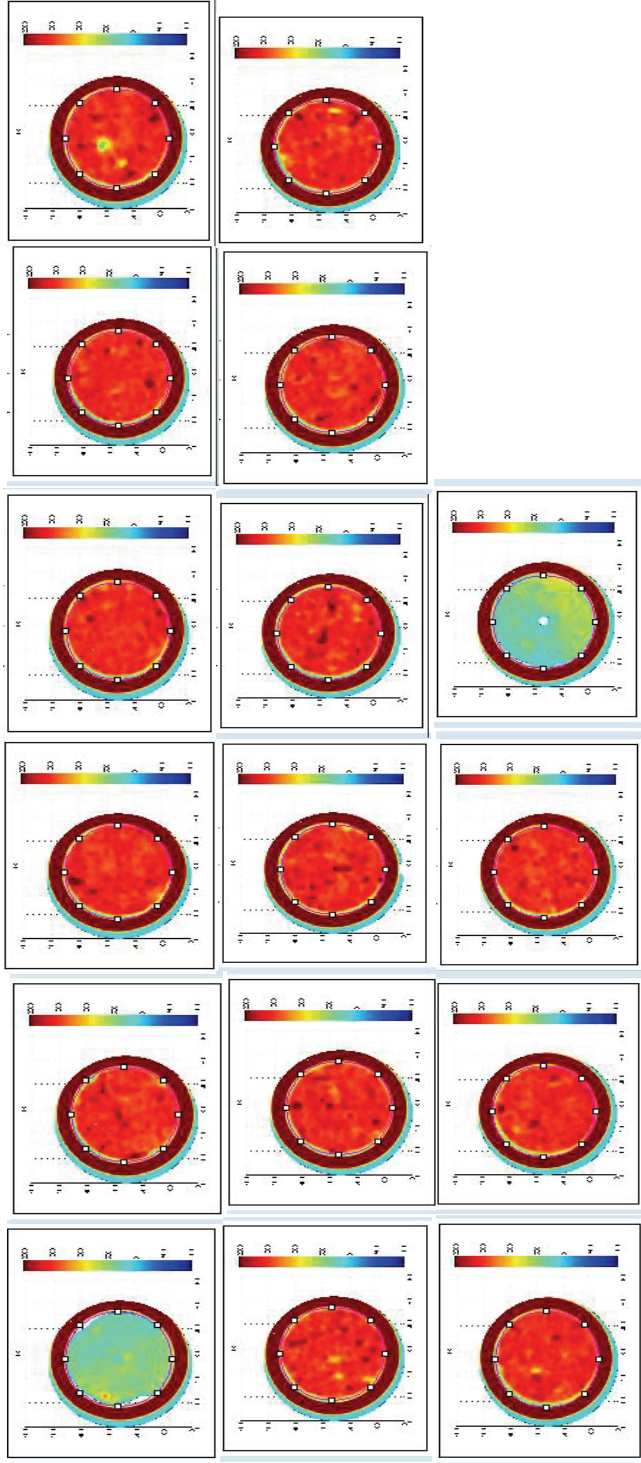


**Figure 8.4** CT Scan Images of Core#8, 100% n-Decane Saturated ( $CT_0$ ).

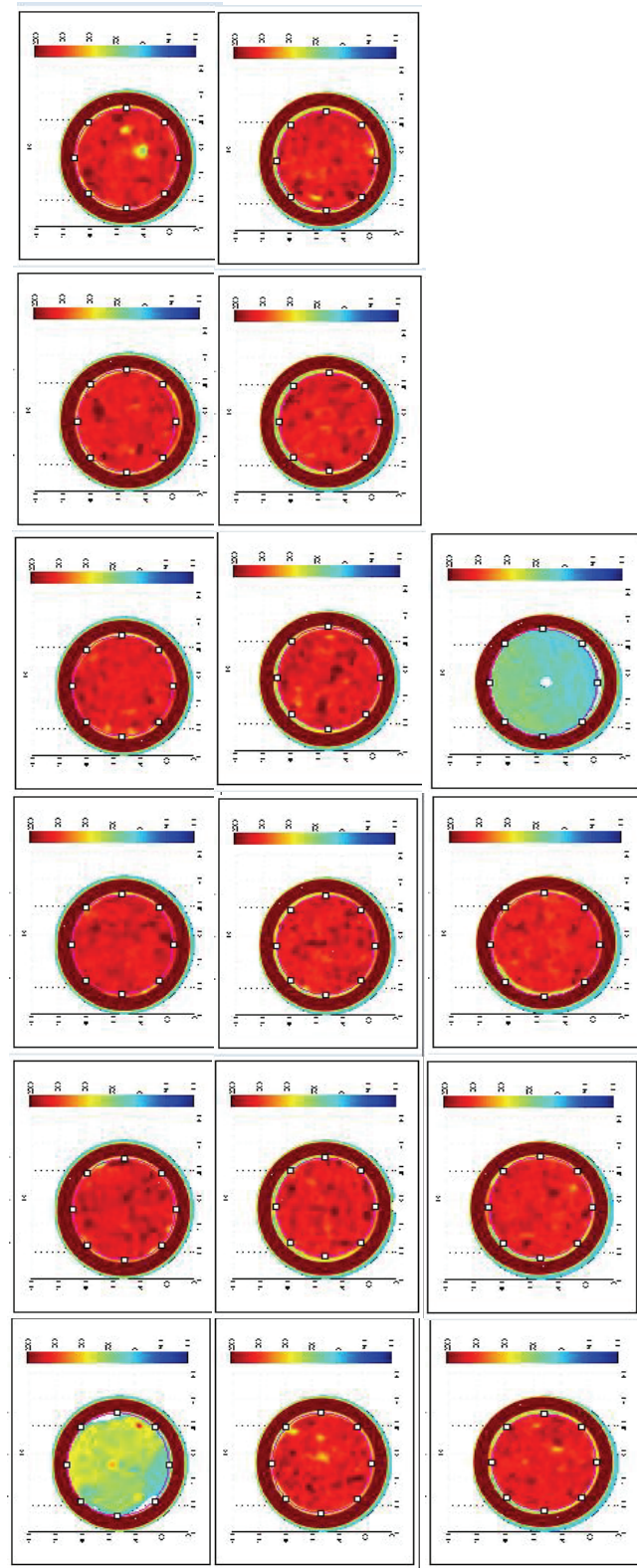


**Figure 8.5** CT Scan Images of Core#8, Irreducible Water Saturated ( $CT_x$ ).

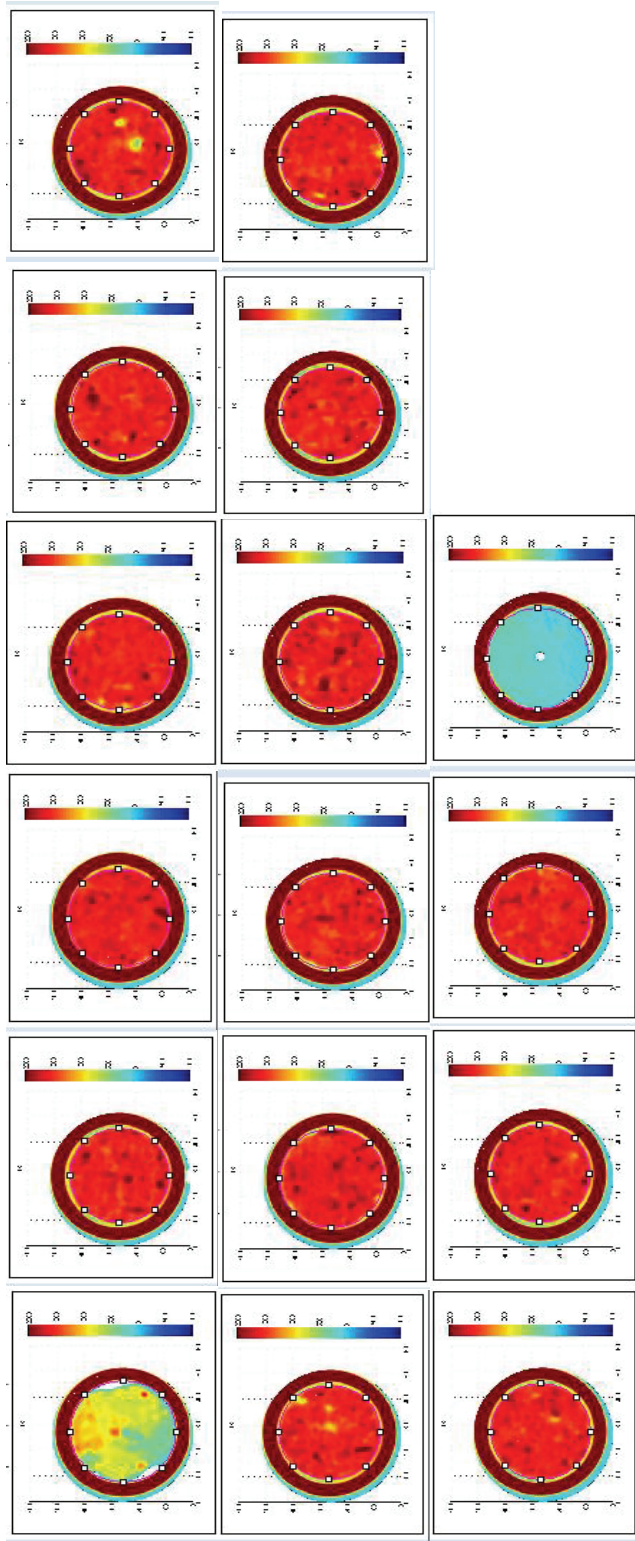


**Figure 8.6** CT Scan Images of Core#8, Waterflooded ( $CT_y$ ).

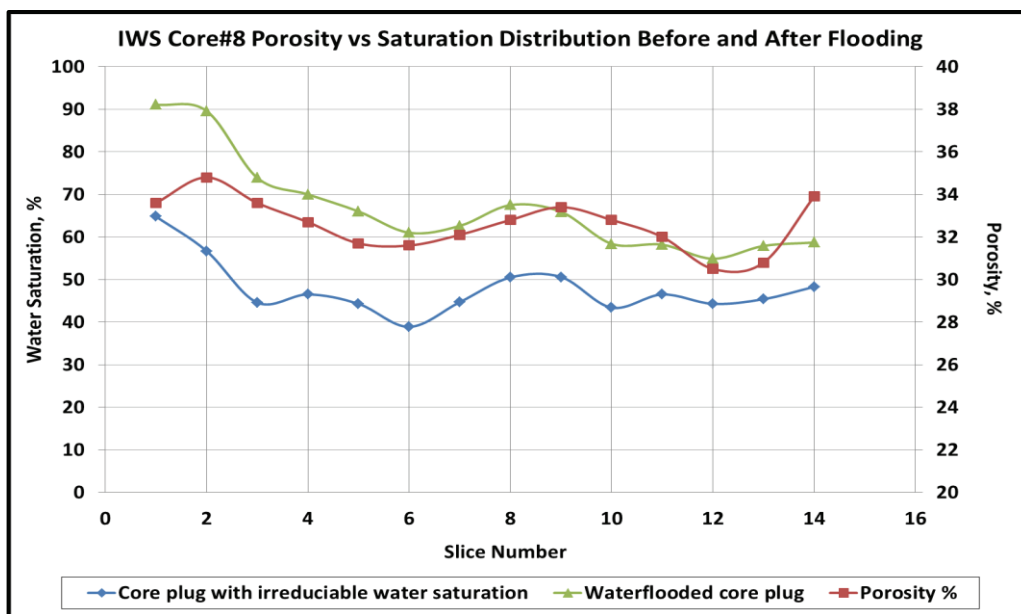


Figure 8.7 Change in Porosity and Water Saturation along Core#8.

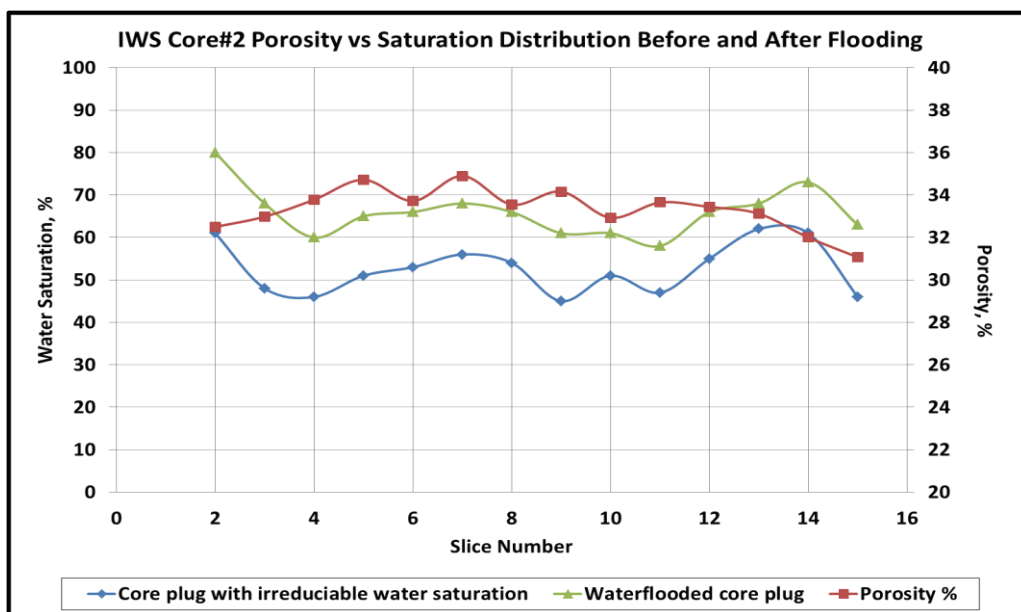


Figure 8.8 Change in Porosity and Water Saturation along Core #2.

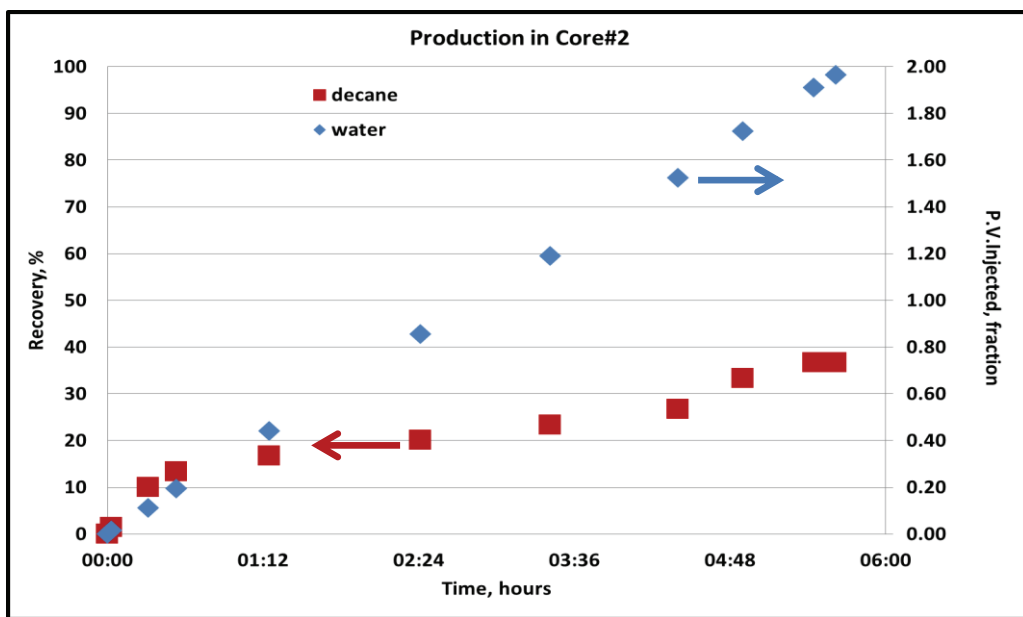


Figure 8.9 n-Decane and Water Production values of Run #1.

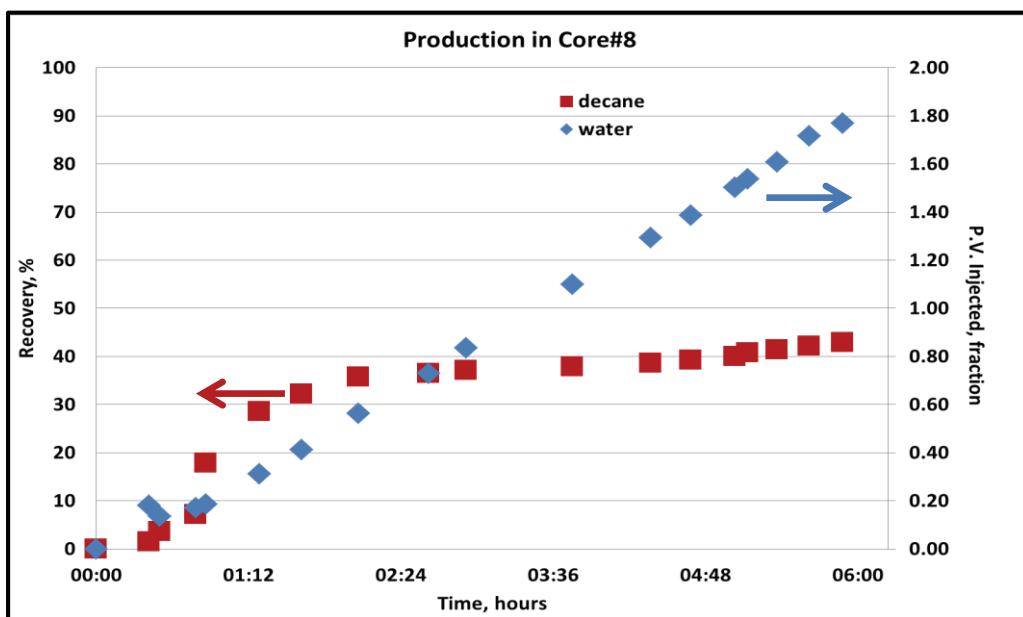
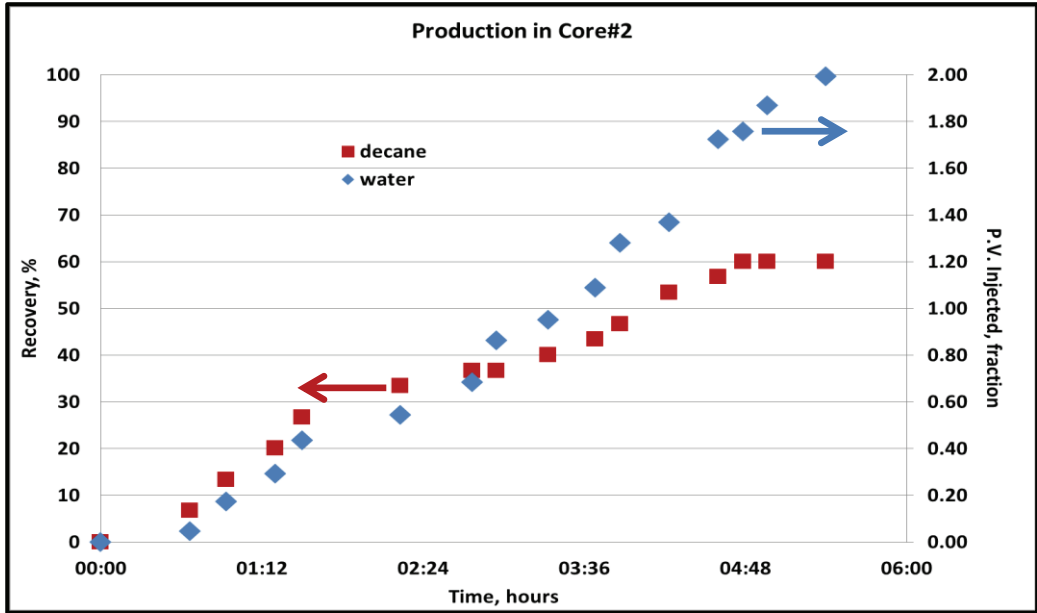
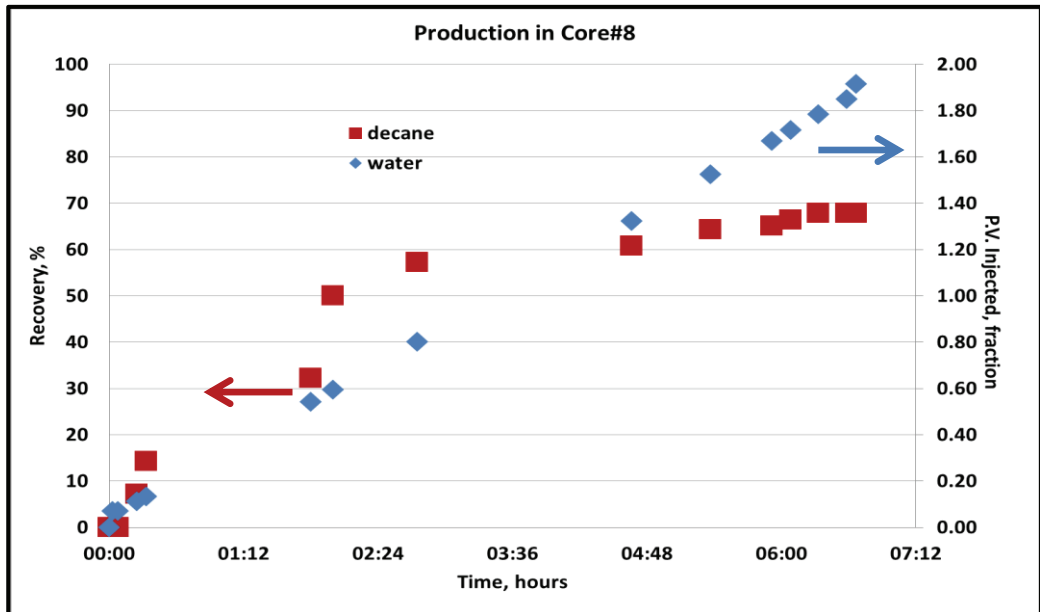


Figure 8.10 n-Decane and Water Production values of Run #3.



**Figure 8.11** n-Decane and Water Production values of Run #2.



**Figure 8.12** n-Decane and Water Production values of Run #4.

Another interpretation on Runs #1 to #4 is done by finding an equivalent fracture permeability to sustain the observed flow rate under real experimental conditions. In order to calculate equivalent fracture permeability a single fracture that has an aperture capable to transmit the observed flow rate need to define.

The equivalent fracture aperture can be obtained by using CL which was described in Chapter 3. CL is the steady-state solution to the Navier-Stokes equations for laminar viscous flow between two smooth parallel plates and given as Equation 3.6. If the measured quantities (flow rate, inlet and outlet pressures as well as viscosity of flowing fluids) are inserted in Equation 3.6 the equivalent fracture aperture (b) can be estimated. In Equation 3.6, flow rate is known from the pumping rate and the fluids are assumed to be incompressible which makes the inlet and outlet flow rates equal. Water and n-decane viscosities under the experimental conditions are very similar with the values of 0.89 cP and 0.86 cP @ 27 °C, respectively. The length of the fracture (L) is actually the length of core plug, 7.4 cm.

Equation 3.12 is used to find the equivalent fracture permeability after obtaining equivalent fracture aperture form Equation 3.6. An example for this procedure is given for Run #1 by utilizing the data given in **Table 8.5**. It is unfortunate that this Run had very monotonous characteristics with the same numerical values throughout the test. The data for Runs #2, #3 and #4 are given in APPENDIX-C.

$$Q = \frac{b^3}{12\mu} \left( \frac{\Delta p}{L} \right) \quad (\text{Equation 3.6})$$

$$k_f = k_{ff} \frac{a.b}{a.h} = k_{ff} \frac{b}{h} = \frac{b^3}{12h} \quad (\text{Equation 3.12})$$

Runs with core #2 (naturally fractured core) indicates a constant behavior with time, no change in equivalent fracture properties (**Figure 8.13** and **Figure 8.14**). On the other hand, the results for core #8, a non-fractured core plug, showed variation with time for equivalent fracture properties (**Figure 8.15** and **Figure 8.16**).

**Table 8.5** CL Rates at 0.1 ml/min Pump injection in Core#2 (Run #1).

Time (hours)	Injection Rate (cm <sup>3</sup> /min)	P <sub>inlet</sub> (bar-g)	P <sub>outlet</sub> (bar-g)	Production Rate (cm <sup>3</sup> /min)	Equivalent Fracture Aperture (mm)	k <sub>f</sub> (cm <sup>2</sup> )	k <sub>f</sub> (md)
00:00	0	0	0	0	0	0	0
00:02	0.10	0.10	0.08	0.10	0.185	1.43 E-09	143
00:19	0.10	0.09	0.07	0.10	0.185	1.43 E-09	143
00:32	0.10	0.08	0.06	0.10	0.185	1.43 E-09	143
01:15	0.10	0.08	0.06	0.10	0.185	1.43 E-09	143
02:25	0.10	0.09	0.07	0.10	0.185	1.43 E-09	143
03:25	0.10	0.09	0.07	0.10	0.185	1.43 E-09	143
04:24	0.10	0.10	0.08	0.10	0.185	1.43 E-09	143
04:54	0.10	0.10	0.08	0.10	0.185	1.43 E-09	143
05:27	0.10	0.10	0.08	0.10	0.185	1.43 E-09	143
05:37	0.10	0.09	0.07	0.10	0.185	1.43 E-09	143

After the experiments, the core #2 fracture aperture also measured with the microscopic view and measurement in the naturally fractured core#2 as 0.214 mm (213.63  $\mu\text{m}$ ), 0.171 mm (171.33  $\mu\text{m}$ ), 0.136 mm (136,19  $\mu\text{m}$ ) and 0. 121 mm (121,31  $\mu\text{m}$ ) in **Figure 8.17**.

Using Equation 3.12 the calculated fracture permeability with respect to the experimental units in cm<sup>2</sup> as 1.43 E-9 then converted to md as 143 given in the last column of the **Table 8.5**. The calculated and measured equivalent fracture apertures showed some differences. Calculated equivalent fracture apertures showed higher values. This is due to the assuming the fractures as a smooth plate not including the roughness and tortuosity of the fractures which are obviously detected during microscope views.

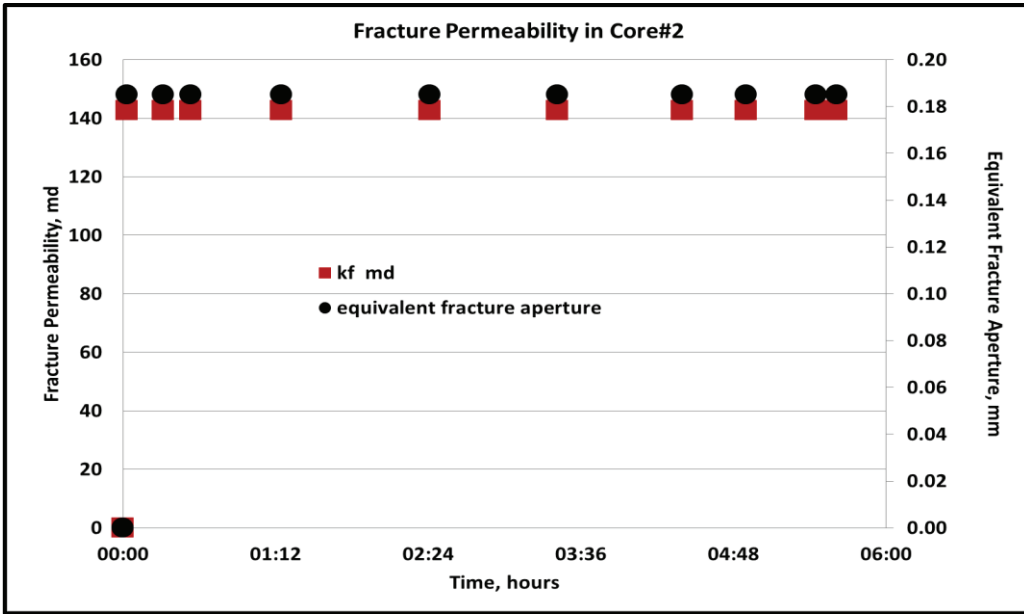


**Figure 8.13** Equivalent Fracture Aperture and Permeability for Run #1.

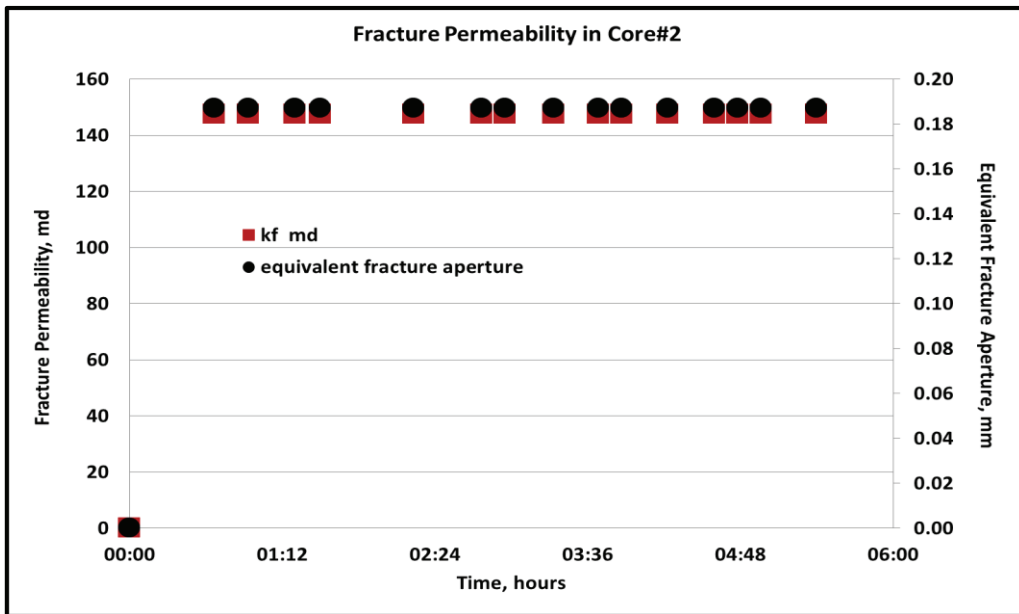


**Figure 8.14** Equivalent Fracture Aperture and Permeability for Run #2.



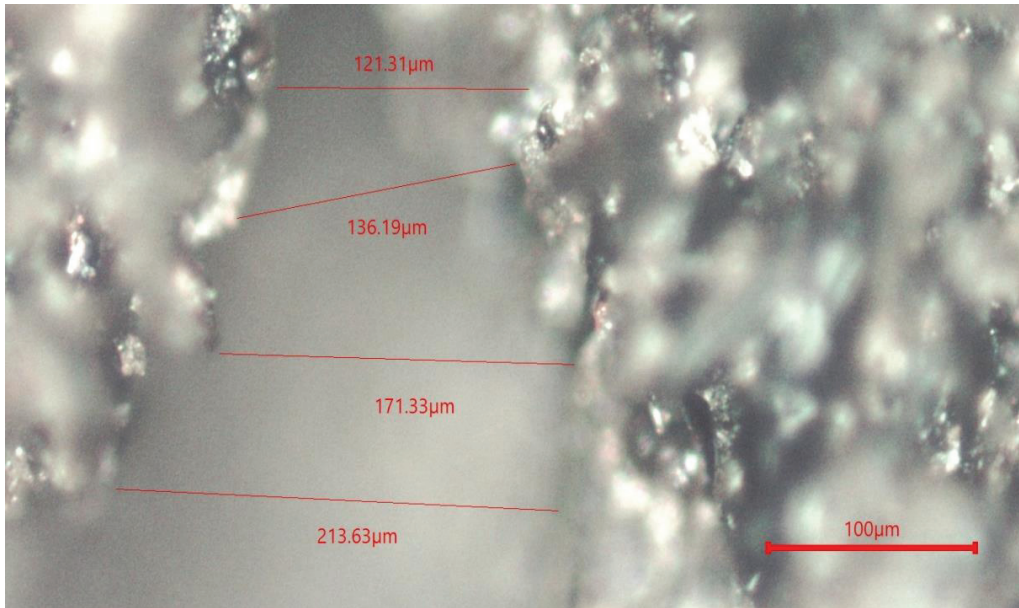


**Figure 8.17** Naturally Fractured Core#2 Fracture Aperture Measurement by Microscope.

## 8.2 Porosity Calculation of Artificially Fractured Cores

The porosity calculations were done for artificially fractured core#3 using the CT numbers obtained after each experiment. The named sequence of the scans given in procedure; dry scanned CT numbers, 100% water saturated scanned CT numbers, with CT number of water ( $CT_{\text{water}} = 0$ ) and CT number of air ( $CT_{\text{air}} = -1000$ ) were used to calculate the porosity of the each thin section. However, the calculation was performed by a selection done from the images seperated by the fracture. They were named as left and right halves of the images, then CT numbers calculated by the same way.

The dry left and right (**Figure 8.18** and **8.19**) and water saturated left and right (**Figure 8.20** and **8.21**) scanned core views average CT numbers and calculated values used in **Equation 3.6** are listed in **Table 8.6** and **Table 8.7**. Results of each thin section porosity from the obtained left and right half sides CT numbers, the average porosity of the artificially fractured core#3 were calculated as 34.09% (left half) and 34.37% (right half). This result also confirmed with the total calculated CT numbers of the core#3 porosity (34.29%) in **Table 8.8a**.

The experimental calculation of the artificially fractured core#3 porosity also shown in **Table 8.8b** as 34%.

**Table 8.6** CT Numbers of Artificially Fractured Core#3  
Left Matrix, Dry ( $CT_{dry}$ ) and Water Saturated ( $CT_{wsat}$ ).

slice	Dry Scanned	Water Saturated	Porosity
#	CT#	CT#	fraction
1	-10	-11	
2	1,012	1,329	0.297
3	1,013	1,497	0.464
4	1,028	1,392	0.343
5	1,054	1,387	0.313
6	1,087	1,411	0.304
7	1,081	1,347	0.245
8	1,078	1,540	0.441
9	1,062	1,421	0.338
10	1,024	1,464	0.420
11	1,020	1,472	0.432
12	945	1,340	0.375
13	998	1,292	0.273
14	1,029	1,386	0.336
15	998	1,203	0.184
16	0	1,100	
		<b>average porosity</b>	<b>34.09%</b>

**Table 8.7** CT Numbers of Artificially Fractured Core#3  
Right Matrix, Dry ( $CT_{dry}$ ) and Water Saturated ( $CT_{wsat}$ ).

slice	Dry Scanned	Water Saturated	Porosity
#	CT#	CT#	fraction
1	-10	-11	
2	1,017	1,390	0.373
3	1,131	1,429	0.298
4	1,093	1,428	0.334
5	1,067	1,478	0.411
6	1,088	1,511	0.423
7	961	1,448	0.486
8	1,177	1,504	0.327
9	1,218	1,462	0.243
10	1,196	1,452	0.256
11	1,196	1,457	0.260
12	1,126	1,393	0.266
13	955	1,424	0.468
14	1,099	1,421	0.322
15	1,060	1,397	0.337
16	0	0	0.343
		<b>average porosity</b>	<b>34.37%</b>

**Table 8.8a** CT Numbers of Artificially Fractured Core#3, Dry ( $CT_{dry}$ ) and Water Saturated ( $CT_{wsat}$ ).

slice	Dry Scanned	Water Saturated	Porosity
#	CT#	CT#	fraction
1	-10	-10	
2	1,012	1,007	0.300
3	1,013	1,008	0.466
4	1,028	1,023	0.345
5	1,054	1,049	0.315
6	1,087	1,082	0.306
7	1,081	1,076	0.247
8	1,078	1,073	0.444
9	1,062	1,057	0.341
10	1,024	1,019	0.423
11	1,020	1,015	0.434
12	945	940	0.377
13	998	993	0.275
14	1,029	1,024	0.338
15	998	993	0.187
16	0	0	
	<b>average porosity</b>		<b>34.29%</b>

**Table 8.8b** Experimental Porosity Calculation of Core#3.

Core Number	tuff #3af
Length, cm	7.400
Diameter, cm	3.500
Area, cm <sup>2</sup>	9.621
Permeability	
Viscosity of Liquid, cP	1
saturated, gr	130
Dry, gr	106
exp1	
bulk volume, cc	71.16
pore volume, cc	24
porosity, %	<b>34%</b>

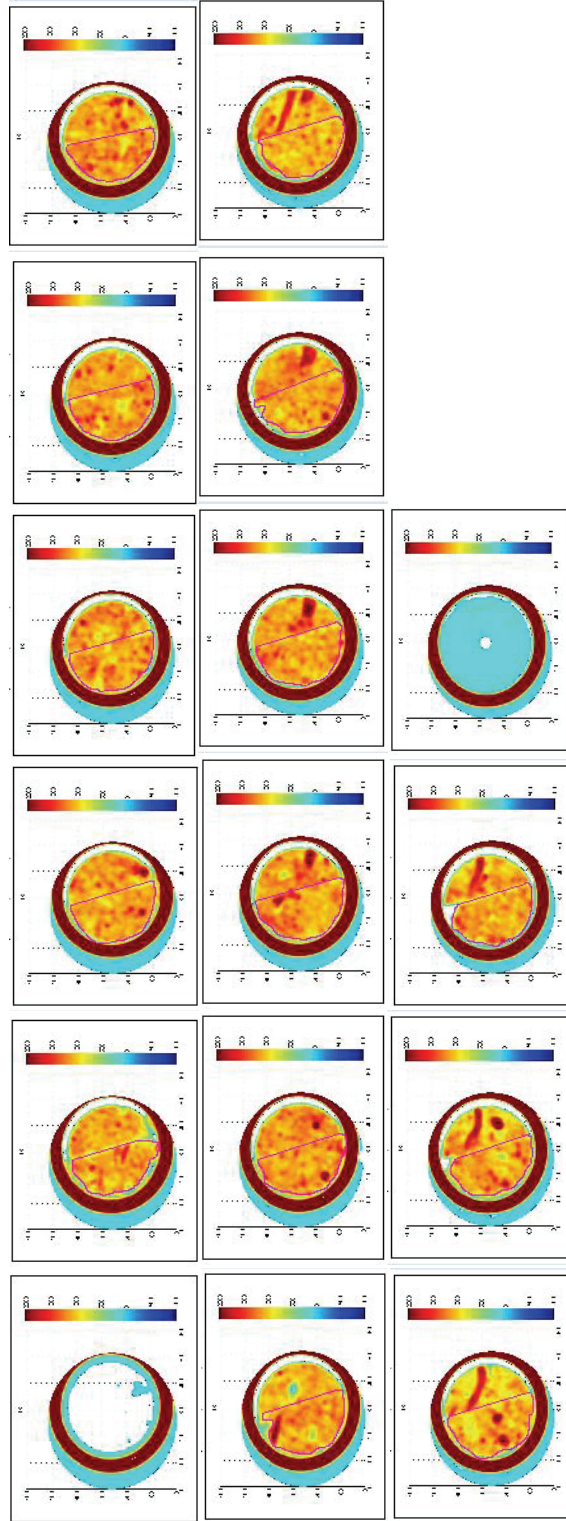


**Figure 8.18** CT Scan Images Artificially Fractured Core#3 Left Half Dry ( $CT_{dry}$ ).

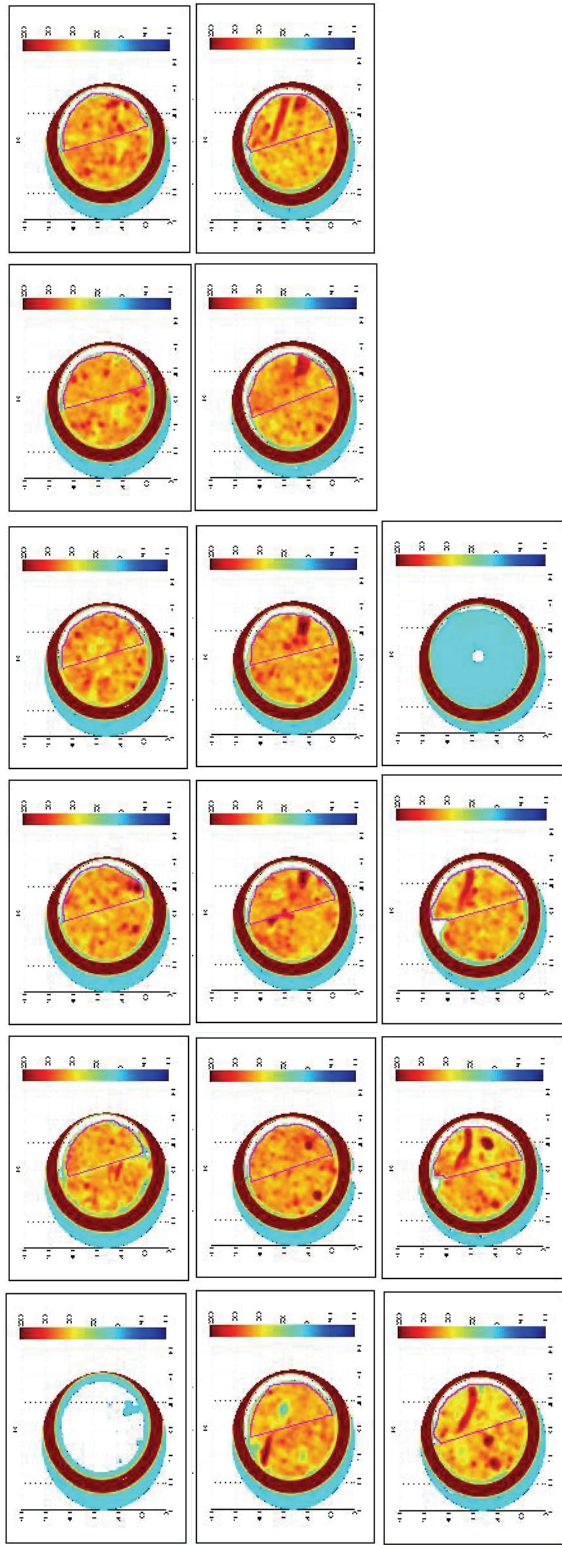


**Figure 8.19** CT Scan Images of Artificially Fractured Core#3 Right Half Dry ( $CT_{dry}$ ).

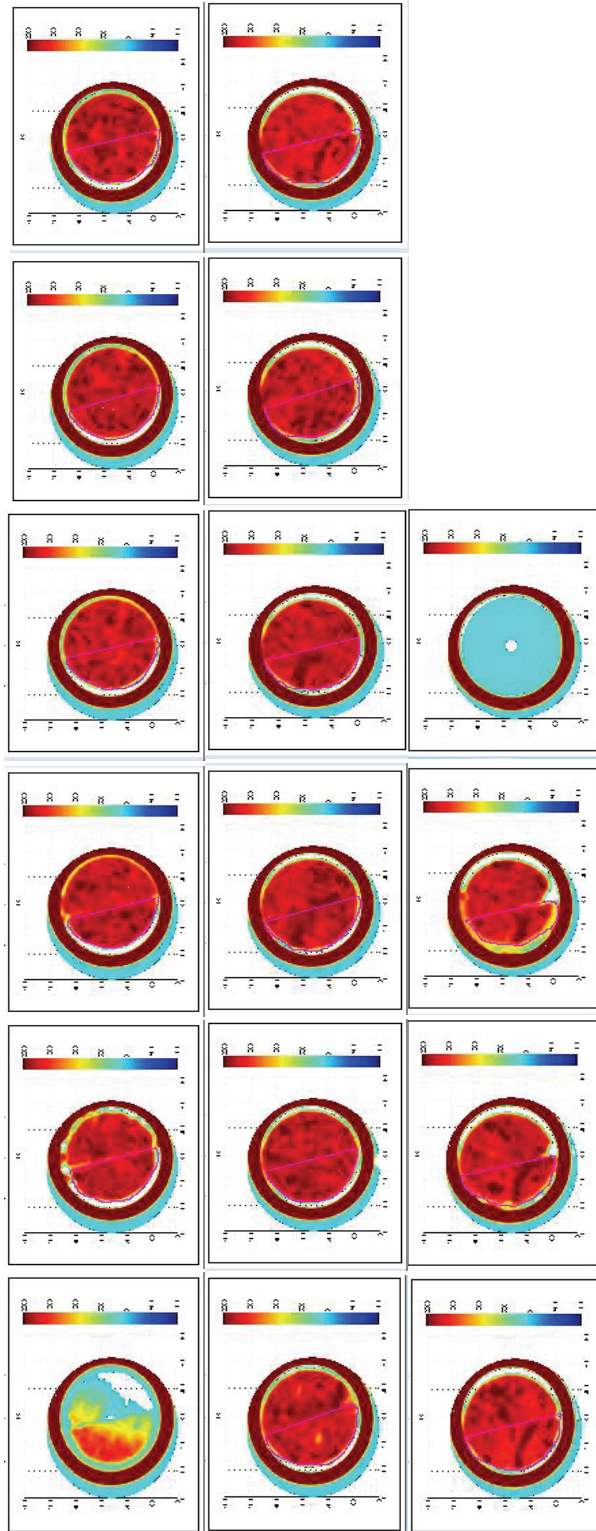


**Figure 8.20** CT Scan Images of Artificially Fractured Core#3 Left Half Water Saturated( $CT_{wsat}$ ).

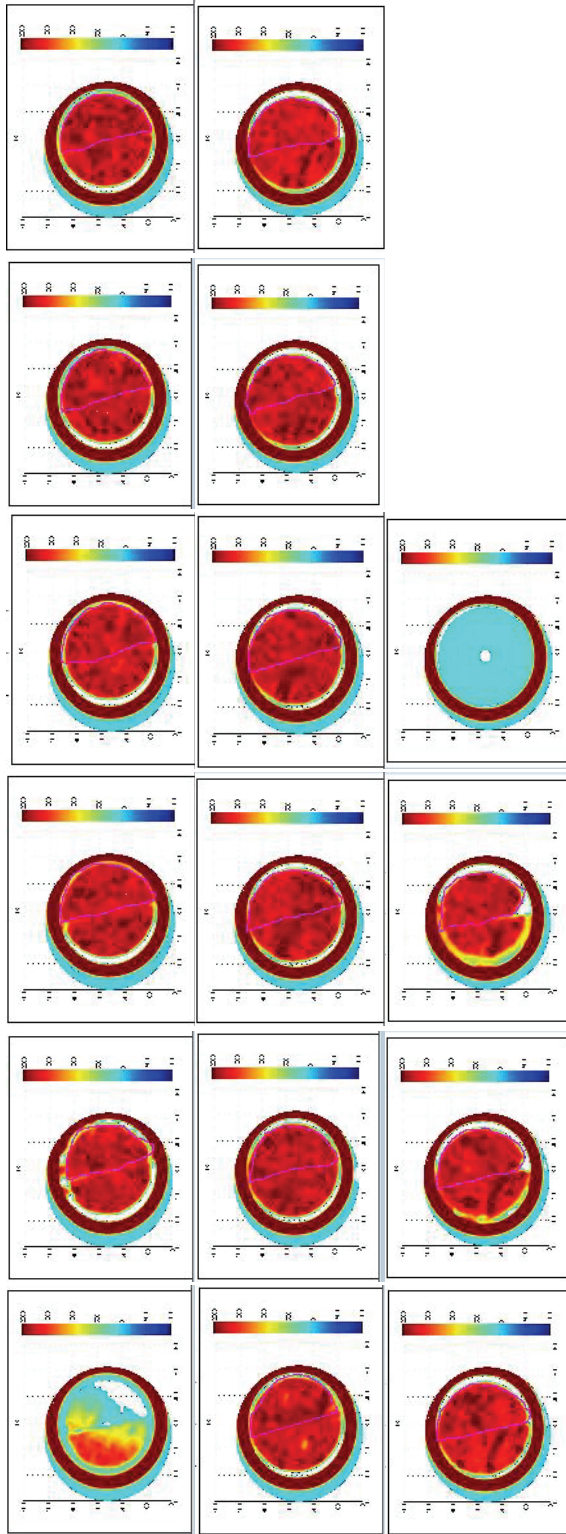


**Figure 8.21** CT Scan Images of Artificially Fractured Core#3 Right Half Water Saturated ( $CT_{wsat}$ ).

Like the calculations in core#3, the named sequence were used to calculate the porosity of the each thin section. Results of each thin section porosity from the obtained left and right half sides CT numbers, the average porosity of the artificially fractured core#7 was calculated as 32.09% (left half) **Table 8.9** and 32.00% (right half) **Table 8.10** (APPENDIX-D).

Moreover, this result was also confirmed with the total calculated CT numbers of the core#7 porosity (32.14%) in **Table 8.11a**.

The experimental calculation of the artificially fractured core#7 porosity was also shown in **Table 8.11b** as 32.00%.

**Table 8.9** CT Numbers of Artificially Fractured Core#7  
Left Matrix, Dry ( $CT_{dry}$ ) and Water Saturated ( $CT_{wsat}$ ).

slice #	Dry Scanned CT#	Water Saturated CT#	Porosity fraction
1	-11	-10	
2	1,158	1,453	0.296
3	1,152	1,503	0.351
4	1,148	1,493	0.345
5	1,148	1,491	0.343
6	1,162	1,483	0.32
7	1,159	1,475	0.316
8	1,154	1,460	0.306
9	1,156	1,468	0.312
10	1,148	1,481	0.332
11	1,145	1,427	0.282
12	1,153	1,512	0.359
13	1,154	1,505	0.351
14	1,150	1,525	0.375
15	1,145	1,350	0.205
16	-1	0	
		<b>average porosity</b>	<b>32.09%</b>

**Table 8.10** CT Numbers of Artificially Fractured Core#7  
Right Matrix, Dry ( $CT_{dry}$ ) and Water Saturated ( $CT_{wsat}$ ).

slice	Dry Scanned	Water Saturated	Porosity
#	CT#	CT#	fraction
1	-10	-10	
2	1,163	1,431	0.268
3	1,157	1,491	0.333
4	1,153	1,483	0.33
5	1,153	1,448	0.295
6	1,167	1,472	0.305
7	1,164	1,490	0.326
8	1,159	1,524	0.365
9	1,161	1,478	0.316
10	1,153	1,507	0.354
11	1,150	1,557	0.407
12	1,158	1,495	0.337
13	1,159	1,501	0.342
14	1,155	1,470	0.315
15	1,150	1,338	0.188
16	0	0	
		<b>average porosity</b>	<b>32.00%</b>

**Table 8.11a** CT Numbers of Artificially Fractured Core#7, Dry ( $CT_{dry}$ ) and Water Saturated ( $CT_{wsat}$ ).

slice	Dry Scanned	Water Saturated	Porosity
#	CT#	CT#	fraction
1	50	-70	
2	1,056	1,370	0.314
3	1,051	1,371	0.320
4	1,046	1,370	0.323
5	1,047	1,369	0.322
6	1,061	1,371	0.310
7	1,058	1,373	0.315
8	1,053	1,373	0.320
9	1,055	1,372	0.317
10	1,047	1,373	0.326
11	1,044	1,373	0.329
12	1,051	1,372	0.321
13	1,052	1,372	0.320
14	1,049	1,371	0.322
15	1,043	1,381	0.338
16	0	50	
	<b>average porosity</b>		<b>32.14%</b>

**Table 8.11b** Experimental Porosity Calculation of Core#7.

Core Number	tuff #7af
Length, cm	7.400
Diameter, cm	3.700
Area, cm <sup>2</sup>	10.752
Permeability	
Viscosity of Liquid, cP	1
saturated, gr	138.5
Dry, gr	113.05
expl	
bulk volume, cc	79.5
pore volume, cc	25.45
<b>porosity, %</b>	<b>32%</b>

### 8.3 Analysis of Polymer Gel Injection

In this part of the study permeability changes compared on the cores before artificial fracture and after artificial fracture. In addition, the permeability change was measured after polymer gel injection (Canbolat and Parlaktuna, 2012).

The permeability of the Core#3 was measured prior to the fracturing process by water injection (**Figure 8.22**). The measured permeability was found 81.262 md for the core. Then, the artificial fracture was created on the core#3. Later, permeability of the core was measured as 284.557 md (**Figure 8.23**).

Finally, polymer gel injected core permeability was measured as 15.315 md (**Figure 8.24**). Polymer gel injection for fracture isolation showed an obvious permeability reduction. Artificially fractured core#3 was saturated with water and then decane (Run#5). The saturation of the core was found by CT measurements as  $S_w$  48.71% and  $S_D$  51.29% and experimental value as  $S_w$  49.47% and  $S_D$  50.53% respectively. Then this core produced with 2 PV injected water. 4.5 cc decane is produced out of 14 cc in the core achieving a recovery of 33.33% OOIP (**Figure 8.25**).

Later, 4,500 ppm concentration of polymer gel scaled and prepared (1.521 gr polymer gel + 30 cc cross linker) then injected to the produced core#3 (polymer gel operation and the second production was started in 1 hour 53 minutes later). 2 cc more decane produced from the core recovering 13.33% of OOIP. In **Figure 8.26** the production of the artificially fractured core#3 before and after gel injection graph is given together to show the incremental recovery. Finally, the residual saturation distribution of the core#3 after polymer gel injection calculated by CT measurements as  $S_w$  71.78% and  $S_D$  28.22% (**Figure 8.26**) and experimentally as  $S_w$  28.90% and  $S_D$  71.10% respectively (CT calculated saturation values given in APPENDIX-D).

Following production experiment in artificially fractured core#3, the analysis were done using CL (Equation 3.6). For the first part of the experiment, from the rates, the equivalent fracture aperture calculations were done and fracture permeabilities were found and tabulated in **Table 8.12** (till to the black line). Using the experiment values in core#3, calculated and real flow rates

equalized each other to find the equivalent fracture aperture in mm. Pump injection rate of 0.2 ml/min, equalized to calculated cubic rate with a equivalent fracture aperture of 0.205 to 0.295 mm. This much of aperture variation was due to the vugs present in core overlapped on the artificial fracture.

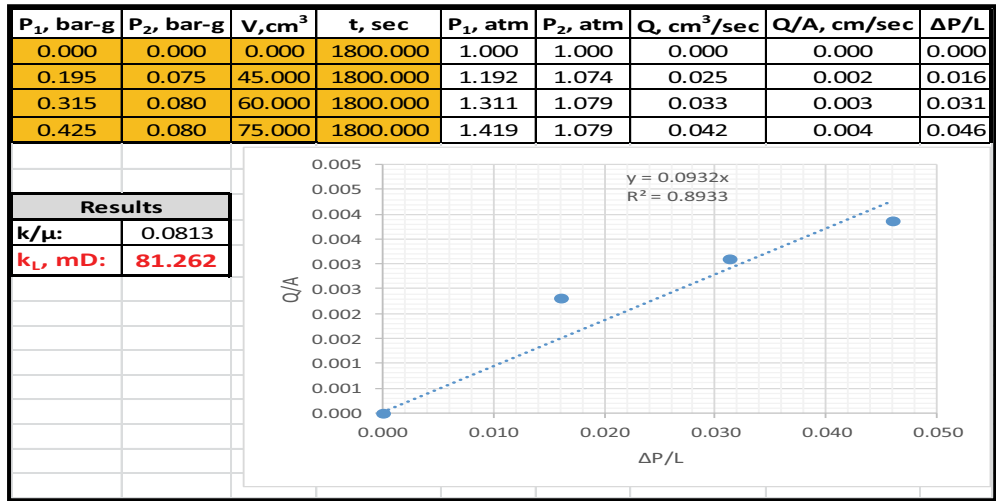


Figure 8.22 Permeability Measurement of Core#3.

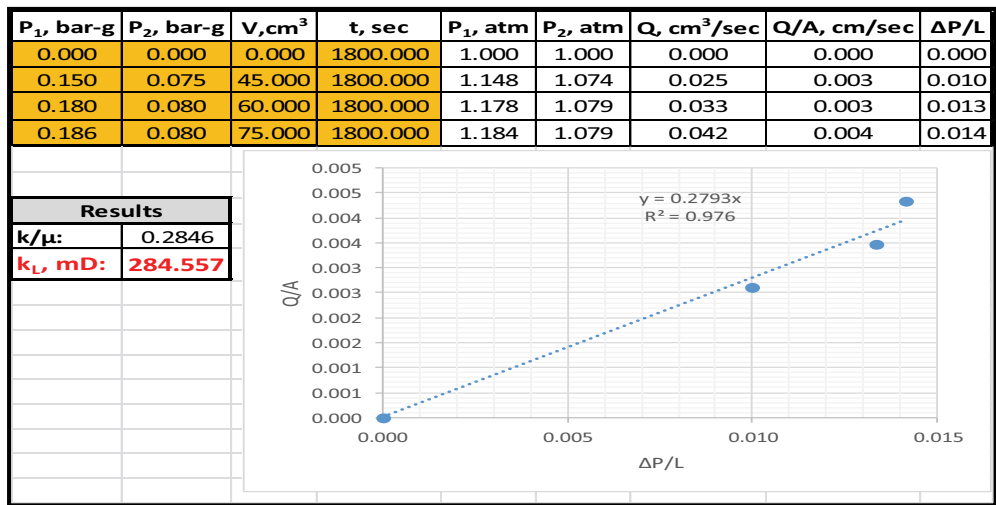


Figure 8.23 Permeability Measurement of Artificially Fractured Core#3.

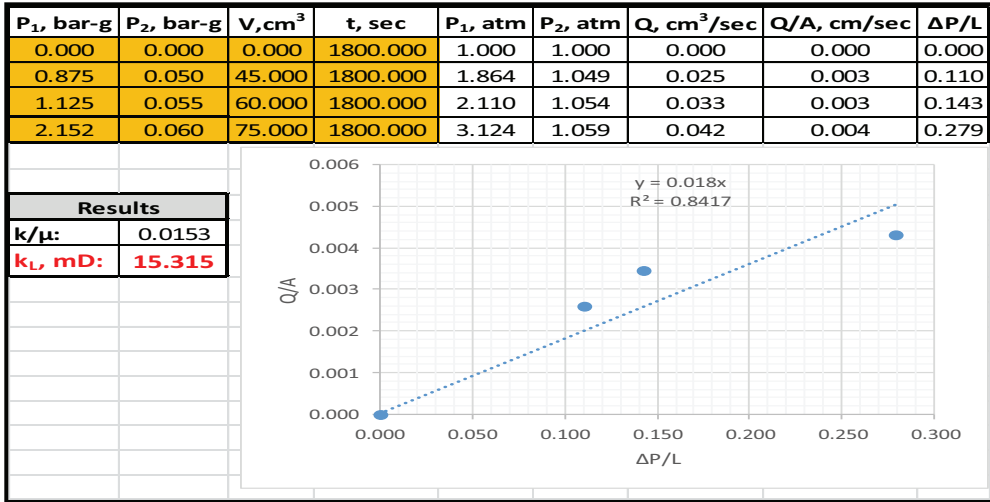


Figure 8.24 Permeability Reduction after 4,500 ppm Polymer Gel Injection to Artificially Fractured Core#3.

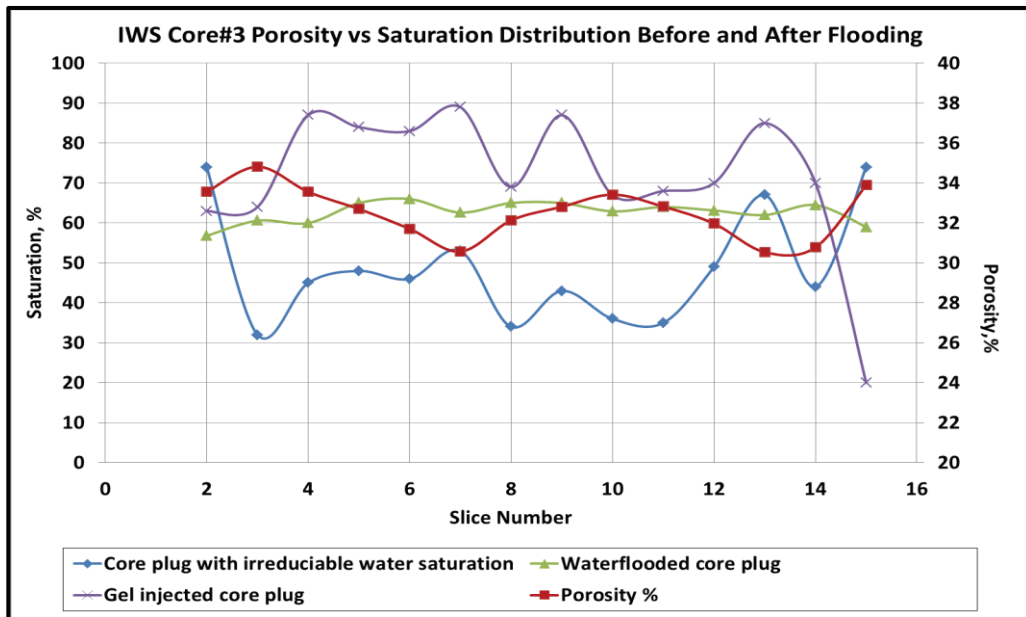
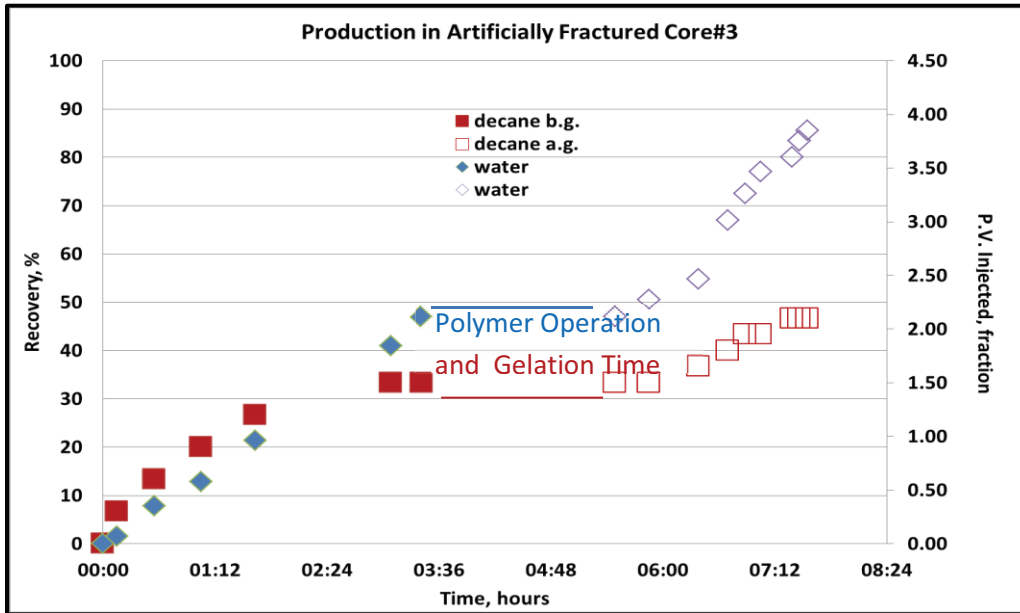


Figure 8.25 Change in Porosity and Water Saturation along Core#3.



**Figure 8.26** 0.2 ml/min Injection Rate, Production in Artificially Fractured Core#3 after Gel Injection Run#5.

Using Equation 3.12 the calculated fracture permeability with respect to the experimental units in  $\text{cm}^2$  as  $5.78021\text{E-}9$  to  $1.9403\text{E-}9$  then converted to md as 578 to 194 given in the last column of the **Table 8.12** (till to the black line).

After polymer gel preparation and injection to isolate the fracture in core#3, some time later production experiment carried on and second part was completed with an incremental recovery. Calculated cubic rates with equivalent fracture apertures were found ranging from 0.0812 to 0.0520 mm. By using the calculated apertures, fracture permeability also calculated with Equation 3.12. The calculated fracture permeability with respect to the experimental units in  $\text{cm}^2$  ranging from  $3.1668\text{E-}11$  to  $1.2058\text{E-}10$ , then converted to md as 3 to 12 given in the last column of the **Table 8.12** (after black line).

In **Figure 8.27** the effect of polymer gel to increase recovery by decreasing equivalent fracture aperture/plugging and in **Figure 8.28** the proof of the calculated fracture permeability decrease with decreasing equivalent fracture aperture of the core#3 are given respectively.

Fracture apertures were measured with the microscopic view and measurement in the artificially fractured core#3 as 0.250 mm (250.25  $\mu\text{m}$ ), 0.217 mm (216.74  $\mu\text{m}$ ) 0.206 mm (206.23  $\mu\text{m}$ ) and 0.137 mm (136.52  $\mu\text{m}$ ) in **Figure 8.29**.

**Table 8.12** Cubic Law Rates at 0.2 ml/min Pump injection in Artificially Fractured Core#3 Run#5.

Time (hours)	Pump Rate (ml/min)	Pinlet (bar-g)	Poutlet (bar-g)	Cubic Rate (ml/min)	Equivalent Fracture Aperture (mm)	$k_f$ (cm <sup>2</sup> )	$k_f$ (md)
00:00	0	0	0	0	0	0	0
00:09	0.2	0.39	0.38	0.20	0.2950	5.7821E-09	578
00:33	0.2	1.29	1.28	0.20	0.2950	5.7821E-09	578
01:03	0.2	2.18	2.15	0.20	0.2050	1.9403E-09	194
01:38	0.2	2.54	2.51	0.20	0.2050	1.9403E-09	194
03:05	0.2	3.19	3.16	0.20	0.2050	1.9403E-09	194
03:25	0.2	3.20	3.17	0.20	0.2050	1.9403E-09	194
05:29	0.2	0.74	0.05	0.20	0.0720	8.4065E-11	8
05:51	0.2	0.58	0.10	0.20	0.0812	1.2058E-10	12
06:23	0.2	0.85	0.09	0.20	0.0695	7.5674E-11	8
06:42	0.2	1.47	0.06	0.20	0.0562	4.0021E-11	4
06:53	0.2	1.71	0.08	0.20	0.0535	3.4416E-11	3
07:03	0.2	1.67	0.08	0.20	0.0546	3.6705E-11	4
07:23	0.2	1.79	0.08	0.20	0.0526	3.2819E-11	3
07:28	0.2	1.92	0.07	0.20	0.0520	3.1668E-11	3
07:33	0.2	1.92	0.07	0.20	0.0520	3.1668E-11	3

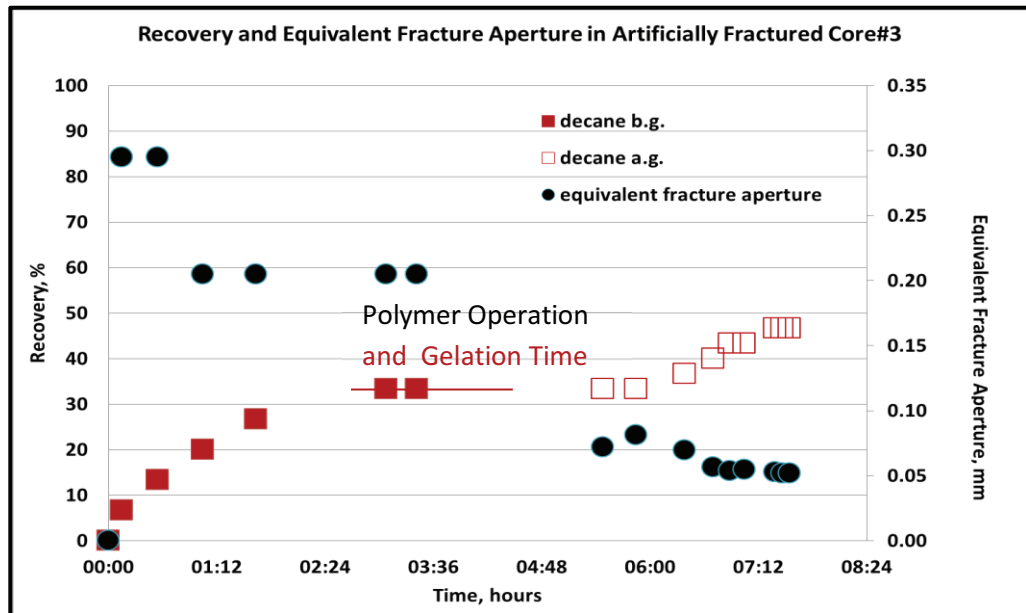


**Figure 8.27** Artificially Fractured Core#3 0.2 ml/min Injection Rate after Gel Injection, Recovery and Equivalent Fracture Aperture Run#5.

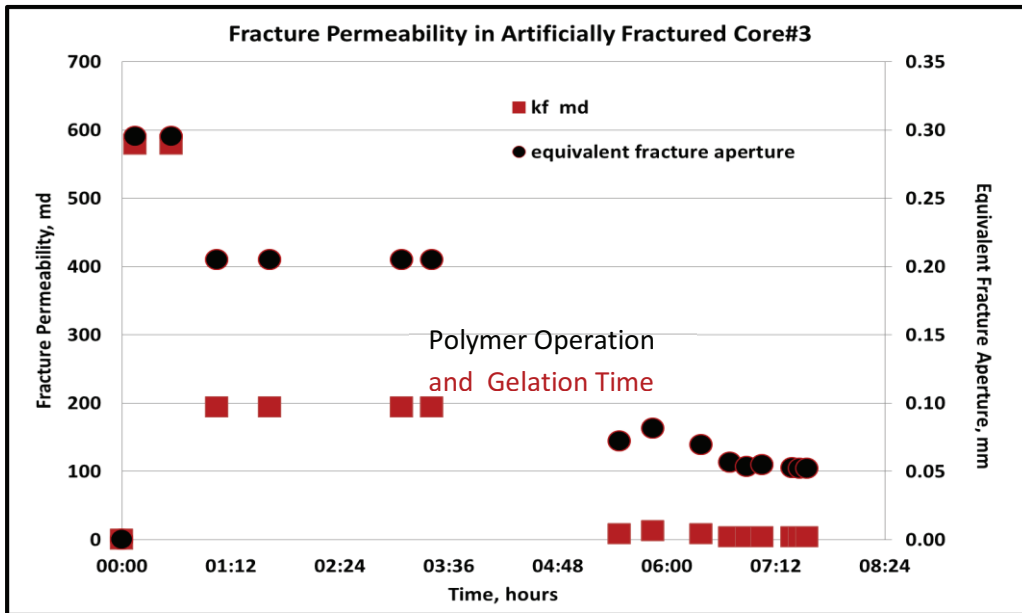


**Figure 8.28** Artificially Fractured Core#3 0.2 ml/min Injection Rate after Gel Injection, Fracture Permeability Run#5.

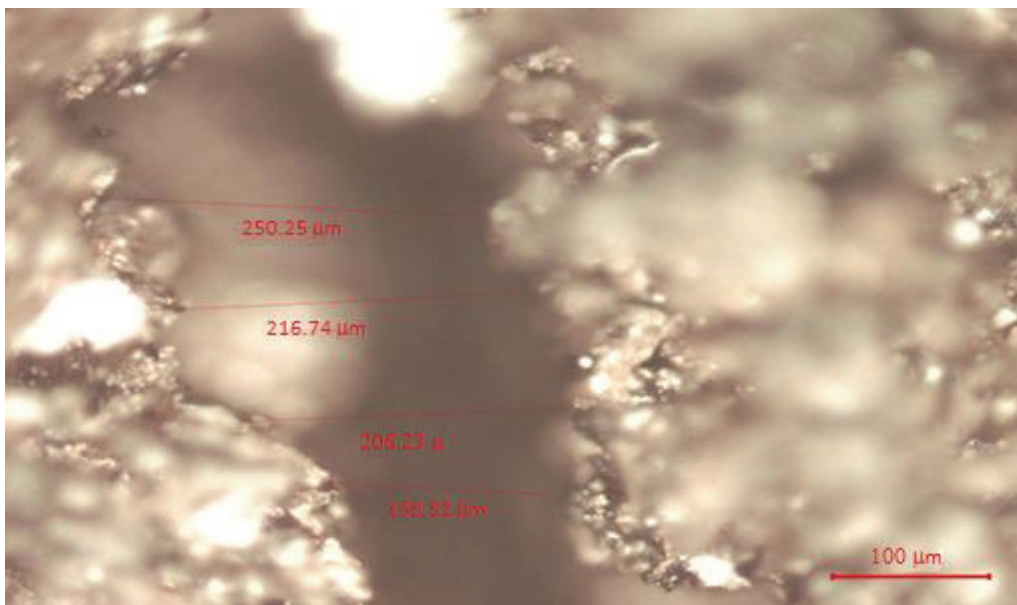


**Figure 8.29** Artificially Fractured Core#3 Fracture Aperture Measurement by Microscope.

Same measurements and procedure were applied to artificially fractured core#7. First, permeability of the core#7 was measured before the fracturing process by water injection. The measured permeability was found 115.863 md for core#7 (**Figure 8.30**). Then, the artificial fracture was created on the core#7. Later, permeability of the core was measured as 292.629 md (**Figure 8.31**). Polymer gel was injected to the core and permeability was measured as 21.332 md (**Figure 8.32**). By this way polymer gel injection for fracture isolation showed a permeability reduction obviously.

Then, the recovery and saturation calculations were done with the experiment in core#7 (Run#6). Artificially fractured core#7 was saturated with water and then decane. The saturation of the core was found by CT measurements as  $S_W$  41.00% and  $S_D$  59.00% and experimental value as  $S_D$  41.70% and  $S_W$  58.30% respectively (**Figure 8.33**) (CT calculated saturation values given in APPENDIX-D). Then this core produced with 2 PV injected water. 4 cc decane is produced out of 14 cc in the core achieving a recovery of 28.57% OOIP (**Figure 8.34**).

Later, 4,500 ppm concentration of polymer gel prepared (1.570 gr polymer gel + 30 cc cross linker) and injected to the produced core#7 (polymer gel operation and the second production was started in 1 hour 27 minutes later). 2 cc more decane was produced from the core recovering 14.28% of OOIP (**Figure 8.34**).

Finally, the residual saturation distribution of the core#7 after polymer gel injection calculated by CT measurements as  $S_W$  65.82% and  $S_D$  34.18% (**Figure 8.33**) and experimentally as  $S_D$  33.50% and  $S_W$  66.50% respectively (CT calculated saturation values given in APPENDIX-D). Production experiment carried on artificially fractured core#7. After the experiment, the analysis were done using CL Equation 3.6 and Equation 3.12 for the first part of the experiment. From the rates, the equivalent fracture aperture calculations were done and fracture permeabilities tabulated in **Table 8.13** (till to the black line).

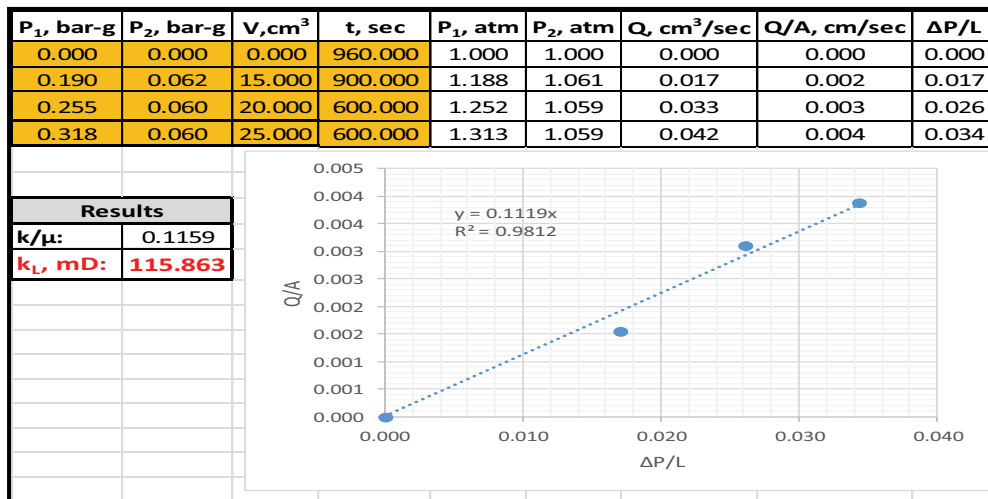


Figure 8.30 Permeability Measurement of Core#7.

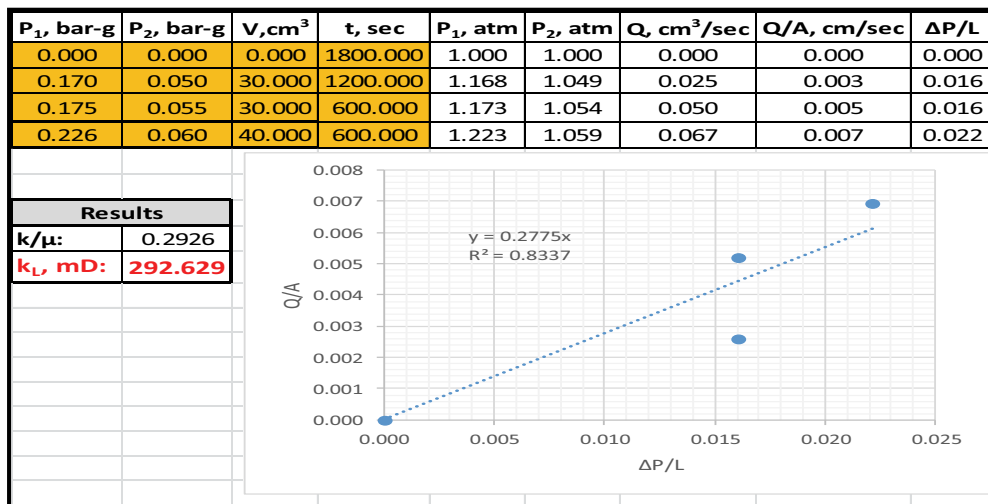


Figure 8.31 Permeability Measurement of Artificially Fractured Core#7.

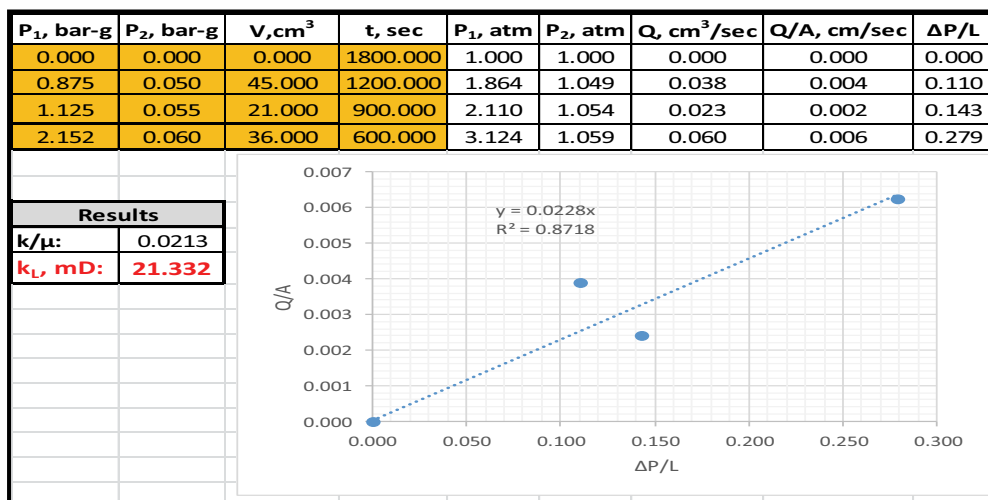


Figure 8.32 Permeability Reduction after 4,500 ppm Polymer Gel Injection to Artificially Fractured Core#7.

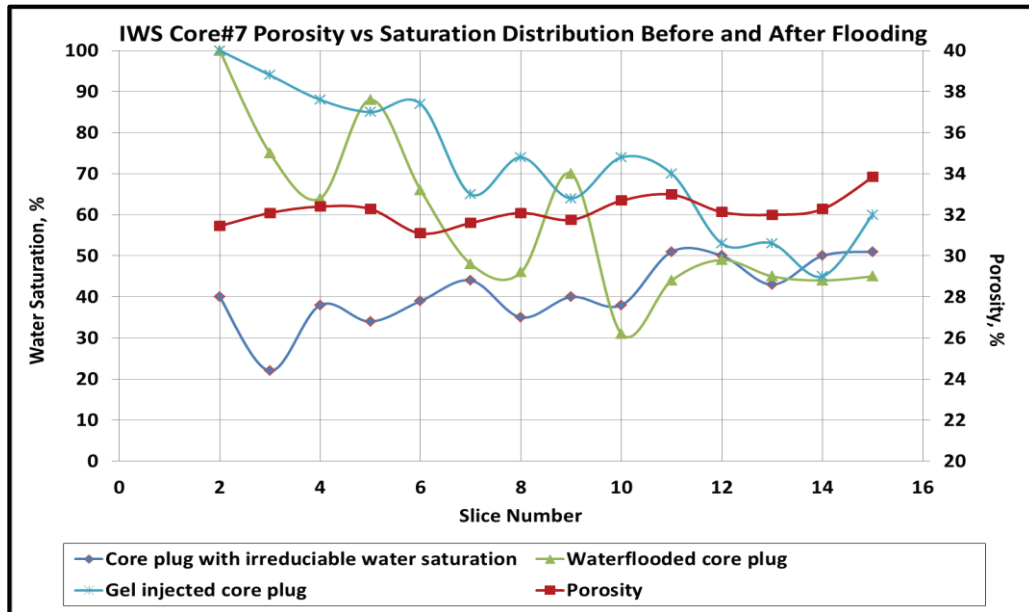


Figure 8.33 Change in Porosity and Water Saturation along Core#7.

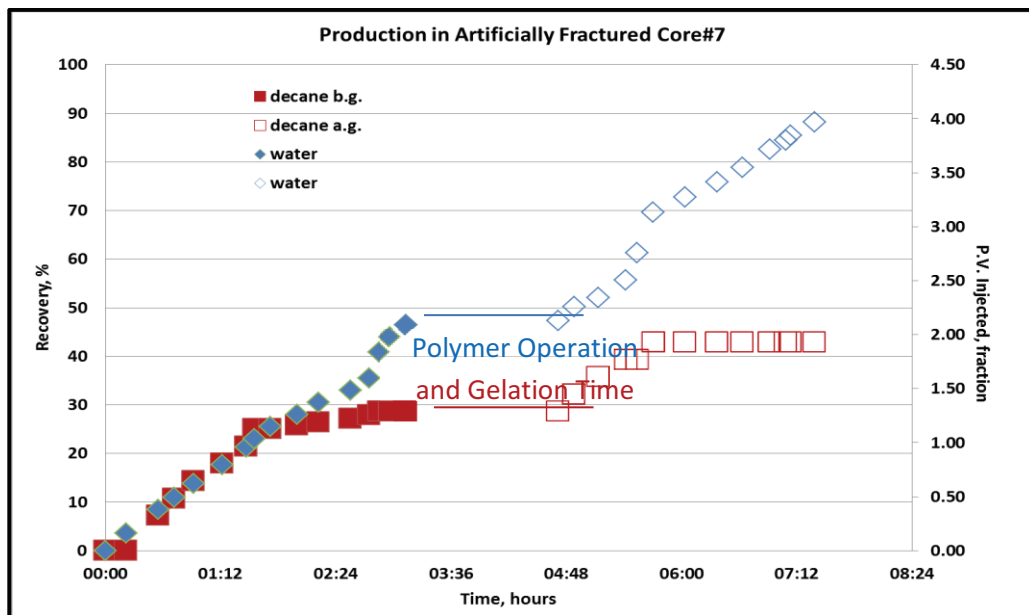


Figure 8.34 0.2 ml/min Injection Rate, Production in Artificially Fractured Core#7 after Gel Injection.

At all rates in the experiment the calculated equivalent fracture apertures were same. Using Equation 3.6 the calculated fracture permeability with respect to the experimental units in  $\text{cm}^2$  as  $2.92 \text{ E-}09$  then converted to md as 292.29 given in the last column of the **Table 8.13**.

Then, polymer gel prepared and injected to the core#7 to isolate the fracture. Some time later core#7 was produced after gel injection. Second part of the experiment was completed. With an incremental recovery. Pump injection rate of 0.2 ml/min, equalized to calculated cubic rates with equivalent fracture apertures ranging from 0.022 to 0.083 mm. By using the calculated apertures fracture permeability also calculated with Equation 3.12. The calculated fracture permeability with respect to the experimental units in  $\text{cm}^2$  ranging from  $2.40 \text{ E-}12$  to  $1.29 \text{ E-}10$ , then converted to md as 0.24 to 12.88 given in the last column of the **Table 8.13** (after black line).

In **Figure 8.35** in the recovery% and fracture aperture graph, constant equivalent fracture aperture in the core#7 is observed in the first part with a 28.57 % oil recovery having a fracture aperture of 0.235 mm. Then, polymer gel injection applied to the core for the isolation of the fracture. The polymer gel decreased the equivalent fracture apertures ranging from 0.022 to 0.083 mm causing an incremental oil production of 14.28%.

In **Figure 8.36** the proof of the calculated fracture permeability decrease with decreasing equivalent fracture aperture of the core#7.

By using the experiment in core#7 calculated and real flow rates equalized each other to find the equivalent fracture aperture in mm. Pump injection rate of 0.2 ml/min, equalized to calculated cubic rate with a equivalent fracture aperture of 0.235 mm. Actual fracture apertures were also measured with the microscopic view and measurement of the artificially fractured core#7 as 0.156 mm (156.11  $\mu\text{m}$ ), 0.261 mm (261.47  $\mu\text{m}$ ) and 0.184 mm (184.33  $\mu\text{m}$ ) in **Figure 8.37**.

**Table 8.13** Cubic Law Rates at 0.2 ml/min Pump injection in Artificially Fractured Core#7.

Time (hours)	Pump Rate (ml/min)	Pinlet (bar-g)	Poutlet (bar-g)	Cubic Rate (ml/min)	Equivalent Fracture Aperture (mm)	$k_f$ (cm <sup>2</sup> )	$k_f$ (md)
00:00	0	0	0	0	0	0	0
00:13	0.2	0.05	0.04	0.20	0.235	2.9229E-09	292
00:33	0.2	0.07	0.06	0.20	0.235	2.9229E-09	292
00:43	0.2	0.07	0.06	0.20	0.235	2.9229E-09	292
00:55	0.2	0.07	0.06	0.20	0.235	2.9229E-09	292
01:13	0.2	0.07	0.06	0.20	0.235	2.9229E-09	292
01:28	0.2	0.07	0.06	0.20	0.235	2.9229E-09	292
01:33	0.2	0.07	0.06	0.20	0.235	2.9229E-09	292
01:43	0.2	0.07	0.06	0.20	0.235	2.9229E-09	292
02:00	0.2	0.07	0.06	0.20	0.235	2.9229E-09	292
02:13	0.2	0.07	0.06	0.20	0.235	2.9229E-09	292
02:33	0.2	0.07	0.06	0.20	0.235	2.9229E-09	292
02:45	0.2	0.07	0.06	0.20	0.235	2.9229E-09	292
02:51	0.2	0.07	0.06	0.20	0.235	2.9229E-09	292
02:58	0.2	0.07	0.06	0.20	0.235	2.9229E-09	292
03:08	0.2	0.07	0.06	0.20	0.235	2.9229E-09	292
04:43	0.2	0.51	0.07	0.20	0.083	1.2878E-10	12.88
04:53	0.2	1.29	0.06	0.20	0.059	4.6257E-11	4.63
05:08	0.2	1.89	0.05	0.20	0.052	3.1486E-11	3.15
05:25	0.2	3.68	0.05	0.20	0.041	1.5523E-11	1.55
05:32	0.2	7.64	0.05	0.20	0.032	7.3802E-12	0.74
05:42	0.2	8.21	0.05	0.20	0.031	6.7097E-12	0.67
06:02	0.2	8.695	0.05	0.20	0.031	6.7097E-12	0.67
06:22	0.2	9.18	0.05	0.20	0.031	6.3902E-12	0.64
06:38	0.2	9.665	0.05	0.20	0.030	6.0811E-12	0.61
06:55	0.2	10.15	0.05	0.20	0.029	5.6075E-12	0.56
07:05	0.2	19.44	0.05	0.20	0.024	2.9229E-12	0.29
07:08	0.2	20.00	0.05	0.20	0.024	2.9229E-12	0.29
07:23	0.2	23.65	0.05	0.20	0.022	2.3982E-12	0.24

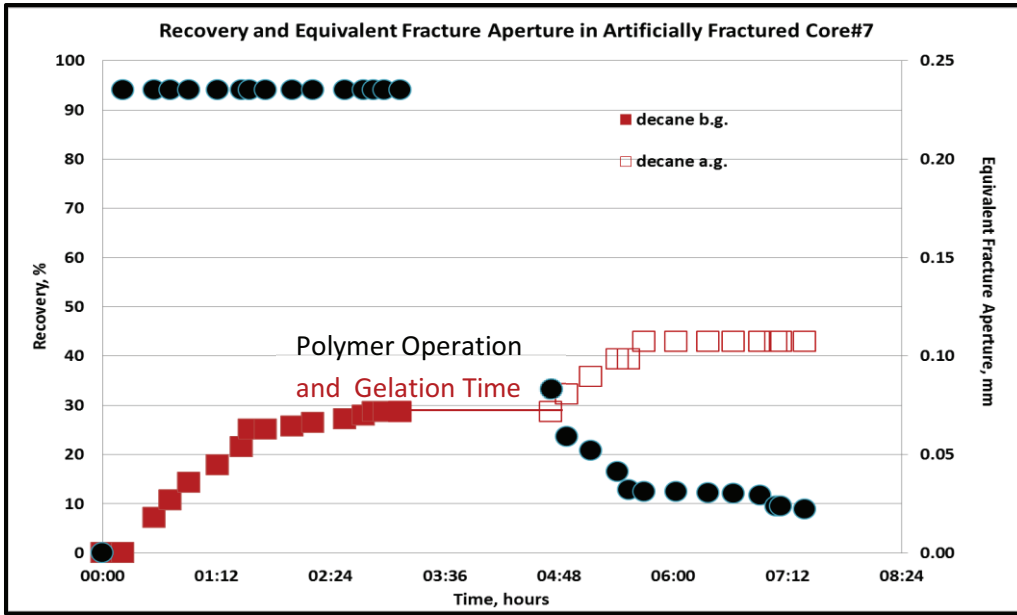


Figure 8.35 Artificially Fractured Core#7 0.2 ml/min Injection Rate, Recovery and Equivalent Fracture Aperture.

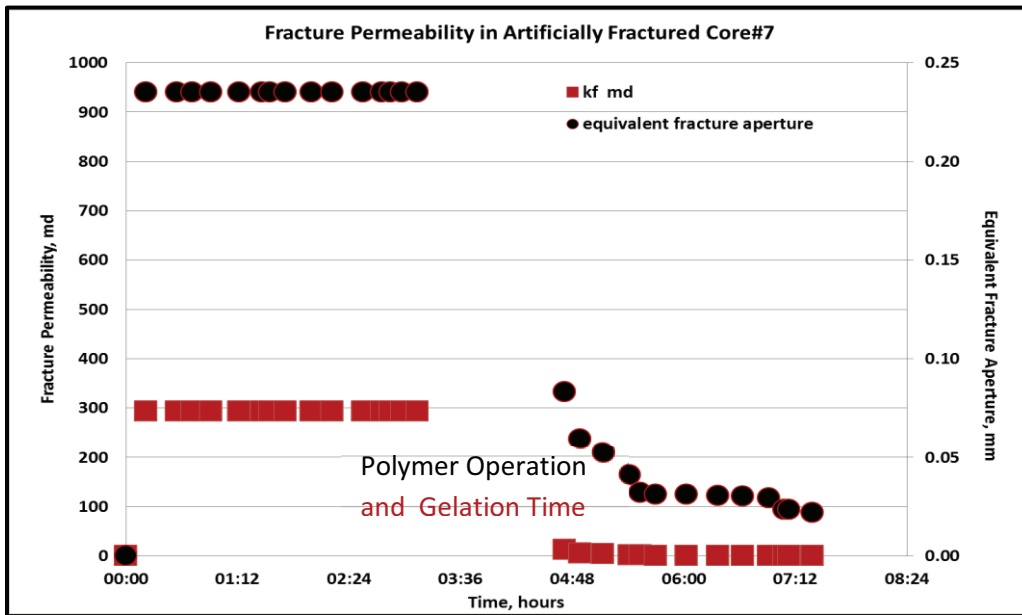
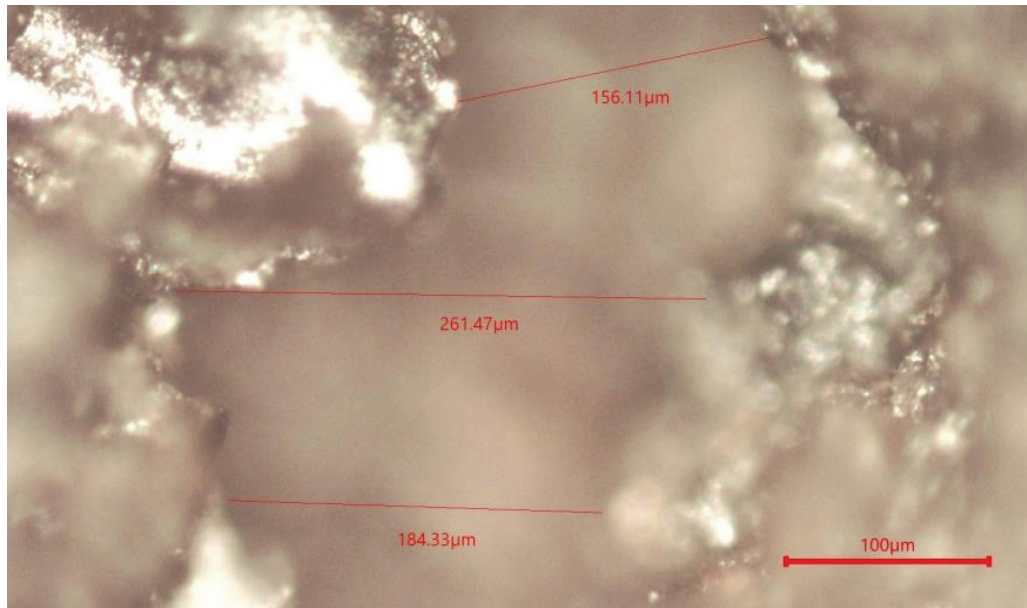


Figure 8.36 Artificially Fractured Core#7 0.2 ml/min Injection Rate, Fracture Permeability.



**Figure 8.37** Artificially Fractured Core#7 Fracture Aperture Measurement by Microscope.

Experiments carried on with the core#5 (CT calculated saturation values given in APPENDIX-D). During the saturation of the core#5 permeability was measured before the experimental run by water injection (**Figure 8.38**). The measured permeability was found 41.132 md for the core. Finally, polymer gel injected core permeability was measured as 7.787 md (**Figure 8.39**). The polymer gel injection showed an obvious permeability reduction in the core#5.

Core#5 was saturated with water and then decane (Run#7). The saturation of the core was found by CT measurements as  $S_w$  43.12% and  $S_D$  56.88% (**Figure 8.40**) and experimental value as  $S_w$  43.04% and  $S_D$  56.96% respectively. After, this core produced with 2 PV injected water. 7 cc decane is produced out of 14 cc in the core achieving a recovery of 50.00% OOIP (**Figure 8.41**). Then calculated CT measurements of the saturation as  $S_D$  29.25% and  $S_w$  70.75% experimental measurement was as  $S_D$  28.00% and  $S_w$  72.00% respectively (CT calculated saturation values given in APPENDIX-D).

Later, 4,500 ppm concentration of polymer gel prepared (1.544 gr polymer gel + 30 cc cross linker) and injected to the produced core#5. After some time, the injection not achieved from front and then from the end (polymer gel operation and the second production was started in 2 hours 28 minutes later) of

the core holder it was succeeded. 2 cc more decane produced from the core. In **Figure 8.41** the production of the core#5 before and after gel injection is given together to show the incremental recovery.

Finally, the residual saturation distribution of the core#5 after polymer gel injection calculated by CT measurements as  $S_w$  76.69% and  $S_D$  23.31% (**Figure 8.40**) and experimentally as  $S_D$  24.00% and  $S_w$  76.00% respectively in **Figure 8.41** (CT calculated saturation values given in APPENDIX-D).

Although there is no obvious fracture naturally detected in core#5, CL also applied to the experiment values. Equivalent fracture aperture calculations were done and fracture permeabilities were found and tabulated in **Table 8.14**. Calculated cubic rates with equivalent fracture apertures were found as ranging from 0.1565 to 0.1768 mm. Actual detected fracture apertures were also measured with the microscopic view and measurement of the fracture structure for core#5 as 0.147 mm (146.98  $\mu$ m), 0.0572 mm (57.15  $\mu$ m) and 0.110 mm (109.53  $\mu$ m) in **Figure 8.42**. Then using the calculated apertures, fracture permeability also calculated using Equation 3.12. The calculated fracture permeability with respect to the experimental units in  $cm^2$  ranging from 5.18E-10 to 8.22E-10, then converted to md as 52 to 82 were given in the last column of the **Table 8.14** (till to the black line).

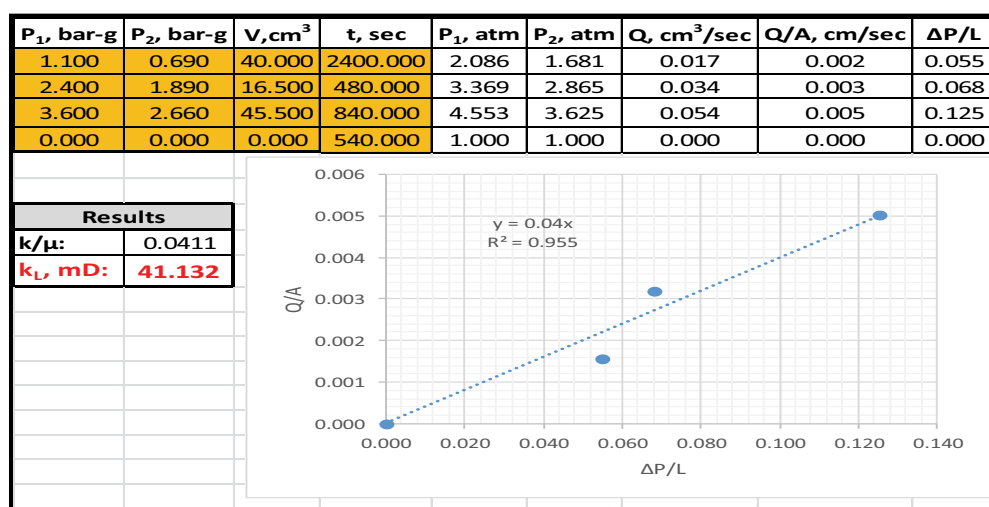


**Figure 8.38** Permeability Measurement of Artificially Fractured Core#5.

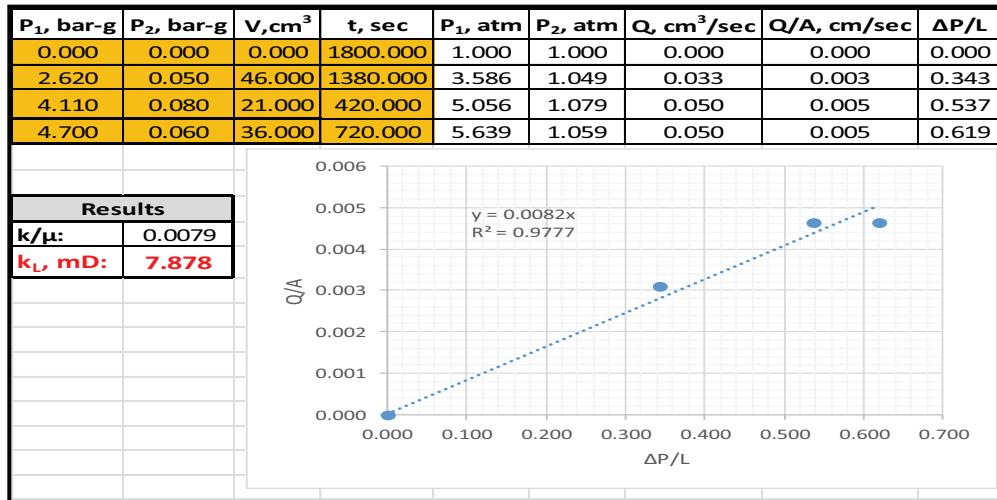


Figure 8.39 Permeability Reduction after 4,500 ppm Polymer Gel Injection to Artificially Fractured Core#5.

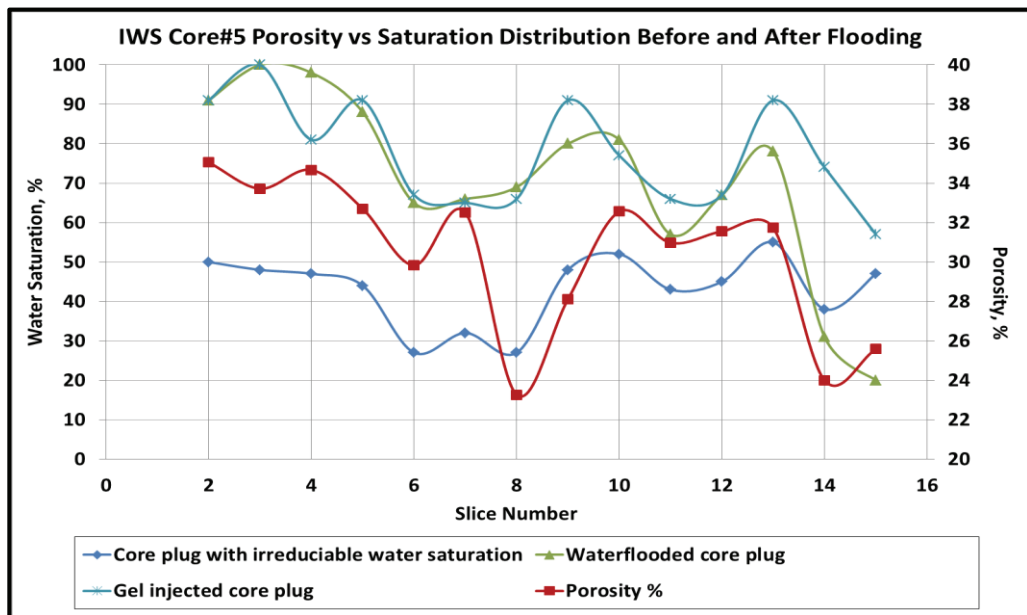


Figure 8.40 Change in Porosity and Water Saturation along Core#5.

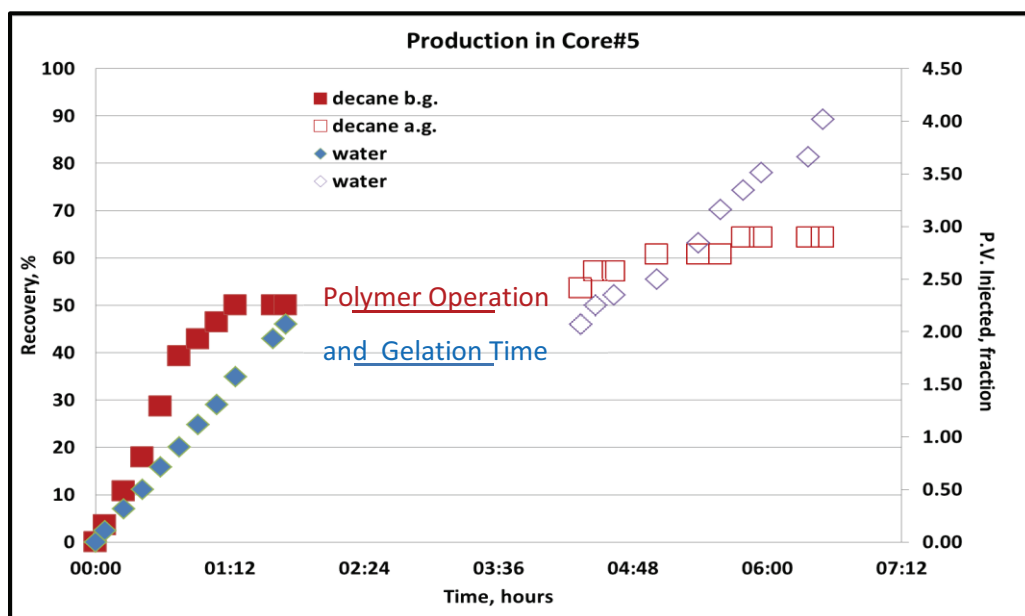
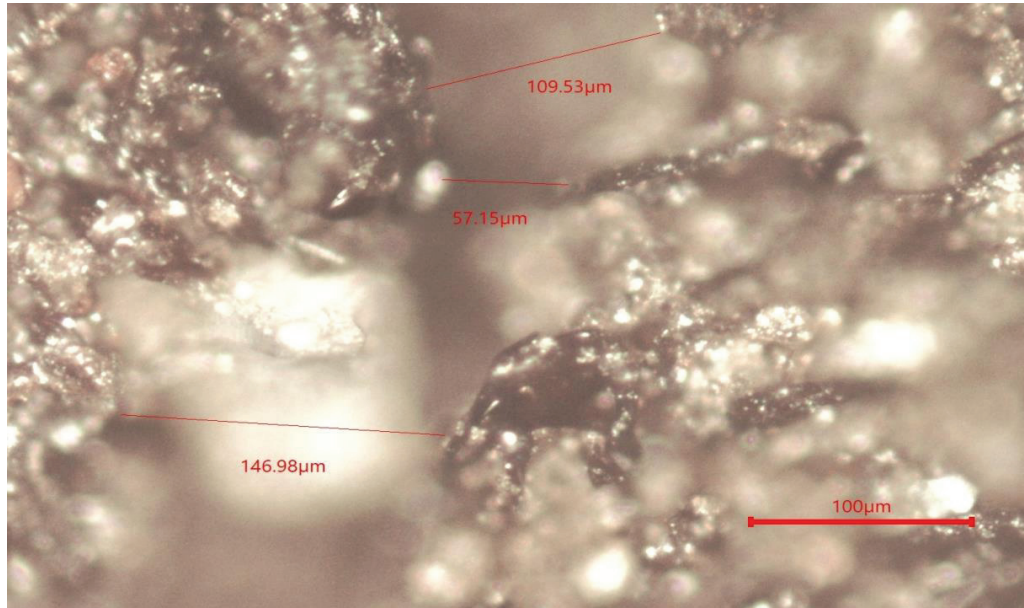


Figure 8.41 0.2 ml/min Injection Rate, Production in Core#5 after Gel Injection.

Table 8.14 Cubic Law Rates at 0.2 ml/min Pump injection in Core#5.

Time (hours)	Pump Rate (ml/min)	Pinlet (bar-g)	Poutlet (bar-g)	Cubic Rate (ml/min)	Equivalent Fracture Aperture (mm)	$k_f$ (cm <sup>2</sup> )	$k_f$ (md)
00:00	0	0	0	0	0	0	0
00:05	0.2	0.13	0.06	0.20	0.1540	8.226E-10	82
00:15	0.2	0.17	0.06	0.20	0.1320	5.180E-10	52
00:25	0.2	0.16	0.06	0.20	0.1370	5.791E-10	58
00:35	0.2	0.15	0.06	0.20	0.1410	6.314E-10	63
00:45	0.2	0.15	0.06	0.20	0.1410	6.314E-10	63
00:55	0.2	0.15	0.06	0.20	0.1410	6.314E-10	63
01:05	0.2	0.16	0.06	0.20	0.1361	5.678E-10	57
01:15	0.2	0.16	0.06	0.20	0.1361	5.678E-10	57
01:35	0.2	0.16	0.06	0.20	0.1361	5.678E-10	57
01:42	0.2	0.16	0.06	0.20	0.1361	5.678E-10	57
04:20	0.2	1.91	0.09	0.20	0.0520	3.167E-11	3
04:28	0.2	0.49	0.06	0.20	0.0845	1.359E-10	14
04:38	0.2	0.49	0.06	0.20	0.0845	1.359E-10	14
05:01	0.2	0.55	0.04	0.20	0.0791	1.113E-10	11
05:23	0.2	0.61	0.04	0.20	0.0768	1.019E-10	10
05:35	0.2	0.65	0.04	0.20	0.0748	9.418E-11	9
05:47	0.2	0.67	0.05	0.20	0.0748	9.418E-11	9
05:57	0.2	0.71	0.05	0.20	0.0725	8.590E-11	9
06:22	0.2	0.87	0.05	0.20	0.0677	6.973E-11	7
06:30	0.2	0.86	0.06	0.20	0.0677	6.973E-11	7



**Figure 8.42** Core#5 Fracture Aperture Measurement by Microscope.

After polymer gel preparation and injection to core#5, using cubic rate equation, equivalent fracture apertures were calculated ranging from 0.0520 to 0.0845 mm. Using the calculated equivalent fracture apertures, fracture permeability also calculated with **Equation 3.12**. The calculated fracture permeability with respect to the experimental units in  $\text{cm}^2$  ranging from  $3.167\text{E-}11$  to  $1.359\text{E-}10$ , then converted to md as 3 to 14 given in the last column of the **Table 8.14** (after black line).

In **Figure 8.43** the effect of polymer gel to increase recovery by increasing sweep efficiency by plugging the permeable path way in the core sweeping the unswept zone.

Microscopic measurements of the fracture apertures were found as 0.0888 mm (88.88  $\mu\text{m}$ ), 0.0450 mm (45.01  $\mu\text{m}$ ), 0.0520 mm (51,71  $\mu\text{m}$ ), 0.0567 mm (56,88  $\mu\text{m}$ ) and 0.0701 mm (70,11  $\mu\text{m}$ ) (**Figure 8.44**). The equivalent fracture aperture decrease observed in core#5 was not very high, due to the undetected main fracture in the core. This shows the homogeneous characteristics of the core#5 rather than heterogeneous. The calculated theoretical fracture permeability decrease with decreasing equivalent fracture aperture of the core#5 is given in **Figure 8.45**.

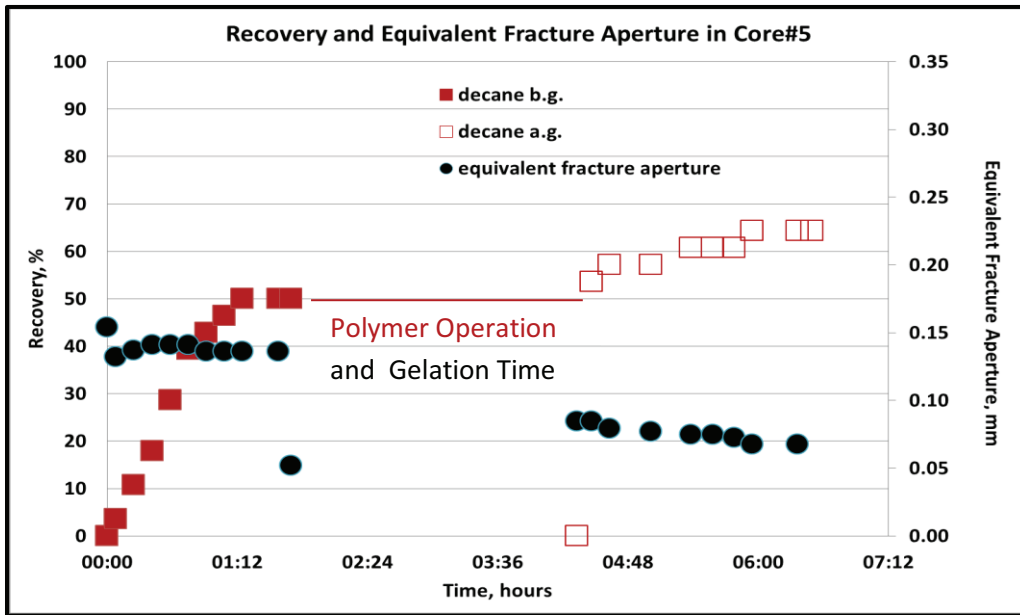


Figure 8.43 Core#5 0.2 ml/min Injection Rate after Gel Injection, Recovery and Equivalent Fracture Aperture.

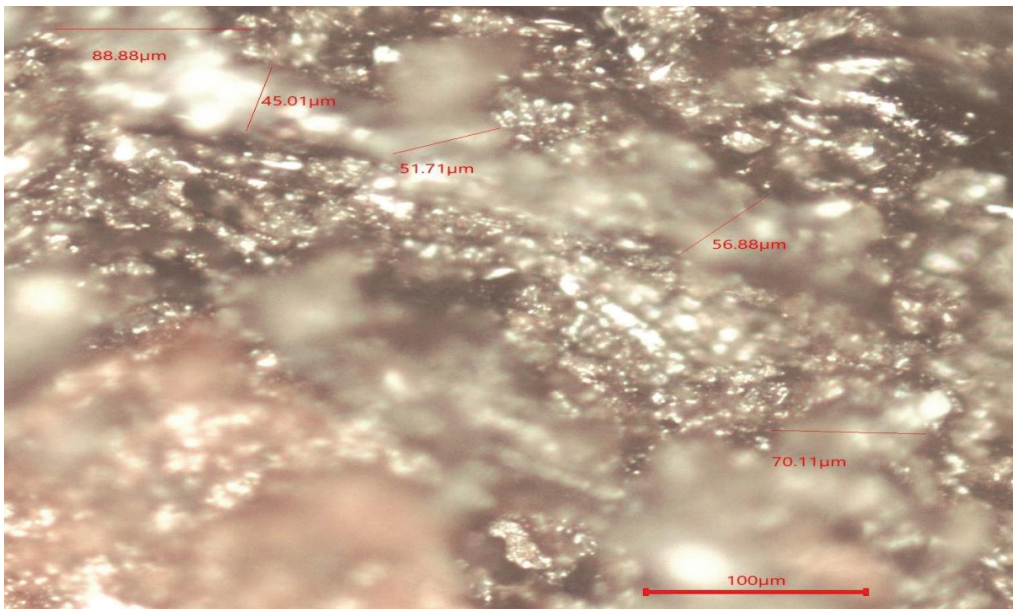


Figure 8.44 Core#5 Fracture Aperture Measurement by Microscope after Gel Injection.

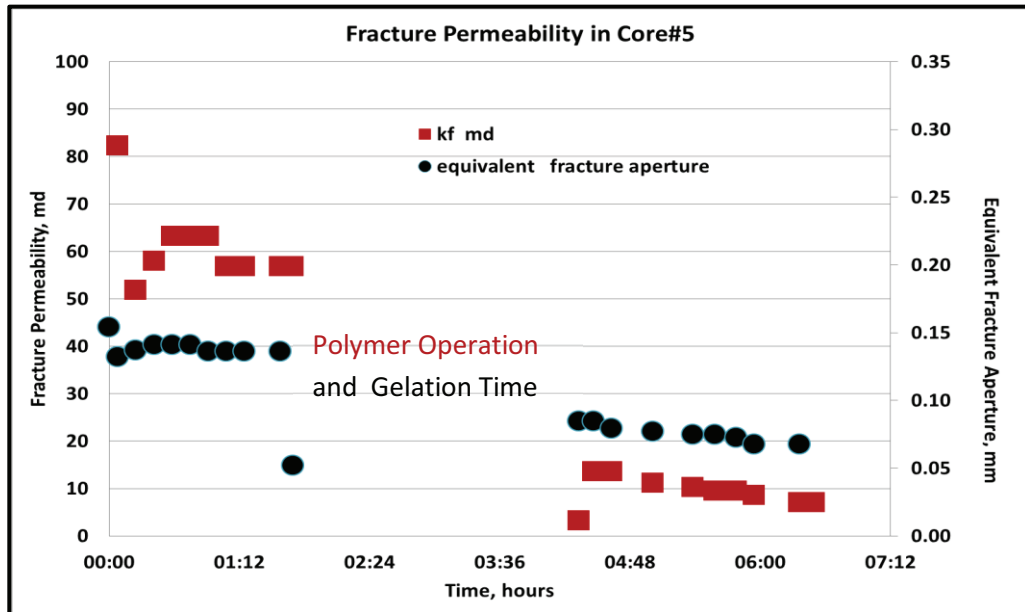


Figure 8.45 Core#5 0.2 ml/min Injection Rate after Gel Injection, Fracture Permeability.

## 8.4 Summary of the Results

### 8.4.1 Porosity

The images, 16 CT scanned cross-sections from each run were converted with **Matlab** code to the desired files for color analysis. Average CT numbers of the slices were obtained from the representative color code scale generated with **ImageJ** software for each 16 views. Obtained CT numbers were used for porosity and saturation calculations. Moreover, using another matlab codes the average CT numbers were calculated directly from the CT scan images as porosity and saturation values. In APPENDIX-E the porosity calculation code is given with the example view and run respectively. The first and last views were not used for porosity calculations. The porosity calculations were done using Equation 2.2 for each core.

The dry scanned CT numbers, 100% water saturated scanned CT numbers, with CT number of water ( $CT_W = 0$ ) and CT number of air ( $CT_A = -1,000$ ) were used in order to calculate the porosity of the each thin section scanned core views.

Results of each thin section porosity from the obtained CT numbers, the average porosity numbers and experimental measured numbers are compared. The minor differences occurred due to the color code conversion of files, are listed in **Table 8.15**.

**Table 8.15** The Comparison of Average Porosity Numbers by CT and Experimental Measurements.

Core	#3	#5	#6	#7	#8	n.f.# 2	a.f.# 3	a.f.# 6	a.f.# 7
Diameter (cm)	3.7	3.7	3.7	3.7	3.7	3.7	3.5	3.5	3.5
Length (cm)	7.4	7.4	7.4	7.4	7.4	7.4	7.4	7.4	7.4
Permeability (md)	81	41	87	116	74	207	285	301	293
Porosity (%)	34	31	32	31	32	34	34	34	32
CT Porosity (%)	34	30.4	32	32	32.5	33.3	34.3	34	32

#### 8.4.2 Saturation

In APPENDIX-E, the saturation calculation code is given with the example view and run respectively. In this code from the CT scan view of the thin section, an average CT number is found and the saturation number of the desired view was calculated. As the porosity calculations, the first and last views were not used for saturation calculations due to total fluid saturations. Saturation distribution of the cores were calculated with the CT numbers obtained after all experiments by the help of Equation 2.5.

Water saturation calculation of the cores were calculated by using, CT numbers of 100% water saturated ( $CT_w$ ), 100% decane saturated, ( $CT_o$ ), saturation value after flooding experiment ( $CT_x$ ). The initial water and oil (decane) saturation values of the cores, before the first flooding and then after the final flooding of all experiments were calculated by using CT numbers of the color codes determined. The results of the experimental and CT calculated vales of all experiments are given in **Table 8.16**.

**Table 8.16** Experimental and CT Scan Calculated Results of the Final Saturations of the Cores.

Core Experiments	Experimental Measurements					CT Calculations	
	SW (%)	SD (%)	Recovery, (%)	Decane in-core, (cc)	Decane produced, (cc)	SW (%)	SD (%)
<b>#2 0.1ml/min</b>	51.37	48.63	---	12.00	---	52.63	47.37
<b>iws</b>	69.63	30.37	36.66	7.50	4.50	65.88	34.12
<b>ios</b>	---	100	60.00	---	15.00	59.60	40.40
<b>#8 0.1ml/min</b>	46.90	53.10	---	13.00	---	47.82	52.18
<b>iws</b>	69.40	30.60	42.5	7.50	5.50	66.83	33.17
<b>ios</b>	---	100	67.85	---	17.00	67.69	32.31
<b>#5 0.2ml/min</b>	43.04	56.96	---	14.00	---	43.12	56.88
<b>Production</b>	---	---	50.00	7.00	---	---	---
<b>Polymer Gel</b>	72.0	28.0	14.28	7.00	2.00	70.75	29.25
<b>Final #5</b>	76.0	24.0	---	5.00	---	76.69	23.31
<b>*a.f. #3 0.2 ml/min</b>	49.47	50.53	---	15.00	---	48.71	51.29
<b>Production</b>	63.87	36.13	33.33	10.00	5.00	62.61	37.39
<b>Polymer Gel</b>	---	---	13.33	7.00	2.00	---	---
<b>Final a.f.#3</b>	71.10	28.90	---	---	---	71.78	28.22
<b>*a.f.#7 0.2 ml/min</b>	41.70	58.30	---	14.00	---	41.00	59.00
<b>Production</b>	58.34	41.66	28.57	10.00	4.00	58.29	41.71
<b>Polymer Gel</b>	---	---	14.28	8.00	2.00	---	---
<b>Final a.f.#7</b>	66.5	33.50	---	---	---	65.82	34.18

All saturation results of each experiment were verified with the CT calculated saturation values. The saturation results of the experiments and CT thin section analysis calculations deviations were due to the size of the cores with heterogeneous and homogeneous characteristics.

Moreover, the color code resolutions after conversion of the files were generated by these minor differences. However, all the experiments confirmed with CT scan calculations.

#### **8.4.3 Polymer Gel Conformance**

Analytical calculations were done for the experimental flow rates using CL for fractured reservoirs (Equation.3.6).The validity of the equation verified by the low

Reynolds number (Equation 3.7) indicating that the CL applicable for each fracture aperture calculation. Equivalent fracture aperture and permeability were calculated for the naturally and artificially fractured cores with both initially water saturated and oil saturated experiments (Equation 3.12).

In **Table 8.17**, initially water saturated (iws) core experiments calculated and real flow rates equalized each other to find the equivalent fracture aperture in mm. With respect to the calculations of core #2 and #8, the range of fracture aperture between 0.010-0.235 mm for both experiments.

The calculated fracture permeability for core#2 and core#8 was given realistic results with respect to measured permeabilities. Total permeability ( $k_T$ ), of the core#2 was measured as 207 md with the experiment (**Table 8.18**). Core#2 fracture permeability ( $k_f$ ) was calculated as average 145 md (**Table 8.17** and **Table 8.18**). Then, using Equation 3.13, the matrix permeability of the core#2 was calculated as 62 md.

In core#8 the the measured permeability ( $k_i$ ) was 74 md and calculated permeabilities of  $k_f$  showed some variations such as 30-76 md (iws environment), 72-292 md (ios environment). Analytical calculations of different  $k_f$  values and the measured permeability ( $k_T$ ), showed that there was no fracture in the core#8. Besides, the initial saturations of the cores might have affected minor or not the measured permeabilities. The deviation in the permeability calculations were due to the homogeneous characteristics of the core#8.

Same analysis were applied to both artificially fractured core#3 and #7 with and without polymer gel injection. The equivalent fracture aperture and permeability calculations were done in **Table 8.17**. Equivalent fracture apertures were found in a range of 0.205-0.295 mm for both cores.

Total permeability ( $k_t$ ), of the artificially fractured core#3 was measured as 285 md experimentally (**Table 8.18**) after fracture. Core#3 fracture permeability ( $k_f$ ) was calculated as average 322 md (**Table 8.17**). That is higher than the measured value. Also the measured ( $k_m$ ) matrix permeability, of the core#3 was 81 md. With respect to Equation 3.13 calculated fracture permeability ( $k_f$ ) 207 md which was lower than the calculated value of 322 md ( $k_{average}$ ).

In artificially fractured core#7 the measured permeability ( $k_i$ ) was 293 md and calculated fracture permeability ( $k_f$ ), was 292 md. These results indicate that, in core#7 there was no or less matrix permeability ( $k_m$ ) (Table 8.18) which was not true. Moreover, the matrix permeability was measured as 116 md before the fracture operation. Measured fracture permeability with respect to Equation 3.13 was 177 md. However, the CL calculated value of the fracture permeability was calculated as 292 md which was higher than the measured. After polymer gel injection artificially fractured Core#3 and Core#7 equivalent fracture aperture decreased to average 0.052-0.082 and 0.022-0.083 mm. Then, fracture permeability decreased to average 10 to 15 fold respectively in both cores. Artificially fractured core #3 and #7, fracture permeability values showed differences due to the higher calculations of the equivalent fracture apertures from CL.

**Table 8.17** Summary of Equivalent Fracture Aperture and Permeability Calculation by Cubic Law for All Cores.

Core #	Equivalent Fracture Aperture, (mm)	$k_f$ Permeability, (md)	Equivalent Fracture Aperture After Gel, (mm)	$k_f$ Permeability After Gel, (md)
n.f.#2 all	0.185-0.187	143-148	---	---
#8 iws	0.110-0.150	30-76	---	---
#8 ios	0.147-0.235	72-292	---	---
a.f.#3	0.205-0.295	194-578	0.052-0.082	3-12
#5	0.132-0.154	52-82	0.052-0.085	3-14
a.f.#7	0.235	292	0.022-0.083	0.024-12.88

Finally, polymer gel was injected to the non fractured Core#5. Equivalent fracture aperture and permeability calculations were done by CL before and after polymer gel injection. Equivalent fracture apertures were calculated in a range of 0.132-0.154 mm before and 0.052-0.085 mm after the polymer gel application (Table 8.17). Fracture permeabilities were calculated in a range of 52-82 md which were above the measured permeability,  $k_t$ , of 41 md (Table 8.18). This shows that the matrix permeability  $k_m$ , is dominant in the flow mechanism of core#5 and concluded as, the core#5 was also homogeneous rather than heterogeneous.

**Table 8.18** Summary of Experimentally Measured Permeability and Fracture Permeability Calculation by Cubic Law for All Cores.

Core #	Permeability, (md)	After Fracture, Permeability, (md)	After Gel, Permeability, (md)	CL Fracture Permeability (md)	Polymer Gel Isolated CL, Permeability, (md)
n.f.#2	207	---	---	143-148	---
#8	74	---	---	72-292	---
a.f.#3	81	285	15	194-578	3-12
#5	41	8	---	52-82	3-14
a.f.#7	116	293	21	292	0.024-12.88

Porosity and saturation calculations of the cores before and after each flooding experiments were calculated by CT scan thin section analysis. By this way the effect of fracture on the residual oil recovery was analyzed. Fracture effect limitation was studied by using polymer gel conformance for the reservoirs in core scale for increasing ultimate recovery.

### 8.5 Improved Cubic Law for Fractured Medium

The equivalent fracture apertures were calculated analytically for both naturally and artificially fractured cores using the CL under laminar flow. Different saturation environments have not given different results for the equivalent fracture apertures. However, in general, CL showed that it is not applicable to homogeneous cores for equivalent fracture aperture calculations by giving different results. This was determined during the core experiments with #5 and #8 in both environments. On the contrary, in the fractured cores, both before and after polymer gel injection the applicability of the CL was checked for analytical equivalent fracture aperture calculations.

Naturally fractured core #2 fracture apertures measured with the microscope as 0.214 mm (213.63  $\mu\text{m}$ ), 0.171 mm (171.33  $\mu\text{m}$ ), 0.136 mm (136.19  $\mu\text{m}$ ) and 0.121 mm (121.31  $\mu\text{m}$ ), respectively. Average equivalent fracture aperture of core#2 was measured as 0.161 mm, which is % 14 less than the CL calculated fracture aperture.

For the artificially fractured cores #3 and #7 the calculated equivalent fracture apertures were also compared with the microscope measurements. Core#3

measured fracture apertures were 0.250 mm (250.25  $\mu\text{m}$ ), 0.217 mm (216.74  $\mu\text{m}$ ) 0.206 mm (206.23  $\mu\text{m}$ ) and 0.137 mm (136.52  $\mu\text{m}$ ). Average equivalent fracture aperture for core#3 was measured as 0.202 mm, which is %19 less than the calculated fracture aperture. Artificially fractured core#7 apertures were done with microscope as 0.156 mm (156.11  $\mu\text{m}$ ), 0.261 mm (261.47  $\mu\text{m}$ ) and 0.184 mm (184.33  $\mu\text{m}$ ). Average equivalent fracture aperture for core#7 was measured as 0.200 mm, which is %15 less than the calculated fracture aperture. Microscope measurements of the fractures gave lower values with respect to analytical calculations (Table 8.19).

**Table 8.19** Summary of Measured Permeability and Fracture Permeability Calculation by Cubic Law for All Cores.

Core #	Equivalent Fracture Aperture, (mm)	Microscope View of Equivalent Fracture Aperture, (mm)	Equivalent Fracture Aperture After Gel, (mm)	Microscope View of Equivalent Fracture Aperture, (mm)
n.f.#2 all	0.185-0.187	0.214, 0.171, 0.136, 0.121	---	---
#8 iws	0.110-0.150	---	---	---
#8 ios	0.147-0.235	---	---	---
a.f.#3	0.205-0.295	0.250, 0.217, 0.206, 0.137	0.052-0.082	---
#5	0.132-0.154	0.147, 0.057, 0.110	0.052-0.085	0.088, 0.045, 0.052, 0.057, 0.070
a.f.#7	0.235	0.156, 0.261, 0.184	0.022-0.083	---

Although there is no obvious natural fracture detected in core#5, CL also applied to the experiment values and equivalent fracture aperture calculations were done. Calculated cubic rates with equivalent fracture apertures were found as ranging from 0.132 to 0.154 mm. Equivalent fracture apertures were measured with the microscopic view and measurement of the fracture structure for core#5 as 0.147 mm (146.98  $\mu\text{m}$ ), 0.057 mm (57.15  $\mu\text{m}$ ) and 0.110 mm (109.53  $\mu\text{m}$ ). Average equivalent fracture aperture for core#5 was measured as 0.105 mm, which is %26 less than the calculated fracture aperture. After the polymer gel application for core#5 microscopic measurements of the fracture apertures were found as 0.088 mm (88.88  $\mu\text{m}$ ), 0.045 mm (45.01  $\mu\text{m}$ ), 0.052 mm (51.71  $\mu\text{m}$ ), 0.057 mm (56.88

$\mu\text{m}$ ) and  $0.070\text{ mm}$  ( $70.11\ \mu\text{m}$ ). Average equivalent fracture aperture after polymer gel application for core#5 was measured as  $0.062\text{ mm}$ , which is %10 less than the calculated fracture aperture.

The calculated and measured equivalent fracture apertures showed some differences. Calculated equivalent fracture apertures showed higher values. This is due to the assuming the fractures as a smooth plate not including the roughness and tortuosity of the fractures which are obviously detected during microscope views. Tortuosity,  $\tau$  is a macroscopic feature defined as the ratio of actual flow path  $L$ , length over a straight-line distance  $L_0$  shown in **Figure 8.46**. Normally, the actual flow field can be obtained through either direct simulation or experimental observation, and it varies depending on aperture field and  $Re$ .

$$\tau = L/L_0 \quad (\text{Equation 8.1})$$

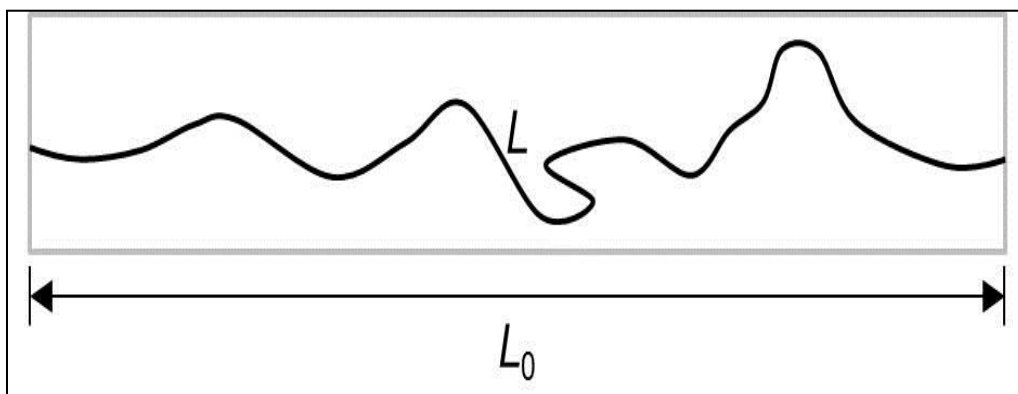


**Figure 8.46** Tortuosity of Rock.

Thus, it is difficult to correct the CL with macroscopic tortuosity since this rests on precise knowledge of flow paths. That's why due to the 15% error, a correction coefficient (  $C$  ) included to the CL equation for equivalent fracture aperture calculation as the tortuosity or the roughness.

Then the improved cubic law equation (ICL) becomes as;

$$Q = C \frac{b^3}{12\mu} \left( \frac{\Delta p}{L} \right) \quad (\text{Equation 8.2})$$

Using the calculated equivalent fracture apertures from CL and measured apertures from different points through the fracture by microscope, the

differences for naturally fractured core #2, artificially fractured cores #3 and #7 are tabulated in **Table 8.20**. In order to assign the coefficient C for ICL equation, for fractured cores flow analysis were applied to measured and calculated values as below.

$$C * \frac{b_{\text{calculated}}^3}{12\mu} \left(\frac{\Delta p}{L}\right) = Q = \frac{b_{\text{measured}}^3}{12\mu} \left(\frac{\Delta p}{L}\right) \quad \Rightarrow$$

To assign a C coefficient for the empirical equation; CL flow rate was equated to ICL flow rate. The flow rate must be the same for every fracture aperture value, b, either calculated or measured. After application of cancellation to the same data Dp, L and m values, the equality remains only with equivalent fracture apertures with C value. Then,

$$C * b_{\text{calculated}}^3 = b_{\text{measured}}^3 \quad \Rightarrow$$

Putting the naturally fractured core #2 measured and calculated equivalent fracture aperture in the above equation:

$$C * 0.186^3 = 0.161^3 \quad \Rightarrow$$

Then, C coefficient calculated as 0.65 for core #2. Calculating C values for the other fractured cores using the same method, for artificially fractured cores #3 and #7, 0.53 and 0.62. respect to the calculations it was understood that the coefficient C was ranged between 0.53 to 0.65 (**Table 8.20**).

**Table 8.20** C Coefficient Calculation for Improved Cubic Law for All Cores.

Core #	Equivalent Fracture Aperture, (mm)	Microscope View of Equivalent Fracture Aperture, (mm)	Difference, (%)	C	Equivalent Fracture Aperture After Gel, (mm)
n.f.#2 all	0.186	0.161	14	0.65	---
a.f.#3	0.250	0.202	19	0.53	0.052-0.082
a.f.#7	0.235	0.200	15	0.62	0.022-0.083



## CHAPTER 9

### CONCLUSIONS AND RECOMENDATIONS

The porosity calculations and saturation distribution of the cores at the end of the experiments were performed using each thin section's scanned core views. Results of each thin section's porosity values from the obtained CT scans, the average porosity and saturation values were verified with experimental measured numbers.

All saturation results of each experiment were verified with the CT calculated saturation values. Differences between saturation results of experiments and CT-thin section analysis calculations were due to the size of the cores with heterogeneous and homogeneous characteristics.

Analytical calculations were performed in different environments, for the experimental flow rates using CL under laminar flow for equivalent fracture aperture calculations. The range is between 0.01 to 0.235 mm.

Naturally fractured core showed heterogeneous structure with the cross sectional views due to a natural fracture determined with CT scanner. Besides, fracture permeability for no fractured core showed more variation (72-292 md), on the contrary naturally fractured core did not (143-145 md).

The equivalent fracture aperture variation (0.147-0.235 mm) in the homogeneous, no fractured core is higher with respect to naturally fractured one (0.185-0.187 mm). This is due to the homogeneous characteristics and variation of orientation of the core rather than heterogeneous. Thus, the analysis, at this point, with homogeneous cores did not give reliable results.

There is a direct relation between fracture permeability with equivalent fracture aperture. The compared experiments with different environments (initially oil saturated and water saturated) in the cores, with calculations of equivalent fracture aperture and fracture permeability, showed similar results (minor deviation was due to rate and saturation environment).

The effect of polymer gel conformance to increase recovery by decreasing equivalent fracture aperture/plugging was validated by the decrease in the calculated fracture permeability with decreasing equivalent fracture aperture in artificially fractured and homogenous no-fracture cores, respectively.

The CL is a widely applied model for predicting fluid flow field in fractures. However, there are still unresolved issues in the application of the CL including errors due to tortuosity, roughness, and inertial effects. The improved cubic law (ICL) developed here provides an approach for more accurately calculating the hydraulic properties and local vertically integrated flow fields for rough and tortuous fractures.

Moreover, using the total permeability  $k_T$  definition calculated matrix permeability  $k_m$  and fracture permeability  $k_f$  also shows that  $k_m$  and  $k_f$  calculated using equivalent fracture apertures gave higher values than the measured ones. That's why due to higher calculated values and the 15% error on equivalent fracture apertures, a correction coefficient (  $C$  ) included to the CL equation for the tortuosity or the roughness effect. Then,  $C$  coefficient was calculated in a range of 0.53 to 0.65.

In this study, artificially and naturally rough single fractures were used, with/without polymer gel application in different environments to give the analytical description. To understand flow behaviour of the fractures with the performance of the ICL using cores having higher roughness with multiple fractures in a different rock type should be a goal for the future work.

## REFERENCES

- Akbar, M., Nurmi, R., Standen, E., Sharma, S., Pinwar, P. Chaturvedi, J.G. and Dennis, B. , (1993), Middle East Well Evaluation Review, No:14 Schlumberger Oil Field Review, 26-42.
- Akin, S. and Kovscek, A. R., (1999), “Imbibition Studies of Low- Permeability Porous Media,” paper 54590 presented at the SPE Western Regional Meeting, Anchorage, 26 – 27 May.
- Al-Muntasheri, G.A., Zitha, P.L.J., and Nasr-El-Din, H.A., (2010), A New Organic Gel System for Water Control: a Computed Tomography Study. SPEJ 15 (1):197-207. SPE 129659.
- Anderson, G., Molesworth, G. Gonzales, B., Al-Harty, S. and Lian, E., (2008) Innovative Water Shut-off Solution Enhances Oil Recovery From a West Venezuela Sandstone Reservoir, Paper SPE 111512, SPE International Symposium and Exhibition on Formation Damage Control held in Lafayette, Louisiana, U.S.A., 13-15 February.
- Bandis, S.C., Makurat, A. and Vik, G., (1985), Predicted and measured hydraulic conductivity of rock joints. Proceedings of the International Symposium on Fundamentals of Rock Joints, Bjorkliden, Sweden, 15–20 September, pp 269–280.
- Barton, N.R., Bandis, S.C. and Bakhtar, K., (1985), Strength, deformation and conductivity coupling of rock joints. Int J Rock Min Sci Geomech Abstr 22 (3):121–140.
- Bear, J., (1972), Dynamics of Fluids in Porous Media, 764 pp., Dover, Mineola, N.Y.
- Brown S.R., Scholz C.H.,(1985), The closure of random elastic surfaces in contact. J Geophys Res 90:5531–5545.

Brown, S. R., (1987), Fluid flow through rock joints: The effect of surface roughness, *J. Geophys. Res.*, 92(B2), 1337 – 1347.

Brush, D. J., and Thomson, N. R., (2003), Fluid flow in synthetic rough-walled fractures: Navier-Stokes, Stokes, and local cubic law simulations, *Water Resour. Res.*, 39(4), 1085, doi:10.1029/2002WR001346.

Buckley, J.S. and Liu, Y.,(1998), Some Mechanisms of Crude Oil/Brine/Solid Interactions, *J. Pet. Sci. Eng.*20, 155.

Burrafato, G., Pitoni, E., Vietina, G., Mauri, L. and Chiappa, L., (1999), Rigless WSO Treatments in Gas Fields. Bullheading Gels and Polymers in Shaly Sands: Italian Case Histories, Paper SPE 54747, European Formation Damage Conference held in The Hague, The Netherlands, 31 May-1 June.

Cardenas, M. B., D. T. Slotke, R. A. Ketcham, and J. M. Sharp Jr., (2007), Navier-Stokes flow and transport simulations using real fractures shows heavy tailing due to eddies, *Geophys. Res. Lett.*, 34, L14404, doi:10.1029/2007GL030545.

Canbolat, S. and Parlaktuna, M.,(2012), Well Selection Criteria for Water Shut-Off Polymer Gel Injection in Carbonates, SPE 158059, 12. SPE/ADIPEC, Abu Dhabi International Petroleum Exhibition & Conference held in Abu Dhabi, UAE, 11-14 November.

Chen, L.B., (1989), Fluorescent Labeling of Mitochondria, in *Fluorescence Microscopy of Living Cells in Culture: Part A*, Wang, Y.L. and Taylor, D.L. eds., Academic Press,.

Cholet, H.,(2000), *Well Production Practical Handbook*, Editions TECHNIP 27 rue Ginox, 75737 Paris Cedex 15 France.

Cook A.M., Myer L.R., Cook N.G.W, Doyle F.M (1990)., The effect of tortuosity on flow through a natural fracture. Rock mechanics contributions and challenges, *Proceedings of the 31st US Symposium on Rock Mechanics*. Golden, CO, June.

Demir, M., Topgüder, N.N., Yılmaz, M.; Karakeçe, Y., Ince, Y., Karabakal, U. Gould, J.H., (2008), Water Shutoff Gels Improved Oil Recovery in Naturally Fractured Raman Heavy Oilfield, Paper SPE 116878, 2008 SPE Russian Oil & Gas Technical Conference and Exhibition held in Moscow, Russia, 28–30 October.

Der Sarkissian, J., Prado, M. and Rauseo, O., (2005), Lessons Learned From Four Selective Water Shut-off Treatments in Mature Reservoirs in Maracaibo Lake, Paper SPE 96528, SPE Offshore Europe 2005 held in Aberdeen, Scotland, UK, 6-9 September.

Fulleylove, R.J., Morgan, J.C., Stevens, D.G. and Trasher, D.R., (1996), Water Shut-Off in Oil Production Wells – Lessons from 12 treatments, Paper SPE 36211, 7<sup>th</sup> Abu Dhabi International Petroleum Exhibition and Conference, held in Abu Dhabi, UAE, 13-16 October.

Gangi A.F., (1978), Variation of whole and fractured porous rock permeability with confining pressure. *Int J Rock Min Sci Geomech Abstr* 15:249–257.

Ge, S., (1997), A governing equation for fluid flow in rough fractures, *Water Resour. Res.*, 33(1), 53–61.

Ghafoori, M. R., Roostaeinen, M. and Sajjadian, V.A., (2008), Secondary Porosity; a Key Parameter Controlling the Hydrocarbon Production in Heterogeneous Carbonate Reservoirs (Case Study) the Society of Petrophysicists and Well Log Analysts (SPWLA) 49th Annual Logging Symposium held in Edinburgh, Scotland, May 25-28.

Green, D. W. and Willhite, G. P., (1998), Enhanced Oil Recovery, “SPE Text Book Series”.

Hakami, E. and Barton, N., (1990), Aperture measurements and flow experiments using transparent replicas of rock joints. In *Proceedings of the International Symposium on Rock Joints*, Loen, Norway: 383-390.

Hakami, E., and Larsson, E., (1996), Aperture measurements and flow experiments on a single natural fracture, *Int. J. Rock Mech. Min. Sci. Geomech. Abstr.*, 33 (4), 395–404.

Hardy, M., Botermans, W., Hamouda, A., Valdal, J. and Warren, J., (1999), The First Carbonate Field Application of a New Organically Cross-linked Water Shutoff Polymer System, Paper SPE 50738, SPE International Symposium on Oil field Chemistry held in Houston, Texas, 16-19 February.

Honarpour, M. M., Cromwell, V., Hatton, D. and Satchwell, R., (1985), Reservoir Rock Descriptions Using Computed Tomography, paper 14272 presented at the 60th Annual Technical Conference and Exhibition of the SPE, Las Vegas, 22 – 25 September.

Hunt, P. K., Engler, P. and Bajsarowicz, C., (1988), Computed Tomography as a Core Analysis Tool: Applications, Instrument Evaluation, and Image Improvement Techniques, JPT, September.

Lanaro, F., A, (1999), random field model for aperture and roughness of rock fractures. Licentiate Thesis, Royal Institute of Technology, Sweden.

Larson, J.B., (1999), Production Well Water Shut Off Polymer Treatment in the Weber Sandstone-Ashley Valley Field, Uintah County, UT, Paper SPE 55629, SPE Rocky Mountain Regional Meeting held in Gillette, Wyoming, 15-18 May.

Liron, Y., Paran, Y., Zatorsky, N. G., Geiger, B., Kam, Z., (2006), Laser Autofocusing System for High-Resolution Cell Biological Imaging, Journal of Microscopy, 221:145–151.

Liu, R., Jiang Y., Li, B., Wang X. and Huang, H., (2014) Experimental and numerical study of fracture aperture estimation and characteristics of non-linear fluid flow through artificial fracture intersections Rock Engineering and Rock Mechanics: Structures in and on Rock Masses –Taylor & Francis Group, London.

Lomize, G. M., (1951), Flow in Fractured Rocks (in Russian), 127 pp., Gosenergoizdat, Moscow.

Makki, A., (2003), Rigless Water Shut-off Experience, Paper SPE 81443, SPE 13<sup>th</sup> Middle East Oil Show & Conference held in Bahrain, 5-8 April.

MacGregor, K. W., Park, E. I. and Sincock, K. J., (1991), Effective Unconsolidated Core Preservation in the Arctic Environment: An Aid to Accurate Reservoir Evaluation, Paper SPE 22128 presented at the International Arctic Technology Conference, Anchorage, 29 – 31 May.

MATLAB and Statistics Toolbox Release 2014a, The MathWorks, Inc., Natick, Massachusetts, United States.

Moradi-Araghi, A., Bjornson, G. and Doe, P.H., (2012), A Review of Thermally Stable Gels for Fluid Diversion in Petroleum Production, *J. of Petroleum Science and Engineering*, 48, 2005. Nelson B. E., Well Cementing Fundamentals, *Oilfield Review Summer 2012*:24, no. 2, Schlumberger.

Nicholl, M. J., H. Rajaram, R. J. Glass, and R. Detwiler, (1999), Saturated flow in a single fracture: Evaluation of the Reynolds equation in measured aperture fields, *Water Resour. Res.*, 35(11), 3361 – 3373.

Nicholl, M. J., and R. L., (2001), Detwiler, Simulation of flow and transport in a single fracture: Macroscopic effects of underestimating local head loss, *Geophys. Res. Lett.*, 28(23), 4355–4358, doi:10.1029/2001GL013647.

Perez, D., Faragachan, F.E., Ramirez Barrera, A. and Feraud, J.P., (2001), Applications of Polymer Gel for Establishing Zonal Isolations and Water Shutoff in Carbonate Formations, *SPE Drilling & Completion*, 16, 3.

Portwood, J.T., (1999), Lessons learned from Over 300 Producing Well Water Shut-off Gel Treatments, Paper SPE 52127, SPE Mid-Continent Operations Symposium held in Oklahoma City, Oklahoma, 28-31 March.

Portwood, J.T., (2005), The Kansas Arbuckle Formation: Performance Evaluation and Lessons Learned From More Than 200 Polymer-Gel Water-Shutoff Treatments, Paper SPE 94096, Presented at the SPE Production and Operations Symposium, Oklahoma City, 17-19 April.

Price, J.H. and Gough, D.A., (1994), Comparison of Phase-Contrast and Fluorescence Digital Autofocus for Scanning Microscopy, *Cytometry*, 16:283–297.

Renshaw, C. E., (1995), On the relationship between mechanical and hydraulic apertures in rough-walled fractures, *J. Geophys. Res.*, 100(B12), 24, 629 – 24, 636.

Renshaw, C.E. and Park, J. C., (1997), Effect of mechanical interactions on the scaling of fracture length and aperture. *Nature* 386, 482-484.

Renshaw, C. E., Dadakis, J. S. and Brown S. R., (2000), Measuring fracture apertures: A comparison of methods, *Geophys. Res. Lett.*, 27(2), 289–292,.

Sarkar, S., Toksöz, M.N. and Burns D.R., (2004), *Fluid Flow Modeling in Fractures*. Massachusetts Institute of Technology. Massachusetts Institute of Technology. Cambridge. MA 02139.

Seright, R.S., Lane, R.H. and Sydansk R.D., (2003), A Strategy for Attacking Excess Water Production, *SPE Production and Facilities*, 158-169, August.

Siddiqui, S. and Khamees, A.A., (2004), Dual-Energy CT-Scanning Applications in Rock Characterization. Paper SPE 90520 presented at SPE Annual Technical Conference and Exhibition. Houston, Texas, 26-29 September.

Sydansk, R., (1988), A New Conformance Improvement Treatment Chromium (III) Gel Technology, Paper SPE 17329, Presented at the SPE Enhanced Oil Recovery Symposium, Tulsa, Oklahoma.

Sydansk, R.D. and Smith, T.B., (1988), Field Testing of a New Conformance Improvement Treatment Chromium (III) Gel Technology, Paper SPE 17383 Presented at the SPE Enhanced Oil Recovery Symposium, Tulsa, Oklahoma.

Sydansk, R.D., (1990), A Newly Developed Chromium (III) Gel Technology. *SPE Res.Eng.*5(3):346–352.SPE-19308-PA.doi:10.2118/19308-PA.

Sydansk, R.D., and Sothwell, G.P., (1998), More than 12 years of Experience with a Successful Conformance-Control Polymer Gel Technology, Paper SPE 49315, Annual Technical Conference and Exhibition, New Orleans 27-30 September.

- Tatone, B.S.A. and Grasselli, G., (2012), Quantitative measurements of fracture aperture and directional roughness from rock cores. *Rock Mechanics and Rock Engineering* 45:619–629.
- Tsang, Y. W., and Tsang, C. F., (1990), Hydrological characterization of variable-aperture fractures, in *Rock Joints*, edited by N. Barton and O. Stephansson, pp. 423–431, A. A. Balkema, Brookfield, Vt.,.
- van Eijden, J. , (2004), Gel-Cement, A Water Shut-off System: Qualification in a Syrian Field, Paper SPE 88765, 11<sup>th</sup> Abu Dhabi International Petroleum Exhibition and Conference, held in Abu Dhabi, UAE, 10-13 October.
- van Golf-Racht T.D., (1982), *Fundamentals of Fractured Reservoir Engineering*, Elsevier Scientific Publishing Company, Amsterdam-Oxford-New York.
- van Golf-Racht T.D. and Fernand, S., (1994), Water-Coning in a Fractured Reservoirs, Paper SPE 28572, Annual Technical Conference and Exhibition held in New Orleans, L.A., U.S.A., 25-28 September.
- Vinegar, H. J., (1986), X-Ray CT and NMR Imaging of Rocks, *JPT* (March) 257.
- Vinegar, H. J. and Wellington, S. L., (1987 ), Tomographic Imaging of Three-Phase Flow Experiments, *Rev. Sci. Instrum.* No. 58, 1, (January ) 96.
- Wang, L., and Cardenas, M. B., (2014), Non-Fickian transport through two-dimensional rough fractures, Assessment and prediction, *Water Resour. Res.*, 50, 871–884, doi:10.1002/2013WR014459.
- Wang, S. Y., Ayril, S. and Gryte, C. C., (1984), Computer-Assisted Tomography for the Observation of Oil Displacement in Porous Media, *SPE Journal* 53, February.
- Wang, J.S.Y, Narasimhan, T.N and Scholz, C.H., (1988), Aperture correlation of a fractal fracture, *Journal of Geophysics. Res.* 93(B4): 2216-2224.
- Wellington, S. L. and Vinegar, (1987), H. J., X-Ray Computerized Tomography, *JPT* 885, August.

Willhite, G. P. and Pancake, R. E., (2004), Controlling Water Production Using Gel Polymer System, Paper SPE 89464 Presented at the SPE/DOE Symposium on Improved Oil Recovery, Tulsa, Oklahoma.

Witherspoon, P.A., Wang, J.S.Y., Iwai, K. and Gale J.E., (1980), Validity of Cubic Law for Fluid Flow in a deformable rock fracture. *J Water Resource Research*.16(6): 1016-1024.

Withjack, E. M. and Akervoll, I., (1988), Computed Tomography Studies of 3-D Miscible Displacement Behavior in a Laboratory Five-Spot Model, Paper SPE 18096 presented at the 63rd Annual Technical Conference and Exhibition of the SPE, Houston, 2-5 October.

Withjack, E.M., Devier, C.; and Michael, G., (2003), The Role of X-Ray Computed Tomography in Core Analysis. Paper SPE 83467 presented at SPE Western Regional/AAPG Pacific Section Joint Meeting. Long Beach, California, 19-24 May.

Xiao, W.M., Deng, R.G. and Xia, C.C., (2013), Assessment of two methods for quantitative measurement of rock fracture aperture, *Rock Characterisation, Modelling and Engineering Design Methods – Feng, Hudson & Tan (Eds) Taylor & Francis Group, London,*.

Zimmerman, R.W., and Bodvarsson, G.O., (1966), Hydraulic Conductivity of Rock Fractures. *J. Transport in Porous Media*. 23:1-30. Netherlands.

Zimmerman, R. W., Kumar, S. and Bodvarsson, G. S., (1991), Lubrication theory analysis of the permeability of rough-walled fracture, *Int. J. Rock Mech.*, 28, 325–331.

Zimmerman R W, Al-Yaarubi, A, Pain C.C et al., (2004), Non-linear regimes of fluid flow in rock fractures , *International Journal of Rock Mechanics and Mining Sciences*, 41: 163–169.

Zimmerman, R.W. & Yeo I., (2006), Fluid flow in rock fractures: From Navier-Stokes Equations to the Cubic Law. *J Geophysical Monograph*: 122 (410): 213:224. USA.

## APPENDIX-A

### CORE SAMPLE XRF ANALYSIS

**Preset Sample Data**

Sample Name scanbolat Dilution Material M-HWC  
 Description Sample Mass (g) 6.2500  
 Method press Dilution Mass (g) 1.4000  
 Job Number 0 Dilution Factor 0.8170  
 Sample State Pressed tablet, 40 mm Sample rotation Yes  
 Sample Type Pellet\_40 Date of Receipt 09/22/2016  
 Sample Status AAXXXX Date of Evaluation 09/22/2016

**Table A.1** Core Sample Element Analysis.

Z	Symbol	Element	Concentration %	Abs. Error %
11	Na <sub>2</sub> O	Sodiumoxide	7.57	0.14
12	MgO	Magnesiumoxide	1.220	0.028
13	Al <sub>2</sub> O <sub>3</sub>	Aluminumoxide	16.68	0.02
14	SiO <sub>2</sub>	Siliconoxide	58.65	0.04
15	P <sub>2</sub> O <sub>5</sub>	Phosphorusoxide	0.0657	0.0037
16	SO <sub>3</sub>	Sulfurtrioxide	0.1420	0.0009
17	Cl	Chlorine	0.1484	0.0004
19	K <sub>2</sub> O	Potassiumoxide	4.4240	0.015
20	CaO	Calciumoxide	6.032	0.013
22	TiO <sub>2</sub>	Titaniumdioxide	0.7547	0.0034
23	V <sub>2</sub> O <sub>5</sub>	Vanadiumoxide	0.00740	0.00100
24	Cr <sub>2</sub> O <sub>3</sub>	Chromiumoxide	0.1166	0.0035
25	MnO	Manganesoxide	0.0781	0.0027
26	Fe <sub>2</sub> O <sub>3</sub>	Ironoxide	3.5330	0.007
27	CoO	Cobaltoxide	0.0862	0.0076
28	NiO	Nickeloxide	0.03753	0.00093
29	CuO	Copperoxide	0.0184	0.0013
30	ZnO	Zincoxide	0.0197	0.0014
31	Ga	Gallium	< 0.00010	(0.0)
32	Ge	Germanium	< 0.00010	(0.0)
33	As <sub>2</sub> O <sub>3</sub>	Arsenicoxide	0.00668	0.00031
34	Se	Selenium	0.00016	0.00010
35	Br	Bromine	0.00101	0.00014
37	Rb <sub>2</sub> O	Rubidiumoxide	0.01096	0.00018
38	SrO	Strontiumoxide	0.04818	0.00029
39	Y	Yttrium	0.00383	0.00034

**Table A.1** continued Core Sample Element Analysis.

<b>Z</b>	<b>Symbol</b>	<b>Element</b>	<b>Concentration %</b>	<b>Abs. Error %</b>
40	ZrO <sub>2</sub>	Zirconiumoxide	< 0.068	(0.058)
41	Nb <sub>2</sub> O <sub>5</sub>	Niobiumoxide	0.00428	0.00015
42	Mo	Molybdenum	< 0.0010	(0.00050)
46	Pd	Palladium	0.00	0.00
47	Ag	Silver	0.00144	0.00002
48	Cd	Cadmium	< 0.00051	(0.0)
49	In	Indium	< 0.00051	(0.0)
50	SnO <sub>2</sub>	Tin oxide	0.00891	0.00027
51	Sb <sub>2</sub> O <sub>5</sub>	Antimonyoxide	0.00158	0.00031
52	Te	Tellurium	0.0209	0.0029
53	I	Iodine	< 0.00071	(0.0)
55	Cs	Cesium	< 0.00081	(0.0)
56	Ba	Barium	0.088	0.088
57	La	Lanthanum	< 0.0010	(0.0)
58	Ce	Cerium	0.01132	0.00098
72	Hf	Hafnium	0.0202	0.0014
73	Ta <sub>2</sub> O <sub>5</sub>	Tantalumoxide	0.1263	0.0032
74	WO <sub>3</sub>	Tungstenoxide	< 0.00025	(0.0)
80	Hg	Mercury	< 0.00020	(0.0)
81	Tl	Thallium	0.00127	0.00012
82	PbO	Leadoxide	0.00453	0.00028
83	Bi	Bismuth	< 0.00020	(0.0)
90	Th	Thorium	0.00333	0.00029
92	U	Uranium	0.00176	0.00017
		<b>Sum</b>	<b>100.00</b>	

APPENDIX-B

INITIALLY WATER SATURATED DECANE FLOODED NATURALLY  
FRACTURED CT SCAN IMAGES OF CORE#2

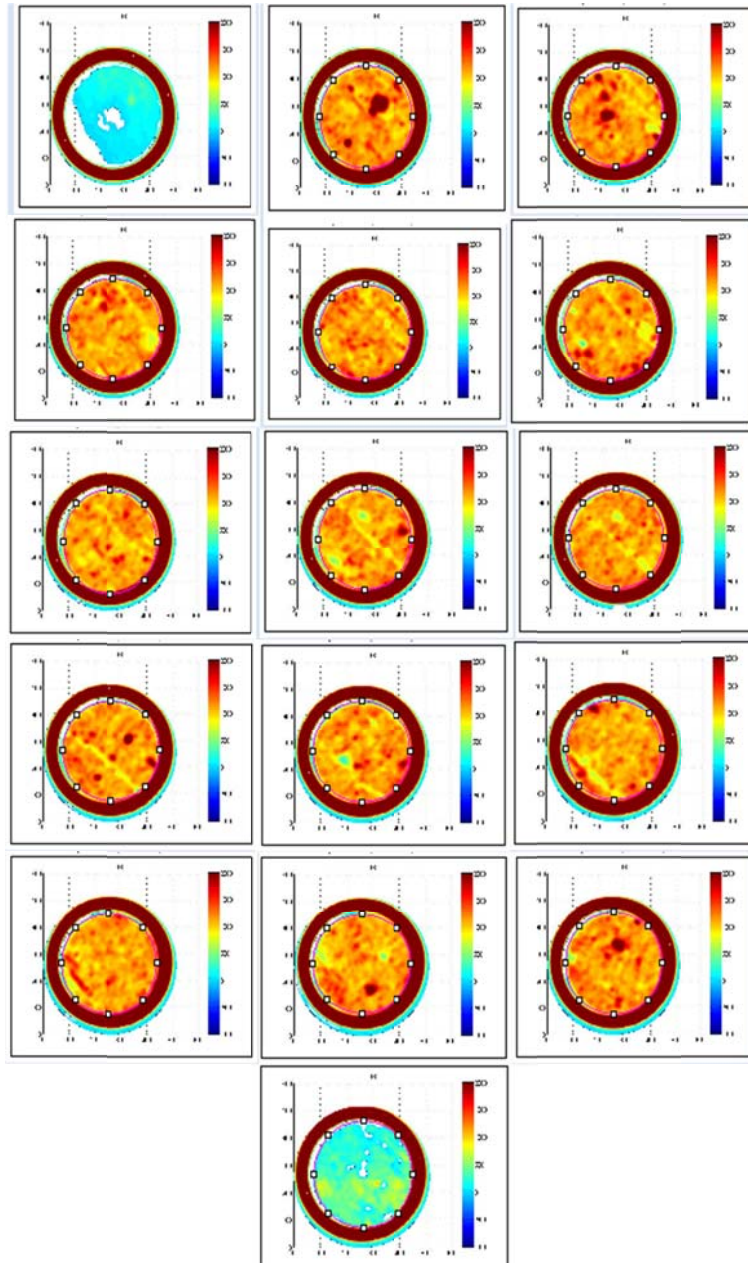
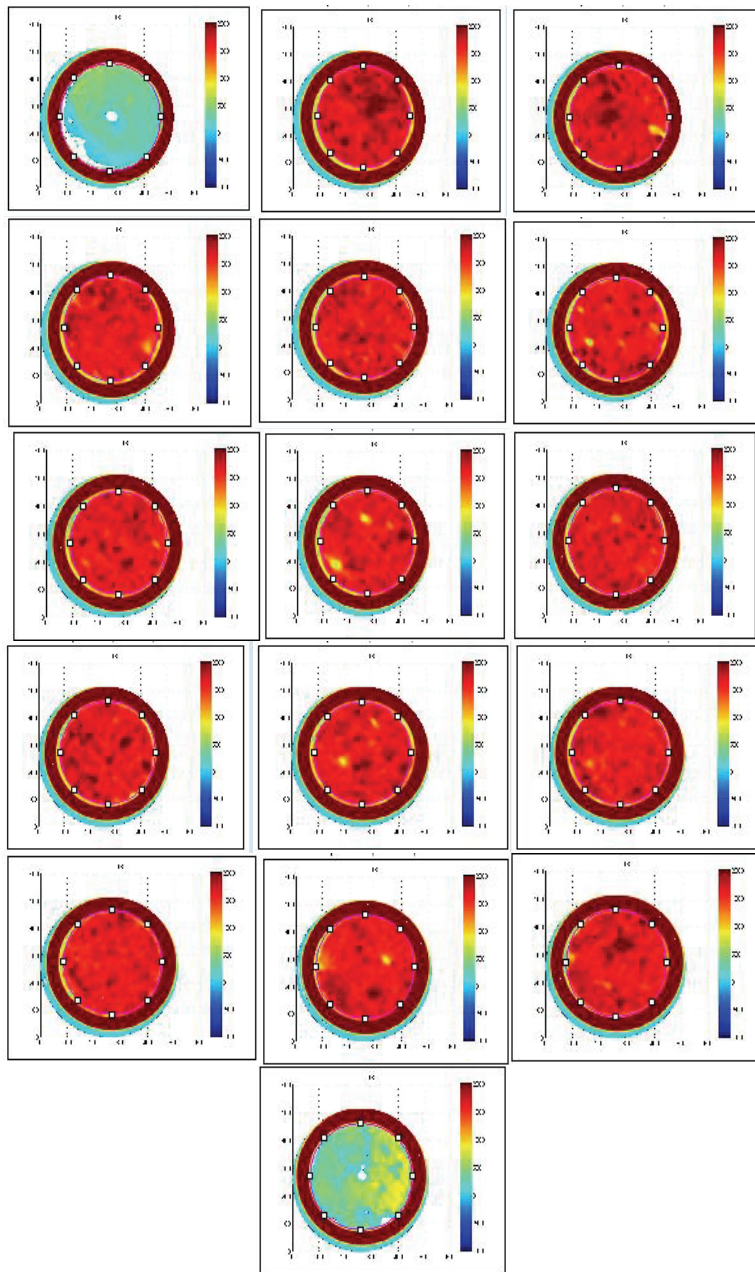
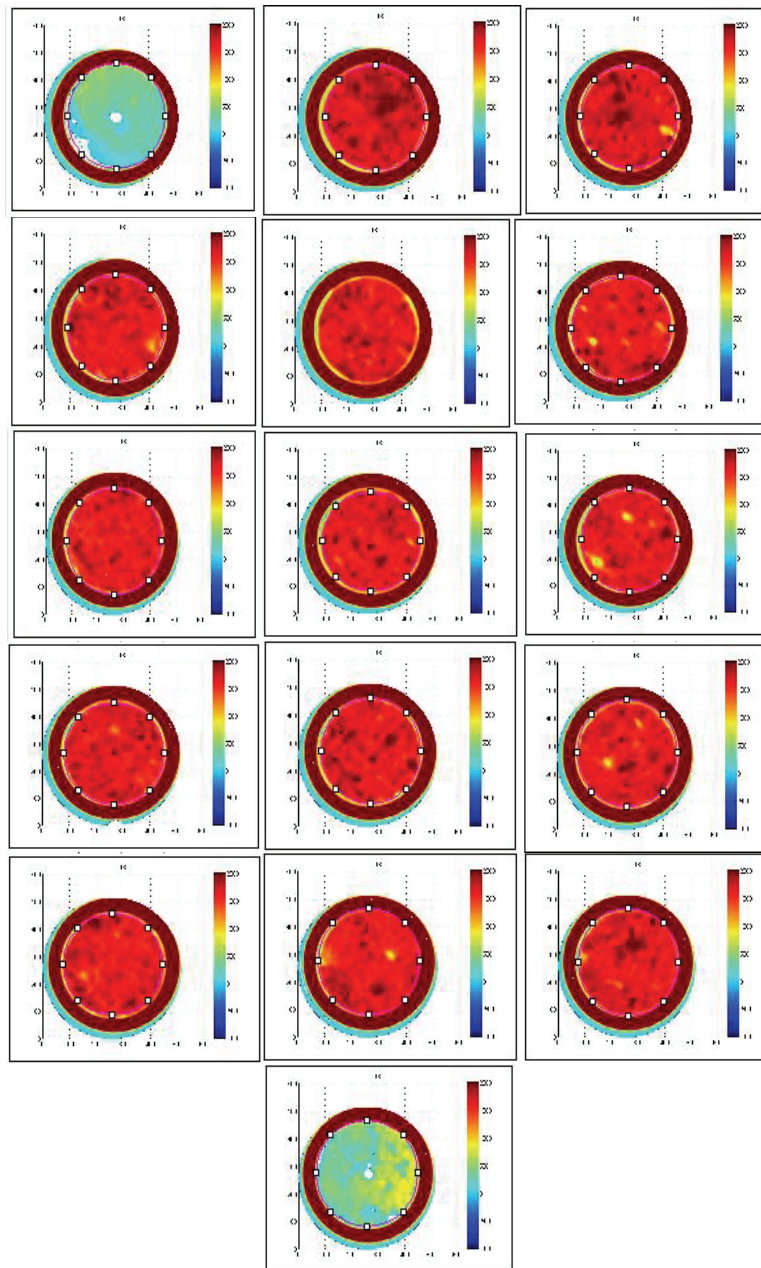


Figure B.1 CT Slice Views of Core#2 Dry.



**Figure B.2** CT Slice Views of Core#2 Water Saturated.



**Figure B.3** CT Slice Views of Core#2 Decane Flooded.

**Initially Decane Saturated Water Flooded Naturally Fractured CT Scan  
Images of Core#2**

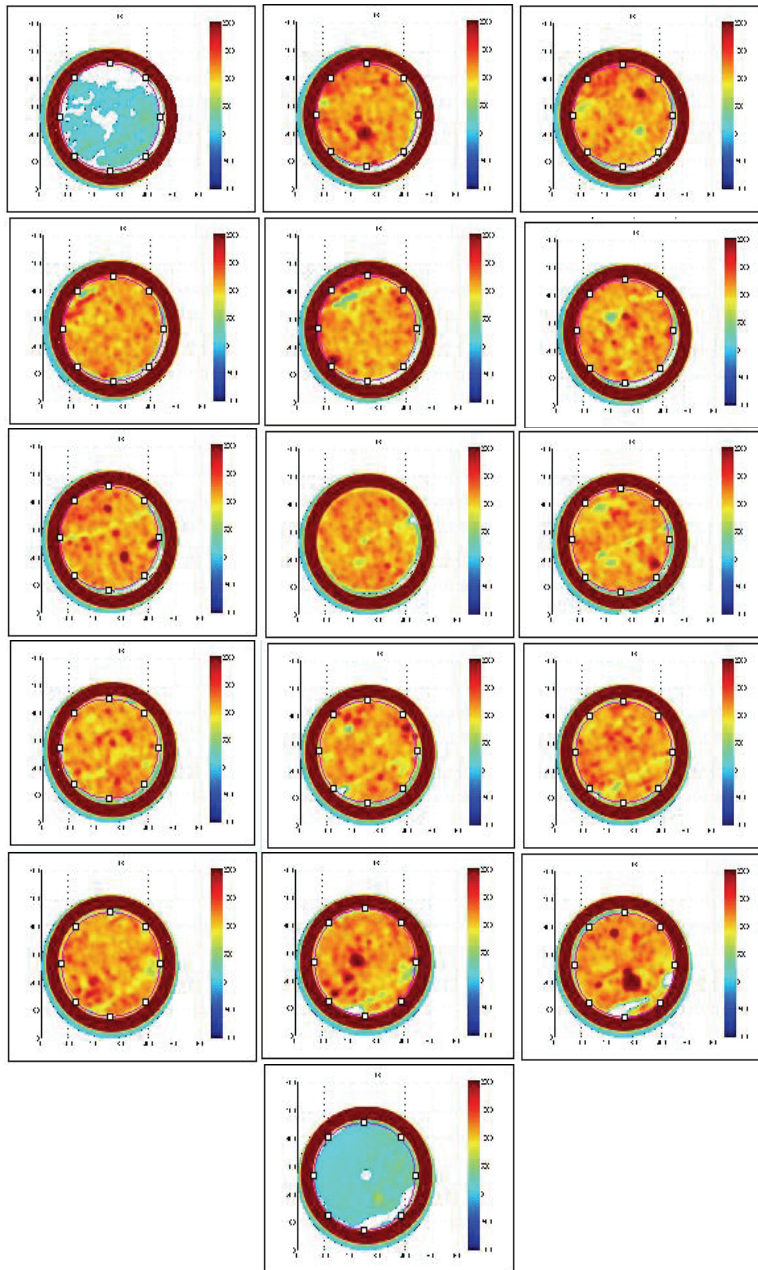


**Figure B.4** CT Slice Views of Core#2 Dry Scanned.

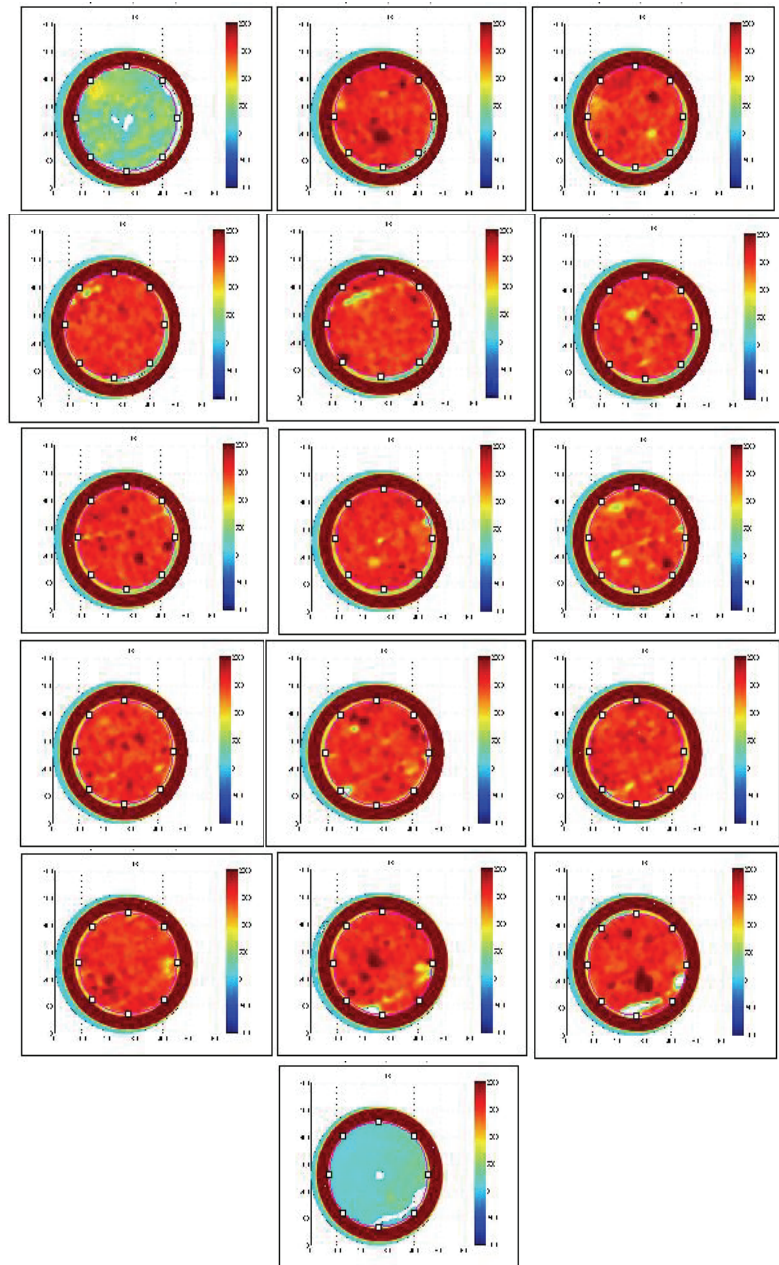
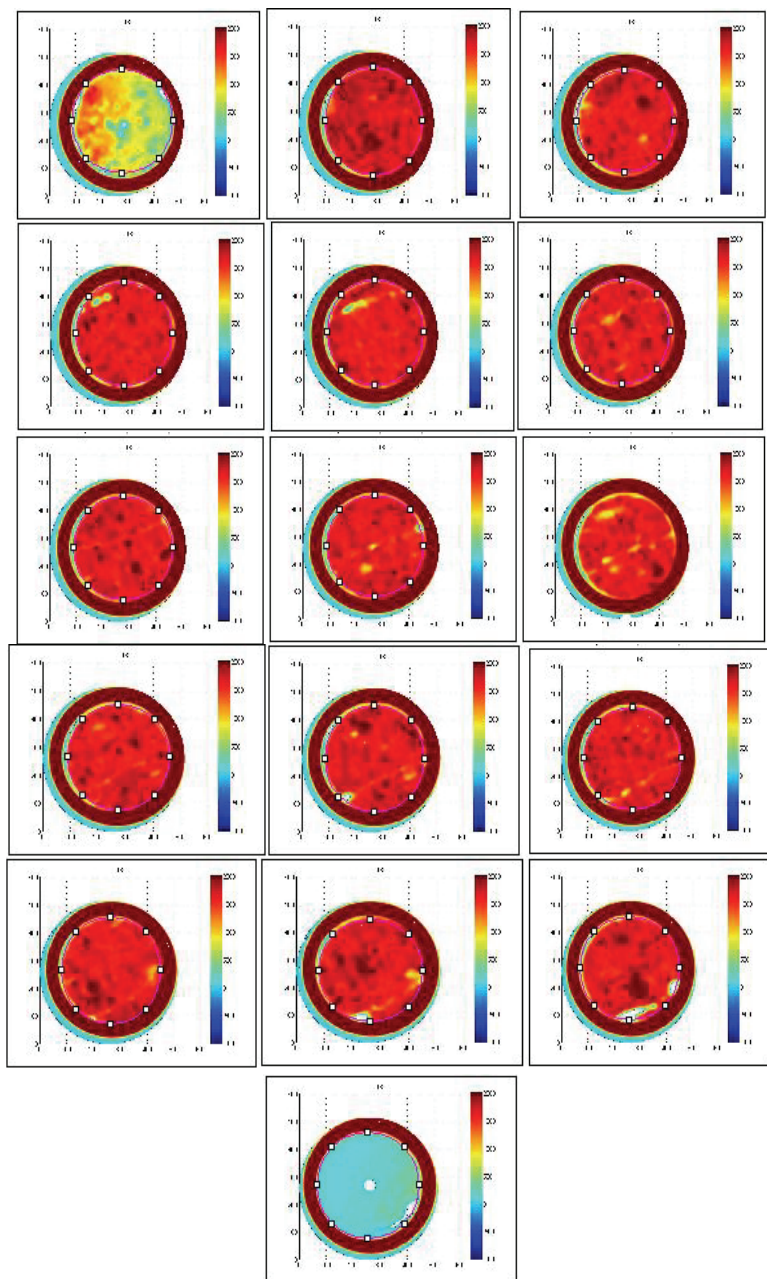


Figure B.5 CT Slice Views of Core#2 Decane Saturated.



**Figure B.6** CT Slice Views of Core#2 Water Flooded.

**Initially Water Saturated Decane Flooded Naturally Fractured CT Numbers of Core#2**

**Table B.1** CT Numbers of Slices for Core#2 Porosity Calculation.

Porosity	area	dry mean	CT#	22 water	area	100 % water saturated mean	CT#	fraction
21 dry								
1	40,260	184,441	-90	1	40,260	173,764	620	
2	40,260	135,935	1,075	2	40,260	77,924	1,400	0.3250
3	40,260	138,254	1,057	3	40,260	81,484	1,387	0.3298
4	40,260	141,596	1,032	4	40,260	86,326	1,370	0.3378
5	40,260	142,269	1,027	5	40,260	85,123	1,374	0.3472
6	40,260	141,967	1,029	6	40,260	87,259	1,366	0.3372
7	40,260	143,626	1,017	7	40,260	87,481	1,366	0.3490
8	40,260	142,503	1,025	8	40,260	88,883	1,361	0.3355
9	40,260	142,034	1,029	9	40,260	86,183	1,370	0.3416
10	40,260	139,715	1,046	10	40,260	84,714	1,376	0.3293
11	40,260	141,867	1,030	11	40,260	87,241	1,366	0.3365
12	40,260	140,992	1,037	12	40,260	85,981	1,371	0.3344
13	40,260	140,957	1,037	13	40,260	86,801	1,368	0.3312
14	40,260	139,655	1,047	14	40,260	87,160	1,367	0.3200
15	40,260	137,353	1,064	15	40,260	84,894	1,375	0.3107
16	40,260	175,000	-120	16	40,260	170,771	615	
							<b>average <math>\Phi</math></b>	<b>33.32%</b>

**Table B.2** CT Numbers of Slices for Core#2 Saturation Calculation.

Saturation	area	100 % water saturated mean	CT#	2d2	area	100 % decane saturated mean	CT#
2w1							
1	40,260	173,764	620	1	40,260	158,25	-285
2	40,260	77,924	1,400	2	40,260	76,938	1,100
3	40,260	81,484	1,387	3	40,260	85,932	1,071
4	40,260	86,326	1,370	4	40,260	87,334	1,067
5	40,260	85,123	1,374	5	40,260	87,683	1,066
6	40,260	87,259	1,366	6	40,260	85,447	1,073
7	40,260	87,481	1,366	7	40,260	84,707	1,075
8	40,260	88,883	1,361	8	40,260	86,819	1,068
9	40,260	86,183	1,370	9	40,260	91,341	1,054
10	40,260	84,714	1,376	10	40,260	87,925	1,065
11	40,260	87,241	1,366	11	40,260	85,942	1,071
12	40,260	85,981	1,371	12	40,260	85,957	1,071
13	40,260	86,801	1,368	13	40,260	85,883	1,071
14	40,260	87,160	1,367	14	40,260	85,503	1,073
15	40,260	84,894	1,375	15	40,260	89,969	1,058
16	40,260	170,771	615	16	40,260	171,309	-285

**Table B.3** CT Numbers of Slices for Core#2 Saturation Calculation.

<b>2wd</b>	<b>area</b>	<b>decane after water mean</b>	<b>CT#</b>	<b>saturation Sw</b>	<b>saturation Sp</b>
1	40,260	160,746	590		
2	40,260	83,943	1,253	61%	39%
3	40,260	85,776	1,234	48%	52%
4	40,260	87,079	1,221	46%	54%
5	40,260	85,773	1,234	51%	49%
6	40,260	85,16	1,240	53%	47%
7	40,260	83,954	1,253	56%	44%
8	40,260	85,12	1,241	54%	46%
9	40,260	86,416	1,228	45%	55%
10	40,260	85,113	1,241	51%	49%
11	40,260	86,576	1,226	47%	53%
12	40,260	84,254	1,250	55%	45%
13	40,260	82,755	1,265	62%	38%
14	40,260	82,507	1,268	61%	39%
15	40,260	87,622	1,215	46%	54%
16	40,260	170,548	605		
				<b>52.63%</b>	<b>47.37%</b>

**Table B.4** CT Numbers of Slices for Core#2 Saturation Calculation.

2wdw	area	water after decane mean	CT#	saturation Sw	saturation Sp
1	40,260	176,022	615		
2	40,260	80,209	1,300	80%	20%
3	40,260	82,592	1,276	68%	32%
4	40,260	84,792	1,253	60%	40%
5	40,260	83,431	1,267	65%	35%
6	40,260	82,925	1,272	66%	34%
7	40,260	81,949	1,282	68%	32%
8	40,260	83,238	1,269	66%	34%
9	40,260	83,939	1,262	61%	39%
10	40,260	83,824	1,263	61%	39%
11	40,260	85,102	1,250	58%	42%
12	40,260	82,626	1,275	66%	34%
13	40,260	81,989	1,282	68%	32%
14	40,260	80,394	1,298	73%	27%
15	40,260	85,072	1,250	63%	37%
16	40,260	170,972	605		
				<b>65.88%</b>	<b>34.12%</b>

**Initially Decane Saturated Decane Flooded Naturally Fractured CT Numbers of Core#2**

**Table B.5** CT Numbers of Slices for Core#2 Porosity Calculation.

<b>Porosity</b>	<b>area</b>	<b>dry mean</b>	<b>CT#</b>	<b>22 water</b>	<b>area</b>	<b>100 % water saturated mean</b>	<b>CT#</b>	<b>fraction</b>
<b>21dry</b>								
1	40,260	184,441	-90	1	40,260	173,764	620	
2	40,260	135,935	1,075	2	40,260	77,924	1,400	0.3250
3	40,260	138,254	1,057	3	40,260	81,484	1,387	0.3298
4	40,260	141,596	1,032	4	40,260	86,326	1,370	0.3378
5	40,260	142,269	1,027	5	40,260	85,123	1,374	0.3472
6	40,260	141,967	1,029	6	40,260	87,259	1,366	0.3372
7	40,260	143,626	1,017	7	40,260	87,481	1,366	0.3490
8	40,260	142,503	1,025	8	40,260	88,883	1,361	0.3355
9	40,260	142,034	1,029	9	40,260	86,183	1,370	0.3416
10	40,260	139,715	1,046	10	40,260	84,714	1,376	0.3293
11	40,260	141,867	1,030	11	40,260	87,241	1,366	0.3365
12	40,260	140,992	1,037	12	40,260	85,981	1,371	0.3344
13	40,260	140,957	1,037	13	40,260	86,801	1,368	0.3312
14	40,260	139,655	1,047	14	40,260	87,160	1,367	0.3200
15	40,260	137,353	1,064	15	40,260	84,894	1,375	0.3107
16	40,260	175,000	-120	16	40,260	170,771	615	
							<b>average <math>\Phi</math></b>	<b>33.32%</b>

**Table B.6** CT Numbers of Slices for Core#2 Saturation Calculation.

Saturation	area	100 % water saturated mean	CT#	2d2	area	100 % decane saturated mean	CT#
2w1							
1	40,260	173,764	620	1	40,260	158,25	-285
2	40,260	77,924	1,400	2	40,260	76,938	1,100
3	40,260	81,484	1,387	3	40,260	85,932	1,071
4	40,260	86,326	1,370	4	40,260	87,334	1,067
5	40,260	85,123	1,374	5	40,260	87,683	1,066
6	40,260	87,259	1,366	6	40,260	85,447	1,073
7	40,260	87,481	1,366	7	40,260	84,707	1,075
8	40,260	88,883	1,361	8	40,260	86,819	1,068
9	40,260	86,183	1,370	9	40,260	91,341	1,054
10	40,260	84,714	1,376	10	40,260	87,925	1,065
11	40,260	87,241	1,366	11	40,260	85,942	1,071
12	40,260	85,981	1,371	12	40,260	85,957	1,071
13	40,260	86,801	1,368	13	40,260	85,883	1,071
14	40,260	87,160	1,367	14	40,260	85,503	1,073
15	40,260	84,894	1,375	15	40,260	89,969	1,058
16	40260	170,771	615	16	40,260	171,309	-285

**Table B.7** CT Numbers of Slices for Core#2 Saturation Calculation (ios).

2dw	area	water after decane mean	CT#	saturation Sw	saturation Sp
1	40,260	192,77	-50		
2	40,260	133,456	1,278	59%	41%
3	40,260	137,707	1,269	63%	37%
4	40,260	140,918	1,263	65%	35%
5	40,260	138,472	1,268	66%	34%
6	40,260	140,068	1,265	65%	35%
7	40,260	139,067	1,267	66%	34%
8	40,260	141,837	1,261	66%	34%
9	40,260	143,311	1,258	65%	35%
10	40,260	142,651	1,260	63%	37%
11	40,260	141,779	1,261	64%	36%
12	40,260	140,471	1,264	64%	36%
13	40,260	141,329	1,262	64%	36%
14	40,260	137,367	1,270	67%	33%
15	40,260	140,338	1,264	65%	35%
16	40,260	175,665	-60		
				<b>59.60%</b>	<b>40.40%</b>

**Initially Water Saturated Decane Flooded CT Numbers of Core#8**

**Table B.8** CT Numbers of Slices for Core#8 Porosity Calculation.

Porosity	area	dry mean	CT#	82 water	area	100 % water saturated mean	CT#	fraction
81								
1	40,260	182,012	580	1	40,260	169,219		
2	40,260	144,024	1,050	2	40,260	87,552	1,386	0.3355
3	40,260	143,745	1,052	3	40,260	83,939	1,400	0.3482
4	40,260	143,968	1,051	4	40,260	87,376	1,386	0.3356
5	40,260	141,963	1,061	5	40,260	86,882	1,388	0.3270
6	40,260	140,872	1,067	6	40,260	87,918	1,384	0.3171
7	40,260	139,339	1,075	7	40,260	88,720	1,381	0.3057
8	40,260	141,209	1,065	8	40,260	87,297	1,387	0.3213
9	40,260	140,696	1,068	9	40,260	84,913	1,396	0.3281
10	40,260	141,324	1,065	10	40,260	84,221	1,399	0.3342
11	40,260	142,257	1,060	11	40,260	86,958	1,388	0.3282
12	40,260	141,157	1,066	12	40,260	87,646	1,385	0.3197
13	40,260	139,441	1,075	13	40,260	88,933	1,380	0.3054
14	40,260	139,162	1,076	14	40,260	87,974	1,384	0.3078
15	40,260	144,529	1,047	15	40,260	87,375	1,386	0.3390
16	40,260	212,529	0	16	40,260	171,052		
							<b>averageΦ</b>	<b>32.52%</b>

**Table B.9** CT Numbers of Slices for Core#8 Saturation Calculation.

Saturation	area	100 % water saturated mean	CT#	8d	area	100 % decane saturated mean	CT#
8w							
1	40,260	169,219	600	1	40,260	172,707	610
2	40,260	87,552	1,386	2	40,260	102,303	1,100
3	40,260	83,939	1,400	3	40,260	96,680	1,130
4	40,260	87,376	1,386	4	40,260	98,655	1,119
5	40,260	86,882	1,388	5	40,260	99,409	1,115
6	40,260	87,918	1,384	6	40,260	99,947	1,112
7	40,260	88,720	1,381	7	40,260	99,439	1,115
8	40,260	87,297	1,387	8	40,260	99,354	1,116
9	40,260	84,913	1,396	9	40,260	96,924	1,129
10	40,260	84,221	1,399	10	40,260	97,069	1,128
11	40,260	86,958	1,388	11	40,260	97,784	1,124
12	40,260	87,646	1,385	12	40,260	98,440	1,120
13	40,260	88,933	1,380	13	40,260	101,023	1,107
14	40,260	87,974	1,384	14	40,260	98,520	1,120
15	40,260	87,375	1,386	15	40,260	99,039	1,117
16	40,260	171,052	610	16	40,260	173,334	611

**Table B.10** CT Numbers of Slices for Core#8 Saturation Calculation.

<b>8wd</b>	<b>area</b>	<b>decane after water mean</b>	<b>CT#</b>	<b>saturation Sw</b>	<b>saturation Sp</b>
1	40,260	168,308	600		
2	40,260	89,328	1,285	65%	35%
3	40,260	88,333	1,283	57%	43%
4	40,260	94,578	1,238	45%	55%
5	40,260	94,130	1,242	47%	53%
6	40,260	95,203	1,233	44%	56%
7	40,260	96,805	1,218	39%	61%
8	40,260	94,761	1,237	45%	55%
9	40,260	91,735	1,264	50%	50%
10	40,260	91,577	1,265	51%	49%
11	40,260	94,540	1,239	43%	57%
12	40,260	93,979	1,244	47%	53%
13	40,260	95,741	1,228	44%	56%
14	40,260	94,404	1,240	45%	55%
15	40,260	93,562	1,247	48%	52%
16	40,260	170,281	605		
				<b>47.82%</b>	<b>52.18%</b>

**Table B.11** CT Numbers of Slices for Core#8 Saturation Calculation.

8wdw	area	water after decane mean	CT#	saturation Sw	saturation Sp
1	40,260	171,636	615		
2	40,260	82,397	1,360	91%	9%
3	40,260	81,279	1,372	90%	10%
4	40,260	86,439	1,317	74%	26%
5	40,260	87,407	1,306	70%	30%
6	40,260	88,750	1,292	66%	34%
7	40,260	90,095	1,277	61%	39%
8	40,260	89,372	1,285	63%	37%
9	40,260	87,136	1,309	68%	32%
10	40,260	87,393	1,306	66%	34%
11	40,260	90,025	1,278	58%	42%
12	40,260	90,371	1,274	58%	42%
13	40,260	92,011	1,257	55%	45%
14	40,260	90,532	1,273	58%	42%
15	40,260	90,308	1,275	59%	41%
16	40,260	170,586	605		
				<b>66.83%</b>	<b>33.17%</b>

**Initially Decane Saturated Water Flooded CT Numbers of Core#8**

**Table B.12** CT Numbers of Slices for Core#8 Porosity Calculation.

Porosity	area	dry mean	CT#	82 water	area	100 % water saturated mean	CT#	fraction
81 dry								
1	40,260	182,012	580	1	40,260	169,219	600	
2	40,260	144,024	1,050	2	40,260	87,552	1,386	0.3355
3	40,260	143,745	1,052	3	40,260	83,939	1,400	0.3482
4	40,260	143,968	1,051	4	40,260	87,376	1,386	0.3356
5	40,260	141,963	1,061	5	40,260	86,882	1,388	0.3270
6	40,260	140,872	1,067	6	40,260	87,918	1,384	0.3171
7	40,260	139,339	1,075	7	40,260	88,720	1,381	0.3057
8	40,260	141,209	1,065	8	40,260	87,297	1,387	0.3213
9	40,260	140,696	1,068	9	40,260	84,913	1,396	0.3281
10	40,260	141,324	1,065	10	40,260	84,221	1,399	0.3342
11	40,260	142,257	1,060	11	40,260	86,958	1,388	0.3282
12	40,260	141,157	1,066	12	40,260	87,646	1,385	0.3197
13	40,260	139,441	1,075	13	40,260	88,933	1,380	0.3054
14	40,260	139,162	1,076	14	40,260	87,974	1,384	0.3078
15	40,260	144,529	1,047	15	40,260	87,375	1,386	0.3390
16	40,260	212,529	0	16	40,260	171,052	610	
							<b>average <math>\Phi</math></b>	<b>32.52%</b>

**Table B.13** CT Numbers of Slices for Core#8 Saturation Calculation.

Saturation	area	100 % water saturated mean	CT#	8d	area	100 % decane saturated mean	CT#
8w	40,260	169,219	600	1	40,260	172,707	610
1	40,260	87,552	1,386	2	40,260	102,303	1,100
2	40,260	83,939	1,400	3	40,260	96,680	1,130
3	40,260	87,376	1,386	4	40,260	98,655	1,119
4	40,260	86,882	1,388	5	40,260	99,409	1,115
5	40,260	87,918	1,384	6	40,260	99,947	1,112
6	40,260	88,720	1,381	7	40,260	99,439	1,115
7	40,260	87,297	1,387	8	40,260	99,354	1,116
8	40,260	84,913	1,396	9	40,260	96,924	1,129
9	40,260	84,221	1,399	10	40,260	97,069	1,128
10	40,260	86,958	1,388	11	40,260	97,784	1,124
11	40,260	87,646	1,385	12	40,260	98,440	1,120
12	40,260	88,933	1,380	13	40,260	101,023	1,107
13	40,260	87,974	1,384	14	40,260	98,520	1,120
14	40,260	87,375	1,386	15	40,260	99,039	1,117
15	40,260	171,052	610	16	40,260	173,334	611

**Table B.14** CT Numbers of Slices for Core#8 Saturation Calculation.

8wdw	area	water after decane mean	CT#	saturation Sw	saturation Sp
1	40,260	171,636	615		
2	40,260	82,397	1,360	91%	9%
3	40,260	81,279	1,372	90%	10%
4	40,260	86,439	1,317	86%	14%
5	40,260	87,407	1,306	70%	30%
6	40,260	88,750	1,292	66%	34%
7	40,260	90,095	1,277	61%	39%
8	40,260	89,372	1,285	63%	37%
9	40,260	87,136	1,309	68%	32%
10	40,260	87,393	1,306	66%	34%
11	40,260	90,025	1,278	58%	42%
12	40,260	90,371	1,274	58%	42%
13	40,260	92,011	1,257	55%	45%
14	40,260	90,532	1,273	58%	42%
15	40,260	90,308	1,275	59%	41%
16	40,260	170,586	605		
				<b>67.69%</b>	<b>32.31%</b>

## APPENDIX-C

### SAMPLE FRACTURE APERTURE & PERMEABILITY CALCULATION

The influence of aperture on flow is commonly described by the steady-state solution to the Navier-Stokes equations for laminar viscous flow between two smooth parallel plates. This solution, known as the cubic law, stated previously.

$$Q = \frac{b^3}{12\mu} \left( \frac{\Delta P}{L} \right) \quad (\text{Equation 3.6})$$

Q	m <sup>3</sup> /s	6E+7 ml/min	0.1 ml/min
b	m	1,000 mm	mm
μ	Pas	1,000 cP	0.87 cP
L	m	1,000 mm	74 mm
P	Pa	1E-5 bar	bar

$$0.1 = (b^3 * (0.00001 * (P_{\text{inlet}} - P_{\text{outlet}})) / (12 * 0.87 / 1000 * 74)) * 60000000$$

$$b = 0.185 \text{ mm}$$

$$k_f = k_{ff} \frac{a \cdot b}{a \cdot h} = k_{ff} \frac{b}{h} = \frac{b^3}{12h} \quad (\text{Equation 3.12})$$

b	m	1,000 mm	0.0185 cm
h	m	1,000 mm	3.7 cm

$$= (b)^3 / 12 / 0.37 \Rightarrow$$

$$k_f = 1.43E-09 \text{ cm}^2 \Rightarrow \Rightarrow$$

$$k_f = 143 \text{ md}$$

**Table C.1** Cubic Law Rates at 0.1 ml/min Pump injection in Core#2 (Run#1).

Time (hours)	Pump Rate (ml/min)	Pinlet (bar-g)	Poutlet (bar-g)	Cubic Rate (ml/min)	Equivalent Fracture Aperture (mm)	$k_f$ (cm <sup>2</sup> )	$k_f$ (md)
00:00	0	0	0	0	0	0	0
00:02	0.10	0.10	0.08	0.10	0.185	1.43E-09	143
00:19	0.10	0.09	0.07	0.10	0.185	1.43E-09	143
00:32	0.10	0.08	0.06	0.10	0.185	1.43E-09	143
01:15	0.10	0.08	0.06	0.10	0.185	1.43E-09	143
02:25	0.10	0.09	0.07	0.10	0.185	1.43E-09	143
03:25	0.10	0.09	0.07	0.10	0.185	1.43E-09	143
04:24	0.10	0.10	0.08	0.10	0.185	1.43E-09	143
04:54	0.10	0.10	0.08	0.10	0.185	1.43E-09	143
05:27	0.10	0.10	0.08	0.10	0.185	1.43E-09	143
05:37	0.10	0.09	0.07	0.10	0.185	1.43E-09	143

**Table C.2** Initially Oil Saturated Cubic Law Rates at 0.1 ml/min Pump injection in Core#2 (Run#2).

Time (hours)	Pump Rate (ml/min)	Pinlet (bar-g)	Poutlet (bar-g)	Cubic Rate (ml/min)	Equivalent Fracture Aperture (mm)	$k_f$ (cm <sup>2</sup> )	$k_f$ (md)
00:00	0	0	0	0	0	0	0
00:40	0.10	0.13	0.11	0.10	0.187	1.475E-09	148
00:56	0.10	0.11	0.09	0.10	0.187	1.475E-09	148
01:18	0.10	0.13	0.11	0.10	0.187	1.475E-09	148
01:30	0.10	0.11	0.09	0.10	0.187	1.475E-09	148
02:14	0.10	0.11	0.09	0.10	0.187	1.475E-09	148
02:46	0.10	0.13	0.11	0.10	0.187	1.475E-09	148
02:57	0.10	0.11	0.09	0.10	0.187	1.475E-09	148
03:20	0.10	0.13	0.11	0.10	0.187	1.475E-09	148
03:41	0.10	0.11	0.09	0.10	0.187	1.475E-09	148
03:52	0.10	0.11	0.09	0.10	0.187	1.475E-09	148
04:14	0.10	0.11	0.09	0.10	0.187	1.475E-09	148
04:36	0.10	0.13	0.11	0.10	0.187	1.475E-09	148
04:47	0.10	0.11	0.09	0.10	0.187	1.475E-09	148
04:58	0.10	0.11	0.09	0.10	0.187	1.475E-09	148
05:24	0.10	0.13	0.11	0.10	0.187	1.475E-09	148

**Table C.3** Initially Water Saturated Cubic Law Rates at 0.1 ml/min Pump injection in Core#8 (Run#3).

Time (hours)	Pump Rate (ml/min)	Pinlet (bar-g)	Poutlet (bar-g)	Cubic Rate (ml/min)	Equivalent Fracture Aperture (mm)	$k_f$ (cm <sup>2</sup> )	$k_f$ (md)
00:00	0.00	0.00	0.00	0.00	0.000	0	0
00:25	0.10	0.19	0.09	0.10	0.110	3.01E-10	30
00:30	0.10	0.15	0.06	0.10	0.111	3.09E-10	31
00:47	0.10	0.15	0.06	0.10	0.111	3.09E-10	31
00:52	0.10	0.15	0.08	0.10	0.121	4.00E-10	40
01:17	0.10	0.13	0.07	0.10	0.127	4.63E-10	46
01:37	0.10	0.12	0.07	0.10	0.135	5.49E-10	55
02:04	0.10	0.10	0.06	0.10	0.150	7.60E-10	76
02:37	0.10	0.10	0.06	0.10	0.150	7.60E-10	76
02:55	0.10	0.10	0.06	0.10	0.150	7.60E-10	76
03:45	0.10	0.10	0.06	0.10	0.150	7.60E-10	76
04:22	0.10	0.10	0.06	0.10	0.150	7.60E-10	76
04:41	0.10	0.10	0.06	0.10	0.150	7.60E-10	76
05:02	0.10	0.10	0.06	0.10	0.150	7.60E-10	76
05:08	0.10	0.10	0.06	0.10	0.150	7.60E-10	76
05:22	0.10	0.10	0.06	0.10	0.150	7.60E-10	76
05:37	0.10	0.10	0.06	0.10	0.150	7.60E-10	76
05:53	0.10	0.10	0.06	0.10	0.150	7.60E-10	76
06:02	0.10	0.10	0.06	0.10	0.150	7.60E-10	76

**Table C.4** Initially Oil Saturated Cubic Law Rates at 0.1 ml/min Pump injection in Core#8 (Run#4).

Time (hours)	Pump Rate (ml/min)	Pinlet (bar-g)	Poutlet (bar-g)	Cubic Rate (ml/min)	Equivalent Fracture Aperture (mm)	$k_f$ (cm <sup>2</sup> )	$k_f$ (md)
00:00	0	0	0	0	0	0	0
00:02	0.10	0.1	0.09	0.10	0.235	2.92E-09	292
00:05	0.10	0.09	0.07	0.10	0.185	1.43E-09	143
00:15	0.10	0.09	0.07	0.10	0.185	1.43E-09	143
00:20	0.10	0.09	0.07	0.10	0.185	1.43E-09	143
01:48	0.10	0.09	0.07	0.10	0.185	1.43E-09	143
02:00	0.10	0.09	0.06	0.10	0.161	9.40E-10	94
02:45	0.10	0.09	0.07	0.10	0.185	1.43E-09	143
04:40	0.10	0.09	0.05	0.10	0.147	7.17E-10	72
05:22	0.10	0.08	0.06	0.10	0.185	1.43E-09	143
05:55	0.10	0.09	0.06	0.10	0.161	9.40E-10	94
06:05	0.10	0.08	0.06	0.10	0.185	1.43E-09	143
06:20	0.10	0.09	0.06	0.10	0.160	9.23E-10	92
06:35	0.10	0.09	0.06	0.10	0.160	9.23E-10	92
06:40	0.10	0.09	0.06	0.10	0.160	9.23E-10	92



**APPENDIX-D**

**INITIALLY WATER SATURATED DECANE FLOODED  
ARTIFICIALLY FRACTURED CT NUMBERS OF CORE#3**

**Table D.1** CT Numbers of Slices for Core#3 Porosity Calculation.

Porosity	Area	dry mean	CT#	3afm2 water	area	100 % water saturated mean	CT#	fraction
3afm1 dry								
1	40,258	221,217	-10	1	40,258	208,489	-11	
2	40,258	140,989	1,007	2	40,258	78,713	1,306	0.2996
3	40,258	140,878	1,008	3	40,258	69,543	1,474	0.4666
4	40,258	139,605	1,023	4	40,258	75,311	1,369	0.3456
5	40,258	137,445	1,049	5	40,258	75,574	1,364	0.3150
6	40,258	134,679	1,082	6	40,258	74,266	1,388	0.3061
7	40,258	135,160	1,076	7	40,258	77,758	1,324	0.2478
8	40,258	135,419	1,073	8	40,258	67,236	1,517	0.4439
9	40,258	136,777	1,057	9	40,258	73,729	1,398	0.3409
10	40,258	139,962	1,019	10	40,258	71,341	1,441	0.4227
11	40,258	140,290	1,015	11	40,258	70,916	1,449	0.4344
12	40,258	146,580	940	12	40,258	78,095	1,317	0.3775
13	40,258	142,127	993	13	40,258	80,752	1,269	0.2757
14	40,258	139,480	1,024	14	40,258	75,632	1,363	0.3382
15	40,258	142,091	993	15	40,258	85,587	1,180	0.1866
16	40,258	210,355	0	16	40,258	209,821	1,100	
							<b>average <math>\Phi</math></b>	<b>34.29%</b>

**Table D.2** CT Numbers of Slices for Core#3 Saturation Calculation.

Saturation	area	water 100 % saturated mean	CT#	3afmd2	area	100 % decane saturated mean	CT#
3afmw1							
1	40,258	208,489	-11	1	40,258	172,707	615
2	40,258	78,713	1,306	2	40,258	102,303	1,085
3	40,258	69,543	1,474	3	40,258	96,680	1,115
4	40,258	75,311	1,369	4	40,258	98,655	1,104
5	40,258	75,574	1,364	5	40,258	99,409	1,100
6	40,258	74,266	1,388	6	40,258	99,947	1,097
7	40,258	77,758	1,324	7	40,258	99,439	1,100
8	40,258	67,236	1,517	8	40,258	99,354	1,101
9	40,258	73,729	1,398	9	40,258	96,924	1,114
10	40,258	71,341	1,441	10	40,258	97,069	1,113
11	40,258	70,916	1,449	11	40,258	97,784	1,109
12	40,258	78,095	1,317	12	40,258	98,440	1,105
13	40,258	80,752	1,269	13	40,258	101,023	1,092
14	40,258	75,632	1,363	14	40,258	98,520	1,105
15	40,258	85,587	1,180	15	40,258	99,039	1,102
16	40,258	209,821	1,100	16	40,258	173,334	616

**Table D.3** CT Numbers of Slices for Core#3 Saturation Calculation.

<b>3afmwd2</b>	<b>area</b>	<b>decane after water mean</b>	<b>CT#</b>	<b>saturation Sw</b>	<b>saturation Sp</b>
1	40,258	164,445	550		
2	40,258	74,162	1,249	74%	26%
3	40,258	67,243	1,230	32%	68%
4	40,258	68,009	1,224	45%	55%
5	40,258	68,619	1,228	48%	52%
6	40,258	67,733	1,230	46%	54%
7	40,258	69,973	1,219	53%	47%
8	40,258	65,022	1,241	34%	66%
9	40,258	66,52	1,236	43%	57%
10	40,258	67,954	1,232	36%	64%
11	40,258	67,538	1,228	35%	65%
12	40,258	72,462	1,210	49%	51%
13	40,258	73,167	1,210	67%	33%
14	40,258	70,655	1,219	44%	56%
15	40,258	82,803	1,160	74%	26%
16	40,258	169,473	400		
				<b>48.71%</b>	<b>51.29%</b>

**Table D.4** CT Numbers of Slices for Core#3 Saturation Calculation.

3afmwd2	area	water after decane and gel mean	CT#	saturation Sw	saturation Sd
1	40,258	207,489	1,200		
2	40,258	78,115	1,224	63%	37%
3	40,258	66,994	1,347	64%	36%
4	40,258	68,258	1,333	87%	13%
5	40,258	67,361	1,322	84%	16%
6	40,258	66,854	1,338	83%	17%
7	40,258	69,302	1,298	89%	11%
8	40,258	64,447	1,386	69%	31%
9	40,258	65,473	1,360	87%	13%
10	40,258	66,311	1,334	67%	33%
11	40,258	67,294	1,341	68%	32%
12	40,258	71,475	1,254	70%	30%
13	40,258	71,522	1,241	85%	15%
14	40,258	69,361	1,286	70%	30%
15	40,258	82,977	1,070	20%	80%
16	40,258	208,821	1,120		
				<b>71.78%</b>	<b>28.22%</b>

**Initially Water Saturated Decane Flooded Artificially Fractured CT Numbers of Core#3 Left Matrix**

**Table D.5** CT Numbers of Slices for Core#3 Porosity Calculation.

Porosity	area	dry mean	CT#	3lm 2	area	100 % water saturated mean	CT#	fraction
3lm1 dry								
1	40,258	221,217	-10	1	40,258	208,489	-11	
2	17,250	140,989	1,032	2	17,250	78,713	1,329	0.2976
3	17,250	140,878	1,033	3	17,250	69,543	1,497	0.4646
4	17,250	139,605	1,048	4	17,250	75,311	1,392	0.3436
5	17,250	137,445	1,074	5	17,250	75,574	1,387	0.3130
6	17,250	134,679	1,107	6	17,250	74,266	1,411	0.3041
7	17,250	135,160	1,101	7	17,250	77,758	1,347	0.2458
8	17,250	135,419	1,098	8	17,250	67,236	1,540	0.4419
9	17,250	136,777	1,082	9	17,250	73,729	1,421	0.3389
10	17,250	139,962	1,044	10	17,250	71,341	1,464	0.4207
11	17,250	140,290	1,040	11	17,250	70,916	1,472	0.4324
12	17,250	146,580	965	12	17,250	78,095	1,340	0.3755
13	17,250	142,127	1,018	13	17,250	80,752	1,292	0.2737
14	17,250	139,480	1,049	14	17,250	75,632	1,386	0.3362
15	17,250	142,091	1,018	15	17,250	85,587	1,203	0.1846
16	40,258	210,355	0	16	40,258	209,821	1,100	
							<b>Average <math>\Phi</math></b>	<b>34.09%</b>

**Table D.6** CT Numbers of Slices for Core#3 Saturation Calculation.

Saturation	area	100 % water saturated mean	CT#	3lmd2	area	100 % decane saturated mean	CT#
3lmd1							
1	40,258	208,489	-11	1	40,258	172,707	615
2	17,250	78,713	10329	2	17,250	102,303	1,085
3	17,250	69,543	1,497	3	17,250	96,680	1,115
4	17,250	75,311	1,392	4	17,250	98,655	1,104
5	17,250	75,574	1,387	5	17,250	99,409	1,100
6	17,250	74,266	1,411	6	17,250	99,947	1,097
7	17,250	77,758	1,347	7	17,250	99,439	1,100
8	17,250	67,236	1,540	8	17,250	99,354	1,101
9	17,250	73,729	1,421	9	17,250	96,924	1,114
10	17,250	71,341	1,464	10	17,250	97,069	1,113
11	17,250	70,916	1,472	11	17,250	97,784	1,109
12	17,250	78,095	1,340	12	17,250	98,440	1,105
13	17,250	80,752	1,292	13	17,250	101,023	1,092
14	17,250	75,632	1,386	14	17,250	98,520	1,105
15	17,250	85,587	1,203	15	17,250	99,039	1,102
16	40,258	209,821	1,100	16	40,258	173,334	616

**Table D.7** CT Numbers of Slices for Core#3 Saturation Calculation.

<b>3Imwd2</b>	<b>area</b>	<b>decane after water mean</b>	<b>CT#</b>	<b>saturation Sw</b>	<b>saturation Sp</b>
1	40,258	164,445	550		
2	17,250	74,162	1,259	71%	29%
3	17,250	67,243	1,240	33%	67%
4	17,250	68,009	1,234	45%	55%
5	17,250	68,619	1,238	48%	52%
6	17,250	67,733	1,240	46%	54%
7	17,250	69,973	1,229	52%	48%
8	17,250	65,022	1,251	34%	66%
9	17,250	66,52	1,246	43%	57%
10	17,250	67,954	1,242	37%	63%
11	17,250	67,538	1,238	36%	64%
12	17,250	72,462	1,220	49%	51%
13	17,250	73,167	1,220	64%	36%
14	17,250	70,655	1,229	44%	56%
15	17,250	82,803	1,170	67%	33%
16	40,258	169,473	400		
				<b>47.80%</b>	<b>52.20%</b>

**Table D.8** CT Numbers of Slices for Core#3 Saturation Calculation.

3lmwdw3	area	water after decane and gel	CT#	saturation Sw	saturation Sp
1	40,258	207,489	1,200		
2	17,250	78,115	1,224	57%	43%
3	17,250	66,994	1,347	61%	39%
4	17,250	68,258	1,333	80%	20%
5	17,250	67,361	1,322	77%	23%
6	17,250	66,854	1,338	77%	23%
7	17,250	69,302	1,298	80%	20%
8	17,250	64,447	1,386	65%	35%
9	17,250	65,473	1,360	80%	20%
10	17,250	66,311	1,334	63%	37%
11	17,250	67,294	1,341	64%	36%
12	17,250	71,475	1,254	63%	37%
13	17,250	71,522	1,241	75%	25%
14	17,250	69,361	1,286	64%	36%
15	17,250	82,977	1,070	62%	132%
16	40,258	208,821	1,120		
				<b>62.42%</b>	<b>37.58%</b>

**Initially Water Saturated Decane Flooded Artificially Fractured CT Numbers of Core#3 Right Matrix**

**Table D.9** CT Numbers of Slices for Core#3 Porosity Calculation.

Porosity	area	dry mean	CT#	3rm2	area	100 % water saturated mean	CT#	fraction
3rm1 dry								
1	40,258	221,217	-10	1	40,258	208,489	-11	
2	17,250	143,843	1,017	2	17,250	76,147	1,390	0.3737
3	17,250	136,792	1,131	3	17,250	72,475	1,429	0.2985
4	17,250	139,122	1,093	4	17,250	72,657	1,428	0.3344
5	17,250	140,736	1,067	5	17,250	67,892	1,478	0.4115
6	17,250	139,463	1,088	6	17,250	64,835	1,511	0.4235
7	17,250	147,242	961	7	17,250	70,708	1,448	0.4870
8	17,250	133,978	1,177	8	17,250	65,476	1,504	0.3276
9	17,250	131,410	1,218	9	17,250	69,464	1,462	0.2434
10	17,250	132,814	1,196	10	17,250	70,380	1,452	0.2564
11	17,250	132,790	1,196	11	17,250	69,929	1,457	0.2608
12	17,250	137,073	1,126	12	17,250	75,933	1,393	0.2662
13	17,250	147,636	955	13	17,250	73,006	1,424	0.4688
14	17,250	138,731	1,099	14	17,250	73,224	1,421	0.3220
15	17,250	141,189	1,060	15	17,250	75,517	1,397	0.3374
16	40,258	210,355	0	16	40,258	209,821	0	
							<b>average <math>\Phi</math></b>	<b>34.37%</b>

**Table D.10** CT Numbers of Slices for Core#3 Saturation Calculation.

Saturation	area	100 % water saturated mean	CT#	3rmd2	area	100 % decane saturated mean	CT#
3rmw1	40,258	208,489	-11	1	40,258	172,707	615
1	17,250	76,147	1,390	2	17,250	102,303	1,085
2	17,250	72,475	1,429	3	17,250	96,680	1,115
3	17,250	72,657	1,428	4	17,250	98,655	1,104
4	17,250	67,892	1,478	5	17,250	99,409	1,100
5	17,250	64,835	1,511	6	17,250	99,947	1,097
6	17,250	70,708	1,448	7	17,250	99,439	1,100
7	17,250	65,476	1,504	8	17,250	99,354	1,101
8	17,250	69,464	1,462	9	17,250	96,924	1,114
9	17,250	70,38	1,452	10	17,250	97,069	1,113
10	17,250	69,929	1,457	11	17,250	97,784	1,109
11	17,250	75,933	1,393	12	17,250	98,440	1,105
12	17,250	73,006	1,424	13	17,250	101,023	1,092
13	17,250	73,224	1,421	14	17,250	98,520	1,105
14	17,250	75,517	1,397	15	17,250	99,039	1,102
15	40,258	209,821	1,100	16	40,258	173,334	616

**Table D.11** CT Numbers of Slices for Core#3 Saturation Calculation.

<b>3rmwd2</b>		<b>decane after water mean</b>	<b>CT#</b>	<b>saturation Sw</b>	<b>saturation S<sub>D</sub></b>
1	40,258	164,445	550		
2	17,250	73,662	1,120	11%	89%
3	17,250	66,743	1,324	66%	34%
4	17,250	67,509	1,271	52%	48%
5	17,250	68,119	1,317	57%	43%
6	17,250	67,233	1,327	55%	45%
7	17,250	69,473	1,282	52%	48%
8	17,250	64,522	1,371	44%	56%
9	17,250	66,02	1,352	48%	52%
10	17,250	67,454	1,337	55%	45%
11	17,250	67,038	1,319	45%	55%
12	17,250	71,962	1,242	48%	52%
13	17,250	72,667	1,241	45%	55%
14	17,250	70,155	1,281	55%	45%
15	17,250	82,303	1,031	45%	55%
16	40,258	169,473	400		
				<b>48.56%</b>	<b>51.44%</b>

**Table D.12** CT Numbers of Slices for Core#3 Saturation Calculation.

3rmwdw3	area	water after decane and gel mean	CT#	saturation S <sub>w</sub>	saturation S <sub>D</sub>
1	40,258	207,489	1,200		
2	17,250	78,365	1,249	54%	46%
3	17,250	67,244	1,372	82%	18%
4	17,250	68,508	1,358	78%	22%
5	17,250	67,611	1,347	65%	35%
6	17,250	67,104	1,363	64%	36%
7	17,250	69,552	1,323	64%	36%
8	17,250	64,697	1,411	57%	43%
9	17,250	65,723	1,385	58%	42%
10	17,250	66,561	1,359	55%	45%
11	17,250	67,544	1,366	74%	26%
12	17,250	71,725	1,279	60%	40%
13	17,250	71,772	1,266	53%	47%
14	17,250	69,611	1,311	65%	35%
15	17,250	83,227	1,095	55%	45%
16	40,258	208,821	1,120		
				<b>63.16%</b>	<b>36.84%</b>

**Initially Water Saturated Decane Flooded Artificially Fractured  
CT Scan Images of Core#7**

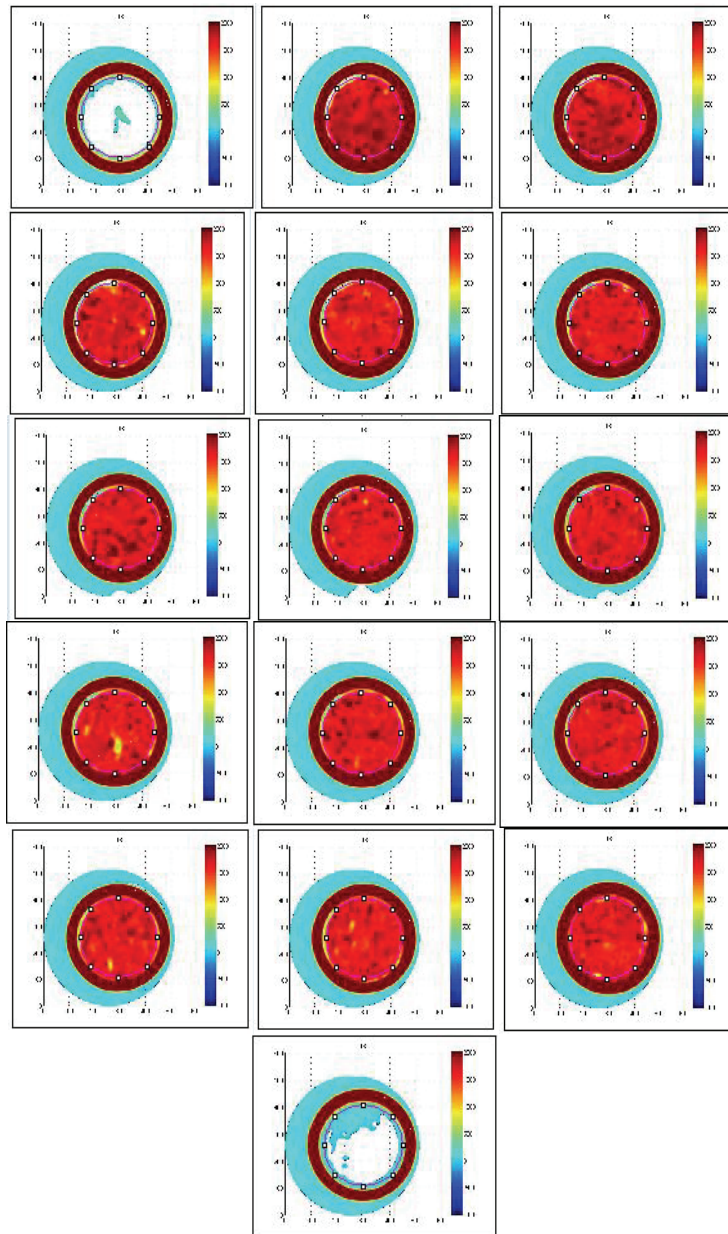


**Figure D.1** CT Slice Views of Core#7 Water Saturated.

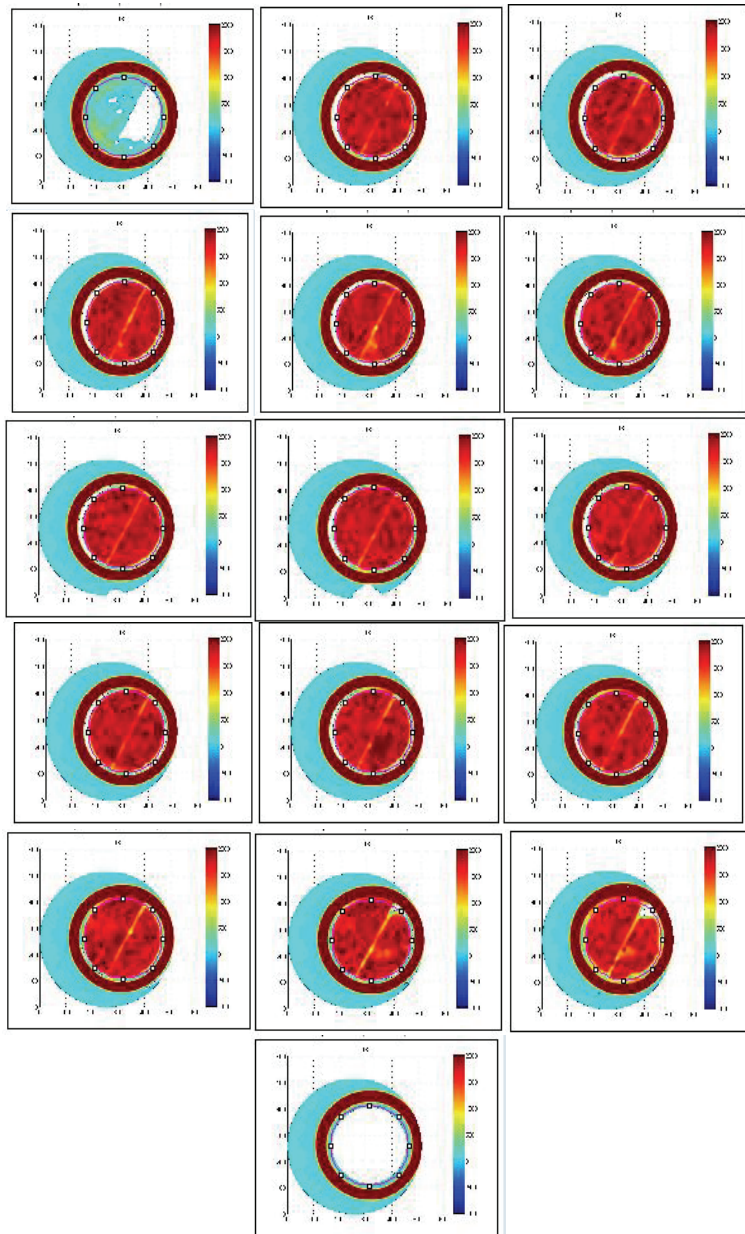


**Figure D.2** CT Slice Views of Artificially Fractured Core#7 Water Saturated.

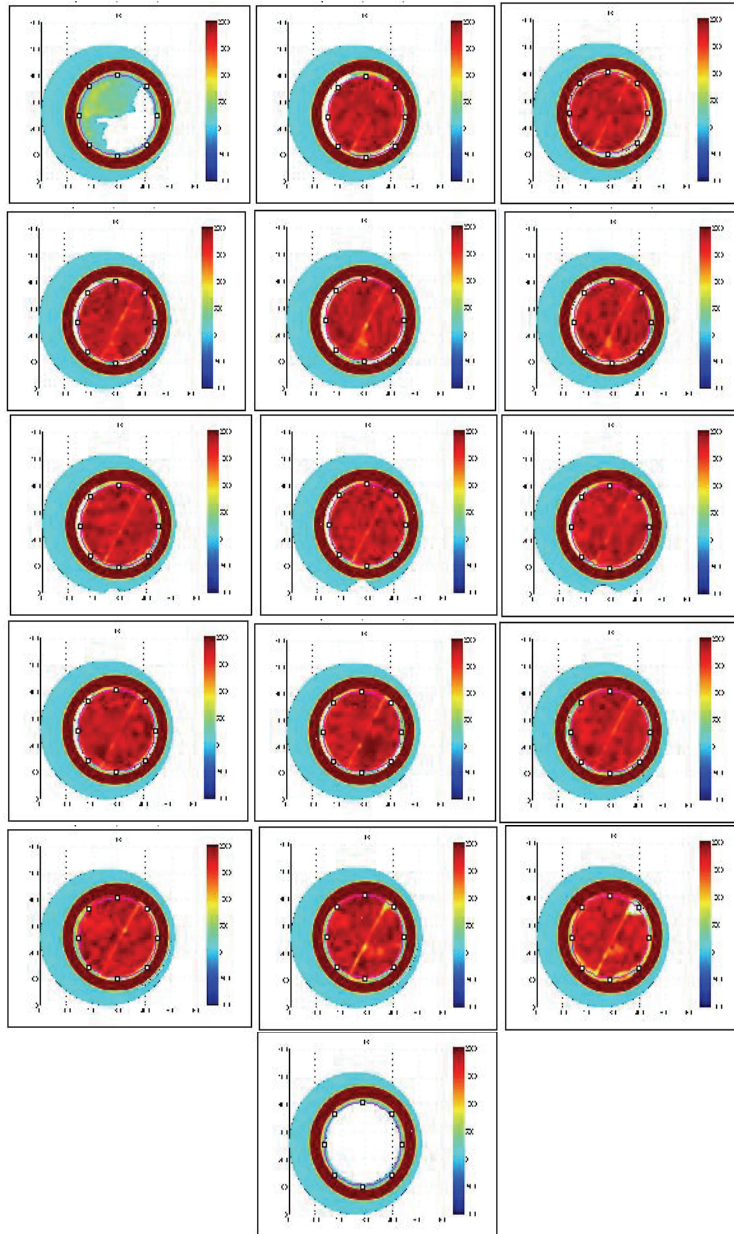


**Figure D.3** CT Slice Views of Artificially Fractured Core#7 Decane Flooded.

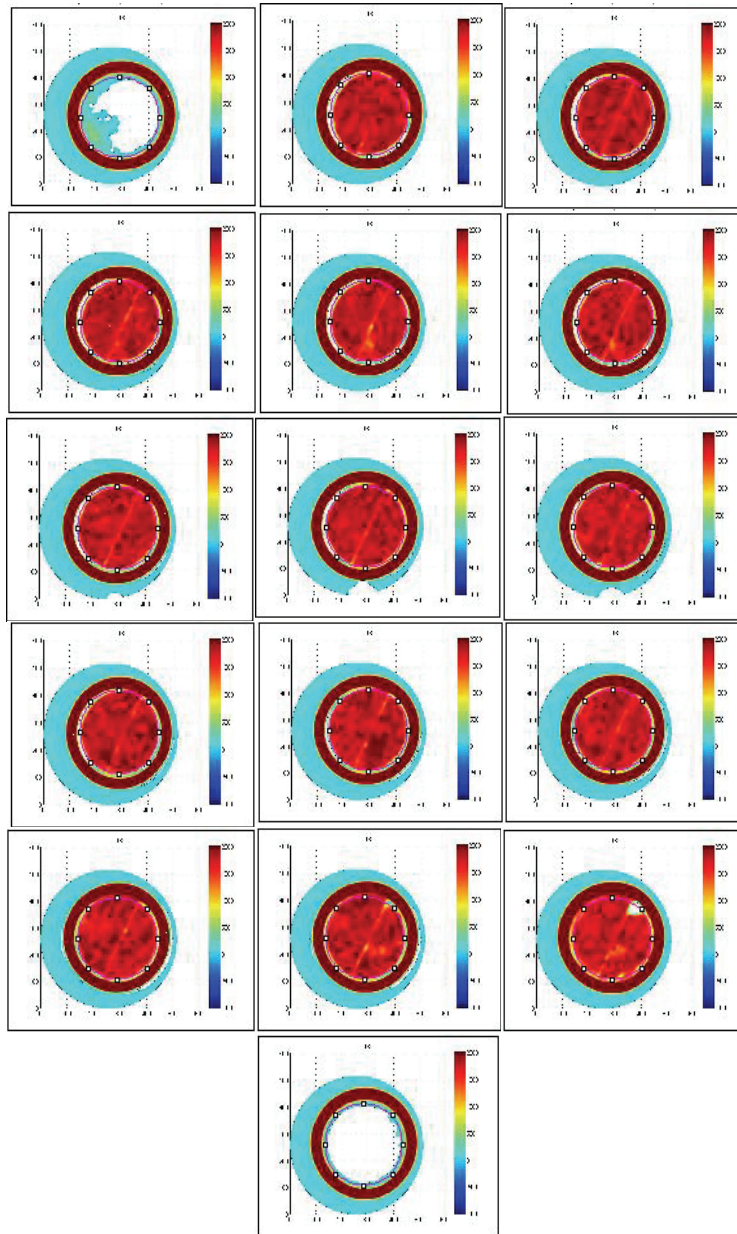


**Figure D.4** CT Slice Views of Artificially Fractured Core#7 Water Flooded for Production.

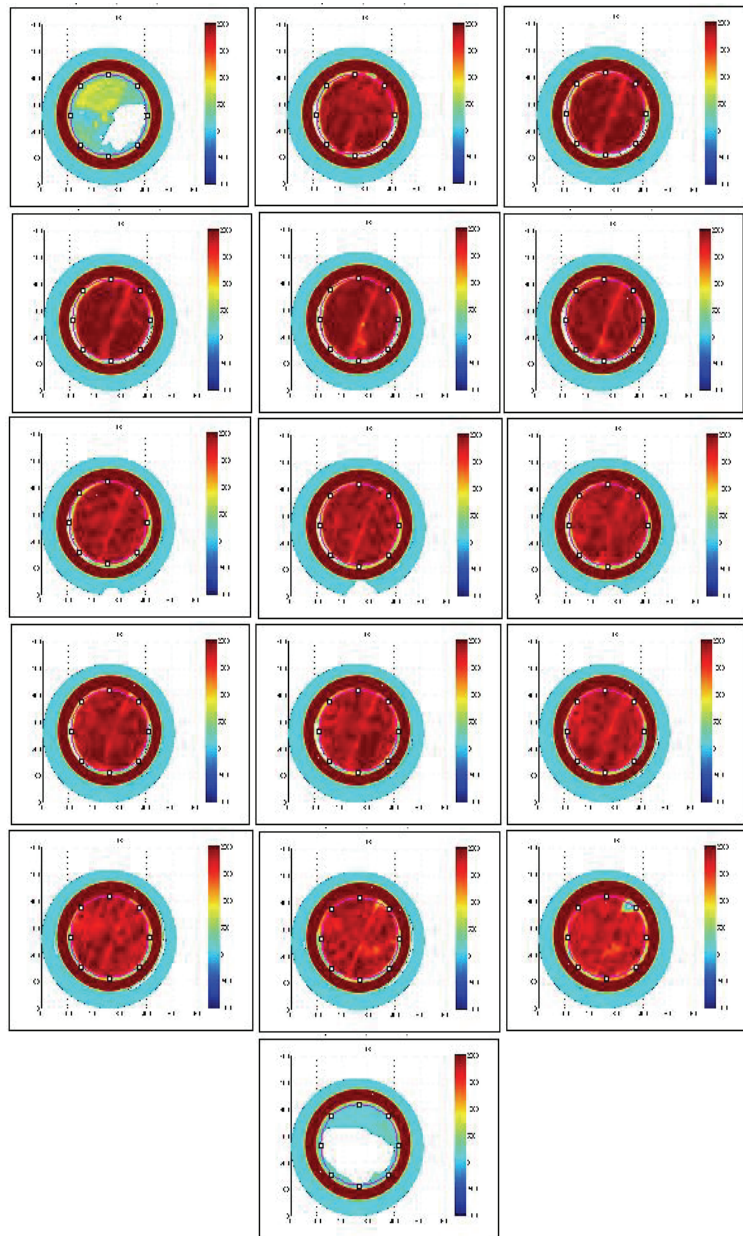


**Figure D.5** CT Slice Views of Artificially Fractured Core#7 Polymer Gel Injected then Produced.

**Initially Water Saturated Decane Flooded Artificially Fractured CT Numbers of Core#7**

**Table D.13** CT Numbers of Slices for Core#7 Porosity Calculation.

Porosity	area	mean	CT#	7af1	area	water	CT#	fraction
7af0 dry								
1	40,258	195,133	50	1	40,258	204,117	-70	
2	40,258	133,002	1,056	2	40,258	80,570	1,370	0.3145
3	40,258	134,323	1,050	3	40,258	80,539	1,371	0.3209
4	40,258	135,310	1,046	4	40,258	81,655	1,370	0.3240
5	40,258	135,260	1,046	5	40,258	82,859	1,369	0.3228
6	40,258	131,889	1,060	6	40,258	78,140	1,371	0.3109
7	40,258	132,634	1,057	7	40,258	79,406	1,373	0.3160
8	40,258	133,829	1,052	8	40,258	79,664	1,373	0.3209
9	40,258	133,260	1,054	9	40,258	81,393	1,372	0.3175
10	40,258	135,267	1,046	10	40,258	83,201	1,373	0.3269
11	40,258	135,969	1,043	11	40,258	85,055	1,373	0.3298
12	40,258	134,160	1,051	12	40,258	84,065	1,372	0.3213
13	40,258	133,863	1,052	13	40,258	82,724	1,372	0.3200
14	40,258	134,737	1,048	14	40,258	84,938	1,371	0.3227
15	40,258	136,028	1,043	15	40,258	85,893	1,381	0.3384
16	40,258	243,090	0	16	40,258	229,592	50	
							<b>average <math>\Phi</math></b>	<b>32.14%</b>

**Table D.14** CT Numbers of Slices for Core#7 Saturation Calculation.

Saturation	area	100 % water saturated mean	CT#	7afd1	area	100 % decane saturated mean	CT#
7afw0							
1	40,258	204,117	-70	1	40,258	172,707	630
2	40,258	80,570	1,370	2	40,258	102,303	1,185
3	40,258	80,539	1,371	3	40,258	96,68	1,215
4	40,258	81,655	1,370	4	40,258	98,655	1,204
5	40,258	82,859	1,369	5	40,258	99,409	1,200
6	40,258	78,14	1,371	6	40,258	99,947	1,197
7	40,258	79,406	1,373	7	40,258	99,439	1,200
8	40,258	79,664	1,373	8	40,258	99,354	1,201
9	40,258	81,393	1,372	9	40,258	96,924	1,214
10	40,258	83,201	1,373	10	40,258	97,069	1,213
11	40,258	85,055	1,373	11	40,258	97,784	1,209
12	40,258	84,065	1,372	12	40,258	98,440	1,205
13	40,258	82,724	1,372	13	40,258	101,023	1,192
14	40,258	84,938	1,371	14	40,258	98,520	1,205
15	40,258	85,893	1,381	15	40,258	99,039	1,202
16	40,258	229,592	1,100	16	40,258	173,334	631

**Table D.15** CT Numbers of Slices for Core#7 Saturation Calculation.

<b>7afwd1</b>	<b>area</b>	<b>decane after water mean</b>	<b>CT#</b>	<b>saturation Sw</b>	<b>saturation Sb</b>
1	40,258	190,462	-11		
2	40,258	67,338	1,259	40%	60%
3	40,258	61,774	1,249	22%	78%
4	40,258	62,950	1,267	38%	62%
5	40,258	63,594	1,257	34%	66%
6	40,258	63,098	1,264	39%	61%
7	40,258	66,680	1,276	44%	56%
8	40,258	65,031	1,297	35%	65%
9	40,258	66,303	1,277	40%	60%
10	40,258	64,775	1,300	38%	62%
11	40,258	65,540	1,297	51%	49%
12	40,258	68,379	1,289	50%	50%
13	40,258	69,054	1,287	43%	57%
14	40,258	69,789	1,288	50%	50%
15	40,258	76,669	1,204	51%	49%
16	40,258	169,473	400		
				<b>41.00%</b>	<b>59.00%</b>

**Table D.16** CT Numbers of Slices for Core#7 Saturation Calculation.

7afwd2	area	water after decane mean	CT#	saturation Sw	saturation S <sub>D</sub>
1	40,258	218,127	650		
2	40,258	76,305	1,220	100%	0%
3	40,258	73,931	1,240	75%	25%
4	40,258	76,222	1,220	64%	36%
5	40,258	77,578	1,208	88%	12%
6	40,258	76,527	1,218	66%	34%
7	40,258	73,950	1,240	48%	52%
8	40,258	72,232	1,255	46%	54%
9	40,258	74,173	1,238	70%	30%
10	40,258	72,061	1,257	31%	69%
11	40,258	71,703	1,260	44%	56%
12	40,258	72,665	1,252	49%	51%
13	40,258	71,870	1,259	45%	55%
14	40,258	72,376	1,254	44%	56%
15	40,258	80,512	1,183	45%	55%
16	40,258	239,973	450		
				<b>58.30%</b>	<b>41.70%</b>

**Table D.17** CT Numbers of Slices for Core#7 Saturation Calculation after Gel Injection and Production.

7afwdwg	area	water after decane mean	CT#	saturation Sw	saturation Sp
1	40,258	200,922	-100		
2	40,258	75,676	1,305	65%	35%
3	40,258	77,115	1,362	94%	6%
4	40,258	74,634	1,350	88%	12%
5	40,258	75,959	1,343	85%	15%
6	40,258	74,988	1,349	87%	13%
7	40,258	73,435	1,312	65%	35%
8	40,258	70,556	1,329	74%	26%
9	40,258	73,307	1,316	64%	36%
10	40,258	70,252	1,331	74%	26%
11	40,258	70,678	1,323	70%	30%
12	40,258	71,743	1,294	53%	47%
13	40,258	71,916	1,287	53%	47%
14	40,258	71,839	1,280	45%	55%
15	40,258	83,119	1,209	60%	40%
16	40,258	242,565	1,120		
				<b>65.82%</b>	<b>34.18%</b>

**Initially Water Saturated Decane Flooded Artificially Fractured CT Numbers of Core#7 Left Matrix**

**Table D.18** CT Numbers of Slices for Core#7 Porosity Calculation.

Porosity	area	dry mean	CT#	7lmw2	area	100 % water saturated mean	CT#	fraction
7lm1 dry	40,258	213,168	-11	1	40,258	214,062	-10	
1	17,250	122,002	1,158	2	17,250	74,825	1,453	0.2958
2	17,250	123,323	1,152	3	17,250	71,091	1,503	0.3508
3	17,250	124,310	1,148	4	17,250	71,806	1,493	0.3454
4	17,250	124,260	1,148	5	17,250	71,984	1,491	0.3428
5	17,250	120,889	1,162	6	17,250	72,622	1,483	0.3204
6	17,250	121,634	1,159	7	17,250	73,214	1,475	0.3157
7	17,250	122,829	1,154	8	17,250	74,319	1,460	0.3060
8	17,250	122,260	1,156	9	17,250	73,722	1,468	0.3115
9	17,250	124,267	1,148	10	17,250	72,770	1,481	0.3324
10	17,250	124,969	1,145	11	17,250	76,808	1,427	0.2819
11	17,250	123,160	1,153	12	17,250	70,434	1,512	0.3588
12	17,250	122,863	1,154	13	17,250	70,898	1,505	0.3514
13	17,250	123,737	1,150	14	17,250	69,389	1,525	0.3750
14	17,250	125,028	1,145	15	17,250	82,631	1,350	0.2050
15	40,258	218,805	-1	16	40,258	218,494	1,100	
16							<b>average <math>\Phi</math></b>	<b>32.09%</b>

**Table D.19** CT Numbers of Slices for Core#7 Saturation Calculation.

Saturation	area	100 % water saturated mean	CT#	7lmd2	area	100 % decane saturated mean	CT#
7lmw1							
1	40,258	214,062	-10	1	40,258	172,707	630
2	17,250	74,825	1453	2	17,250	102,303	1,185
3	17,250	71,091	1503	3	17,250	96,680	1,215
4	17,250	71,806	1493	4	17,250	98,655	1,204
5	17,250	71,984	1491	5	17,250	99,409	1,200
6	17,250	72,622	1483	6	17,250	99,947	1,197
7	17,250	73,214	1475	7	17,250	99,439	1,200
8	17,250	74,319	1460	8	17,250	99,354	1,201
9	17,250	73,722	1468	9	17,250	96,924	1,214
10	17,250	72,770	1481	10	17,250	97,069	1,213
11	17,250	76,808	1427	11	17,250	97,784	1,209
12	17,250	70,434	1512	12	17,250	98,440	1,205
13	17,250	70,898	1505	13	17,250	101,023	1,192
14	17,250	69,389	1525	14	17,250	98,520	1,205
15	17,250	82,631	1350	15	17,250	99,039	1,202
16	40,258	218,494	1100	16	40,258	173,334	631

**Table D.20** CT Numbers of Slices for Core#7 Saturation Calculation.

7Imwd2	area	decane after water mean	CT#	saturation Sw	saturation Sb
1	40,258	190,362	-11		
2	17,250	66,838	1,293	40%	60%
3	17,250	61,274	1,274	21%	79%
4	17,250	62,450	1,306	35%	65%
5	17,250	63,094	1,289	31%	69%
6	17,250	62,598	1,302	37%	63%
7	17,250	66,180	1,322	44%	56%
8	17,250	64,531	1,359	61%	39%
9	17,250	65,803	1,323	43%	57%
10	17,250	64,275	1,363	56%	44%
11	17,250	65,040	1,357	68%	32%
12	17,250	67,879	1,344	45%	55%
13	17,250	68,554	1,341	48%	52%
14	17,250	69,289	1,342	43%	57%
15	17,250	76,169	1,210	5%	95%
16	40,258	216,568	50		
				<b>41.18%</b>	<b>58.82%</b>

**Table D.21** CT Numbers of Slices for Core#7 Saturation Calculation.

7lmwd2	area	water after decane mean	CT#	saturation Sw	saturation Sb
1	40,258	218,127	650		
2	17,250	77,405	1,237	100%	0%
3	17,250	75,031	1,258	45%	55%
4	17,250	77,322	1,238	52%	48%
5	17,250	78,678	1,226	76%	24%
6	17,250	77,627	1,235	59%	41%
7	17,250	75,050	1,258	43%	57%
8	17,250	73,332	1,273	40%	60%
9	17,250	75,273	1,256	71%	29%
10	17,250	73,161	1,274	75%	25%
11	17,250	72,803	1,278	55%	45%
12	17,250	73,765	1,269	58%	42%
13	17,250	72,970	1,276	44%	56%
14	17,250	73,476	1,272	51%	49%
15	17,250	81,612	1,200	80%	20%
16	40,258	239,973	450		
				<b>60.73%</b>	<b>39.27%</b>

**Table D.22** CT Numbers of Slices for Core#7 Saturation Calculation after Gel Injection and Production.

7lmmwdwg	area	water after decane and gel mean	CT#	saturation Sw	saturation Sp
1	40,258	200,922	-100		
2	17,250	75,276	1,369	69%	31%
3	17,250	76,715	1,452	82%	18%
4	17,250	74,234	1,434	80%	20%
5	17,250	75,559	1,425	77%	23%
6	17,250	74,588	1,432	82%	18%
7	17,250	73,035	1,379	65%	35%
8	17,250	70,156	1,403	78%	22%
9	17,250	72,907	1,384	67%	33%
10	17,250	69,852	1,407	73%	27%
11	17,250	70,278	1,396	100%	0%
12	17,250	71,343	1,353	48%	52%
13	17,250	71,516	1,343	48%	52%
14	17,250	71,439	1,332	40%	60%
15	17,250	81,719	1,230	19%	81%
16	40,258	242,565	1,120		
				<b>66.30%</b>	<b>33.70%</b>

**Initially Water Saturated Decane Flooded Artificially Fractured CT Numbers of Core#7 Right Matrix**

**Table D.23** CT Numbers of Slices for Core#7 Porosity Calculation.

Porosity	area	dry mean	CT#	7rm1	area	100 % water saturated mean	CT#	fraction
7rm0 dry								
1	40,258	213,168	-10	1	40,258	214,062	-10	
2	17,250	125,002	1,163	2	17,250	77,536	1,431	0.2680
3	17,250	126,323	1,157	3	17,250	71,920	1,491	0.3335
4	17,250	127,310	1,153	4	17,250	72,644	1,483	0.3298
5	17,250	127,260	1,153	5	17,250	75,928	1,448	0.2945
6	17,250	123,889	1,167	6	17,250	73,648	1,472	0.3049
7	17,250	124,634	1,164	7	17,250	72,000	1,490	0.3256
8	17,250	125,829	1,159	8	17,250	68,813	1,524	0.3646
9	17,250	125,260	1,161	9	17,250	73,110	1,478	0.3164
10	17,250	127,267	1,153	10	17,250	70,339	1,507	0.3543
11	17,250	127,969	1,150	11	17,250	65,718	1,557	0.4065
12	17,250	126,160	1,158	12	17,250	71,540	1,495	0.3369
13	17,250	125,863	1,159	13	17,250	70,936	1,501	0.3421
14	17,250	126,737	1,155	14	17,250	73,835	1,470	0.3147
15	17,250	128,028	1,150	15	17,250	86,200	1,338	0.1880
16	40,258	218,805	0	16	40,258	218,494	0	
							<b>average <math>\Phi</math></b>	<b>32.00%</b>

**Table D.24** CT Numbers of Slices for Core#7 Saturation Calculation.

Saturation	area	100 % water saturated mean	CT#	7rmdI	area	100 % decane saturated mean	CT#
7rmdI	area	100 % water saturated mean	CT#	7rmdI	area	100 % decane saturated mean	CT#
1	40,258	214,062	-10	1	40,258	172,707	630
2	17,250	77,536	1,431	2	40,258	102,303	1,185
3	17,250	71,920	1,491	3	40,258	96,680	1,215
4	17,250	72,644	1,483	4	40,258	98,655	1,204
5	17,250	75,928	1,448	5	40,258	99,409	1,200
6	17,250	73,648	1,472	6	40,258	99,947	1,197
7	17,250	72,000	1,490	7	40,258	99,439	1,200
8	17,250	68,813	1,524	8	40,258	99,354	1,201
9	17,250	73,110	1,478	9	40,258	96,924	1,214
10	17,250	70,339	1,507	10	40,258	97,069	1,213
11	17,250	65,718	1,557	11	40,258	97,784	1,209
12	17,250	71,540	1,495	12	40,258	98,440	1,205
13	17,250	70,936	1,501	13	40,258	101,023	1,192
14	17,250	73,835	1,470	14	40,258	98,52	1,205
15	17,250	86,200	1,338	15	40,258	99,039	1,202
16	40,258	218,494	1,100	16	40,258	173,334	631

**Table D.25** CT Numbers of Slices for Core#7 Saturation Calculation.

7rmwd2	area	decane after water mean	CT#	saturation Sw	saturation Sp
1	40,258	190,462	-11		
2	17,250	66,338	1,296	45%	55%
3	17,250	60,774	1,279	23%	77%
4	17,250	61,950	1,309	38%	62%
5	17,250	62,594	1,293	37%	63%
6	17,250	62,098	1,305	39%	61%
7	17,250	65,680	1,323	42%	58%
8	17,250	64,031	1,357	48%	52%
9	17,250	65,303	1,325	42%	58%
10	17,250	63,775	1,361	50%	50%
11	17,250	64,540	1,356	42%	58%
12	17,250	67,379	1,343	48%	52%
13	17,250	68,054	1,341	48%	52%
14	17,250	68,789	1,342	52%	48%
15	17,250	75,669	1,220	13%	87%
16	40,258	216,568	50		
				<b>40.63%</b>	<b>59.37%</b>

**Table D.26** CT Numbers of Slices for Core#7 Saturation Calculation.

<b>7rmwd2</b>	<b>area</b>	<b>water after decane mean</b>	<b>CT#</b>	<b>saturation Sw</b>	<b>saturation Sp</b>
1	40,258	218,127	650		
2	17,250	78,505	1,237	100%	0%
3	17,250	76,131	1,258	47%	53%
4	17,250	78,422	1,238	55%	45%
5	17,250	79,778	1,226	76%	24%
6	17,250	78,727	1,235	61%	39%
7	17,250	76,150	1,258	45%	55%
8	17,250	74,432	1,273	41%	59%
9	17,250	76,373	1,256	71%	29%
10	17,250	74,261	1,274	45%	55%
11	17,250	73,903	1,278	55%	45%
12	17,250	74,865	1,269	58%	42%
13	17,250	74,070	1,276	44%	56%
14	17,250	74,576	1,272	51%	49%
15	17,250	82,712	1,200	100%	0%
16	40,258	239,973	450		
				<b>60.92%</b>	<b>39.08%</b>

**Table D.27** CT Numbers of Slices for Core#7 Saturation Calculation after Gel Injection and Production.

7rmwdwg	area	water after decane and gel mean	CT#	saturation S <sub>w</sub>	saturation S <sub>p</sub>
1	40,258	200,922	-100		
2	17,250	74,876	1,374	77%	23%
3	17,250	76,315	1,457	88%	12%
4	17,250	73,834	1,439	84%	16%
5	17,250	75,159	1,430	93%	7%
6	17,250	74,188	1,437	87%	13%
7	17,250	72,635	1,384	63%	37%
8	17,250	69,756	1,408	64%	36%
9	17,250	72,507	1,389	67%	33%
10	17,250	69,452	1,412	68%	32%
11	17,250	69,878	1,401	100%	0%
12	17,250	70,943	1,358	53%	47%
13	17,250	71,116	1,348	51%	49%
14	17,250	71,039	1,337	50%	50%
15	17,250	81,319	1,235	24%	76%
16	40,258	242,565	1,120		
				<b>69.19%</b>	<b>30.81%</b>

**Initially Water Saturated Decane Flooded CT Scan Images of Core#5**

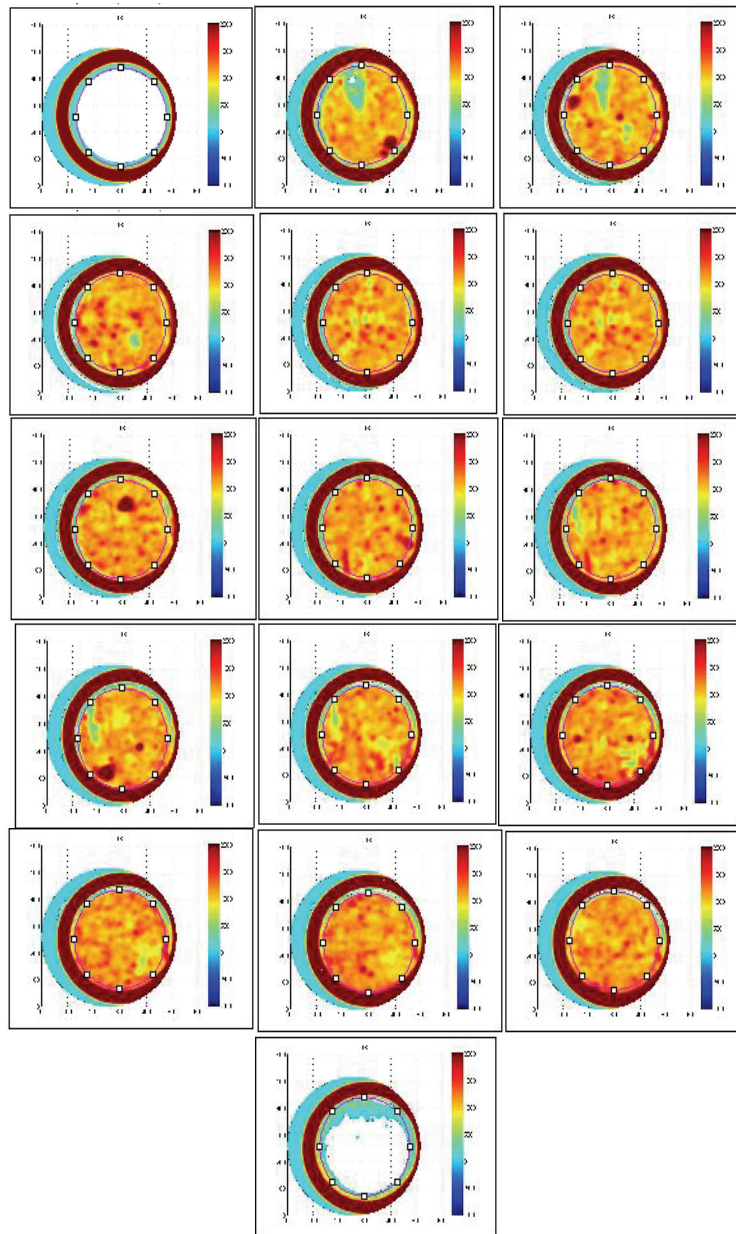


**Figure D.6** CT Slice Views of Core#5 Dry.

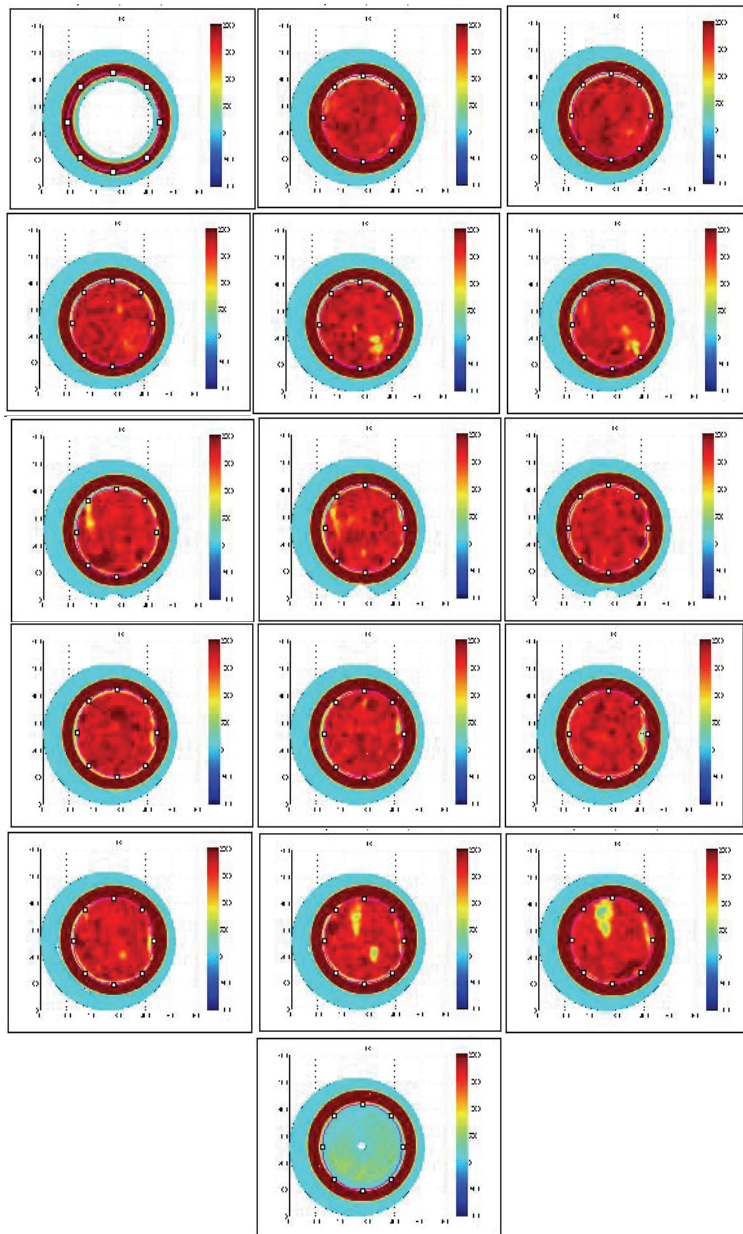


**Figure D.7** CT Slice Views of Core#5 Water Saturated.

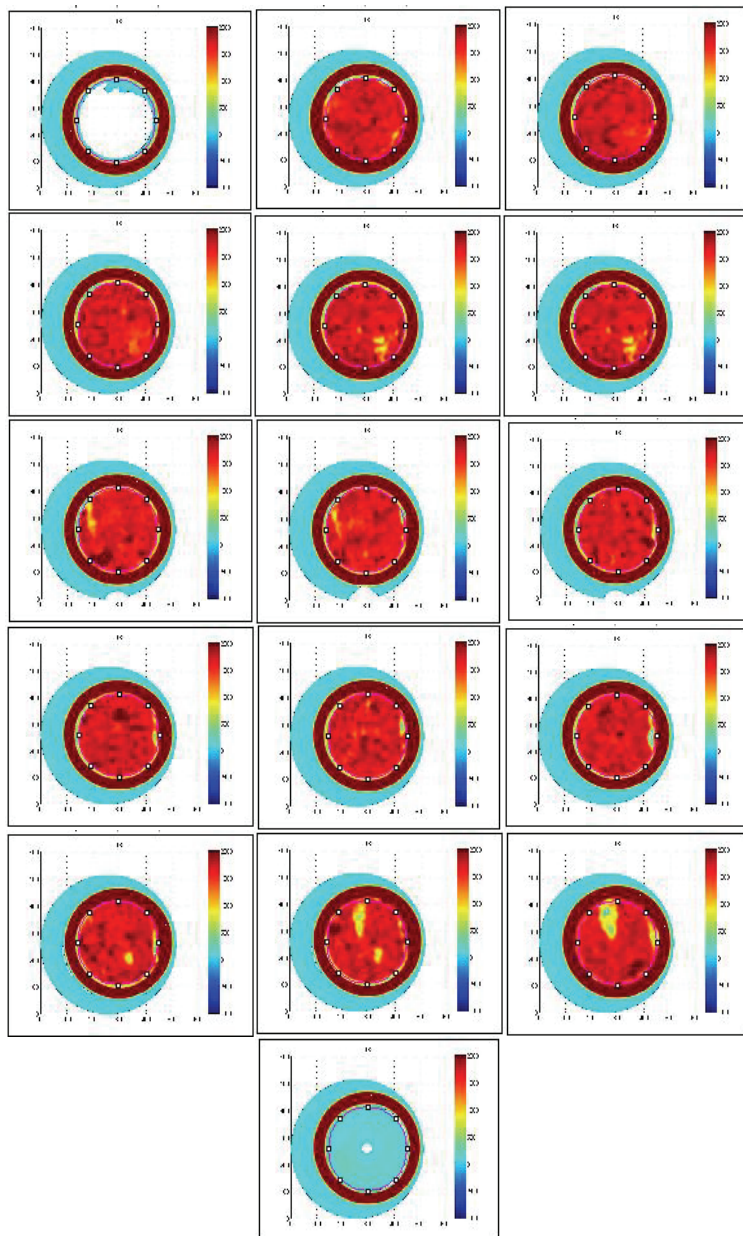


**Figure D.8** CT Slice Views of Core#5 Before Production.

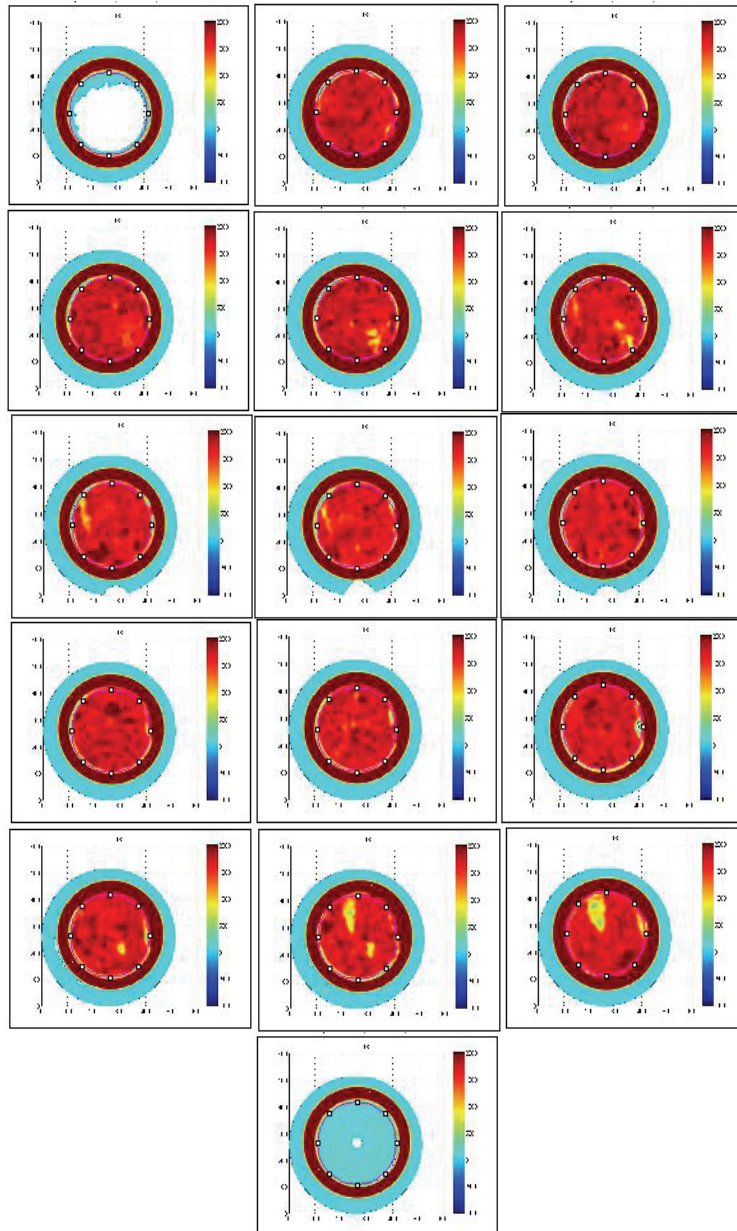


**Figure D.9** CT Slice Views of Core#5 After Production.

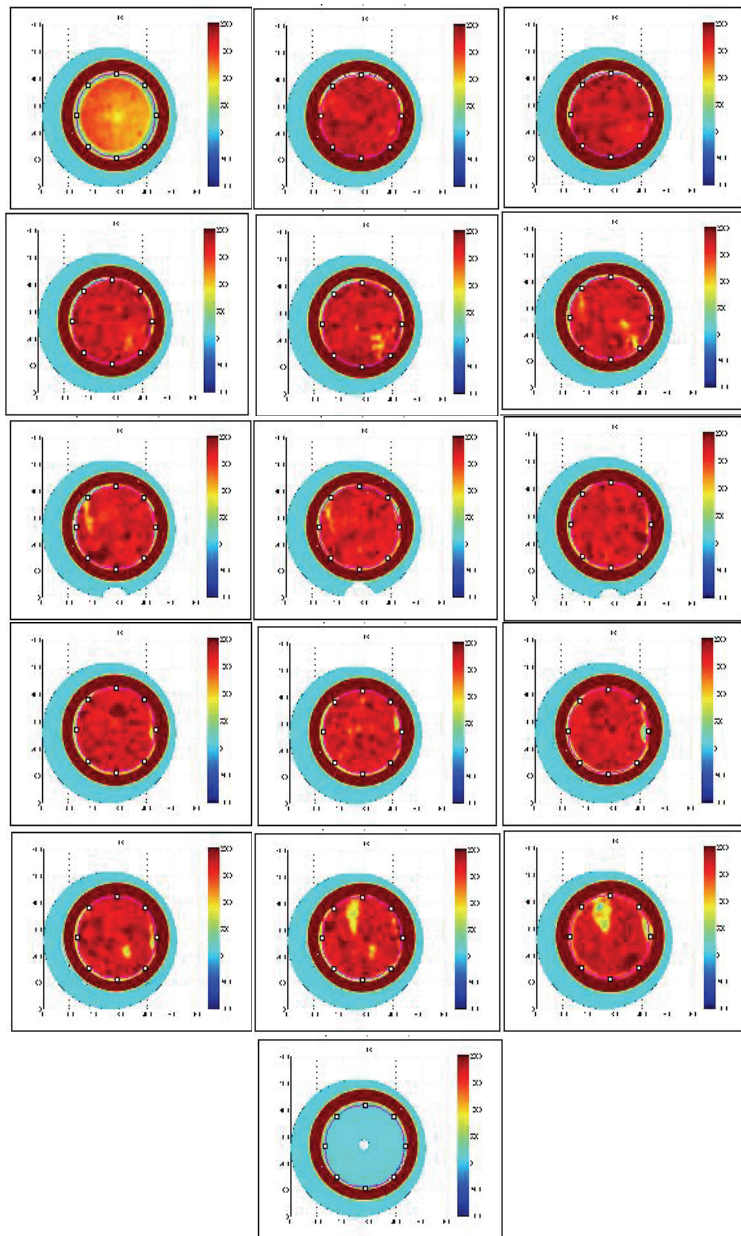


Figure D.10 CT Slice Views of Core#5 After Polymer Gel Injection.

**Initially Water Saturated Decane Flooded CT Numbers of Core#5**

**Table D.28** CT Numbers of Slices for Core#5 Porosity Calculation.

Porosity	area	dry mean	CT#	52	area	100 % water saturated mean	CT#	Fraction
51dry								
1	40,260	239,878	50	1	40,260	200,023	-5	
2	40,260	144,736	1,006	2	40,260	78,932	1,357	0.3505
3	40,260	138,696	1,053	3	40,260	75,796	1,390	0.3372
4	40,260	139,651	1,045	4	40,260	75,594	1,392	0.3467
5	40,260	139,461	1,047	5	40,260	77,313	1,374	0.3270
6	40,260	137,574	1,061	6	40,260	78,642	1,360	0.2983
7	40,260	141,764	1,029	7	40,260	79,168	1,354	0.3250
8	40,260	134,769	1,083	8	40,260	82,793	1,316	0.2326
9	40,260	135,619	1,076	9	40,260	78,836	1,358	0.2811
10	40,260	136,543	1,069	10	40,260	75,317	1,395	0.3256
11	40,260	137,359	1,063	11	40,260	77,415	1,373	0.3097
12	40,260	141,832	1,029	12	40,260	80,118	1,344	0.3155
13	40,260	143,705	1,014	13	40,260	81,311	1,331	0.3173
14	40,260	140,242	1,041	14	40,260	86,073	1,281	0.2400
15	40,260	142,485	1,023	15	40,260	86,211	1,279	0.2558
16	40,260	170,984	360	16	40,260	169,692	1,100	
							<b>average <math>\Phi</math></b>	<b>30.44%</b>

**Table D.29** CT Numbers of Slices for Core#5 Saturation Calculation.

Saturation	area	100 % water saturated mean	CT#	5d2	area	100 % decane saturated mean	CT#
Sw1	40,260	200,023	-5	1	40,260	172,707	630
1	40,260	78,932	1,357	2	40,260	102,303	1,110
2	40,260	75,796	1,390	3	40,260	96,68	1,140
3	40,260	75,594	1,392	4	40,260	98,655	1,129
4	40,260	77,313	1,374	5	40,260	99,409	1,125
5	40,260	78,642	1,360	6	40,260	99,947	1,122
6	40,260	79,168	1,354	7	40,260	99,439	1,125
7	40,260	82,793	1,316	8	40,260	99,354	1,126
8	40,260	78,836	1,358	9	40,260	96,924	1,139
9	40,260	75,317	1,395	10	40,260	97,069	1,138
10	40,260	77,415	1,373	11	40,260	97,784	1,134
11	40,260	80,118	1,344	12	40,260	98,440	1,130
12	40,260	81,311	1,331	13	40,260	101,023	1,117
13	40,260	86,073	1,281	14	40,260	98,520	1,130
14	40,260	86,211	1,279	15	40,260	99,039	1,127
15	40,260	169,692	1,100	16	40,260	173,334	631

**Table D.30** Saturation Calculation of CT Numbers of Slices for Core#5 Before Production.

<b>Swd2</b>	<b>area</b>	<b>decane after water mean</b>	<b>CT#</b>	<b>saturation Sw</b>	<b>saturation Sb</b>
1	40,260	233,190	-5		
2	40,260	80,131	1,233	50%	50%
3	40,260	77,839	1,261	48%	52%
4	40,260	78,449	1,254	47%	53%
5	40,260	79,984	1,235	44%	56%
6	40,260	83,852	1,188	27%	73%
7	40,260	82,994	1,198	32%	68%
8	40,260	84,748	1,177	27%	73%
9	40,260	79,229	1,244	48%	52%
10	40,260	77,022	1,271	52%	48%
11	40,260	79,848	1,237	43%	57%
12	40,260	80,709	1,226	45%	55%
13	40,260	79,984	1,235	55%	45%
14	40,260	83,852	1,188	38%	62%
15	40,260	82,994	1,198	47%	53%
16	40,260	170,112	350		
				<b>43.12%</b>	<b>56.88%</b>

**Table D.31** Saturation Calculation of CT Numbers of Slices for Core#5 After Production.

<b>5wdw</b>	<b>area</b>	<b>water after decane mean</b>	<b>CT#</b>	<b>saturation Sw</b>	<b>saturation S<sub>D</sub></b>
1	40,260	228,446	-5		
2	40,260	76,940	1,334	91%	9%
3	40,260	71,325	1,426	100%	0%
4	40,260	73,766	1,386	98%	2%
5	40,260	76,293	1,345	88%	12%
6	40,260	80,518	1,276	65%	35%
7	40,260	80,478	1,277	66%	34%
8	40,260	81,673	1,257	69%	31%
9	40,260	78,260	1,313	80%	20%
10	40,260	76,478	1,347	81%	19%
11	40,260	80,938	1,269	57%	43%
12	40,260	80,646	1,274	67%	33%
13	40,260	80,083	1,283	78%	22%
14	40,260	86,608	1,177	31%	69%
15	40,260	87,771	1,158	20%	80%
16	40,260	170,300	350		
				<b>70.75%</b>	<b>29.25%</b>

**Table D.32** Saturation Calculation of CT Numbers of Slices for Core#5 After Polymer Gel Injection.

<b>Swdwtg</b>	<b>area</b>	<b>water after decane and gel mean</b>	<b>CT#</b>	<b>saturation Sw</b>	<b>saturation Sw</b>
1	40,260	137,057	985		
2	40,260	74,896	1,352	90%	10%
3	40,260	73,857	1,367	91%	9%
4	40,260	75,539	1,343	81%	19%
5	40,260	74,992	1,351	91%	9%
6	40,260	79,704	1,281	67%	33%
7	40,260	80,261	1,273	65%	35%
8	40,260	81,726	1,252	66%	34%
9	40,260	75,881	1,338	91%	9%
10	40,260	75,937	1,337	77%	23%
11	40,260	79,014	1,291	66%	34%
12	40,260	80,186	1,274	67%	33%
13	40,260	77,691	1,311	91%	9%
14	40,260	82,442	1,241	74%	26%
15	40,260	88,549	1,151	57%	43%
16	40,260	170,742	350		
				<b>76.69%</b>	<b>23.31%</b>

## APPENDIX-E

### CORE SAMPLE NUMERICAL POROSITY CALCULATION CODE BY MATLAB

```
infoDry = dicominfo('I:\NEW THESIS\experi data\sccore51\sccore5_11.dcm');  
infoWet = dicominfo('I:\NEW THESIS\experi data\sccore52\sccore52_11.dcm');
```

```
YDry = dicomread(infoDry);  
YDry_D = double(YDry);  
YDry_D1 = zeros(512,512);  
counter = 0;  
total = 0;  
for i = 1:512  
for j = 1:512  
if (YDry_D(i,j)<-1000 || YDry_D(i,j)>4000)  
YDry_D1(i,j) = NaN;  
elseif ((sqrt((i-256)^2+(j-256)^2)) > 180)  
YDry_D1(i,j) = NaN;  
else  
YDry_D1(i,j) = YDry_D(i,j);  
counter = counter + 1;  
total = total + YDry_D(i,j);  
end  
end  
end
```

```
Figure('Name','Dry');  
sDry = surf(YDry_D1, 'EdgeColor','none');  
averageDry = total/counter  
view(2);
```

```
%Figure('Name', 'DryImage')  
%imshow(YDry,[]);
```

```
YWet = dicomread(infoWet);  
YWet_D = double(YWet);  
YWet_D1 = zeros(512,512);  
counter = 0;  
total = 0;  
for i = 1:512  
for j = 1:512  
if (YWet_D(i,j)<-1000 || YWet_D(i,j)>4000)
```

```

        YWet_D1(i,j) = NaN;
elseif ((sqrt((i-256)^2+(j-256)^2)) > 180)

        YWet_D1(i,j) = NaN;
else
        YWet_D1(i,j) = YWet_D(i,j);
counter = counter + 1;
total = total + YWet_D(i,j);
end
end
end

Figure('Name','Wet');
sWet = surf(YWet_D1, 'EdgeColor','none');
averageWet = total/counter
view(2);

%Figure('Name', 'WetImage')
%imshow(YWet,[]);

Difference = (YWet_D1 - YDry_D1)/1000;

Figure('Name','Difference');
sDifference = surf(Difference, 'EdgeColor','none');
view(2);

porosity = (averageWet - averageDry)/1000

```

## EXECUTION RESULT

```
>>CTAnalyse
```

```
averageDry= 1.1026e+03
```

```
averageWet    = 1.4714e+03
```

```
porosity      = 0.3688
```

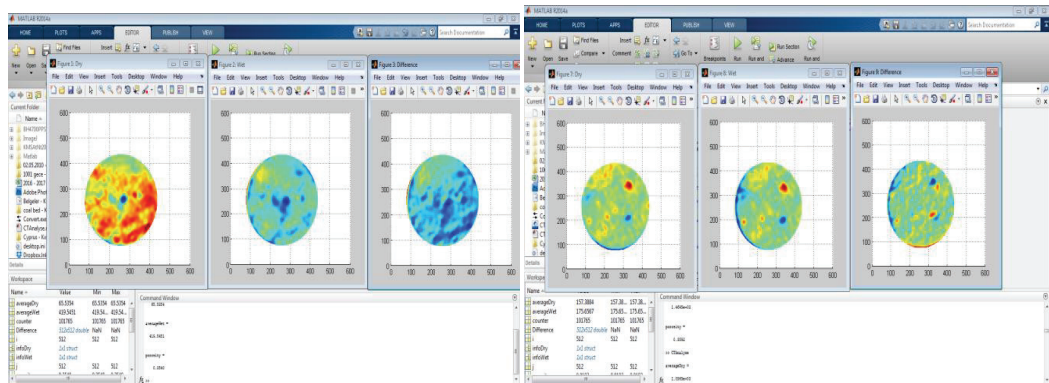


Figure E.1 Porosity Calculation of CT Slice Views of 0 and 3 for Core#2.

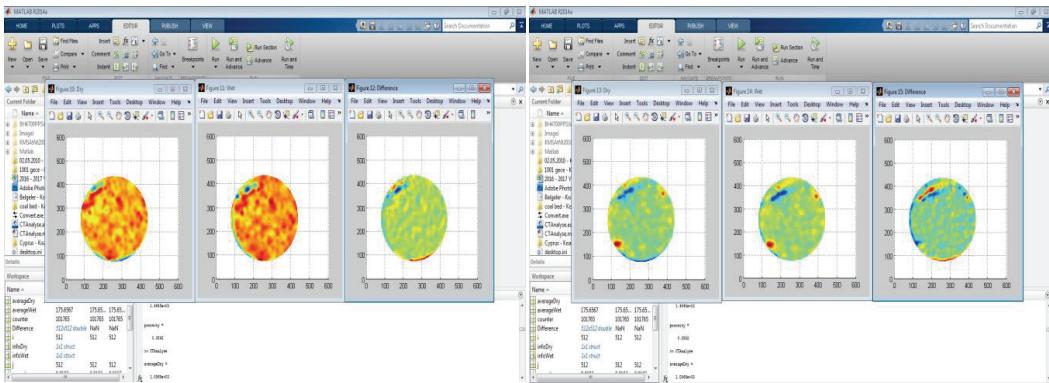


Figure E.2 Porosity Calculation of CT Slice Views of 4 and 5 for Core#2.

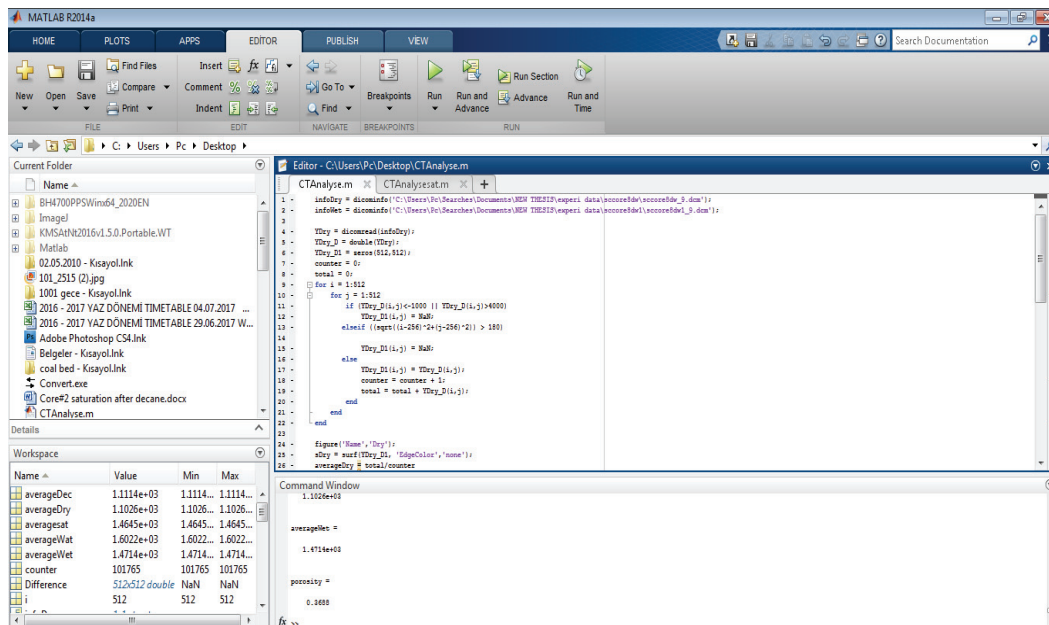
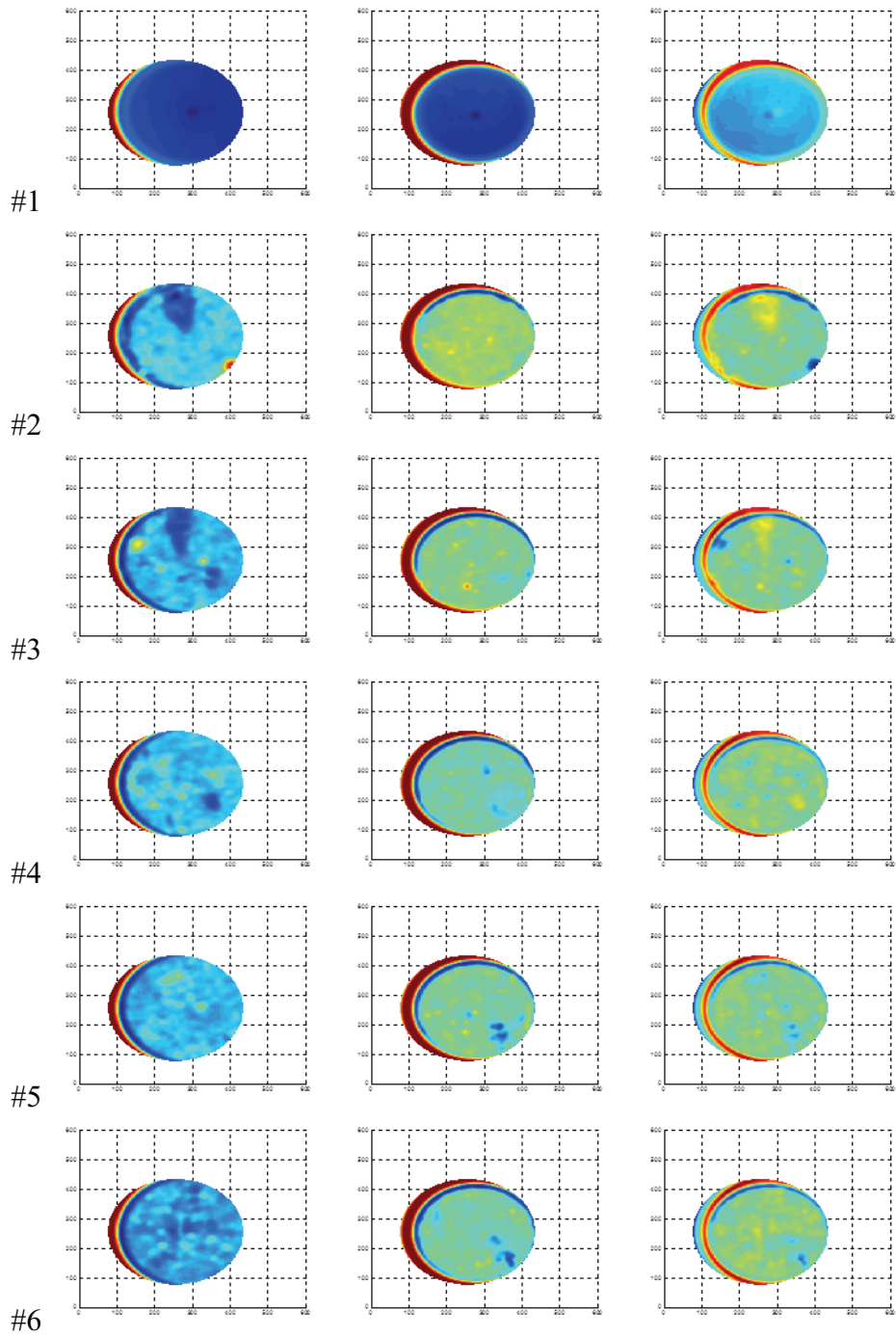
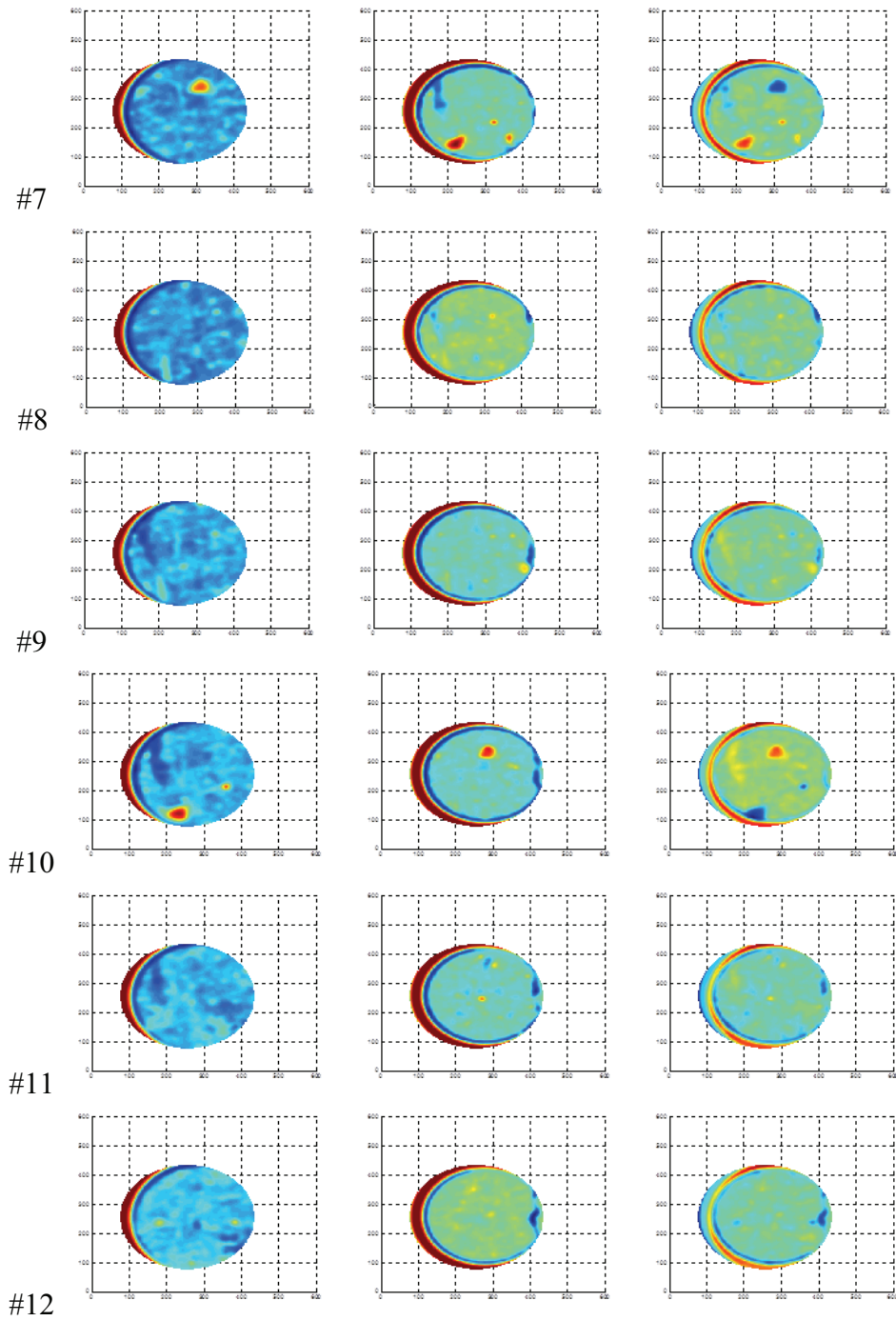


Figure E.3 Porosity Calculation Code of CT Slice Views of Core#2.



**Figure E.4** Porosity Calculation Code of CT Slice Views of Dry, Wet, Difference, for Core#5.



**Figure E.5** Porosity Calculation Code of CT Slice Views of Dry, Wet, Difference, for Core#5.

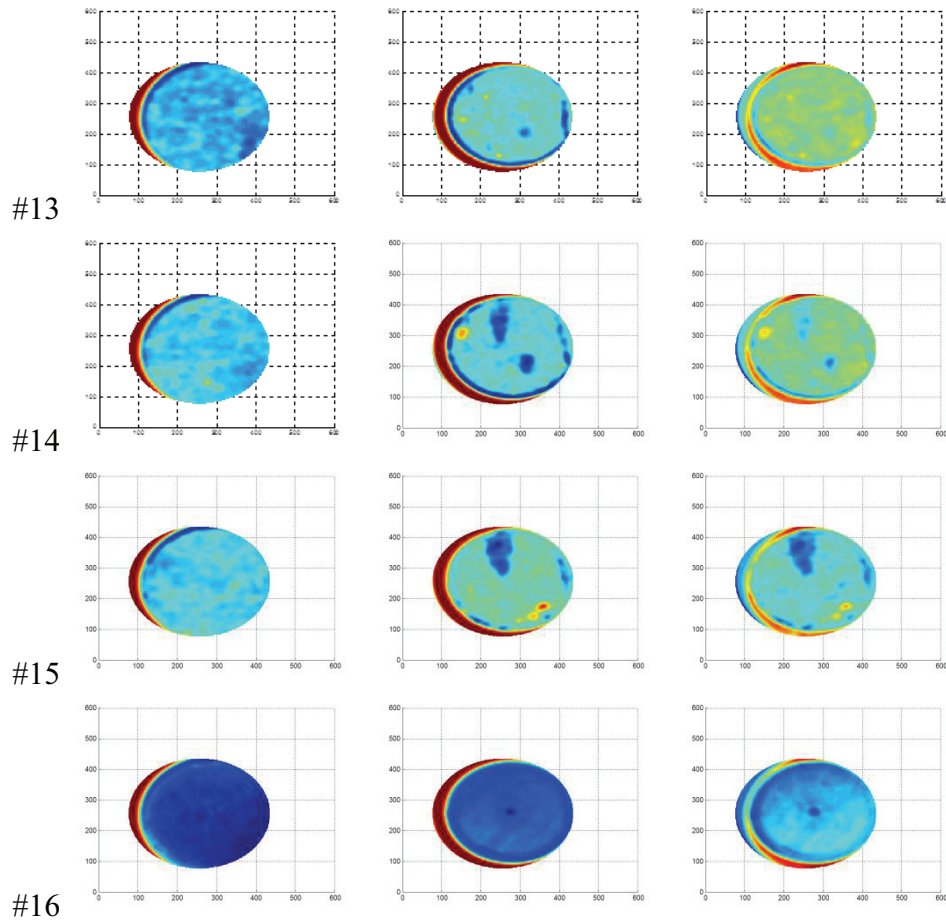


**Figure E.6** Porosity Calculation Code of CT Slice Views of Dry, Wet, Difference, for Core#5.

**CORE SAMPLE NUMERICAL SATURATION CALCULATION CODE  
BY MATLABFORCORE5 INITIAL SATURATIONS**

```

infosat = dicominfo('I:\NEW THESIS\thesis data\core#5\SC CORE 5WD\SC
CORE 5WD_15');
infoDec = dicominfo('I:\NEW THESIS\thesis data\core#2\SC CORE9-RD\SC
CORE9-RD_15.dcm');
infoWat = dicominfo('I:\NEW THESIS\thesis data\core#5\SC CORE 5W\SC
CORE 5W_15.dcm');

```

```

Ysat = dicomread(infosat);
Ysat_D = double(Ysat);
Ysat_D1 = zeros(512,512);
counter = 0;
total = 0;
for i = 1:512
for j = 1:512
if (Ysat_D(i,j)<-1000 || Ysat_D(i,j)>4000)
    Ysat_D1(i,j) = NaN;
elseif ((sqrt((i-256)^2+(j-256)^2)) > 180)

    Ysat_D1(i,j) = NaN;
else
    Ysat_D1(i,j) = Ysat_D(i,j);
    counter = counter + 1;
    total = total + Ysat_D(i,j);
end
end
end

```

```

Figure('Name','Sat');
ssat = surf(Ysat_D1, 'EdgeColor','none');
averagesat = total/counter
view(2);
%Figure('Name', 'satImage')
%imshow(Ysat,[]);
YDec = dicomread(infoDec);
YDec_D = double(YDec);
YDec_D1 = zeros(512,512);
counter = 0;
total = 0;
for i = 1:512
for j = 1:512
if (YDec_D(i,j)<-1000 || YDec_D(i,j)>4000)
    YDec_D1(i,j) = NaN;
elseif ((sqrt((i-256)^2+(j-256)^2)) > 180)

    YDec_D1(i,j) = NaN;
else

```

```

        YDec_D1(i,j) = YDec_D(i,j);
        counter = counter + 1;
        total = total + YDec_D(i,j);
end
end
end

Figure('Name','Dec');
ssat = surf(YDec_D1, 'EdgeColor','none');
averageDec = total/counter
view(2);

%Figure('Name', 'DecImage')
%imshow(YDec,[]);

YWat = dicomread(infoWat);
YWat_D = double(YWat);
YWat_D1 = zeros(512,512);
counter = 0;
total = 0;
for i = 1:512
for j = 1:512
if (YWat_D(i,j)<-1000 || YWat_D(i,j)>4000)
    YWat_D1(i,j) = NaN;
elseif ((sqrt((i-256)^2+(j-256)^2)) > 180)

    YWat_D1(i,j) = NaN;
else
    YWat_D1(i,j) = YWat_D(i,j);
    counter = counter + 1;
    total = total + YWat_D(i,j);
end
end
end

Figure('Name','Wat');
sWat = surf(YWat_D1, 'EdgeColor','none');
averageWat = total/counter
view(2);
%Figure('Name', 'WatImage')
%imshow(YWat,[]);
%Difference = (YWat_D1 - YDec_D1)/1000;
%Figure('Name','Difference');
%Difference = surf(Difference, 'EdgeColor','none');
%view(2);
saturation = (averagesat - averageDec)/(averageWat - averageDec)*10*4.6

```

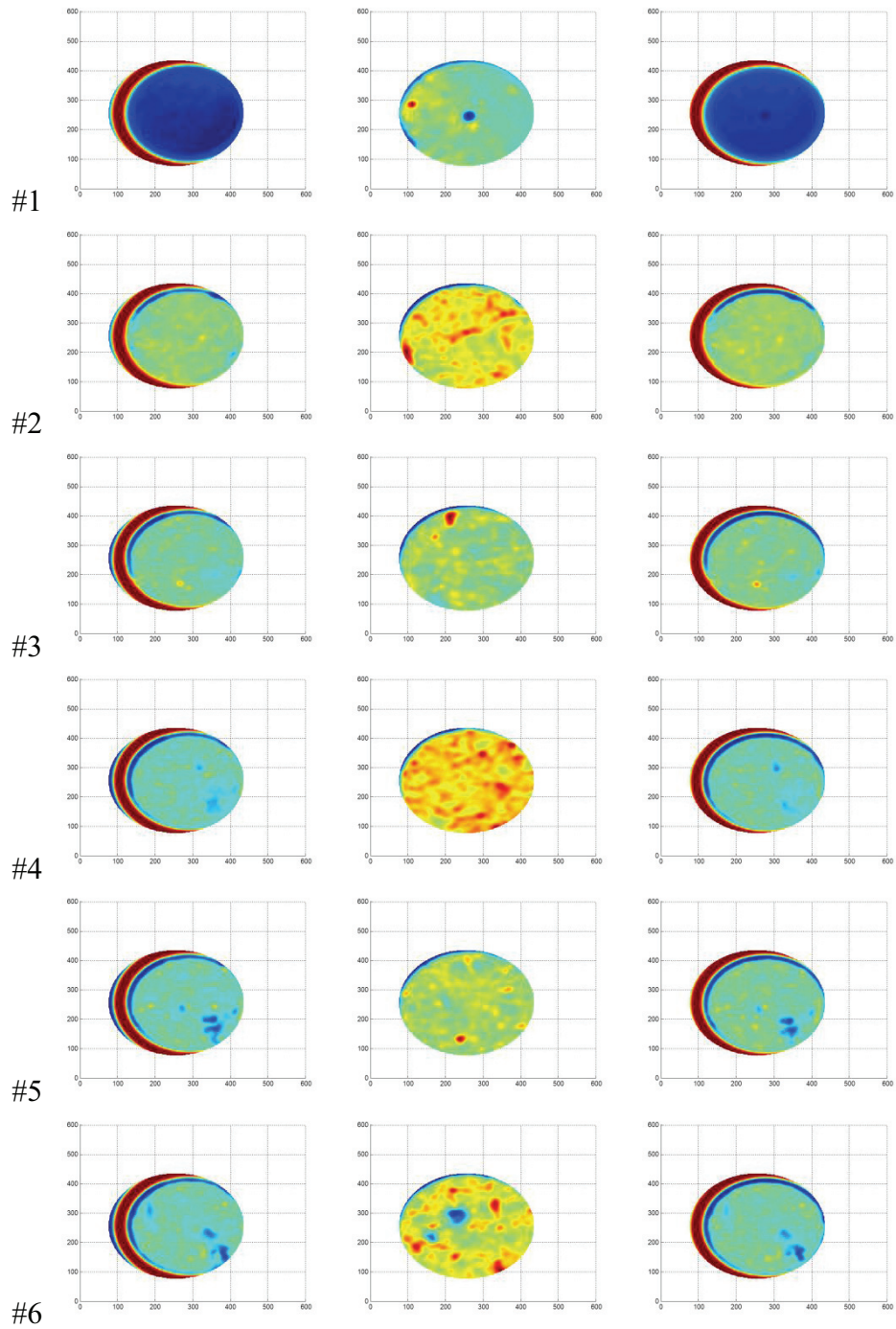


**Figure E.7** Saturation Calculation Code of CT Slice Views of Saturation (left), 100% Decane (center), 100% Water (right) for Core#5.

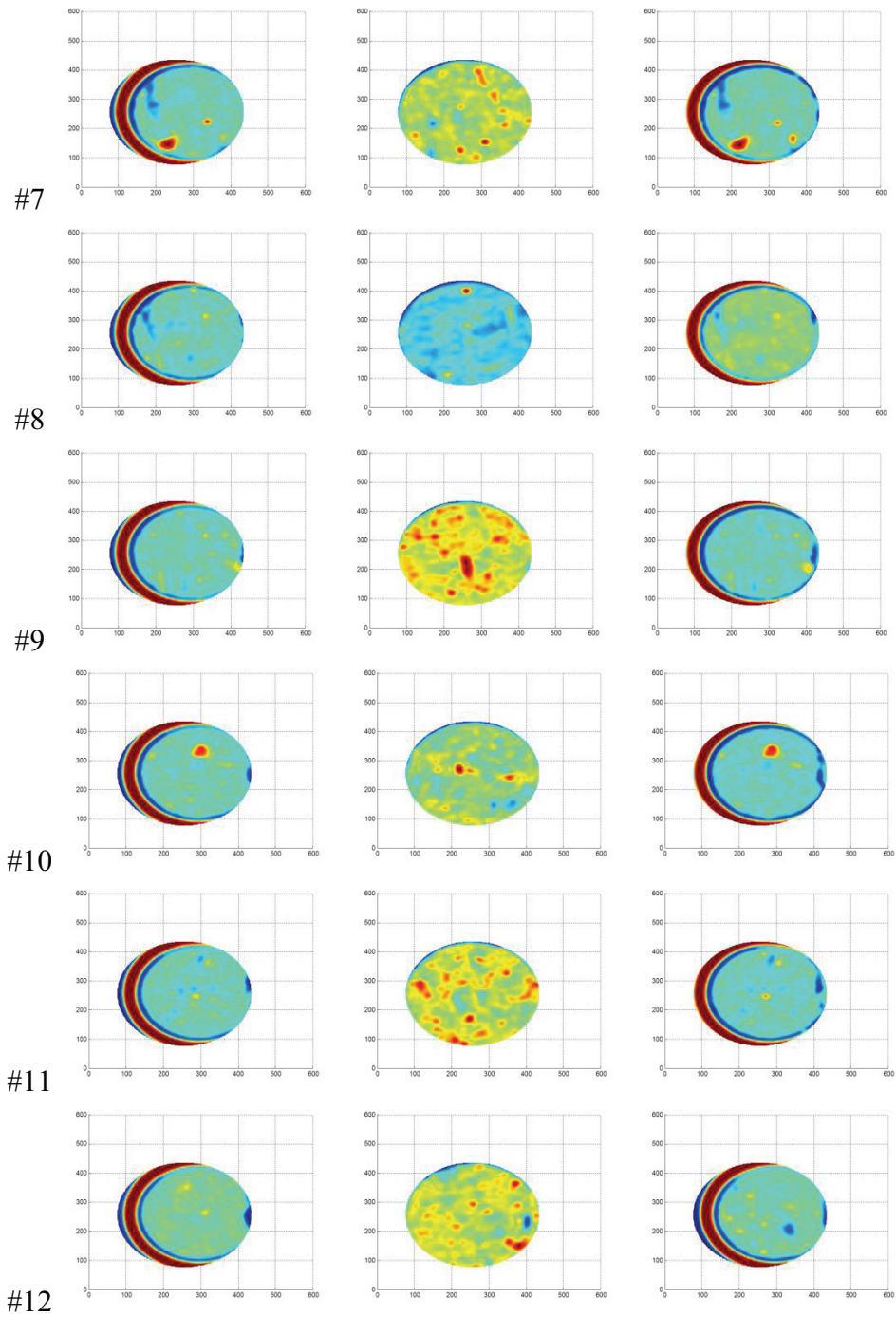


**Figure E.8** Saturation Calculation Code of CT Slice Views of Saturation (left), 100% Decane (center), 100% Water (right) for Core#5.

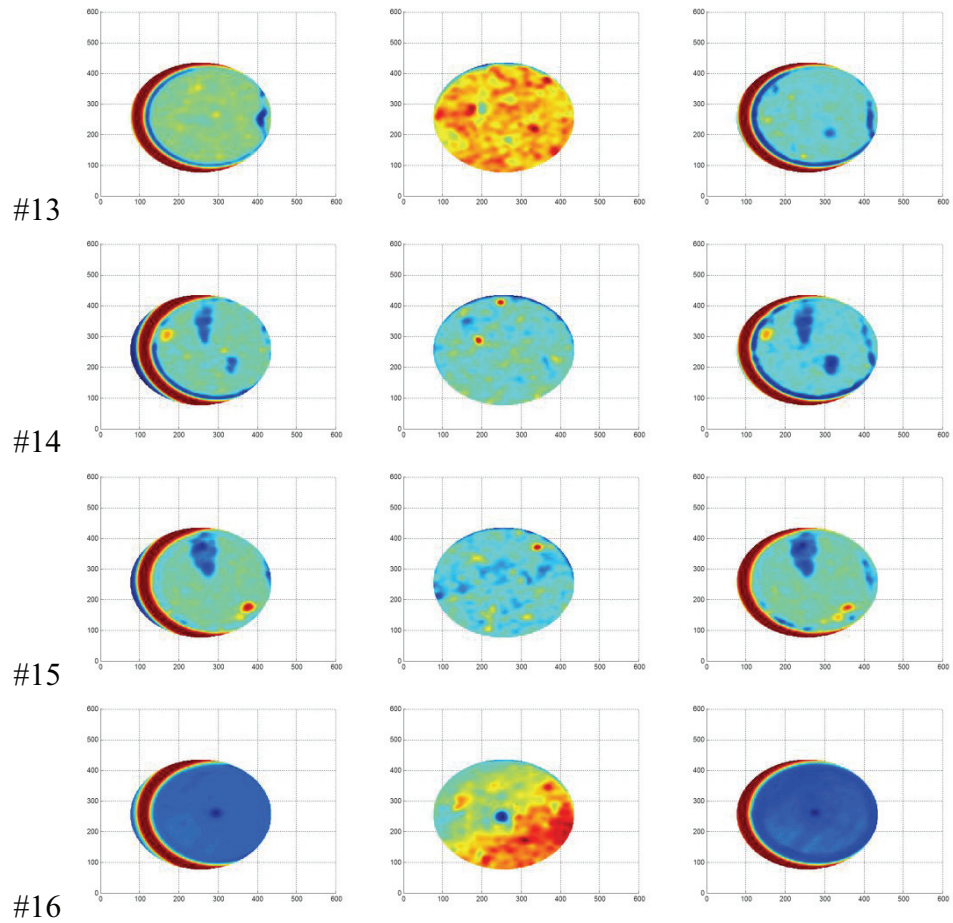


**Figure E.9** Saturation Calculation Code of CT Slice Views of Saturation (left), 100% Decane (center), 100% Water (right) for Core#5.

**CORE SAMPLE NUMERICAL SATURATION CALCULATION CODE  
BY MATLAB FOR CORE 5 AFTER PRODUCTION**

```
infosat = dicominfo('I:\NEW THESIS\thesis data\core#5\SC CORE 5WDP\SC
CORE 5WDP_15.dcm');
infoDec = dicominfo('I:\NEW THESIS\thesis data\core#2\SC CORE9-RD\SC
CORE9-RD_15.dcm');
infoWat = dicominfo('I:\NEW THESIS\thesis data\core#5\SC CORE 5W\SC
CORE 5W_15.dcm');
```

```
Ysat = dicomread(infosat);
Ysat_D = double(Ysat);
Ysat_D1 = zeros(512,512);
counter = 0;
total = 0;
for i = 1:512
for j = 1:512
if (Ysat_D(i,j)<-1000 || Ysat_D(i,j)>4000)
    Ysat_D1(i,j) = NaN;
elseif ((sqrt((i-256)^2+(j-256)^2)) > 180)

    Ysat_D1(i,j) = NaN;
else
    Ysat_D1(i,j) = Ysat_D(i,j);
    counter = counter + 1;
    total = total + Ysat_D(i,j);
end
end
end
```

```
Figure('Name','Sat');
ssat = surf(Ysat_D1, 'EdgeColor','none');
averagesat = total/counter
view(2);
```

```
%Figure('Name', 'satImage')
%imshow(Ysat,[]);
```

```
YDec = dicomread(infoDec);
YDec_D = double(YDec);
YDec_D1 = zeros(512,512);
counter = 0;
total = 0;
for i = 1:512
for j = 1:512
if (YDec_D(i,j)<-1000 || YDec_D(i,j)>4000)
    YDec_D1(i,j) = NaN;
elseif ((sqrt((i-256)^2+(j-256)^2)) > 180)

    YDec_D1(i,j) = NaN;
```

```

else
    YDec_D1(i,j) = YDec_D(i,j);
    counter = counter + 1;
    total = total + YDec_D(i,j);
end
end
end

Figure('Name','Dec');
ssat = surf(YDec_D1, 'EdgeColor','none');
averageDec = total/counter
view(2);

%Figure('Name', 'DecImage')
%imshow(YDec,[]);

YWat = dicomread(infoWat);
YWat_D = double(YWat);
YWat_D1 = zeros(512,512);
counter = 0;
total = 0;
for i = 1:512
for j = 1:512
if (YWat_D(i,j)<-1000 || YWat_D(i,j)>4000)
    YWat_D1(i,j) = NaN;
elseif ((sqrt((i-256)^2+(j-256)^2)) > 180)

    YWat_D1(i,j) = NaN;
else
    YWat_D1(i,j) = YWat_D(i,j);
    counter = counter + 1;
    total = total + YWat_D(i,j);
end
end
end

Figure('Name','Wat');
sWat = surf(YWat_D1, 'EdgeColor','none');
averageWat = total/counter
view(2);

%Figure('Name', 'WatImage')
%imshow(YWat,[]);

%Difference = (YWat_D1 - YDec_D1)/1000;

%Figure('Name','Difference');
%Difference = surf(Difference, 'EdgeColor','none');
%view(2);
saturation = (averagesat - averageDec)/(averageWat - averageDec)*100*0.73

```

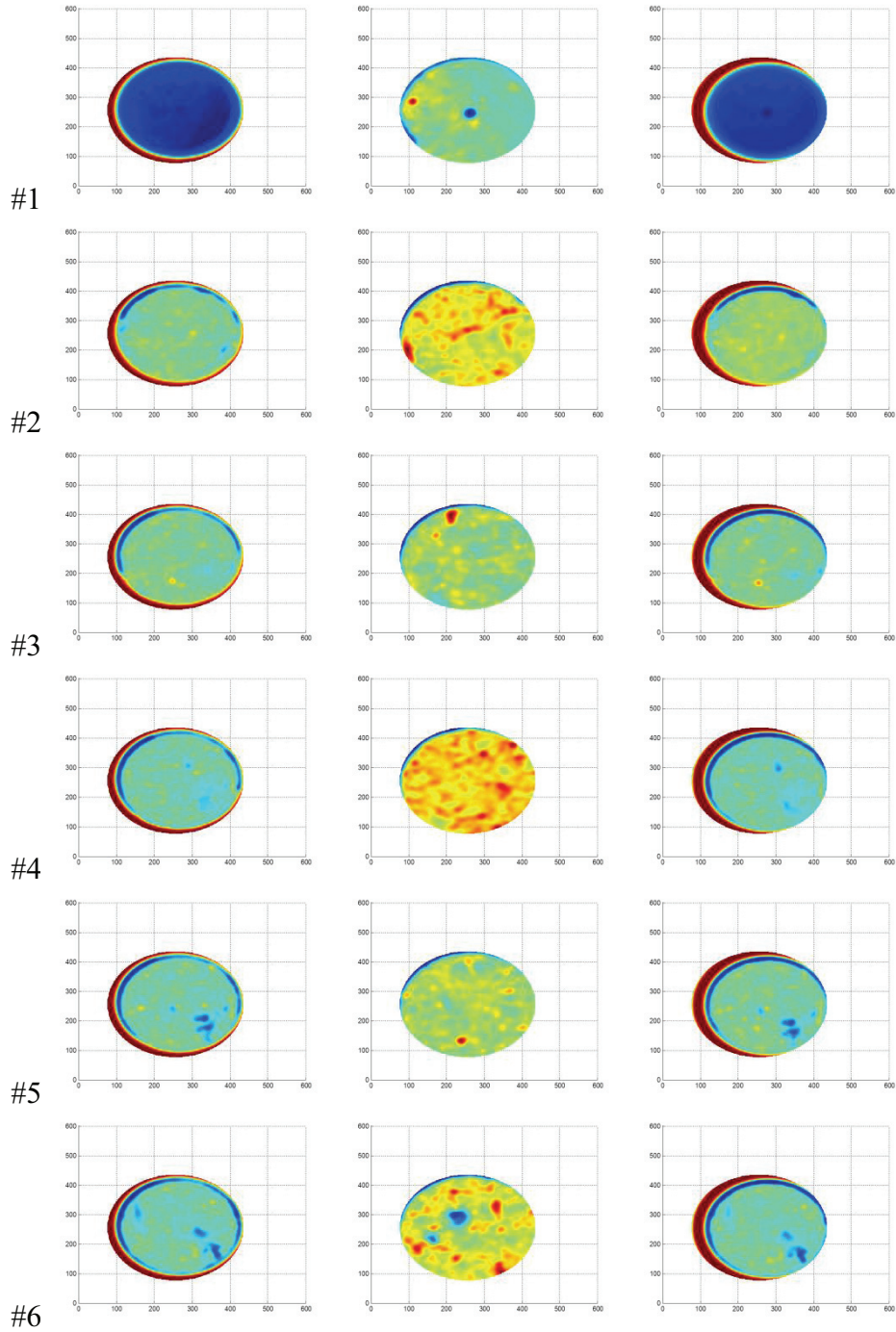


**Figure E.10** Saturation Calculation Code of CT Slice Views of Saturation (left), 100% Decane (center), 100% Water (right) for Core#5.

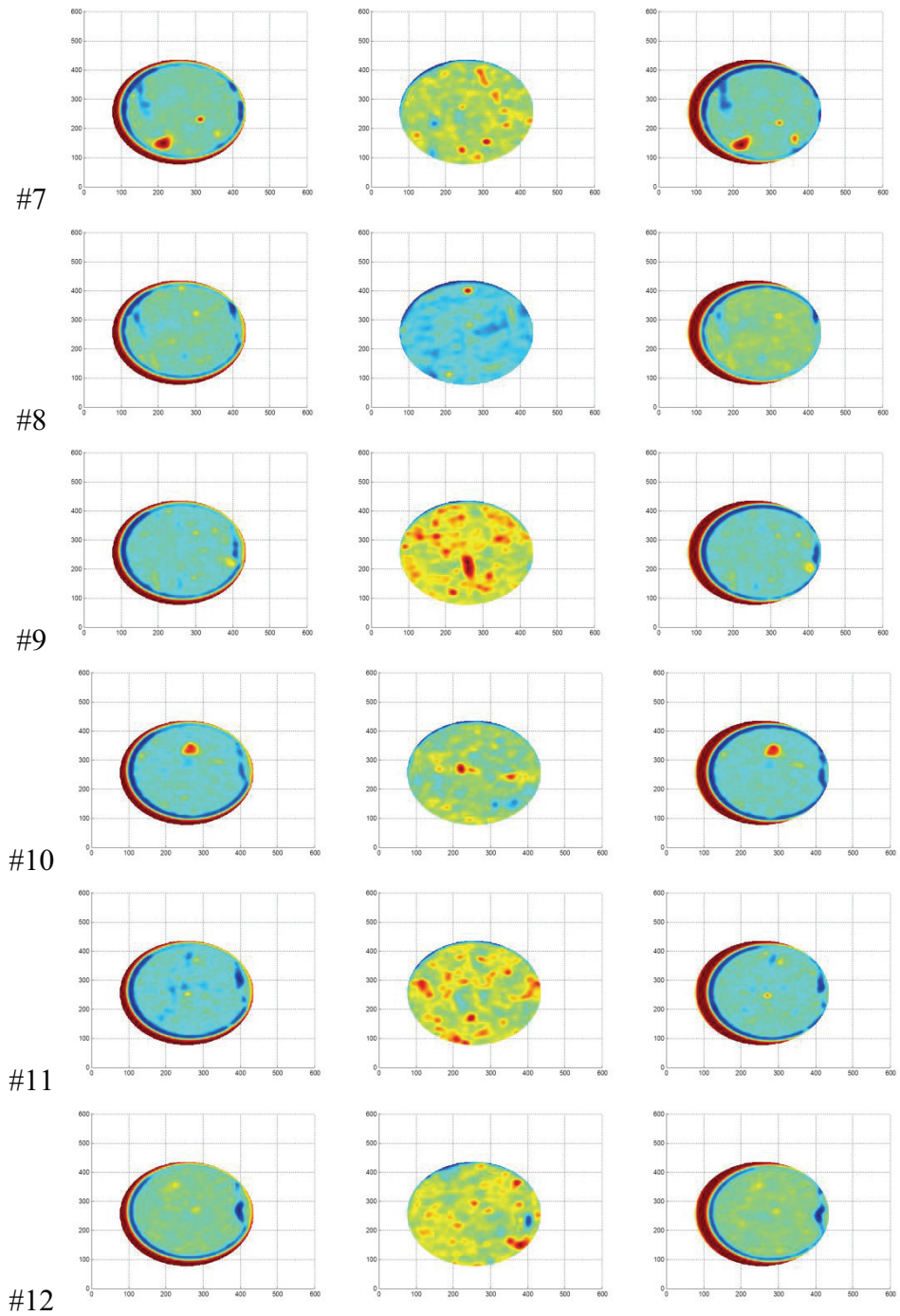


**Figure E.11** Saturation Calculation Code of CT Slice Views of Saturation (left), 100% Decane (center), 100% Water (right) for Core#5.

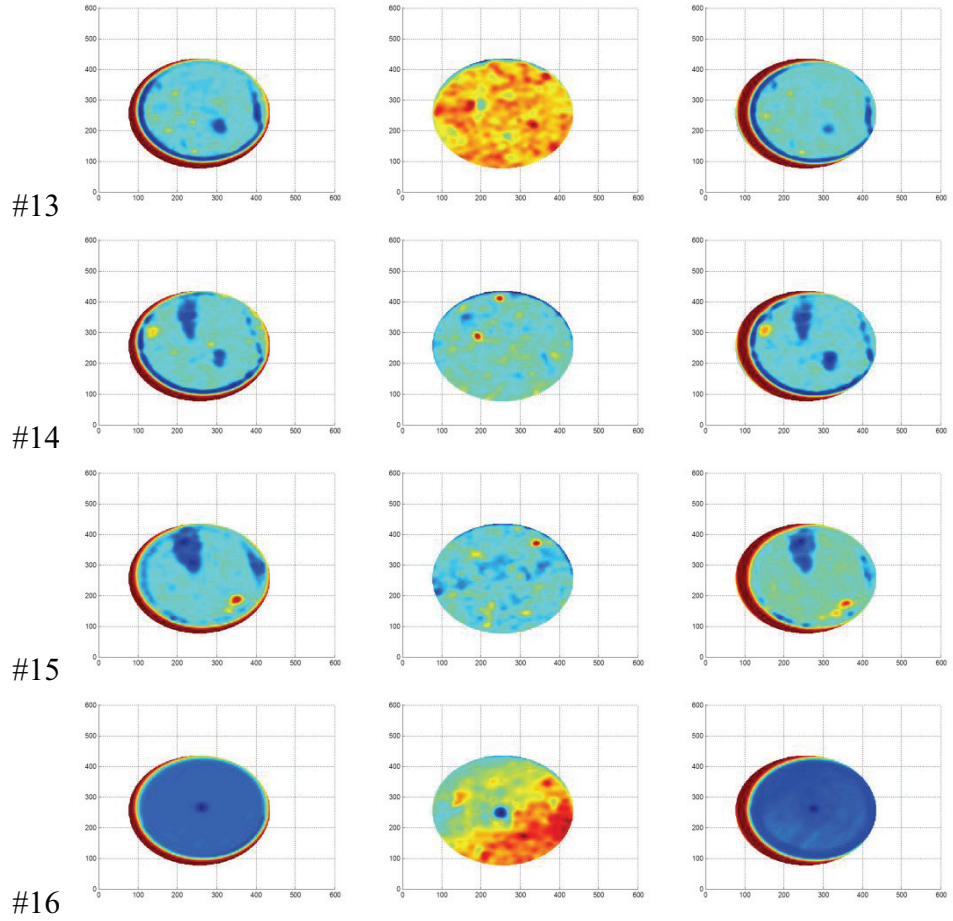


**Figure E.12** Saturation Calculation Code of CT Slice Views of Saturation (left), 100% Decane (center), 100% Water (right) for Core#5.

**CORE SAMPLE NUMERICAL SATURATION CALCULATION CODE  
BY MATLAB FOR CORE5 AFTER POLYMER GEL INJECTION**

```

infosat = dicominfo('I:\NEW THESIS\thesis data\core#5\SC CORE 5SWDPG\SC
CORE 5SWDPG_15.dcm');
infoDec = dicominfo('I:\NEW THESIS\thesis data\core#2\SC CORE9-RD\SC
CORE9-RD_15.dcm');
infoWat = dicominfo('I:\NEW THESIS\thesis data\core#5\SC CORE 5W\SC
CORE 5W_15.dcm');

Ysat = dicomread(infosat);
Ysat_D = double(Ysat);
Ysat_D1 = zeros(512,512);
counter = 0;
total = 0;
for i = 1:512
for j = 1:512
if (Ysat_D(i,j)<-1000 || Ysat_D(i,j)>4000)
    Ysat_D1(i,j) = NaN;
elseif ((sqrt((i-256)^2+(j-256)^2)) > 180)

    Ysat_D1(i,j) = NaN;
else
    Ysat_D1(i,j) = Ysat_D(i,j);
    counter = counter + 1;
    total = total + Ysat_D(i,j);
end
end
end

Figure('Name','Sat');
ssat = surf(Ysat_D1, 'EdgeColor','none');
averagesat = total/counter
view(2);

%Figure('Name', 'satImage')
%imshow(Ysat,[]);

YDec = dicomread(infoDec);
YDec_D = double(YDec);
YDec_D1 = zeros(512,512);
counter = 0;
total = 0;
for i = 1:512
for j = 1:512
if (YDec_D(i,j)<-1000 || YDec_D(i,j)>4000)
    YDec_D1(i,j) = NaN;
elseif ((sqrt((i-256)^2+(j-256)^2)) > 180)

    YDec_D1(i,j) = NaN;

```

```

else
    YDec_D1(i,j) = YDec_D(i,j);
    counter = counter + 1;
    total = total + YDec_D(i,j);
end
end
end

Figure('Name','Dec');
ssat = surf(YDec_D1, 'EdgeColor','none');
averageDec = total/counter
view(2);

%Figure('Name', 'DecImage')
%imshow(YDec,[]);

YWat = dicomread(info Wat);
YWat_D = double(YWat);
YWat_D1 = zeros(512,512);
counter = 0;
total = 0;
for i = 1:512
for j = 1:512
if (YWat_D(i,j)<-1000 || YWat_D(i,j)>4000)
    YWat_D1(i,j) = NaN;
elseif ((sqrt((i-256)^2+(j-256)^2)) > 180)

    YWat_D1(i,j) = NaN;
else
    YWat_D1(i,j) = YWat_D(i,j);
    counter = counter + 1;
    total = total + YWat_D(i,j);
end
end
end

Figure('Name','Wat');
sWat = surf(YWat_D1, 'EdgeColor','none');
averageWat = total/counter
view(2);

%Figure('Name', 'WatImage')
%imshow(YWat,[]);
%Difference = (YWat_D1 - YDec_D1)/1000;
%Figure('Name','Difference');
%sDifference = surf(Difference, 'EdgeColor','none');
%view(2);

saturation = (averagesat - averageDec)/(averageWat - averageDec)*100/1.34

```

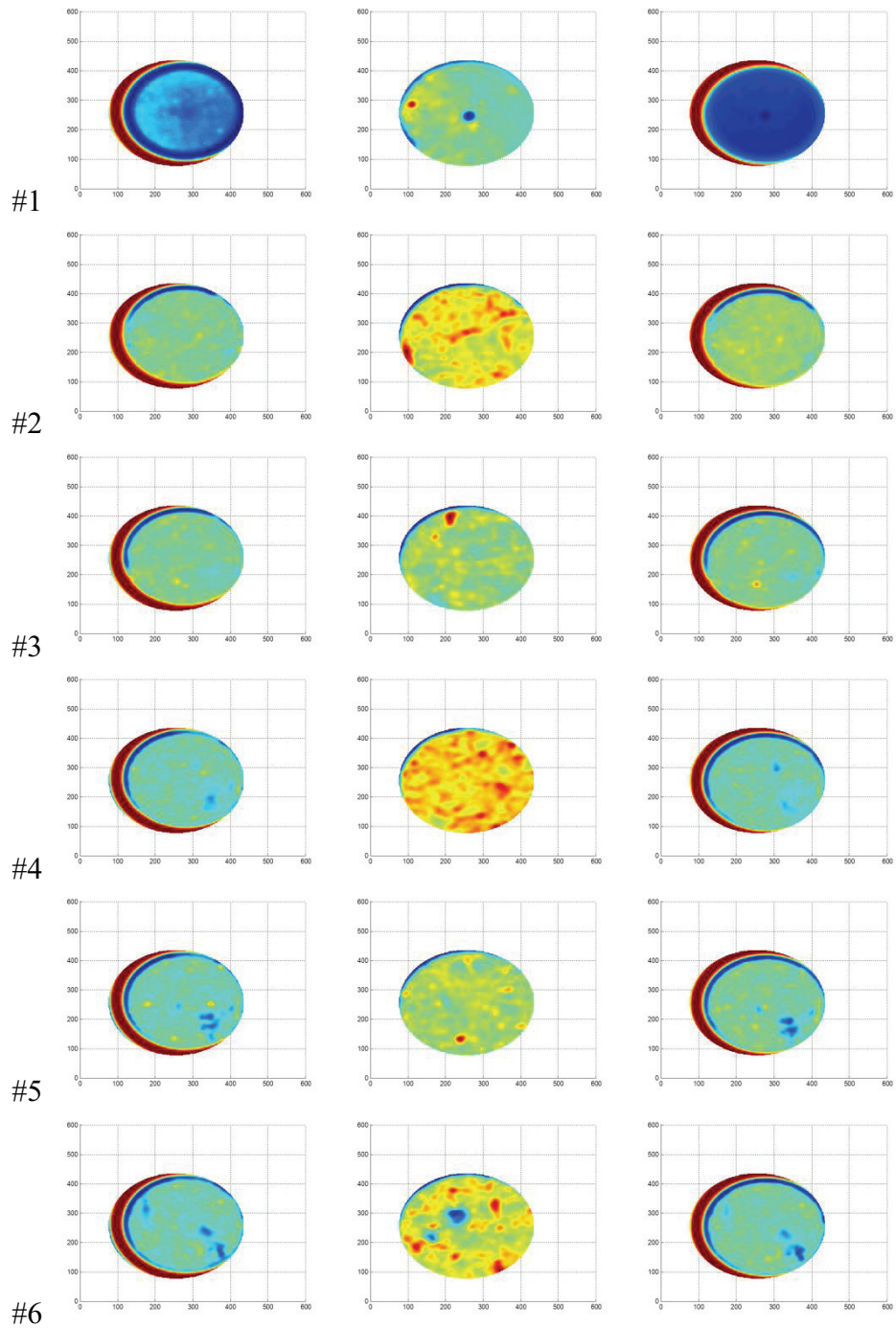


**Figure E.13** Saturation Calculation Code of CT Slice Views of Saturation (left), 100% Decane (center), 100% Water (right) for Core#5.

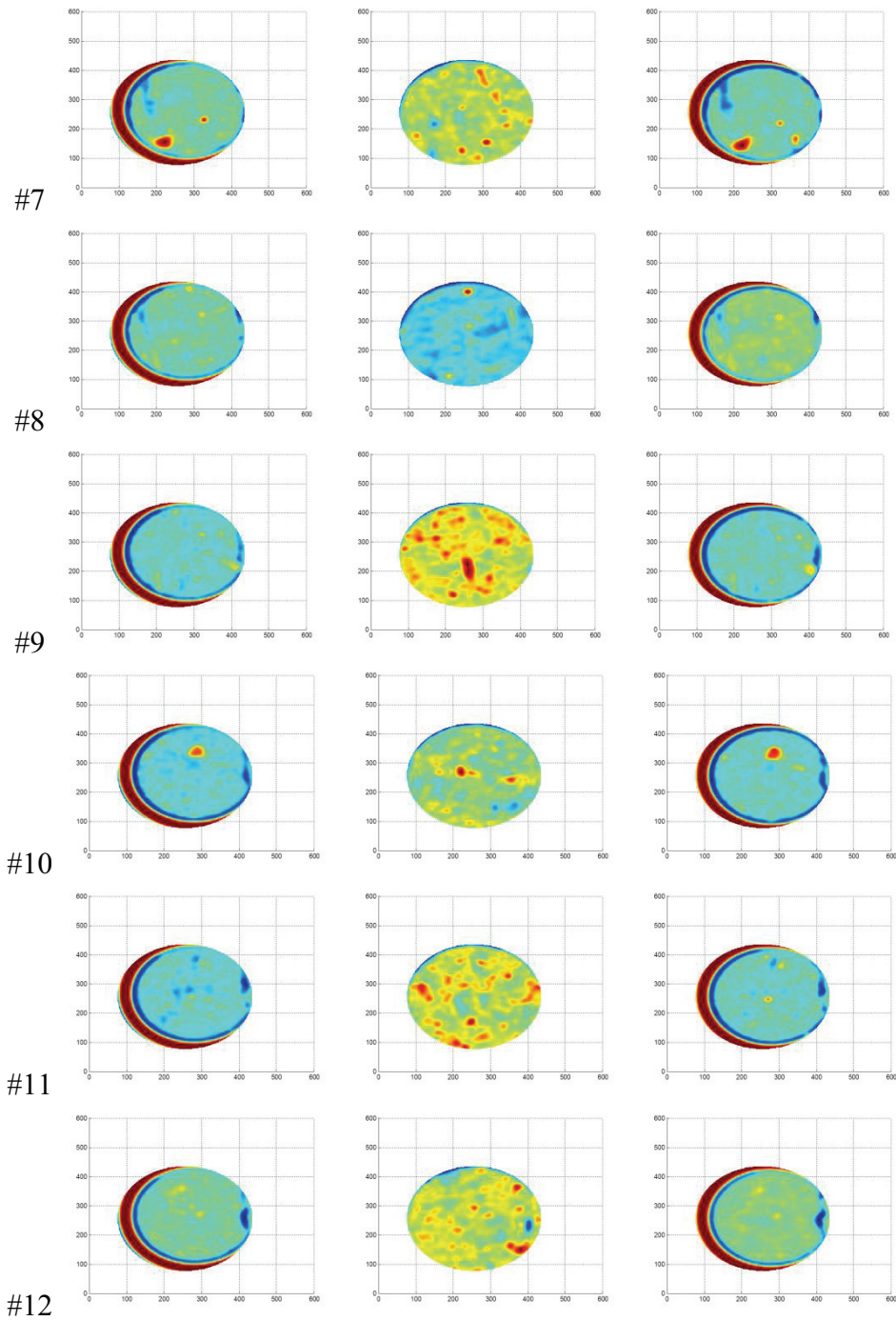


**Figure E.14** Saturation Calculation Code of CT Slice Views of Saturation (left), 100% Decane (center), 100% Water (right) for Core#5.

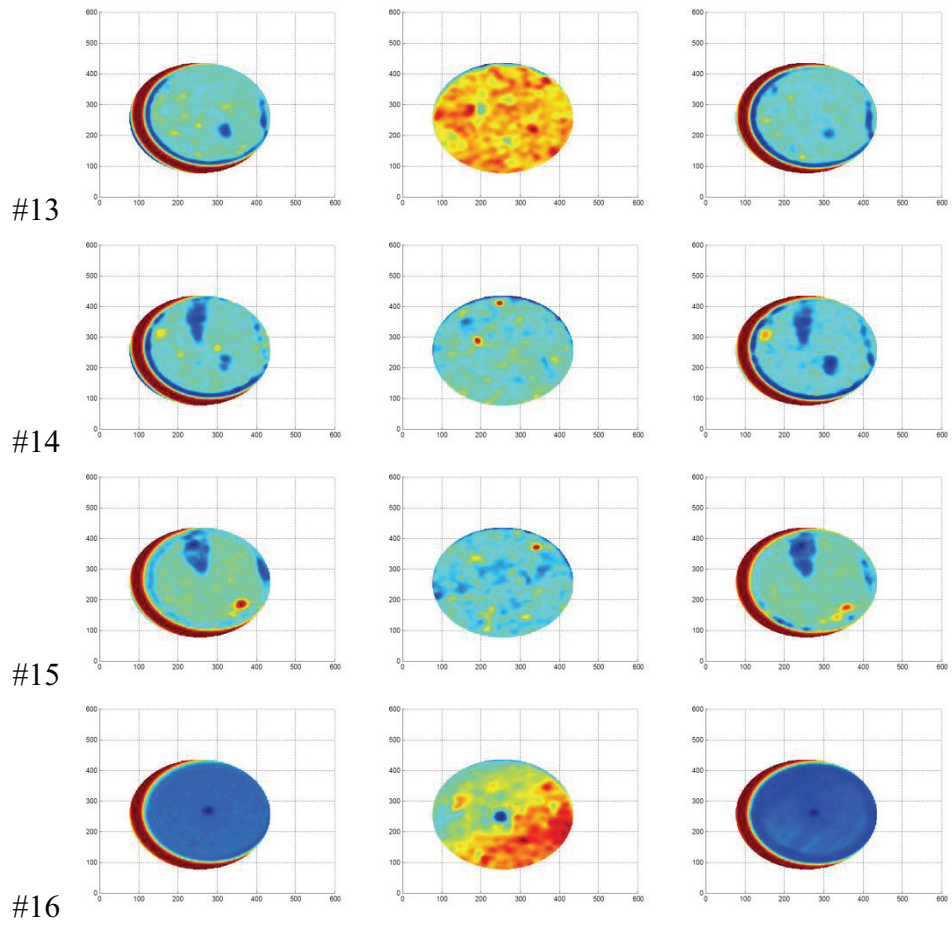


**Figure E.15** Saturation Calculation Code of CT Slice Views of Saturation (left), 100% Decane (center), 100% Water (right) for Core#5.



## CURRICULUM VITAE

**Surname, Name:** Canbolat, Serhat

**Nationality:** Turkish (TC)

**Date and Place of Birth:** 08 October 1973, Ankara

**Marital Status:** Single

Phone: +90 312 210 28 95

email: canbolats@yahoo.com

### EDUCATION

Degree	Institution	Year of Graduation
MS	University of Alberta Edmonton, Canada Petroleum Engineering	2005
MS	METU Petroleum and Natural Gas Engineering	2003
BS	METU Petroleum and Natural Gas Engineering	1997
High School	Gazi Anadolu High School, Ankara	1991

### WORK EXPERIENCE

Year	Place	Enrollment
2016-Present	Near East University North Cyprus	Instructor
2012-2015	TIWAY Turkey LCC.	Reservoir Manager
2006-2011	Aladdin Middle East Ltd.	Reservoir Engineer
2003- 2005	University of Alberta Petroleum Eng.Dept.	Research Assistant
2001-2002	METU Petroleum and Natural Gas Eng.Dept.	Research Assistant
1998-2000	Turkish Petroleum Co.	Well Completion Engineer
1996 July	Turkish Petroleum Co.	Intern Engineering Student
1994 July	Aladdin Middle East Ltd.	Intern Engineering Student

### FOREIGN LANGUAGES

Advanced English, Intermediate German

### PUBLICATIONS

1.Fracture Effect Limitation on Residual Oil Saturation: Aperture Shrinkage, SPE 189467, SPE International Conference and Exhibition on Formation Damage Control held in Lafayette, Louisiana, USA, 7-9 February 2018.

2.Well Selection Criteria for Water Shut-Off Polymer Gel Injection in Carbonates, SPE 158059, 12.SPE Abu Dhabi International Petroleum Exhibition & Conference held in Abu Dhabi, UAE, 11-14 November 2012.